GDAŃSK UNIVERSITY OF TECHNOLOGY

GDAŃSK UNIVERSITY OF TECHNOLOGY
FACULTY OF OCEAN ENGINEERING AND SHIP TECHNOLOGY

Polish Maritime Research

No 1 (101) 2019
Vol. 26

ADDRESS OF PUBLISHER & EDITOR'S OFFICE:

GDAŃSK UNIVERSITY OF TECHNOLOGY

Faculty of Ocean Engineering & Ship Technology
G. Narutowicza 11/12
80-233 Gdańsk, POLAND

Price:
single issue: 25 PLN

Prices for abroad
single issue:
- in Europe EURO 15
- overseas USD 20

WEB:
pg.edu.pl/pmr

e-mail : pmr@pg.edu.pl

ISSN 1233-2585

CONTENS

ADDRESS OF PUBLISHER & EDITOR'S OFFICE:

GDAŃSK UNIVERSITY OF TECHNOLOGY

Faculty of Ocean Engineering & Ship Technology
G. Narutowicza 11/12
80-233 Gdańsk, POLAND

Editorial

POLISH MARITIME RESEARCH is the scientific journal with a worldwide circulation. This journal is published quarterly (four times a year) by Gdansk University of Technology (GUT). On September, 1994, the first issue of POLISH MARITIME RESEARCH was published. The main objective of this journal is to present original research, innovative scientific ideas, and significant findings and application in the field of **:**

Naval Architecture, Ocean Engineering and Underwater Technology,

The scope of the journal covers selected issues related to all phases of product lifecycle and corresponding technologies for offshore floating and fixed structures and their components.
All researchers are invited to submit their original papers for peer review and publications related to methods of the design; production and manufacturing; maintenance and operational processes of such technical items as:

- all types of vessels and their equipment,
- fixed and floating offshore units and their components,
- autonomous underwater vehicle (AUV) and remotely operated vehicle (ROV).

We welcome submissions from these fields in the following technical topics:

- ship hydrodynamics: buoyancy and stability; ship resistance and propulsion, etc.,
- structural integrity of ship and offshore unit structures: materials; welding; fatigue and fracture, etc.,
- marine equipment: ship and offshore unit power plants: overboarding equipment; etc.

We are pleased to invite you
to participate in the

International Symposium on Fluid Acoustics

IFA2019

Sopot

May 20-22,2019

We invite representatives of scientific, medical, and technical communities with experience in:

- research in water environment
- using acoustic methods for medical diagnosis
- constructing acoustic and ultrasonic research equipment
- technical diagnostics
- imaging of phenomena occurring in liquids

Creating a platform for exchanging experiences with the possibilities offered by analogous methods in various applications may be an inspiration to expand research methods through the use of solutions from another area of science.

POLSKA AKADEMIA NAUK

POLITECHNIKA GDAŃSKA

www.ifa2019.pl

Coastal, Offshore and Ocean Engineering Conference 2019

08.11.2019

4th edition

When and where	Gdansk Poland Gdansk University of Technology **Faculty of Ocean Engineering and Ship Technology**
Date	08.11.2019
Focus	Practical application with modern technological and scientific achievements following aspects of coastal, offshore and ocean engineering.
Conference aim and scope	• Coastal facilities, coastal processes, sediment transport, ports & harbors, satellite observations etc. • Offshore structures, floating facilities, pipeline, wave impact on coastal and offshore structures, marine renewables, offshore operations, foundation engineering, ocean mining etc. • Naval architecture; marine structural mechanics; safety and reliability; materials, computational fluid dynamics, vibrations, hydrodynamics, fluid-structure interaction, underwater technology, coastal engineering, marine environmental engineering. • Additional session is planed „Water lubrication" - as a continuation of scientific seminar entitled Gdansk International Seminar on Water Lubricated Bearings WatLuBe initiated in 2016
Publications	All accepted and paid papers will be published in journal Polish Maritime Research
Fee	• Invited speakers, guests – free. Fee consist two parts: • Participation in conference - 100 zł (included: participant ID, printed special issue of PMR, coffee, dinner) - paid till 30.09.2019. • Open access journal publishing – Open Access and Article Processing Charge (APC) - 500 euro
Additional information	https://pg.edu.pl/coo

sciendo

POLISH MARITIME RESEARCH 1 (101) 2019 Vol. 26; pp. 6-14
10.2478/pomr-2019-0001

ANALYSIS OF IMPACT OF SHIP MODEL PARAMETERS ON CHANGES OF CONTROL QUALITY INDEX IN SHIP DYNAMIC POSITIONING SYSTEM

Tacjana Niksa Rynkiewicz
Anna Witkowska
Gdańsk University of Technology, Poland

ABSTRACT

In this work there is presented an analysis of impact of ship model parameters on changes of control quality index in a ship dynamic positioning system designed with the use of a backstepping adaptive controller. Assessment of the impact of ship model parameters was performed on the basis of Pareto-Lorentz curves and ABC method in order to determine sets of the parameters which have either crucial, moderate or low impact on objective function. Simulation investigations were carried out with taking into account integral control quality indices.

Keywords: backstepping, ship dynamic positioning, system's susceptibility

INTRODUCTION

The main ship control classification system covers a control at greater speeds and that at low speeds. It is usually assumed that ship motion at a speed higher than 2m/s [11, 14, 15, 17, 22], is that carried out at greater speeds and deals with course keeping and motion along a given trajectory. Such motion control operations are performed in two degrees of freedom (2DOF). They cover ship longitudinal motion and rotation, i.e. heading change. And, ship motion control at a speed below 2m/s concerns a precision control and covers dynamic positioning (DP) whose aim is to keep a ship in a constant position and heading at a high level of external disturbances resulting from sea environmental effects of wind, waves, sea current and shallow water acting on ship hull [19].

The manoeuvring of ship at dynamic positioning covers 3DOF control (i.e. in three directions of motion). In this case there is possible to independently control ship position (x, y) and its rotation r by changing bow heading angle relative to north.

Ship's structure and sea environment disturbances acting on it make that ship is not capable of changing direction of its motion (its orientation) on the spot. Taking into account an aim of control one strives to minimize deviations from a given position and heading by making use of ship propulsion and motion control devices such as screw propellers, rudders, azimuth propellers, thrusters.

Most of contemporary DP ship control methods are based on equations of mathematical model of object kinematics and dynamics [9, 22, 28]. Changes in point of operation of the system and impact of hydrodynamic phenomena result

in that the ship kinematics and dynamics equations contain nonlinearities as well as variable coefficients.

Control over nonlinear systems with uncertainties still constitutes rather a not recognized field. The adaptive control method such as disturbance rejection control (ADSC), backstepping [10, 24, 25] as well as its modifications either of DSC (dynamic surface control) type [20, 26, 27] or other adaptive methods based on artificial intelligence theory [1, 3, 12, 16], make it possible to design a dynamically varying feedback loop. The fundamental idea of the adaptive designing of control rule consists first of all in the assessing of value of an unknown parameter as well as the determining of its estimate. Next, the static part of the controller which contains estimated parameters is continuously actualized, depending on varying operational conditions of the system.

From the point of view of adaptive controller resistance analysis, information as to the impact of model parametric uncertainties on to control quality of the system, is crucial. In order to determine the impact of parameters of a multi-parameter model on dynamic properties of control system there can be used a. o. numerical methods such as Monte Carlo [27, 28], or Pareto [29] approach as well as artificial intelligence methods, which facilitate assessment of imprecise values as well as their interpretation in case of uncertain data [5, 21]. In the classic Monte Carlo method, the susceptibility of the system is subject to assessing in the situation when all parameters deviate from their nominal values simultaneously. By applying Pareto rule the system is subject to quality analysis. For an assumed variability range of estimated parameters, classification is performed and an impact of particular system parameters on value of objective function is determined.

An original contribution of this work to the considered question is determination of linguistic variables characterizing susceptibility of model parameters as well as determination of their affiliation to appropriate sets which define either crucial, moderate or minimum impact of the parameters on objective function. For this reason, there was carried out a susceptibility analysis of changes in values of control quality index for the ship dynamic positioning system designed with the application of the backstepping adaptive controller [10, 24, 6]. Such system was already proposed by these authors in the paper [25].

In this work simulation investigations on the susceptibility of the system were performed with taking into account the integral control quality index. The assessment of the impact of model parameters on to control quality index was made on the basis of Pareto-Lorentz curves. During designing the control rule there were assumed that parametric uncertainties of damping matrix, Coriolis forces and environmental disturbances, may appear. The RBF neural network [2, 4, 18] was applied in every instant to approximate nonlinear functions containing parametric uncertainties. Rules for network's weights adaptation were determined with the use of Lapunov stability theory, depending on a point of operation of the system. Owing to this the neural network does not require any initial process of tuning the weights off-line.

STRUCTURE OF CONTROL SYSTEM

As far as the multi-layer structure of DP ship control is concerned, two control loops are of interest: the open feedforward loop where coupling signal is generated by the block of disturbance modelling (model of wind) as well as the main feedback control loop where set values of ship position and heading (course angle) are compared with their estimated values. The feedback control loop interacts with the control block directly, the drive control allocation system and measuring systems as well as the systems for ship position and heading estimation. The main control loop (Fig. 1) consists of the following modules: position and heading controller with control allocation system, dynamics of propellers, dynamics of DP ship (controlled object), and the observer of current estimated output values of position, heading and speed components: longitudinal, transverse and angular.

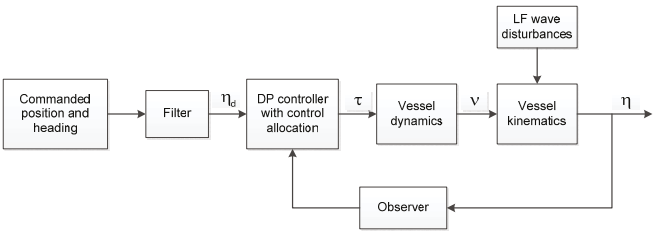

Fig. 1 Structure of DP control system

Based on comparison of the vector of set values of position and heading, $\boldsymbol{\eta}_{\mathbf{d}}$, with the vector of currently estimated values achieved from the observer, the DP controller determines forces and moments necessary to compensate deviations from the set values, in accordance with an assumed value of control error. In this system the DP controller of ship position and heading controls independently motion of the object in three degrees of freedom, determining: set values, the generalized vector of longitudinal and transverse forces and torsion moment for drive control allocation system where distribution of forces to appropriate settings of actuators is performed.

The system based on adaptive model of object, in this case – a ship, contains hydrodynamic description of its dynamic features and makes it possible to determine estimated values of parameters of position and heading. The model describes object's motion and response, with taking into account variable characteristics of resistance and added mass coefficients, depending on acting forces and moments.

MATHEMATICAL MODEL OF DP SHIP

During designing the control rule based on backstepping method and artificial neuronal networks, the mathematical model of motion of a unit dynamically positioned in horizontal plane, described by the following set of differential equations, was assumed [7]:

$$\dot{\boldsymbol{\eta}} = \mathbf{J}(\boldsymbol{\eta})\mathbf{v} \tag{1}$$

$$\mathbf{M}(\mathbf{v})\dot{\mathbf{v}} = \boldsymbol{\tau} + \mathbf{J}(\boldsymbol{\eta})^T\mathbf{b} - \mathbf{D}(\mathbf{v})\mathbf{v} - \mathbf{C}(\mathbf{v})\mathbf{v} \tag{2}$$

where: $\boldsymbol{\tau} = [\tau_x, \tau_y, \tau_z]^T$ – generalized vector of forces and moments acting on the ship, $\boldsymbol{\tau} = [x, y, \psi]^T$ – vector of ship position and heading, $\mathbf{v} = [u, -v, r]^T$ – vector of longitudinal, transverse and angular components of ship speed; the matrices $\mathbf{M} \in R^{3x3}$, $\mathbf{D} \in R^{3x3}$ i $\mathbf{C} \in R^{3x3}$, $\mathbf{J}(\boldsymbol{\eta}) \in R^{3x3}$ define respectively:

Inertia matrix

$$\mathbf{M} = \begin{bmatrix} m_{11} & 0 & 0 \\ 0 & m_{22} & m_{23} \\ 0 & m_{32} & m_{33} \end{bmatrix}$$

Damping matrix

$$\mathbf{D} = \begin{bmatrix} d_{11} & 0 & 0 \\ 0 & d_{22} & d_{23} \\ 0 & d_{32} & d_{33} \end{bmatrix}$$

Matrix of Coriolis forces

$$\mathbf{C}(\mathbf{v}) = \begin{bmatrix} 0 & 0 & c_1 v + c_2 r \\ 0 & 0 & c_3 u" \\ -c_1 v" - c_2 r" & -c_3 u" & 0 \end{bmatrix}$$

and the transformation matrix (dependent on state variables) of ship's gravity centre coordinates into the Earth-fixed coordinate frame:

$$\mathbf{J}(\boldsymbol{\eta}) = \begin{bmatrix} cos\psi & -sin\psi & 0 \\ sin\psi & cos\psi & 0 \\ 0 & 0 & 1 \end{bmatrix}$$

The vector $\mathbf{b} = [b_1, b_2, b_3]^T$ represents non-modelled, slow-varying environmental disturbances. The ship's model takes into account 3DOF motion, namely: longitudinal motion, transverse motion and change in bow heading angle.

The equation system (1)-(2) is of a cascade structure. The vector $\boldsymbol{\tau}$ constitutes the control input to the system, while the vector $\mathbf{v}$ is a "virtual controllable output ". It simultaneously serves as a „virtual control input" for the subsystem (1). The vector of ship's position and heading, $\boldsymbol{\eta}$, is the controllable output from the whole system.

During designing the control rule there was assumed that the ship's dynamics model contains parametric uncertainties in the matrices **D, C, M**, and that components of the vector **b** are unknown but slow-varying. Moreover, there was assumed that all state variables are measurable (or estimated) and limited. The set trajectories of position and heading, $\boldsymbol{\eta}_d = [x_d, y_d, \psi_d]^T$ as well as their derivatives of 1st and 2nd order are smooth and time – limited functions.

DP CONTROLLER

According to the backstepping method, for the system (1)-(2) there were defined new state variables in the form of the control errors $\mathbf{z}_1(t) \in R^{3x1}$ and $\mathbf{z}_2(t) \in R^{3x1}$ as well as the vector of functions for stabilizing the first subsystem, $\boldsymbol{\alpha} \in R^{3x1}$. In the ship-fixed coordinate frame the control errors take the following form:

$$\mathbf{z}_1 = \mathbf{J}(\boldsymbol{\eta})^T(\boldsymbol{\eta} - \boldsymbol{\eta}_d) \tag{3}$$

$$\mathbf{z}_2 = \mathbf{v} - \boldsymbol{\alpha} \tag{4}$$

And, the stabilizing functions vector will be determined during designing the control rule. Based on the model kinematics and dynamics equations (1)-(2), derivatives of the control errors were determined as follows [25]:

$$\dot{\mathbf{z_1}} = -r\mathbf{S}\mathbf{z}_1 + \mathbf{z}_2 + \boldsymbol{\alpha} - \mathbf{J}(\boldsymbol{\eta})^T\dot{\boldsymbol{\eta}}_d \tag{5}$$

$$\mathbf{M}\dot{\mathbf{z_2}} = \boldsymbol{\tau} + \boldsymbol{f}(\boldsymbol{\eta}, \mathbf{v}, \boldsymbol{\eta_d}, \mathbf{v_d}) \tag{6}$$

After denoting the state variables dependent matrix by: $\mathbf{X} = [\boldsymbol{\eta}, \mathbf{v}, \boldsymbol{\eta_d}, \mathbf{v_d}]$, the function $\boldsymbol{f} \in R^{3x1}$ takes the following form:

$$\boldsymbol{f}(\mathbf{X}) = -\mathbf{C}\mathbf{v} - \mathbf{D}\mathbf{v} + \mathbf{J}(\boldsymbol{\eta})^T\mathbf{b} - \mathbf{M}\dot{\boldsymbol{\alpha}} \tag{7}$$

which contains unknown model parameters.

In order to determine the adaptation rule for the parameters of the matrices **M, D, C** and the vector **b** it is necessary to represent the function $\boldsymbol{f}$ in the form of a regression model and proceed further in compliance with the backstepping procedure. The components of the function $\boldsymbol{f} = [f_1, f_2, f_3]^T$ were approximated by three artificial neural networks NN_i of RBF type [25] whose outputs $\hat{\boldsymbol{f}} = [\hat{f}_1, \hat{f}_2, \hat{f}_3]^T$ were defined in the form of the following regression model:

$$\hat{f}_i(\mathbf{X}_i) = \boldsymbol{\varphi}_i^T(\mathbf{X}_i)\boldsymbol{\theta}_i;\ i = 1..3 \tag{8}$$

In the proposed system the number of radialneurons $l = 4$ was determined experimentally.

The input vector for neural network is as follows: $\mathbf{X}_i = [\boldsymbol{\eta}(i), \mathbf{v}(i), \boldsymbol{\eta_d}(i), \mathbf{v_d}(i)]^T \in R^{4x1}$, and the set of values of basis functions of the networks NN_i: $\boldsymbol{\varphi}_i = [\boldsymbol{\varphi}_{i1}, \boldsymbol{\varphi}_{i2}, \ldots, \boldsymbol{\varphi}_{il}]^T \in R^{lx1}$. Selection of the weights $\boldsymbol{\theta}_i = [\boldsymbol{\theta}_{i1}, \boldsymbol{\theta}_{i2}, \ldots, \boldsymbol{\theta}_{il}]^T \in R^{lx1}$ was made during the process of the control system adaptation to varying operational conditions.

The control error dynamics equation (6) supplemented with RBF network equation, takes the following form:

$$\mathbf{M}\dot{\mathbf{z}_2} = \boldsymbol{\tau} + \boldsymbol{\varphi}^T(X)\boldsymbol{\theta} \tag{9}$$

The regression vector, i. e. the vector of RBF network weights, is defined to be: $\boldsymbol{\theta}=[\boldsymbol{\theta}_1^T, \boldsymbol{\theta}_2^T, \boldsymbol{\theta}_3^T]^T \in R^{3lx1}$. And, the regression matrix $\boldsymbol{\varphi}^T \in R^{3x3l}$ is expressed as follows:

$$\boldsymbol{\varphi}^T = \begin{bmatrix} \boldsymbol{\varphi_1}^T(X) & \mathbf{0_{1xl}} & \mathbf{0_{1xl}} \\ \mathbf{0_{1xl}} & \boldsymbol{\varphi_2}^T(X) & \mathbf{0_{1xl}} \\ \mathbf{0_{1xl}} & \mathbf{0_{1xl}} & \boldsymbol{\varphi_3}^T(X) \end{bmatrix} \tag{10}$$

The task for the backstepping controller is to determine the indirect control rule $\boldsymbol{\alpha}$ intended for stabilizing the first subsystem (1), next the control rule $\boldsymbol{\tau}$ for stabilizing the entire system (1)-(2) as well as the adaptation rule for the vector of weights $\boldsymbol{\theta}$, in relation to Lapunov function of the system.

The control rule was determined in relation to the Lapunov function V_α which is a sum of squares of control errors and a component associated with estimation error of an unknown vector of weights $\boldsymbol{\theta}$.

$$\mathbf{V}_a = \frac{1}{2}\mathbf{z}_1^T\mathbf{z}_1 + \frac{1}{2}\mathbf{z}_2^T\mathbf{M}\mathbf{z}_2 + \frac{1}{2}\tilde{\boldsymbol{\theta}}^T\boldsymbol{\Gamma}^{-1}\tilde{\boldsymbol{\theta}} \tag{11}$$

where: $\boldsymbol{\Gamma} > 0$ is the diagonal matrix of controller amplifications, $\dim\boldsymbol{\Gamma} = 3l$ x $3l$, $\tilde{\boldsymbol{\theta}}$ – the vector of estimation errors.

The control rules, $\boldsymbol{\alpha}$, $\boldsymbol{\tau}$ are so selected as the Lapunov function derivative (12) to be negatively half-determined in the new variables system:

$$\dot{\mathbf{V}}_a = -\mathbf{z}_1^T\mathbf{K}_1\mathbf{z}_1 - \mathbf{z}_2^T\mathbf{K}_2\mathbf{z}_2 \leq \mathbf{0} \tag{12}$$

And, $\mathbf{K}_j \in R^{3x3}$, $j = \{1,2\}$, represents the control amplifications matrix which is diagonal and positively determined. Comparing the derivative of the function (11) with the expression (12) one is able to determine the following relations:

- Adaptation mechanism for weights:

$$\dot{\hat{\boldsymbol{\theta}}} = \boldsymbol{\Gamma}\boldsymbol{\varphi}(\mathbf{X})\mathbf{z}_2 \tag{13}$$

- Vector of stabilizing functions $\boldsymbol{\alpha}$, independent of the vector of estimates $\hat{\boldsymbol{\theta}}$:

$$\boldsymbol{\alpha} = -\mathbf{K}_1\mathbf{z}_1 + \mathbf{J}(\boldsymbol{\eta})^T\dot{\boldsymbol{\eta}}_d \tag{14}$$

- Vector of control settings $\boldsymbol{\tau}$, dependent on the vector of estimates $\hat{\boldsymbol{\theta}}$ (weights of RBF network), calculated in accordance with (13), under assumption that the network posesses a sufficient number of neurons:

$$\boldsymbol{\tau} = -\mathbf{K}_2\mathbf{z}_2 - \mathbf{z}_1 - \boldsymbol{\varphi}^T(X)\hat{\boldsymbol{\theta}} \tag{15}$$

If in the system fast varying disturbances do not act then the control rule (15) together with the adaptation rule (13) ensures asymptotic convergence of ship position and heading towards their set values, $\boldsymbol{\eta}(t) \to \boldsymbol{\eta}_d(t)$, at $\mathbf{v}(t) \approx 0$. It also ensures limited changes in the signals $\boldsymbol{\eta}(t)$ i $\mathbf{v}(t)$, $t \to \infty$, at a limited change in values of estimated parameters.

DESCRIPTION OF THE METHOD

For the investigations of impact of ship model parameters on control system quality, the integral quality index J defined to be a sum of squares of control deviations, was assumed:

$$J = \int_{t_0}^{t_n}((x - x_d)^2 + (y - y_d)^2 + (\psi - \psi_d)^2)dt \tag{16}$$

The quality of the control system designed on the basis of ship's mathematical model is affected a.o. by errors resulting from non-exact information on the model parameters, i.e. coefficients of the matrices **M**, **C**, **D** and **b.** Applying the procedure described in [29], one determined a set of basis parameters whose impact on objective function is investigated. Next, for every basis parameter p_i, $i \in \{1,..,n\}$ its variability interval was assumed as follows:

$$p_{imin} < p_i < p_{imax}$$

For the analyzing of impact of particular parameters on value of the objective function J_i in the form of (17):

$$J_i = \frac{|J_{imax} - J_{imin}|}{J_{imax}}, \quad i \in \{1,..,n\} \tag{17}$$

where: $J_{imax} - J_{imin}$ is the difference between maximum and minimum value of the objective function J_i determined for the assumed parameter variability interval p_i, the coefficient w_i corresponding to the parameter p_i was determined, depending on value of the evaluation function (17):

$$w_i = \frac{J_i}{\sum_i J_i}, \quad i \in \{1,..,n\} \tag{18}$$

The coefficient w_i determines a degree of effect of the parameter p_i on evaluation value with respect to the entire set of parameters. After performing the calculations for all parameters one obtains a relative summary value of the the coefficients w_i (18), i. e. the cumulated value S_i:

$$S_i = \sum_{k=1}^{i} w_k = 1 \text{ of the property: } S_n = 1 \tag{19}$$

Based on the obtained values, Pareto-Lorentz curves illustrating a share of each parameter p_i are formed. On the basis of Lorentz curve there is possible to classify the parameters, i.e. to determine affiliation of the parameters to the sets A, B, C, which have crucial, moderate and minimum impact on values of objective function, respectively. To this end, a classification typical for the classic ABC method was used to affiliate parameters: to the set A when values of their cumulated sums S_i were lower than 80%, to the set B when they were comprised within the range <80%, 95%), and to the set C – when over 95%. The above presented analysis was carried out for the set points of the control system operation. Below are presented results of the analysis of basis parameters impact on value of objective function for various changes in values of set ship positions and headings.

SIMULATION INVESTIGATIONS

During ship manoeuvring ship's model parameters vary along with time, depending on many factors, a.o. hydrodynamic coefficients and ship speed. Model errors associated with parametric uncertainties have significant impact on deviation of ship's real trajectory from that assumed. In the analysis of impact of model uncertainties on dynamic features of the control system both quantitative and qualitative methods are used. In the publications [8, 13] Monte Carlo simulations were implemented for quantitative determination of uncertainties in DP system. In this work the authors' attention was focussed on qualitative analysis consisting in application of ABC method and Pareto-Lorentz curves to determine impact of particular parameters on changes in control quality index. The knowledge gained this way may be directly used for tuning the adaptive control system by taking into account range of each of the parameters. Such method has not been so far applied to susceptibility investigations of DP adaptive control system.

For the simulation investigations a mathemetical model of a supply ship of L=76.2m in length and 4591 t mass, was selected. The real dimensionless parameters of the model (1)-(2) were determined by using the Bis scaling system [7] and presented in Tab. 1. In the tests in question tere were selected zero-initial values of position and heading and estimated weights. During the tests with adaptive controller there were considered programmable inertial changes in values of the set longitudinal and transveres position, resulting from occurrence of slow-varying environmental disturbances modelled with the use of Markov process [7]. The parameters presented in Tab.1 are the model basis parameters whose variability range equal to ±20% of their real value was assumed.

Tab.1. Dimensionless values of basis parameters (Bis – scaled)

i	Parameter p_i	Value
1	c_1	-1,8902
2	c_4	-1,1274
3	d_{32}	-0,1073
4	$m_{23}\, m_{32}$	-0,0744
5	d_{23}	-0,0141
6	d_{11}	0,0414
7	d_{33}	0,0568
8	c_2	0,0744
9	m_{33}	0,1278
10	d_{22}	0,1775
11	m_{11}, c_3	1,1274
12	m_{22}	1,8902

Three cases of change in values of set position and heading were considered: for, $\boldsymbol{\eta}_\mathrm{d}$ = (10,10,10), $\boldsymbol{\eta}_\mathrm{d}$ = (5,10,10) and $\boldsymbol{\eta}_\mathrm{d}$ = (10,5,10).

First of all, for the assumed range of changes in basis parameters (Tab. 1) and $\boldsymbol{\eta}_\mathrm{d}$ = (10,10,10) relative values of the quality index J_i (17), coefficients w_i (18) as well as values of the cumulated sum S_i (19) (Tab. 2) were determined.

Tab. 2. List of relative values of the quality index J_i, coefficients w_i and values of the cumulated sum S_i, for $\boldsymbol{\eta}_d$ = (10,10,10)

i	J_i	w_i	S_i
10	0,530871367	2,81E-03	0,50492
3	0,153670167	2,97E-03	0,651078
7	0,121097925	1,46E-01	0,766257
5	0,081978813	4,42E-03	0,844228
12	0,074335195	7,80E-02	0,914929
11	0,046881248	2,99E-02	0,959519
6	0,031399883	1,15E-01	0,989384
4	0,004646388	8,75E-05	0,993803
2	0,003126372	3,29E-04	0,996777
1	0,002951551	5,05E-01	0,999584
9	0,000345541	4,46E-02	0,999912
8	9,20E-05	7,07E-02	1

Applying the ABC rule one is able to conclude that the parameters: d_{22}, d_{32}, d_{33} constitute the group A which has crucial impact on control quality in the tested system. The parameters, d_{23}, m_{22} have moderate impact (group B). And, the remaining basis parameters are of a minimum impact on control quality in the tested system hence they belong to the group C.

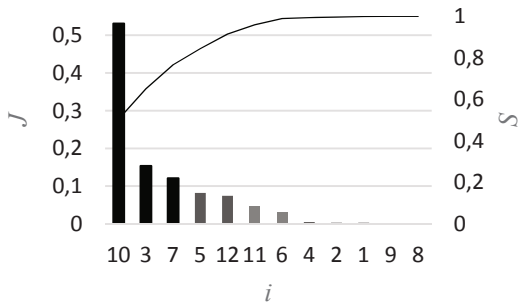

Fig. 2 Pareto-Lorentz diagram which takes into account relations between parameters, their relative values of control quality index J as well cumulated values S, determined for $\boldsymbol{\eta}_d = (10,10,10)$

Fig. 3 presents both the desired and real ship's trajectories for the case $\boldsymbol{\eta}_d = (10,10,10)$, with taking into account the parameters belonging to the group A. The diagrams were depicted for changes in values of the parameters equal to ±20% of their respective real values.

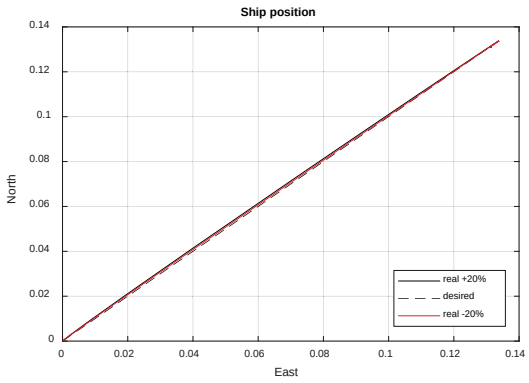

Fig. 3 Diagram of the desired ship's trajectory and real ones for the case: $\boldsymbol{\eta}_d = (10,10,10)$ *with taking into account ±20% change in values of the parameters of the group A*

In an analogous way, for $\boldsymbol{\eta}_d = (5,10,10)$ there were determined the groups of basis parameters of crucial (A), moderate (B) and minimum (C) impact on control quality in the tested system.

The obtained values are listed in Tab. 3 and presented in the form of Pareto-Lorentz diagram (Fig. 4).

Tab. 3. List of relative values of the quality index J_i*, coefficients* w_i *and values of the cumulated sum* S_i*, for* $\boldsymbol{\eta}_d = (5,10,10)$

i	Ji	w_i	S_i
10	0,528009734	0,546174556	0,528009734
3	0,163289371	0,168906923	0,691299105
7	0,123589817	0,127841608	0,814888923
5	0,079851728	0,082598822	0,894740651
12	0,074719631	0,077290169	0,969460282
11	0,015337254	0,015864893	0,984797536
6	0,007303802	0,007555071	0,992101338
4	0,004359707	0,004509692	0,996461045
2	0,001745608	0,001805662	0,998206654
1	0,001311787	0,001356916	0,999518441
9	0,000468859	0,000484989	0,9999873
8	1,26998E-05	1,31367E-05	1

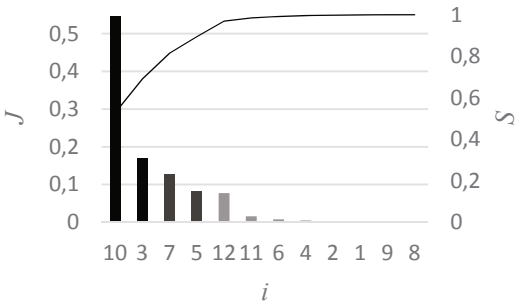

Fig. 4. Pareto-Lorentz diagram which takes into account relations between parameters p_i*, their relative values of control quality index* J_i *as well cumulated values* S_i*, determined for* $\boldsymbol{\eta}_d = (5,10,10)$

It was observed that in the case of $\boldsymbol{\eta}_d = (5,10,10)$, only the parameters d_{22}, d_{32} belong to the group A,i.e. that of crucial impact on control quality in the investigated system, and only, d_{33}, d_{23} – to the group B of a moderate impact. The remaining parameters exert a minimum impact,hence they may be numbered among elements of the group C.

The simulation investigations were conducted also for the third case: $\boldsymbol{\eta}_d = (10,5,10)$.

The obtained values are collected in Tab. 4 and presented graphically in Fig. 5.

Tab. 4. List of relative values of the quality index J_i*, coefficients* w_i *and values of the cumulated sum* S_i*, for* $\boldsymbol{\eta}_d = (10,5,10)$

i	J_i	w_i	S_i
10	0,484719261	0,412553523	0,412553523
11	0,179230742	0,152546598	0,565100121
6	0,151323221	0,12879399	0,693894112
5	0,150468087	0,12806617	0,821960282
12	0,087428568	0,07441207	0,896372352
7	0,061862607	0,052652409	0,949024761
3	0,038088145	0,032417524	0,981442284
4	0,012550981	0,010682372	0,992124656
1	0,007055257	0,00600486	0,998129516
9	0,0007843	0,000667532	0,998797048
2	0,000718445	0,000611482	0,99940853
8	0,000694933	0,00059147	1

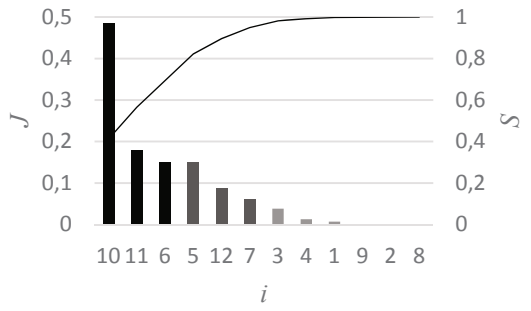

Fig. 5 Pareto-Lorentz diagram which takes into account relations between parameters p_i, their relative values of control quality index J_i as well as the cumulated values S_i, determined for $\boldsymbol{\eta}_d$ = (10,5,10)

The performed simulation investigations made it possible to determine impact of the parameters on control quality index in the tested system, taking into account: $\boldsymbol{\eta}_d$ = (10,10,10), $\boldsymbol{\eta}_d$ = (5,10,10) and $\boldsymbol{\eta}_d$ = (10,5,10), and as well as changes in values of the basis parameters, ranging ±20% of their real values. The parameters were assigned to particular groups in accordance with ABC method (Tab. 5)

Tab. 5. List of basis parameters and their affiliation to particular groups of their significance in the process of the tested system control during successive simulations with taking into account the set values: $\boldsymbol{\eta}_d$ = (10,10,10), $\boldsymbol{\eta}_d$ = (5,10,10) and $\boldsymbol{\eta}_d$ = (10,5,10)

i	(10,10,10)	(5,10,10)	(10,5,10)
1	C	C	C
2	C	C	C
3	A	A	C
4	C	C	C
5	B	B	B
6	C	C	A
7	A	B	B
8	C	C	C
9	C	C	C
10	A	A	A
11	C	C	A
12	B	C	B

In view of a lack of an unambiguous affiliation of the parameters to particular ABC groups in various points of the system operation, the obtained results were properly averaged. Namely, by making use of the relations (17 – 19), the average values of the coefficients J_i, w_i, S_i, were calculated, as presented in Tab. 6. This made it possible to classify again the parameters to particular groups. Now, to the group A belong the parameters: d_{22}, d_{32}, d_{23}, and to the group B: m_{22}, m_{11}, c_3. The remaining ones are of a minimum impact hence they may be assigned to the group C.

Tab. 6. List of relative values of the quality index J_i, coefficients w_i and values of the cumulated sum S_i – averaged values obtained from all simulations

i	J_i	w_i	S_i	Group
1	0,003773	0,003508	0,997524	C
2	0,001863	0,001733	0,999257	C
3	0,118349	0,110047	0,588487	A
4	0,007186	0,006682	0,994016	C
5	0,1041	0,096797	0,685284	A
6	0,063342	0,058899	0,987334	C
7	0,102183	0,095015	0,7803	A
8	0,000267	0,000248	1	C
9	0,000533	0,000496	0,999752	C
10	0,514533	0,47844	0,47844	A
11	0,080483	0,074837	0,855137	B
12	0,078828	0,073298	0,928435	B

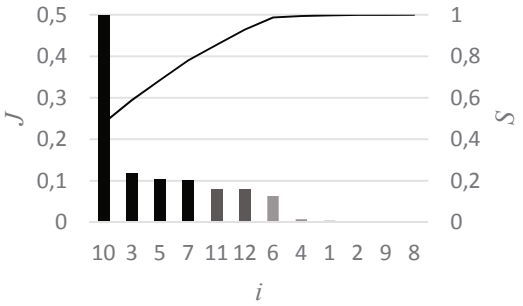

Fig. 6. Pareto-Lorentz diagram which takes into account relations between parameters p_i, relative values of control quality index J_i as well as the cumulated values S_i, obtained during all simulations

The computer simulation results show that the system behaves correctly within the tested range of changes in estimated parameters, amounting to ± 20% of their respective real value, as well as for the assumed level of disturbances.

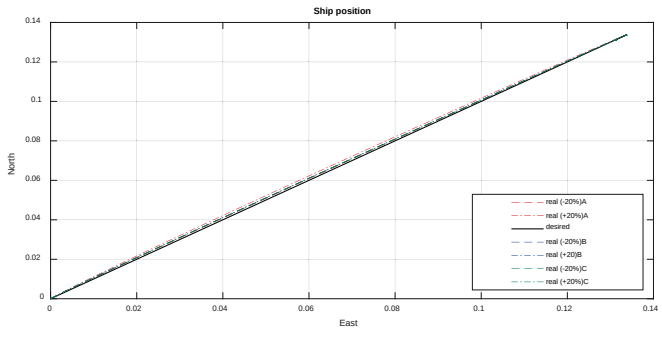

Fig. 7. The desired and real trajectory of the ship for $\boldsymbol{\eta}_d$ = (10,10,10) and ±20% change in averaged values of the parameters classified to the groups A, B, C, respectively

For the parameters of crucial impact on values of the control quality index the ship's position deviations from the desired trajectory (Fig. 7) can be observed. Therefore it can be stated

that the tested control system is more susceptible to changes in values of the parameters belonging to the group A, but less susceptible to model inaccuracies resulting from changes in values of the parameters of the groups B and C.

CONCLUSIONS

In this work there was performed a qualitative analysis of the designed DP ship control system with adaptive backstepping controller and RBF neural network used for estimation of ship model nonlinear function.

The qualitative analysis of the system conducted by means of Pareto-Lorentz diagrams and ABC method made it possible to distinguish which model parameters have crucial, moderate or minimum impact on changes in values of the control quality index.

It was observed that, depending on change in set values of ship position and heading, particular ABC groups contained another set of parameters. It means that each parameter affects the tested system to a different degree. In this case the concluding process based on classic methods may appear imprecise. In the future the investigated system may be tested towards finding its behaviour in function of its operational point with the use of fuzzy sets logic. In the case of multi-parameter adaptive systems, information about impact of model parameters on changes in values of the control quality index may be used for tuning the control system and may effectively simplify analysis of the system resistance against modelling errors.

BIBLIOGRAPHY

1. Boulkroune, A., N. Bounar, M. M'Saad, M. Farza: *Indirect adaptive fuzzy control scheme based on observer for nonlinear systems*: *A novel SPR-filter approach*, Neurocomputing. 135, 2014 pp. 378–387.

2. Buhmann, M.D.: *Radial basis functions: theory and implementations*, Cambridge University Press 2003.

3. Chan, A.K., G.A. Becus: *Online adaptation of RBF centers for adaptive control*, in: Proceedings of 1995 American Control Conference – ACC'95, American Autom Control Council, 1995 pp. 3770–3774.

4. Cover, T.M.: *Geometrical and Statistical Properties of Systems of Linear Inequalities with Applications in Pattern Recognition*, IEEE Transactions on Electronic Computers 1965, pp. 326-334.

5. Cpałka, K.: *Design of Interpretable Fuzzy Systems*, Springer 2017.

6. Du, J., X. Hu, H. Liu, C.L.P. Chen: *Adaptive robust output feedback control for a marine dynamic positioning system based on a high-gain observer*, IEEE Transactions on Neural Networks and Learning Systems. 26, 2015, pp. 2775–2786.

7. Fossen, T.I., S.P. Berge: *Nonlinear vectorial backstepping design for global exponential tracking of marine vessels in the presence of actuator dynamics*, in: Proceedings of the 36th IEEE Conference on Decision and Control, IEEE, 1998, pp. 4237–4242.

8. Kang Y., Li D., Lao D.: *Performance Robustness Comparison of Active Disturbance Rejection Control and Adaptive Backstepping Sliding Mode Control*. In: Xiao T., Zhang L., Fei M. (eds) AsiaSim 2012. AsiaSim 2012. Communications in Computer and Information Science, vol 324. Springer, Berlin, Heidelberg

9. Katebi, M.R., M.J. Grimble, Y. Zhang: *H∞ robust control design of dynamic ship positioning*, IEE Process Control Theory Application. 144, 1997, pp. 110–120.

10. Krstić, M., I. Kanellakopoulos, P. Kokotović: *Nonlinear and adaptive control design*, Wiley 1995.

11. Kuczkowski Ł., Śmierzchalski R. (2017) Path planning algorithm for ship collisions avoidance in environment with changing strategy of dynamic obstacles. In: Mitkowski W., Kacprzyk J., Oprzędkiewicz K., Skruch P. (eds) Trends in Advanced Intelligent Control, Optimization and Automation. KKA 2017. Advances in Intelligent Systems and Computing, vol 577. Springer, Cham, pp. 641–650.

12. Kwan, C., F.L. Lewis: *Robust backstepping control of nonlinear systems using neural networks*, Systems, Man and Cybernetics, Part A: Systems and Humans, IEEE Transactions Vol. 30, No.6, 2000, pp. 753–766.

13. Linkens, D.A., Mahfouf, M. Abood, M.: *Self-adaptive and self-organising control applied to nonlinear multivariable anesthesia: a comparative model-based study*, IEE Proceedings-D, vol. 139, No. 4, July 1992, pp. 381-394

14. Lisowski, J.: *Game control methods in avoidance of ships collisions*, Polish Maritime Research, No. 19, 2012, pp. 3–10.

15. Lisowski, J., A. Lazarowska: *The radar data transmission to computer support system of ship safety*, Solid State Phenomena. 196, 2013, pp. 95–101.

16. Mingyu, F., X. Yujie, Z. Li: *Bio-inspired Trajectory Tracking Algorithm for Dynamic Positioning Ship with System Uncertainties*, Proceedings of the 35th Chinese Control Conference, 2016, pp. 4562–4566.

17. Niksa-Rynkiewicz,T.,Szłapczyński R.: *A framework of a ship domain – based near-miss detection method using Mamdani neuro-fuzzy classification*, Polish Maritime Research, SI (97), 2018, vol. 25, pp. 14-21.

18. Orr, M.J.L.: *Introduction to Radial Basis Function Networks,* 1996.

19. Sorensen, A.: *A survey of dynamic positioning control systems,* Annual Reviews in Control, 35, 2011, pp. 123–136.

20. Swaroop, D., J.K. Hedrick, P.P. Yip, J.C. Gerdes: *Dynamic surface control for a class of nonlinear systems*, IEEE Transactions on Automatic Control. 45, 2000, pp. 1893–1899.

21. Szczypta J., Przybył A., Cpałka K. (2013) Some Aspects of Evolutionary Designing Optimal Controllers. In: Rutkowski L., Korytkowski M., Scherer R., Tadeusiewicz R., Zadeh L.A., Zurada J.M. (eds) *Artificial Intelligence and Soft Computing. ICAISC 2013. Lecture Notes in Computer Science*, vol 7895. Springer, Berlin, Heidelberg.

22. Szlapczynski, R., J. Szlapczynska: *Customized crossover in evolutionary sets of safe ship trajectories*, International Journal of Applied Mathematics and Computer Science. 22, 2012.

23. Tannuri, E.A., A.C. Agostinho, H.M. Morishita, L. Moratelli: *Dynamic positioning systems: An experimental analysis of sliding mode control*, Control Engineering Practice. 18, 2010, pp. 1121–1132.

24. Witkowska, A., R. Śmierzchalski: *Adaptive Dynamic Control Allocation for Dynamic Positioning of Marine Vessel Based on Backstepping Method and Sequential Quadratic Programming.* Ocean Engineering 163, 2018, pp. 570-582.

25. Witkowska, A., T. Niksa-Rynkiewicz: *Motion control of dynamically positioned unit by using backstepping method and artificial neural networks*, to be published in Polish Maritime Research.

26. Yang, Y., J. Du, G. Li, W. Li, C. Guo: *Dynamic Surface Control for Nonlinear Dynamic Positioning System of Ship*, in: Advances in Intelligent and Soft Computing, Springer, Berlin, Heidelberg, 2012, pp. 237–244.

27. Ye, L., Zong, Q., Zhang, X.: *Cascade Disturbance Rejection Control of the Uncertain Nonlinear Systems with Nonlinear Parameterization*, Proceedings of the 34th Chinese Control Conference, July 28-30, 2015, Hangzhou, China, pp. 991-996.

28. Wei W., Donghai L., Jing W.: *Adaptive Control for a Non-minimum Phase Hypersonic Vehicle Model*. American Control Conference (ACC) Washington, DC, USA, June 17-19, 2013.

29. Tykocki J., Jordan A., Surowik D.: *Pareto – ABC Analysis of Temperature Field in High Voltage Three-Phase Cable Systems*. Electrical Review, No. 5, (2014) R 91, pp. 107-112.

CONTACT WITH THE AUTHORS

Tacjana Niksa Rynkiewicz
e-mail: tacniksa@pg.edu.pl

Gdańsk University of Technology
Gabriela Narutowicza 11/12, 80-233 Gdańsk
Poland

Anna Witkowska
e-mail: anna.witkowska@pg.edu.pl

Gdańsk University of Technology
Gabriela Narutowicza 11/12, 80-233 Gdańsk
Poland

POLISH MARITIME RESEARCH 1 (101) 2019 Vol. 26; pp. 15-19
10.2478/pomr-2019-0002

APPLICABILITY OF INLET AIR FOGGING TO MARINE GAS TURBINE

Zygfryd Domachowski
Marek Dzida
Gdańsk University of Technology, Poland

ABSTRACT

The dependency of marine gas turbine on the ambient temperature leads to a decrease of the gas turbine power output in arid areas. Very often gas turbine power output demand is high and the power margins originally designed into the driver , has been exhausted. In such circumstances the inlet air fogging is an effective compensation of gas turbine power. In this paper an analysis of inlet air fogging applicability to marine gas turbine has been conducted. Different areas of ship's voyage have been taken into account. The use of inlet air fogging in marine gas turbine must be evaluated on the basis of turbine characteristics, climate profile of ship's voyage, and expectations of gas turbine power augmentation. The authors expect that the considerations provide useful guidance for users of marine gas turbines to decide the feasibility of installing an inlet air fogging system.

Keywords: marine gas turbine, inlet air fogging, applicability

INTRODUCTION

The marine gas turbine sector is listing of more than 41150 gas turbine installations, 3916 (9,51%) of which are marine gas turbines used for propulsion. This assessment is based on the Forecast International Industrial and Marine Gas Turbine Database. The advantages of gas turbine for ships include the reliability, power density, and low noise. Unfortunately in hot and dry regions gas turbine power is dramatically reduced because of the reduction in gas turbine air mass flow. Temperature – power relationship for LM 500, LM 2500, LM 2500+, LM 6000 gas turbines has been illustrated in Fig.1.

Cooling the air to the wet-bulb temperature can boost the gas turbine power and efficiency. The inlet air fogging of marine gas turbine has been considered. In a stationary application of gas turbine (in the power application and mechanical drive) the selection of the climatic design point for the design of power augmentation system, has been suggested in the literature. This approach can be based on locally collected weather data. A detailed analysis of the evaporative cooling potential in terms of Equivalent Cooling Degree Hours (ECDH) is then carried out. The final decision as to the design point for the cooling system depends on the revenues to be generated by power augmentation and installation costs.

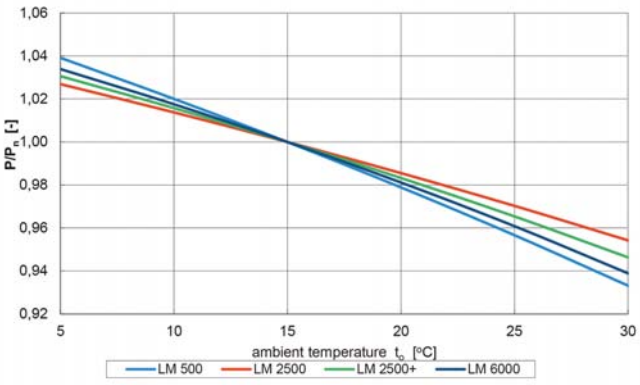

Fig. 1. Typical ambient temperature – power relation for marine gas turbines

The marine gas turbines are advantageous to all fast ships such as cruise ships, fast ferries, fast cold storage ships, general refrigerated ships, fruit carriers, packet ships, mega – yachts, and naval ships. All of them need prime mover operation at maximum performance parameters. Full power operation at optimal parameters results in maximum speed of a ship on one hand and environmentally friendly conditions on the other hand. Above the air temperature design point the thermal efficiency of gas turbine falls, which results in power output decrease. Very often when the gas turbine power output decreases on hot days, the power output demand is high and the designed power margins have been exhausted. In such circumstances the augmenting of gas turbine power output can have an important impact on profitability. This paper is focussed on a climate analysis to determine the expected output power benefits.

Both short and long sea voyage of a ship has been taken into account. The Baltic Sea and the Mediterranean can be considered in case of short voyage of e.g. a gas turbine-propelled ferry. For a long sea voyage the distance between the Baltic Sea region and the Far East area has been assumed as an example. Air temperature data in January and July for some Baltic Sea and Mediterranean ports and on the route from the Baltic Sea to Far East area, have been collected. Having such database , any ship gas turbine operator is able to calculate the potential for evaporative cooling in a region of ship's location. The Equivalent Cooling Degree Hours multiplied by the gas turbine specific cooling number (kW/°C) makes it possible to calculate the (kW – hours) capacity available from using the evaporative fogging.

AIR COOLING AS A WAY OF GAS TURBINE POWER AUGUMENTATION

An ambient temperature increase provokes gas turbine output decrease which induces problem in the ship drive during high power demand. To reduce the dependence of gas turbine output on ambient temperature the power augmentation is needed. When the power output demand is high and the designed power margins have been exhausted an air cooling technology could be considered. There are two possible cooling technologies: an evaporative technology or chilling. In the ship use the evaporative cooling seems to prevail over the chilling. Weight of such installation and its size is smaller.

The evaporative cooling consists in latent heat water vaporization. The evaporating water cools the air at the gas turbine inlet. The effectiveness of evaporative cooler can be defined as follows :

$$E = \frac{T_{1DB} - T_{2DB}}{T_{1DB} - T_{2WB}}$$

where : T_1 denotes inlet temperature, T_2 – exit temperature of evaporative cooler, *DB* – dry bulb, *WB* – wet bulb, as presented by Meher – Homji *et al.* in [1,2].

The direct inlet air fogging is a method of air cooling where demineralized water is converted into a fog by means of special nozzles operating at 7÷14 MPa pressure. This technique is applied on a large scale because of its low first cost and effectiveness attaining near 100%. The relative humidity at the gas turbine inlet will be 100% which gives the lowest temperature possible at the wet bulb temperature.

In a given location it is possible to provide an estimation of the cooling potential if only there are sufficient weather data. The Equivalent Cooling Degree Hours (ECDH) calculations is an useful measure when inlet air fogging is applied. The ECDH is a number (°C – hours) that defines the total amount of cooling that can be derived in a given time period. The ECDH is calculated with a lower limit of Minimum Wet Bulb Temperature (MWBT) varying between 7,2°C (45°F) and 12°C (55°F), see [3, 4]. The MWBT is selected in order to avoid the possibility of inlet icing. The ECDH is calculated as the difference between the coincident dry bulb temperature and the wet bulb temperature, multiplied by the number of hours during which this difference exists if the wet bulb temperature is above the MWBT lower limit. At a given location the ECDH number would be multiplied by the gas turbine specific cooling number (kW/°C) to compute a (kW – hours) capacity available from using the inlet air fogging.

Considering the role of inlet air cooling in marine gas turbine, we take into account a short and long sea voyage of a ship, separately.

THE ROLE OF MARINE GAS TURBINE INLET AIR FOGGING IN A SHORT SEA VOYAGE

The possible role of marine gas turbine inlet air cooling depends on a region of ship`s short voyage, e.g. of a gas turbine ferry. The difference can be observed by comparing the case of the Baltic Sea voyage with the Mediterranean one. In Fig. 2 there is presented the average air temperature on the Baltic Sea coast in winter (January), and summer (July). Similar data are illustrated in Fig. 3 for the Mediterranean.

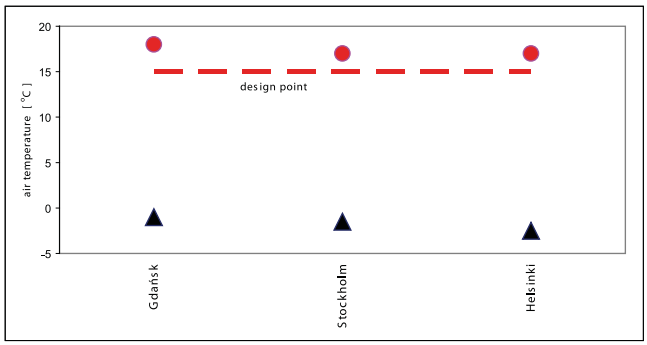

Fig. 2. Average air temperature on the Baltic Sea coast in January (▲), and July (●)

The value of the Average Equivalent Cooling Degree Hours calculated for the Baltic Sea area have been below 6000 (degree-hours) a year and between 12000 and 25000 (degree-hours) for the Mediterranean area, as presented in [5]. Therefore an inlet air fogging implementation would

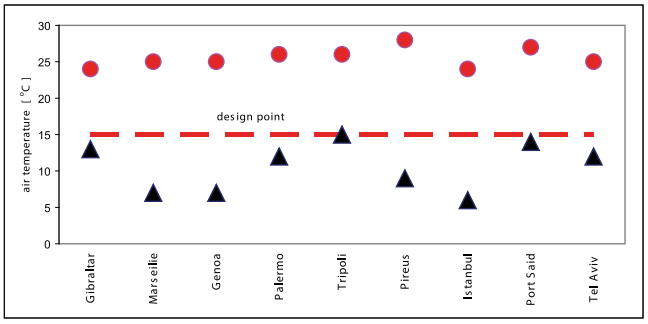

Fig. 3. Average air temperature on the Mediterranean coast in January (▲), and July (●)

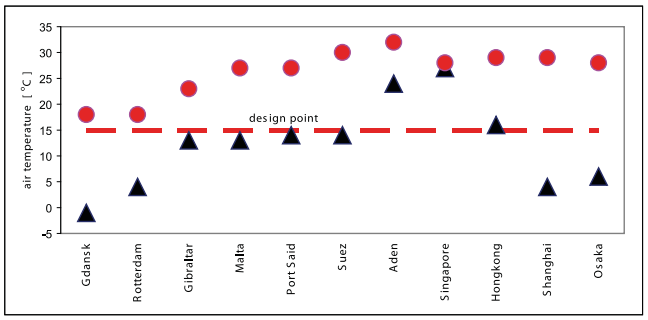

Fig. 4. Average air temperature on the route from the Baltic Sea to Far East area in January (▲), and July (●)

presumably not be profitable for the navigation limited to the Baltic Sea area. It could probably be profitable for the navigation within the Mediterranean area. A lower ECDH value may not eliminate consideration on the use of inlet air fogging since the number of operating hours would also be a deciding factor.

The use of inlet air fogging in marine gas turbine must be evaluated on the basis of turbine characteristics, climate profile of ship's voyage, and expected amount of gas turbine power augmentation.

MARINE GAS TURBINE INLET AIR FOGGING DURING A LONG SEA VOYAGE IN HOT REGION

The average air temperature in several ports along the route of sea voyage between the Baltic Sea region and the Far East area is presented in Fig 4. acc.[5].

Tab. 1 contains monthly and yearly ECDH values available during the voyage from the Baltic Sea to the Far East area. It can be seen that yearly available ECDH value calculated for a voyage from the Baltic Sea region to the Far East area have been between 6000 and 37 000 (degree-hours).

According to [6] the rating power of e.g. LM 2500 gas turbine is equal to 22 375 kW. Therefore its specific cooling number is 68,6 kW/°C, approximately. In a voyage from the Baltic Sea to the Far East area such gas turbine can gain energy between 411 690 kWh and 2 536 755 kWh.

Tab. 1. Monthly and yearly ECDH values available during the voyage from the Baltic Sea to the Far East area, [kWh]

	Jan.	Feb.	Mar.	Apr.	May	Jun.	Jul.	Aug.	Sep.	Oct.	Nov.	Dec.	Yearly
Voyage from the Baltic Sea to the Far East area													
Stockholm	0	0	0	22	394	1189	2269	1786	200	10	0	0	5871
Oslo	0	0	0	11	333	1300	2482	2035	165	1	0	0	6328
Amsterdam	0	0	4	93	686	1110	1565	1675	759	201	9	0	6104
Lisbon	110	151	549	992	1855	2744	3542	3543	2990	1745	661	244	19127
Tripoli	244	620	1710	3030	4602	4993	5087	4954	4274	3582	2103	786	35984
Alexandria	602	730	1336	2609	3061	3043	2916	3122	3266	3051	2412	1313	27462
Madras	2485	2497	3030	3066	4177	4704	3928	3645	2899	2279	1937	2276	36921
Singapore	1595	1498	1708	1402	1439	1485	1546	1632	1377	1428	1040	1162	17313
Manila	2462	2567	3251	3378	3096	2295	2008	1860	1729	1908	2063	2219	28836
Hong Kong	1529	1299	1531	1735	1945	2106	2406	2447	2736	3300	3004	2184	26221
Shanghai	2	47	109	894	1991	1669	1889	1938	1911	1804	587	54	12894
Pusan	0	8	8	585	2025	1815	1507	2041	2265	1922	307	10	12494
Osaka	0	7	38	999	2681	2817	2897	3389	2811	2082	533	16	18271

ROLE OF AMBIENT TEMPERATURE DESIGN POINT FOR MARINE GAS TURBINE IN HOT AREA

Let's assume a gas turbine which drives a ship sailing between the Mediterranean Area and the Far East Area. In such ship's voyage the average ambient temperature exceeds 15°C during the most part of a year, see Fig.4. The relation ambient temperature – marine gas turbine power, presented in Fig. 1, corresponds to the ambient temperature design point equal to 15°C. A similar relation for a gas turbine in which ambient temperature design point has been assumed to be 20°C, is shown in Fig. 5.

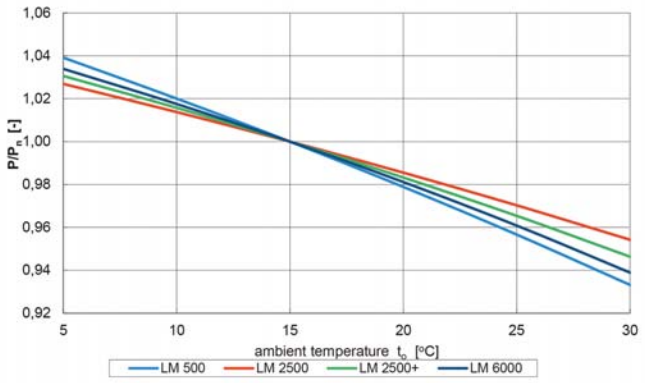

Fig. 5. Relation between ambient temperature and gas turbine power for the Ambient Temperature Design Point of 20°C

It is evident that the selection of ambient temperature design point impacts the available power of gas turbine in a hot area. An example relation for LM2500 marine gas turbine is given in Fig. 6.

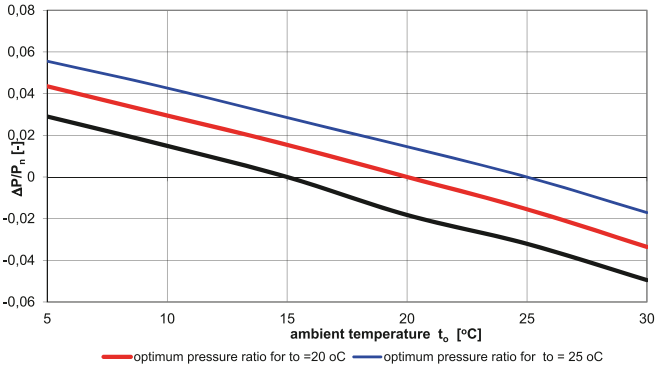

Fig. 6. Example relation between ambient temperature and gas turbine power for different values of Ambient Temperature Design Point

In the same time, for an inlet air system, the selection of the ambient temperature design point will impact the hardware sizing. The design of high pressure pumps and nozzle arrays depends on water flow. On one hand, to implement an inlet air fogging into a marine gas turbine, very little modification of the inlet air system is needed. On the other hand, a detailed technical and economical analysis should be carried out to properly determine size the fogging system. An over-designed fogging system may reduce the economic effectiveness of the system while an under-designed one may lead to a lower power boost than expected.

SUMMARY

The presented investigation has been conducted to examine the applicability of inlet air fogging to marine gas turbine. Different areas of ship's voyage have been taken into account. To apply an inlet air fogging to marine gas turbine several factors should be considered. Among them, the most important are climate profile of ship's voyage, cost of the fogging system to be installed, amount of (MW – hours) boost gained by means of inlet air fogging (i.e. benefit to be attained as a result of it). If an inlet air fogging system is feasible the system should be adjusted to the achievable cooling to avoid its over-sizing or under-sizing.

This work has been completed with the analysis of average ambient temperatures for key ports along the route of both a short and long voyage. This has been done by using the ECDH data along with the cooling design points for a popular marine gas turbine – the LM2500.

This paper was aimed at providing the background analysis for future research.

REFERENCES

1. Meher – Homji, C. B., Mee, T. R.: *Gas Turbine Power Augmentation by Fogging of Inlet Air*. Proceedings of the 28th Turbomachinery Symposium, Turbomachinery Laboratory, Texas A&M University, September 1999, Houston, USA.

2. Meher – Homji, C. B., Mee, T. R.: *Intel Fogging of Gas Turbine Engines, part B: Practical Considerations, Control and O&M Aspects*. Proceedings of ASME Turbo Expo 2000, May 8-11, 2000, Munich, Germany, ASME Paper 2000 – GT-308.

3. Chaker, M.A., Meher – Homji, C. B.: *Inlet Fogging of Gas Turbine Engines: Climatic Analysis of Gas Turbine Evaporative Cooling Potential of International Locations*. Proceedings of ASME Turbo Expo 2002, June 3-6, 2002, Amsterdam, The Netherlands, ASME Paper 2002 – GT – 30559.

4. Chaker, M.A., Meher – Homji, C. B.: *Selection of Climatic Design Points for Gas Turbine Power Augmentation*. Proceedings of ASME Turbo Expo 2011, June 6-10, 2011, Vancouver, British Columbia, Canada, ASME Paper GT2011-46463.

5. Domachowski, Z., Dzida, M.; *Air Fogging of Marine Gas Turbine in Power Output Loss Compensation*. Polish Maritime Research No 4, Vol. 22, 2015, pp. 53–58.

6. *Marine Drive Specifications*, Handbook 1999/2000, Turbomachinery, Vol. 40, No 6, p.124.

CONTACT WITH THE AUTHORS

Zygfryd Domachowski
e-mail: omachow@pg.edu.pl

Gdańsk University of Technology
Narutowicza 11/12, 80-233 Gdansk
Poland

Marek Dzida
e-mail: dzida@pg.edu.pl

Gdańsk University of Technology
Narutowicza 11/12, 80-233 Gdansk
Poland

sciendo

POLISH MARITIME RESEARCH 1 (101) 2019 Vol. 26; pp. 20-29
10.2478/pomr-2019-0003

DYNAMICS OF THE FKT SYSTEM WITH DIFFERENT MOORING LINES

Jo-Ti Wu[1]
Jiahn-Horng Chen[1]
Ching-Yeh Hsin[1]
Forng-Chen Chiu[2]
[1] National Taiwan Ocean University, Keelung, Taiwan
[2] National Taiwan University, Taipei, Taiwan

ABSTRACT

To harness the endless hydrokinetic energy of the Kuroshio current, the joint research team of the National Taiwan University and the National Taiwan Ocean University has developed a floating Kuroshio turbine (FKT) system in Taiwan. In normal operation, the system floats at a certain small depth from the ocean surface to reduce the wave effects and take advantage of faster current speeds. In the present study, the effect of the mooring line on the system dynamics is investigated computationally. Two different auxiliary mooring line designs and, for each design, three different common mooring lines (polyester ropes of neutral buoyancy, iron chains, and 6×19 wires ropes with wire core) are examined. The study makes use of several commercial and in-house packages, integrated to find various coefficients. It is found that the mooring line, the auxiliary mooring line design, and the gravity centre can have a significant effect on system fluctuations in normal operation if the combination of these factors is not properly matched.

Keywords: ocean current energy; floating turbine system; mooring line; system dynamics; surface waves

INTRODUCTION

The greenhouse gas emission due to excess use of fossil fuels has resulted in serious global warming and disastrous climate change. Scientists around the world warn that the likelihood of extreme heat, dryness and precipitation will keep increasing globally [1]. Driven by the need to control the climate change, the development of renewable energy utilisation has become a new technological frontier. Among various possible renewables, marine energy with its abundance in resources and huge power potential can become an important source. The technologies to harness marine energy are far from maturity at present. Many challenges have been addressed in the literature [2]. Coping with these challenges, various devices were devised for harnessing different kinds of marine energy in the past several decades. Among them are the ocean current turbine systems which, in fact, represent another level of deep-water renewable energy technology. With the advancement of technology, several prototypes of ocean energy devices have been developed, e.g. [3–8].

One of the key issues in harnessing ocean current energy is the deep-sea mooring system which connects the current turbine floating in the ocean current and the anchor of some kind fixed on the sea bed. This was a new research topic in the past decade. The interdependency between the mooring and ocean current turbine systems plays a crucial role early in the design phase. Numerous studies have been conducted, but each of them was mostly limited to a particular type of ocean current turbine and mooring system.

Cribbs [9] has developed a numerical procedure to model the mooring system for the 20-kW current turbine system proposed by a research team at the Center for Ocean Energy Technology, Florida Atlantic University. He attempted to optimize the mooring attachment locations on the floating body, the tether arrangement, and the locations of two floating devices attached to the mooring line. Cribbs and Van Zwieten [10] have also studied in detail the sensitivity of system responses to parametric variations. Shibata *et al.* [11] have conducted both experimental and numerical studies to investigate the stability of a V-shape mooring system

connected to an ocean turbine developed by Takagi *et al.* [12]. Rho *et al.* [13] have proposed methods to select and optimize the mooring system for a tidal turbine located in a shallow water region. They concluded that the SPAR type has better performance for a multi-arrayed system. More recently, Tsao and Feng [14] have developed the cross-stream active mooring system to adjust the horizontal position of a current turbine in order to track fast streams and thus increase the power generation capacity.

Waves are a source of system instability for a moored ocean current turbine system. The wave-turbine interaction is an important issue in developing the floating current turbine systems. Shirasawa *et al.* [15] have tested the system dynamics of the ocean current turbine with a single mooring line under the action of waves. Although the ocean current turbine works at the middle layer of the water flow, the wave influence is significant. They pointed out that when the wave length is long, compared to the turbine operation depth, selecting a proper mooring method is important for making the deployment stable. Wu *et al.* [16] have investigated the effect of mooring line design and waves on the dynamics of the current turbine system developed by the research team of the National Taiwan University and the National Taiwan Ocean University. Their results show that the surface waves induce pitching oscillation of the system which becomes significant when the wave propagation is parallel to the current flow and its period is close to the system resonant period.

Recently, Cribbs *et al.* [17] have surveyed the existing mooring standards. They pointed out that modelling mooring dynamics can be complicated and the loads and fatigue cycles of a mooring system can easily be underestimated due to unexpected marine environments. It implies that more studies are indispensable to understand fully the interaction between the mooring and the current turbine system in a very dynamic ocean environment. Finally, it is worth mentioning that some studies were also conducted for mooring systems applied to tidal stream current turbines. Bowie [18] argued that a flexible mooring system offers advantages for tidal current turbines in installation and maintenance. Jo *et al.* [19] have also investigated the mooring system with a duct-type tidal current turbine system in shallow water.

FKT SYSTEM

To harness the endless hydrokinetic energy brought by the Kuroshio current passing Taiwan's east coast from south to north, the floating Kuroshio Turbine (FKT) was designed by the joint team of the National Taiwan University and the National Taiwan Ocean University. Fig. 1 shows a floating device moored to the seabed with an anchor and mooring line system. The rated power of the system is 0.5 MW at the current speed of 1.5 m/sec. The system comprises five major components. The uppermost part is the foil float, equipped with two aft- and two fore-buoyancy engines. The float provides buoyancy for the system. It also serves to provide proper dynamic lift helping the system float or dive more readily. This is accomplished by flooding or draining water out of some of these buoyancy engines to create positive or negative incident angle of the incoming flow to the foil float. Two vertical supports connect the foil float and the current turbine system which consists of two rotors. The turbines are connected by a flat-plate cross beam. The turbines harness the ocean current energy, and electricity is generated by the direct-drive permanent-magnet generator set inside the turbine nacelles.

The FKT project is at the stage of feasibility study. For this purpose, a 1/5 model has been adopted for investigation. The chord length is 4.0 m, the span is 7.5 m, and the rated power is 20kW at the current speed of 1.5m/sec. The water depth is specified to be 50 m. The design operating depth is 10-40 m. A single-line mooring system is provided. Two different short auxiliary mooring line systems: 2-AML and 3-AML, were investigated. The 2-AML system consists only of two side lines, as shown in Fig. 1. These lines connect the trailing points of the nacelles and the main line. The 3-AML system has three lines, with the same two side lines as in the first system and an additional one connected to the midpoint of the cross beam. In each system, the auxiliary lines join together the connector with the main line which is then connected to the anchor on the seabed. It was assumed that all lines can freely slide on the connector. The length of the main line is 40 m. Each of the auxiliary side lines is 5 m long, while the length of the middle line is 3.8 m. To make the system horizontal when it operates under normal conditions, the centres of gravity for the two systems are different. For the 2-AML, the centre is 2.12 m downstream of the trailing point of the nacelle, while for the 3-AML it is 1.69 m. The centre of buoyancy, the same for the two designs, is 1.85 m downstream of the trailing point of the nacelle. The system weight is 15.262 tones when the buoyancy engines are empty and 19.722 tones when they are full of water.

METHOD OF STUDY

The system dynamics was investigated computationally. There are several forces acting on the FKT system. They include buoyancy (mainly from the foil float), weight, hydrodynamic drag when the current passes the system and the mooring lines, dynamic lift due to the foil float, tension forces exerted by the mooring lines, and the propulsive force produced by the contra-rotating turbines.

The system buoyancy and weight were obtained directly from the system design data. The buoyancy is related to the volume of the system which is also available from the design data. The turbine blades were designed using the in-house lifting line and the lifting surface code. The foil float of finite span provides the dynamic lift. The lift coefficient was taken from [20] with the aspect ratio $AR = 2$.

The system drag coefficients were found by using the commercial software FLUENT. The computations were based on the Reynolds-averaged Navier-Stokes equations, which were solved with the standard k-ε turbulence model. The standard wall function was adopted for the flow near the solid wall. The SIMPLE algorithm was employed for nonlinear

iterations between the velocity and pressure fields. It was assumed that the current has a uniform speed of 1.5 m/sec.

We define the drag coefficients

$$C_d = \frac{D}{\frac{1}{2}\rho U^2 A} \quad (1)$$

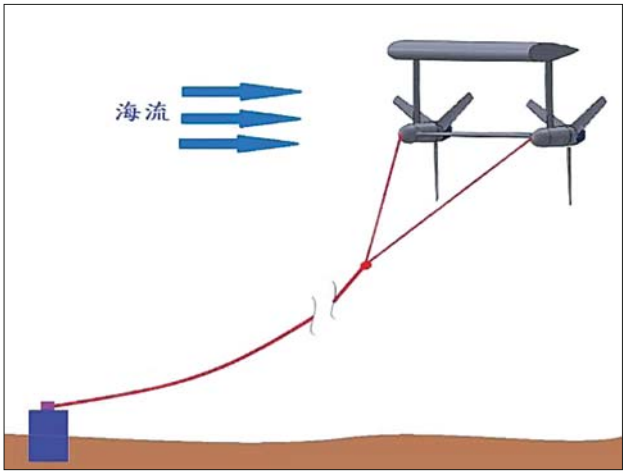

Fig. 1. Schematic of the FKT system

Tab. 1. Drag coefficients for linear and angular motions

Linear motion		
$(C_d)_x$	$(C_d)_y$	$(C_d)_z$
0.173	1.184	1.318
Angular motion		
$(C_d)_{x\text{-axis}}$	$(C_d)_{y\text{-axis}}$	$(C_d)_{z\text{-axis}}$
0.364	0.228	0.012

Tab. 2. Added mass coefficients for linear and angular motions

Linear motion		
$(C_a)_x$	$(C_a)_y$	$(C_a)_z$
0.173	0.369	4.15
Angular motion		
$(C_d)_{x\text{-axis}}$	$(C_d)_{y\text{-axis}}$	$(C_d)_{z\text{-axis}}$
18.2	4.16	1.23

and

$$(C_d)_M = \frac{M}{\frac{1}{2}\rho\omega^2 A_M} \quad (2)$$

for linear and angular motions, respectively. Their exact values obtained by Lo [21] for the 6 degrees of freedom are given in Table 1. In Eqs. (1) and (2), D is the drag, ρ is the fluid density, U is the uniform incoming current speed, A is the projected area of the system in the flow direction, M is the angular drag, ω is the angular velocity, and A_M is the area moment of inertia corresponding to the axis about which the outer flow rotates.

Moreover, we define the added mass coefficients for the linear and angular motions, respectively:

$$C_a = \frac{m_a}{\Delta} \quad (3)$$

and

$$C_a = \frac{I_a}{\Delta \times l_c^2} \quad (4)$$

Their values can be obtained via the commercial code WAMIT, which employs the boundary element method in computations. In Eqs. (3) and (4), m_a is the added mass, Δ is the displacement of the system, I_a is the added moment of inertia, and l_c is the characteristic length corresponding to the rotating axis. The product $\Delta \times l_c^2$ represents the hydrodynamic moment of inertia about the centre of gravity. Table 2 shows the coefficients obtained by Lo [21].

The mooring line can be modelled with a catenary line. With all the coefficients obtained as described above, the system dynamics was analysed by employing the commercial package OrcaFlex. This is a time-domain FEM code widely used in offshore industry. To integrate in time, the implicit generalized-α method was selected which damps numerical oscillations with high-frequency dissipations. Moreover, the FKT system was simplified as lumped mass element.

RESULTS: 2-AML SYSTEM WITHOUT SURFACE WAVES

In this section, the deployment system dynamics of the FKT during deployment is studied computationally. Three kinds of mooring lines, i.e., polyester ropes, iron chains, and 6 × 19 wire with wire core, are considered.

A. Polyester ropes

Three cases were studied in which the rope diameters were d = 0.03 m, 0.1 m, and 0.3 m, respectively. All mooring lines were identical in material and neutrally buoyant. It was assumed in the computations that the bulk modulus is infinite, the axial stiffness is 700 kN, the bending stiffness is 120 kN m^2, the torsional stiffness is 80 kN×m^2, and the Poisson ratio is 0.5. The mass per unit length is 0.707 kg/m, 7.854 kg/m, and 70.68 kg/m for d = 0.03 m, 0.1 m, and 0.3 m, respectively.

The dynamic responses of the system for d = 0.03 m are shown in Fig. 2. No waves are present in this case. It is interesting to see in Figs. 2(a) and (b) that the system appears stable during the flooding process. However, when the turbines start to operate, the FKT system suffers serious pitching and rolling motions, the amplitude of which is quickly amplified.

The results for d = 0.1 m are shown in Fig. 3. Similar system fluctuation phenomena can be found here. The pitching motion results in dynamic lift fluctuations of the foil float and induces system heaving motions. Even though the diameter is larger, the amplitude of temporal fluctuation is almost as big as that for d = 0.03 m. However, the pitching growth rate is slightly smaller, and it takes a longer time for the pitching motion to develop.

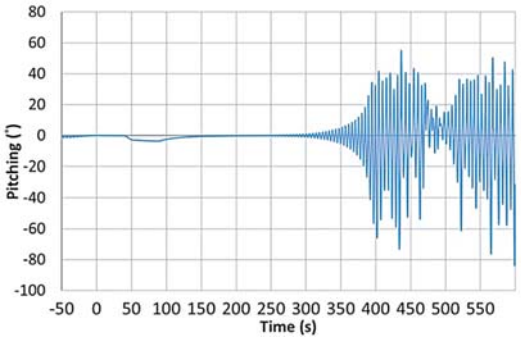

(a) Time-history of system pitching motion

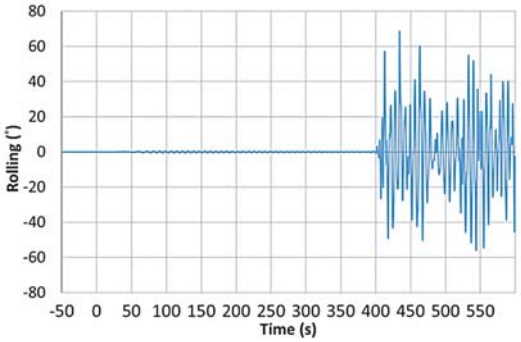

(b) Time-history of system rolling motion

Fig. 2. System dynamics results for d = 0.03 m

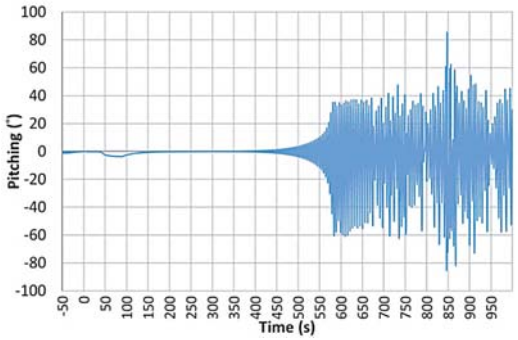

(a) Time-history of system pitching motion

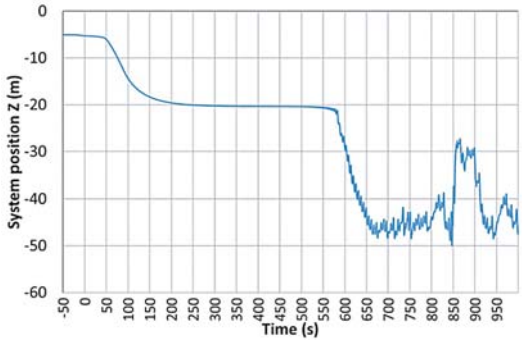

(b) Time-history of system heaving motion

Fig. 3. System dynamics results for d = 0.1 m

Fig. 4 shows the results for d = 0.3 m. Only the heaving motion is shown here because the deployment is fully stable. No pitching and rolling motions have been incurred. The diameter of the mooring line has a significant effect on the system dynamics during deployment. Obviously, it should be large enough to make the system stable during the deployment process.

B. Chains

Fig. 5 shows the geometry of the employed chains. Three different nominal diameters were selected: d = 0.03, 0.04, and 0.05 m. The mass per unit length is $21.9d^2$ te/m, the axial stiffness is $1.01\times108d^2$ kN, and the bending stiffness is 0. The normal and axial drag coefficients are 2.6 and 1.4, while the normal and axial added mass coefficients are 1.0 and 1.4, respectively.

Fig. 6 shows the results of the system heaving motion during the deployment process. For all cases, the motion is stable, and the system reaches its final operating position smoothly. Compared to the case with flexible ropes, the iron chain can obviously lead to safer and much more satisfactory deployment. It is also evident that the chain with a larger nominal diameter is heavier per unit length and, therefore, the FKT system sinks to a deeper position under normal operating conditions.

C. 6×19 wire rope with wire core

Wires have many applications in the offshore industry including towing, mooring and winching. Fig. 7 shows the 6×19 wire rope with wire core which was used in the present study. We assumed the Young's modulus to be 1.13×108 kN/m^2 and the axial stiffness to be $4.04\times10^7d^2$ kN.

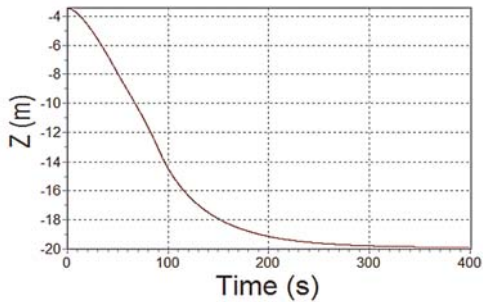

Fig. 4. Time-history of system heaving motion for d = 0.3 m

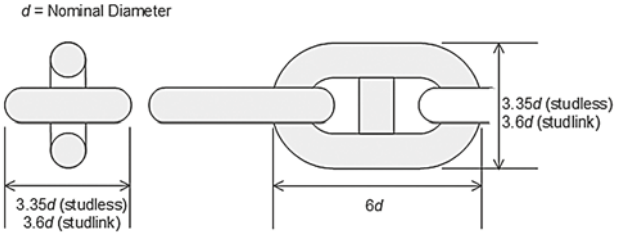

Fig. 5. Geometry of chains used in the study [22]

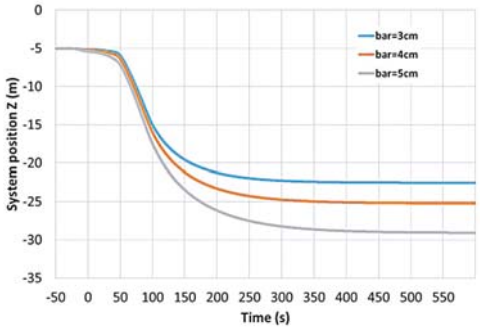

Fig. 6. Heaving motion of system with iron chains of different diameters

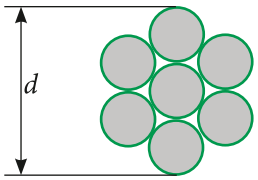

Fig. 7. 6×19 wire rope with wire core [22]

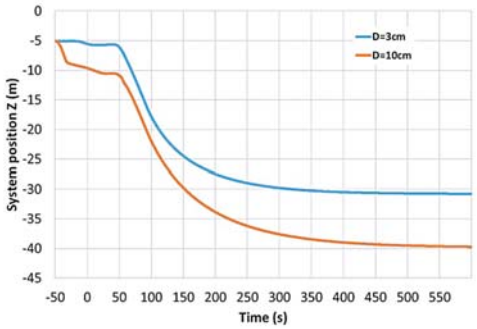

Fig. 8. Heaving motion of system with wire ropes of different diameters

Furthermore, we also assumed that the metallic area is 0.455 ($\pi d^2/4$), where d is the nominal diameter of the wire rope as shown in Fig. 7. For simplicity, the bending stiffness was assumed zero. In this investigation, two different values of d: 0.03 and 0.1 m were examined.

The results are shown in Fig. 8. They are similar to those shown in Fig. 6 for chains. In fact, the wire rope is even heavier. Hence, it can be expected that the deployment would be smooth. Again, there are no fluctuation motions in all six degrees of freedom of the system. Furthermore, the system operates at an even larger depth from the free surface when it settles. It is also interesting to note that during the deployment, it takes about the same time for the system to reach its stable operating position if the deployment incurs no instability. This can be observed in Figs. 4, 6, and 8.

The study seems to imply that for a smooth deployment, the mooring line should be relatively heavy (in terms of its linear mass density). There exists a critical value of the linear mass density which ensures the system to be deployed stably. In fact, a chain of the same shape as the iron one but of neutral buoyance was also investigated, and the results have shown that the system deployment is unstable. Therefore, the material of the mooring line may be considered of no importance, while the only important factor is its linear mass density.

RESULTS: 2-AML SYSTEM WITH SURFACE WAVES

The next studied case represents a more complicated deployment process due to the presence of waves. In fact, this case better reflects a real sea deployment. The wave height was assumed to be 1 m. Since the deployment for the system with flexible ropes is usually not stable in a calm sea if the line diameter is not sufficiently large, only the mooring systems with iron chains and wire rope in waves were analysed. Generally, our study shows that the pitching motion is the most important factor which may cause instability or fluctuations in the system. Hence, the following discussion will focus on system pitching motion only. Before proceeding to the discussion, it should be first mentioned that the system has a natural period of about 5 sec in pitching motion [21], which has been verified by Wu *et al.* [23].

A. Chains

The wave period is a critical parameter which may affect system dynamics. Another parameter which also interacts with the system motion is the wave direction. In the following discussion it is assumed that the incoming wave moves in the opposite direction as that of the current. This is the most critical wave direction, as in the Taiwan area the winter monsoon consistently creates big waves for a few months. The waves also reduce the flow speed of the Kuroshio current in winter.

The pitching motions for d = 0.03 m and different wave periods, T, are shown in Fig. 9. If the period is small, T = 4 sec, the system reaches its stable operation quickly, as shown in Fig. 9(a). However, for T = 5 sec, the system suffers from serious periodic pitching motion. Even at T = 6 sec, the pitching fluctuation is still significant.

A slightly different pattern is shown in Fig. 10 for d = 0.04 m. At T = 4 sec and 6 sec, the long-term behaviour of pitch motion is similar to that when d = 0.03 m. However, at T = 5 sec, the pitching fluctuation is much reduced.

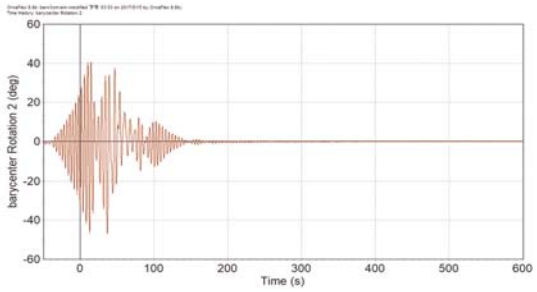

(a) T = 4 sec

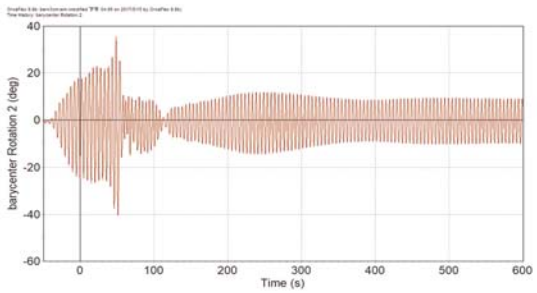

(b) T = 5 sec

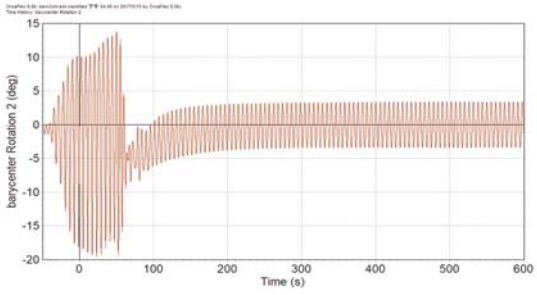

(c) T = 6 sec

Fig. 9. Pitch motion of system with iron chain of d = 0.03 m

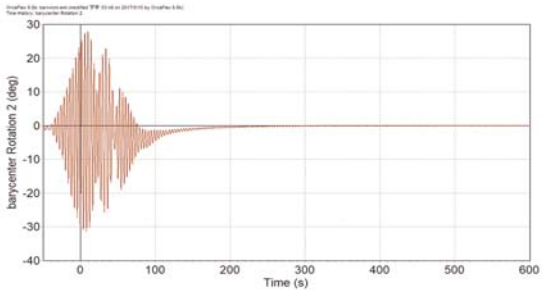

(a) T = 4 sec

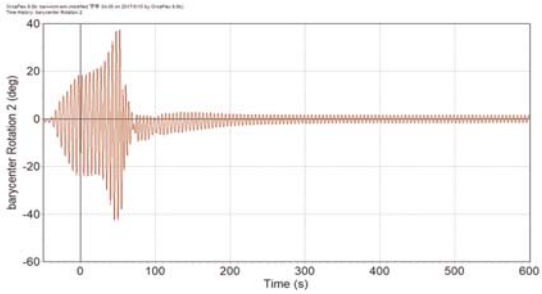

(b) T = 5 sec

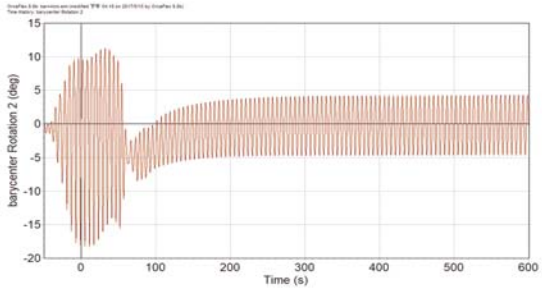

(c) T = 6 sec

Fig. 10. Pitch motion of system with iron chain of d = 0.04 m

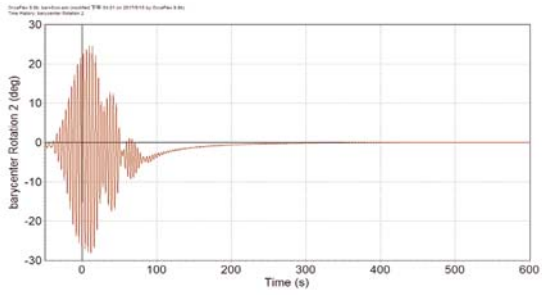

(a) T = 4 sec

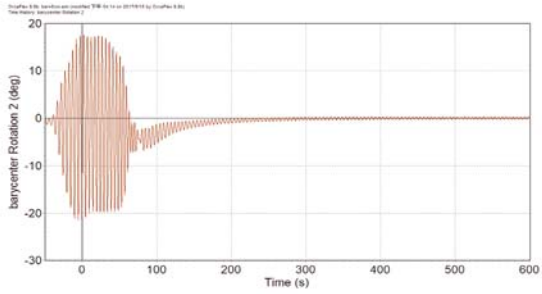

(b) T = 5 sec

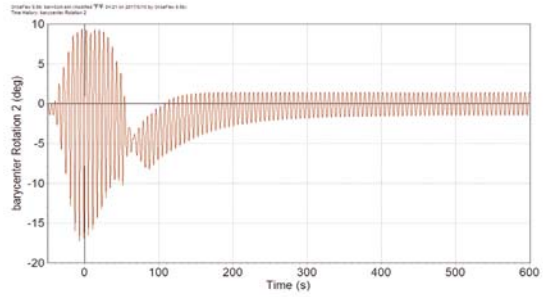

(c) T = 6 sec

Fig. 11. Pitch motion of system with iron chain of d = 0.05 m

The results for d = 0.05 m are shown in Fig. 11. The amplitudes of fluctuations for all cases are reduced. However, at T = 6 sec, despite the fact that the pitching is small, it still can result in mooring line load fluctuations and lead to fatigue problems in long-term operations.

It should be mentioned that the reduction of pitching fluctuations for a chain with larger nominal diameter can be possibly attributed to the fact that the turbine system is located at a deeper position, where the water particle motion due to waves is smaller. Nevertheless, the results do show that the waves have strong impact on the operation of an ocean current turbine. This influence at least refers to the energy harvesting efficiency and system fatigue in long-term operation.

B. 619 Wire Rope with Wire Core

Fig. 12 shows the pitch motion for d = 0.03 m and different wave periods. At T = 4 sec, the computation leads to a blow-up solution which indicates that the system is unstable. At T = 5 sec, the computation does not blow up, but the pitch fluctuation is very intensive and may not be acceptable in practical deployment and operation. The pitching fluctuation is much reduced at T = 6 sec.

Figs. 6 and 8 show that the system with iron chain of d = 0.05 m and that with wire core of d = 0.03 m operate at similar depth if no waves are present. However, under the wave action, the system responses shown in Figs. 11 and 12 are not similar. The response of the wire rope system is much worse, while the mooring with an iron chain appears to exhibit better performance for the present FKT system.

At d = 0.10 m, the results shown in Fig. 13 are evidently much improved. The fluctuation of the system pitch motion is greatly reduced. Of course, for this condition, the wire rope is also much heavier, as can be observed in Fig. 8. In fact, the system operates at a depth close to the sea bed. The system does not fluctuate under normal operating conditions for T = 4 sec and 5 sec. As for the case of T = 6 sec, only a small amplitude of fluctuation is observed.

RESULTS: 3-AML SYSTEM WITH SURFACE WAVES

In this section, the effect of 3-AML system on deployment dynamics in waves is considered. For different mooring lines, Figs. 14–16 show the amplitudes of stably oscillating pitching motion after deployment. It appears that there exists a resonant frequency (or period) in all situations, even though its value slightly varies for different mooring lines. The resonant

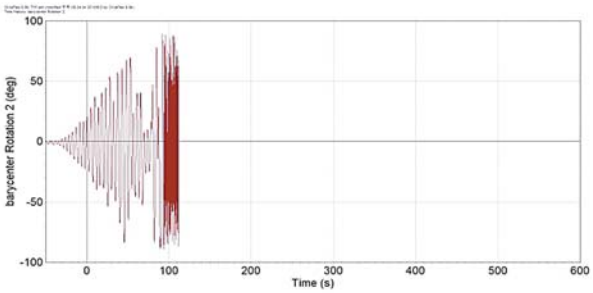

(a) T = 4 sec

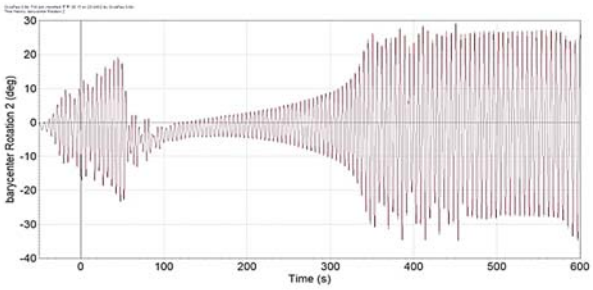

(b) T = 5 sec

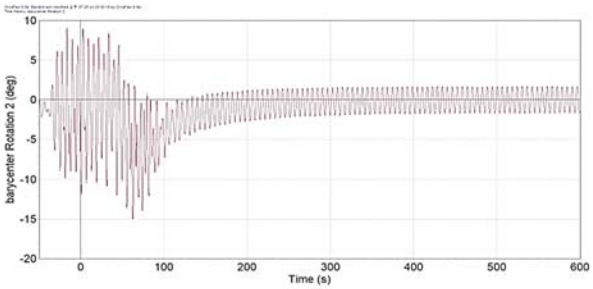

(c) T = 6 sec

Fig. 12. Pitch motion of system with wire rope of d = 0.03 m

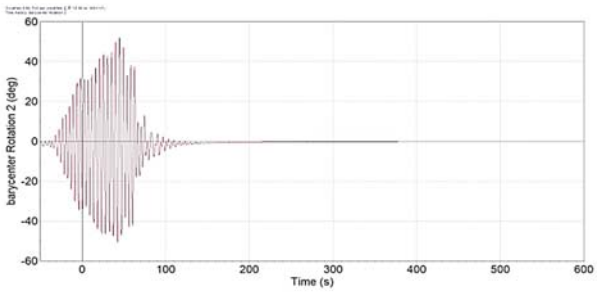

(a) T = 4 sec

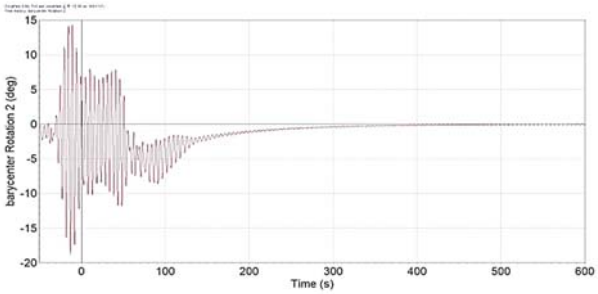

(b) T = 5 sec

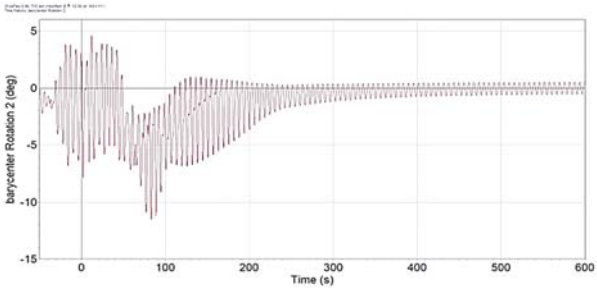

(c) T = 6 sec

Fig. 13. Pitch motion of system with wire rope of d = 0.1 m

frequency shown in Fig. 14 decreases with the increasing line diameter. For $d = 0.03$ m, it is interesting to note the appearance of two peaks, which implies that the diameter in the 3-AML system has a significant effect on FKT system dynamics. In addition, large oscillation of pitch motion can be observed, with the period ranging from 4.83 to 7.85 sec. This is a wide range of wave period, for which the FKT system might not be able to work well. It implies that the 3-AML design is not a robust one, compared to the 2-AML design as shown by Wu [23], if the polyester type of mooring line is employed and the line diameter is small. If the diameter is increased to 0.1 m, the dynamic response is much improved, as shown in Fig. 14(b), and is similar to that of the 2-AML design.

The frequency responses of systems with iron-chain mooring lines are shown in Fig. 15. It shows that at small wave frequencies, 0.8–1.2 rad/sec, (or wave periods of 5.23–7.85 sec), the FKT system responds periodically and more significantly to waves. Compared to the polyester lines, the fluctuations of the system with an iron chain are milder. The peak values appear at around 0.9–1.1 rad/sec.

Fig. 16 shows the results for a wire rope of $d = 0.1$ m with wire core. The fluctuation amplitudes are much smaller than those in the previous two types of mooring lines. The peak appears at around 0.9 rad/sec. However, for a small diameter,

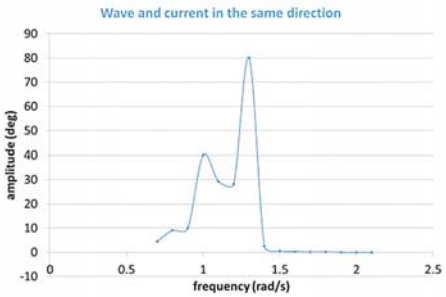

(a) d = 0.03 m

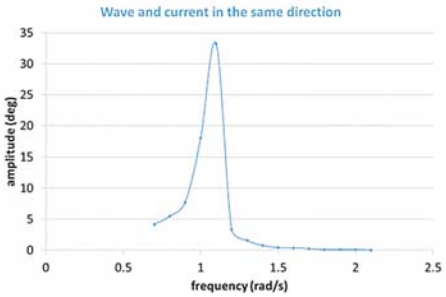

(b) d = 0.1 m

Fig. 14. Amplitudes of pitching responses in frequency domain for 3-AML design with polyester lines

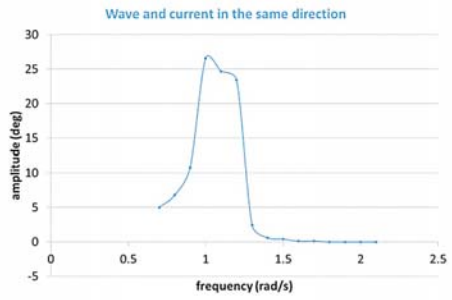

(a) d = 0.3 m

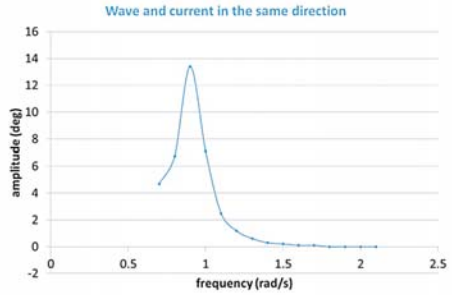

(b) d = 0.04 m

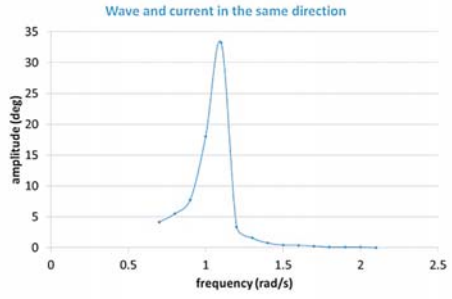

(c) d = 0.05 m

Fig. 15. Amplitudes of pitching responses in frequency domain for 3-AML design with iron chains

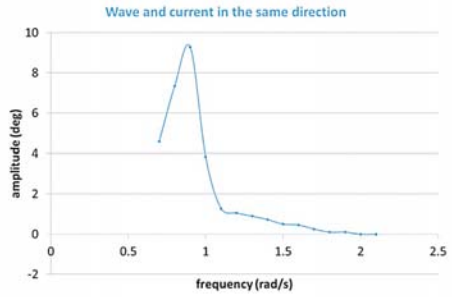

Fig. 16. Amplitudes of pitching responses in frequency domain for 3-AML design with wire rope of d = 0.1 m with wire core

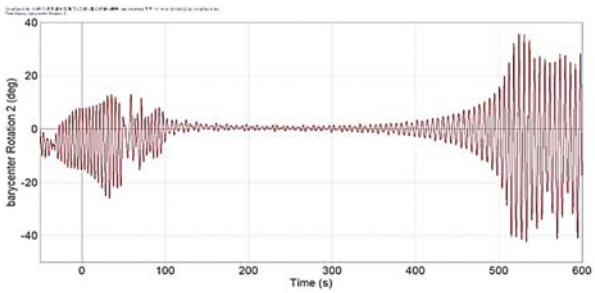

Fig. 17. Pitching responses for 3-AML design with wire rope of d = 0.03 m with wire core at wave period T = 4 sec

d = 0.03m, severe fluctuations appear in a wide frequency range, as shown in Fig. 17 given as an example. It appears that during the deployment process, the system gradually reaches its steady operating state, but the amplitude of the fluctuations is amplified.

To summarize the above computational results, the following observations can be made:

For the 3-AML system, the centre of gravity is closer to the mooring line connection point on the FKT system. The system appears to suffer large amplitude pitching motion more easily than the 2-AML system. The range of the wave period at which the pitching fluctuation becomes significant seems bigger than that of the 2-AML system with the same mooring lines in type and diameter. In addition, the diameter of any type of mooring line must be large enough to make the FKT system reach steady and stable operation. This implies that the mooring lines must exert relatively large restoring forces if the FKT system operates in the ocean current with waves on the free surface.

CONCLUSIONS

In the present study, the effect of mooring line type on the FKT system dynamics has been investigated numerically. Three different types of mooring lines were studied, which were: the polyester rope, the iron chain, and the wire rope. Two types of auxiliary mooring systems were investigated with different centres of gravity for the FKT system to make it horizontal under normal operating conditions.

The performed investigations have shown that without wave impact, the polyester rope can lead to system fluctuation or instability if its diameter is not sufficiently large. The performance of the system with iron chains and wire ropes is much improved. The system fluctuation in deployment can be related to the linear mass density of the mooring line. If the linear mass density is larger than some critical value, the system can exhibit good steadiness under normal operating conditions.

With wave impact, it has been found that, for the 2-AML system, the iron chain can have better performance than the wire rope in the sense that the system fluctuation is much smaller under normal operating conditions. Consequently, it is considered the best choice from among the three examined types of mooring lines for the present floating Kuroshio turbine system with Y-shape mooring line system. However, for the 3-AML design, the wire rope with wire core seems to perform better.

ACKNOWLEDGMENT

The study was made possible with the grant from Ministry of Science and Technology, the Republic of China, under the contract MOST 105-3113-E-002-019-CC2 and funding support from CSBC Corporation.

REFERENCES

1. N.S. Diffenbaugh, D. Singh, and J.S. Mankin, *Unprecedented climate events: Historical changes, aspirational targets, and national commitments*, Sci. Advances, Vol. 4, eaao 3354, 2018.

2. H. Jeffrey, B. Jay, and M. Winskel, *Accelerating the development of marine energy: Exploring the prospects, benefits and challenges*, Technol. Forecast. Soc. Change, Vol. 80, pp. 1306–1316, 2013.

3. J. Van Zwieten, F.R. Driscoll, A. Leonessa, and G. Deane, "*Design of a prototype ocean current turbine---Part I: mathematical modeling and dynamics simulation*, Ocean Eng., Vol. 33, pp. 1485–1521, 2006.

4. F. Chen, The Kuroshio Power Plant, Switzerland: Springer, 2013.

5. IHI Corporation, *Power generation using the Kuroshio Current*, IHI Eng. Review, Vol. 46, pp. 2–5, 2014.

6. J.-Y. Bai, *Ocean current power generation project*, Workshop on Development of Marine Mechanical Energy Industry in Taiwan, Keelung, Taiwan, 2012 (in Chinese).

7. A. Røkke and R. Nilssen, *Marine current turbines and generator preference: A technology review*, Int. Conf. Renew. Energies Power Quality, Bilbao, Spain, 2013.

8. Y. Kyozuka, *Tidal and ocean current power generation*, J. Smart Processing, Vol. 3, pp. 137–145, 2014.

9. A.R. Cribbs, *Model analysis of a mooring system for an ocean current turbine testing platform*, M.S. thesis, Florida Atlantic University, Boca Raton, Florida, USA, Dec. 2010.

10. A.R. Cribbs and J.H. Van Zwieten, "Global numerical analysis of a moored ocean current turbine testing platform," Oceans, Seattle, OR, USA, 2010.

11. M. Shibata, K. Takeda, and K. Takgai, *Mooring and power cable system for current-turbine*, Oceans, San Diego, CA, USA, 2013.

12. K. Takagi, T. Waseda, S. Nagaya, Y. Niizeki, and Y. Oda, *Development of a floating current turbine*, Oceans, Hampton Roads, VA, USA, 2012.

13. Y.-H. Rho, C.-H. Jo, and D.-Y. Kim, *Optimization of mooring system for multi-arrayed tidal turbines in a strong current area*, Proc. ASME 33rd Int. Conf. Ocean, Offshore and Arctic Eng., San Francisco, CA, USA, 2014.

14. C.C. Tsao and A.H. Feng, *Motion Model and Speed Control of the Cross-Stream Active Mooring System for Tracking Short-Term Meandering to Maximize Ocean Current Power Generation,* J. Mech., 1–15, 2017.

15. K. Shirasawa, J. Minami, and T. Shintake, *Scale-model experiments for the surface wave influence on a submerged floating ocean-current turbine*, Energies, Vol. 10, 702, 2017.

16. J.-T. Wu, J.-H. Chen, C.-Y. Hsin, and F.-C. Chiu, *A computational study on system dynamics of an ocean current turbine*, J. Hydrodyn., accepted, 2018.

17. A.R. Cribbs, G.R. Karrsten, J.T. Shelton, R.S. Nicoll, and W.P. Stewart, *Mooring system considerations for renewable energy standards*, Offshore Technology Conf., Houston, TX, USA, 2017.

18. A.E.D. Bowie, *Flexible moorings for tidal current turbines*, M.S. thesis, University of Strathclyde, Glasgow, UK, Sep. 2012.

19. C.H. Jo, D.Y. Kim, B.K. Cho, and M.J. Kim, *Mooring analysis of duct-type tidal current power system in shallow water*, Int. J. Geol. Environ. Eng., Vol. 10, pp. 577–582, 2016.

20. D.W. Atkins, *The CFD assisted design and experimental testing of a wingsail with high lift devices*, Ph.D. dissertation, University of Salford, Salford, UK, 1996.

21. H.Y. Lo, *Dynamic analysis of current turbine system*, M.S. thesis, National Taiwan Ocean University, Keelung, Taiwan, 2017 (in Chinese).

22. OrcaFlex Manual, Ver. 9.5a, Orcina Ltd., Cumbria, UK, 2011.

23. J.-T. Wu, J.-H. Chen, C.-Y. Hsin, and F.-C. Chiu, *A computational study on system dynamics of an ocean current turbine*, J. Hydrodyn., Vol. 30, pp. 395–402, 2018.

CONTACT WITH THE AUTHOR

Jiahn-Horng Chen
jhchen202@gmail.com

National Taiwan Ocean University
2 Pei-ning Road, 20224 Keelung
Taiwan

sciendo

POLISH MARITIME RESEARCH 1 (101) 2019 Vol. 26; pp. 30-39
10.2478/pomr-2019-0004

UNIVERSAL AUTONOMOUS CONTROL AND MANAGEMENT SYSTEM FOR MULTIPURPOSE UNMANNED SURFACE VESSEL

Andrzej Stateczny
Gdańsk University of Technology, Poland
Marine Technology Ltd. Poland
Pawel Burdziakowski
Gdańsk University of Technology, Poland

ABSTRACT

The paper presents design, structure and architecture of the Universal Autonomous Control and Management System (UACAMS) for multipurpose unmanned surface vessel. The system was designed, installed and implemented on the multipurpose platform - unmanned surface vessel named HydroDron. The platform is designed to execute hydrographic survey missions with multi-variant configuration of the survey system (payload?) including multi-beam echo sounder, sonar, LiDAR, automotive radar, photographic and spectral camera systems. The UACAMS designed to provide flexibility that enables to operate on the different kind of surface platform and different type of functional payload. The full system configuration provides all four level of autonomy starting from remotely controlled to full autonomous mission. Each level can be implemented and run depending on user specific requirements. The paper explains the differences between autonomous and automatic mission and shows how the autonomy is implemented into the presented system. The full hardware structural design as well as the software architecture are described. In order to confirm initial assumptions the applied system was tested during four- week sea trials and tuned for a selected vessel to confirm assumptions. In the project, also the original shore control station was designed, produced and tested for the vessel, including specific user controls and radio communication system. Conclusions sum up all crucial points of the design and system implementation process.

Keywords: unmanned surface vessel, autonomous, management, control, system

INTRODUCTION

A proper control of multipurpose unmanned surface vessel, or generally unmanned vehicle, needs an advanced and sophisticated management system. The universal management system designed for multipurpose unmanned vessel, should have ability to deal with different type of functional payload, different tasks and situation. Moreover, general-purpose (universal) systems should have ability to be tailored to manoeuvring parameters of different vessels.

Among Unmanned Surface Vehicle (USV) solutions available on the market , single-hull platforms and catamarans can be indicated. During subsequent visits to Oceanology International Conference held in London in 2012, 2014, 2016 and 2018 it was easily seen a significant increase in number of presented solutions for USV, just as it happens in the market of unmanned aircraft. The USVs are produced in a range from small „pocket" platforms that can be carried in the trunk of the car to larger units of a nearly seagoing range and usually equipped with Multi-Beam Echo Sounder (MBES). see Fig. 1–11 (the photos taken by A. Stateczny during Oceanology International Conferences, London)

Fig. 1. Z-boat

Fig. 2. Ocean Nautical Innovations

Fig. 4. HyCOPS (on the left) and Sonobot (on the right)

Fig. 5. DeepVision

Fig. 6. HyDrone

The HyDrone was introduced to Polish market by Gdynia Maritime University [21,22].

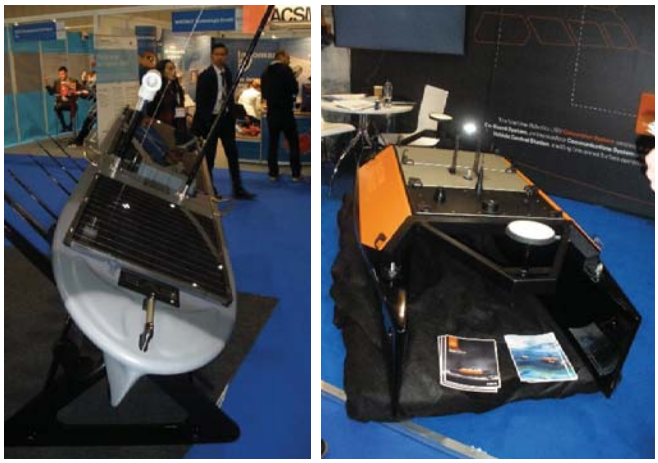

Fig. 7. Solar boat (left)and Marine Robotics (on the right)

Fig. 8. XOCEAN

Fig. 9. Echoboat

Fig. 10. Teledyne Oceanscience

Fig. 11. C-Worker – whole set solutions

The presented overview of USVs offered on the markets indicates that many companies undertake the studies related to the USV development for hydrographic measurements in shallow waters. It is a strongly growing market which clearly could be seen during subsequent visits to the Oceanology International Conference in London.

In recent years in Poland , there were developed unmanned floating platforms such as UPP-1E platform implemented by the Department of Environmental Engineering ,Cracow University of Technology, and Edredon platform – by the Polish Naval Academy. Currently there are not known any attempts to developing ASV construction besides HydroDron constructed by Marine Technology Ltd.

Fig. 12. UPP-1E universal measuring floating platform

The UPP-1E platform is intended for bathymetric measuring but in terms of technology cannot be compared with the Edredon. The differences result from the construction parameters , installation of different sensors and their control systems. The Edredon was built on the basis of RIB hybrid boats (Rigid – Inflatable Boat) in 2009-2011.

Fig. 13. The Edredon during the tests

Both the platforms represent a significant intellectual contribution to the development of design ideas for unmanned floating platforms in Poland.

The new platform named HydroDron, which is under construction by Marine Technology Ltd have significant advantages distinguishing it from the aforementioned solutions. Components installed on the platform are characterized by significantly improved characteristics in comparison with the aforementioned ones.

Fig. 14. The HydroDron during the tests

The HydroDron for hydrographic measurements is the product significantly ahead of previously available solutions on the Polish market and foreign markets. This applies not only to its technical parameters and characteristics, but also a purpose of using. It is assumed that the vehicle is able to operate in shallow waters where due to the presence of underwater obstacles at shallow depths a high precision navigation is required. The platform have a very high computational potential. The Marine Technology company has considerable experience in developing solutions for the maritime economy with a high level of intelligence. This also applies to collision avoidance systems based on solutions which use artificial intelligence and multisensory data fusion. Artificial intelligence is frequently implemented for autonomous navigation [1,14,20] or for optimal ship's trajectory control [16-17]. The combination of multi-task platform with intelligent maneuvering will allow to offer an innovative product in terms of autonomy characterized by novelty on an international scale. Its floating structure allows to perform tasks in an autonomous manner, while ensuring a high accuracy required e.g. in dredging work. It is a technological challenge that the HydroDron design team set itself as the goal. This challenge forces to apply an innovative method of connecting accuracy of platform positioning with that of hydrographic measurements. In this regard the Marine Technology company uses the existing experience in the hydrographic work for developing an innovative product.

UNMANNED VESSEL SYSTEM DESIGN

Unmanned surface vehicle (USV) can be defined as a generic vessel designed to operate without human operator on board. The definition can be referred to any unmanned vehicle, including aerial, ground and underwater, and can be used for any kind of vehicle able to operate without human on board [2]. The typical unmanned vehicle is a part of the unmanned system, in the presented case – Unmanned Vessel System (UVS). While the USV is referred only to the surface platform, the whole unmanned vessel system includes a vehicle, shore control station (SCS), communication and control link (C2) and logistic module (Fig.15).

The basic USV modules are placed on board unmanned platform (vessel) and there are a mission control module, autonomous control module, sensors module, effectors and payload.

The mission control module consists of hardware and software responsible for navigation, orientation and automatic algorithms calculation. This module is fed with data from sensors module, operator's remote commands and autonomous module, and , based on currently established command priorities, it generates appropriate executive commands to the effectors module. Depending on the commands priorities (currently – ordered level of mission) the control module (Fig.16) directs the platform to a desired position and orientation.

The autonomous control module consists of hardware and software responsible for high level autonomous algorithms calculation including dynamic and adaptive path planning, collision avoidance and multisensory fusion. The module is fed with data from sensors module. Based on the sensor data and their fusion, the module continuously analyzes the overall situation and calculates required action. As in the navigation module, depending on the currently ordered level of autonomy, the autonomous control module sends the commands to the mission control module and to the

operator display. In fully autonomous mode, the mission control module's commands are overwritten by the calculated autonomous action. In semi-autonomous mode, the required action is presented onto the operator display as a navigation advice. In this case, the operator can use this information and manually direct the unit to the required action, acknowledge the required action and make the system to automatically perform it, or ignore the suggested action.

The sensors module, a part of the unmanned vessel system, consists of all sensor installed on board the unit.

The sensors module includes all environment, anti-collision, electrical, diagnostic, hydrographic (payload) and navigation sensors. Sensor information can be shared within the system or used only by a specific system.

The supportive systems contain all necessary systems, outside the UVS, which are required to conducting USV mission, such as the global navigation satellite system (GNSS), network for real-time-kinematic (RTK) positioning reference stations, etc.

The effector is defined as a device used to produce a desired change in an object in response to input. In the presented case, the propulsion and ruder system to drive the platform is the effector, as well as all other actuators and servos mounted on board the platform to drive remaining mechanical devices. The input signal to the effectors is generated by the mission control module as a result of automatic control or autonomous control calculations.

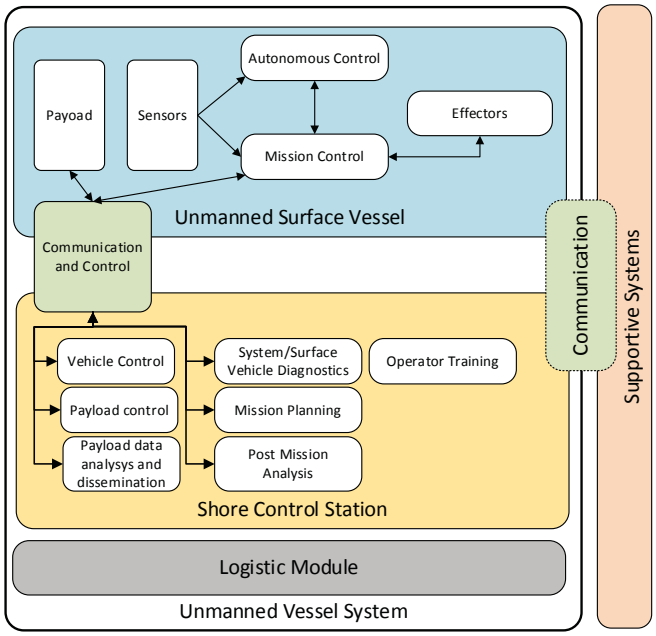

Fig. 15. Unmanned Vessel System modules (acc. these authors)

Depending on main purpose and tasks of a USV, its payload can be differently configured and equipped. In the presented case the USV is designed to carry out hydrographic survey missions in areas of ports, embankments, anchorages, bays and lakes, rivers and other restricted water areas and its main payload equipment includes professional bathymetric systems [23].

The shore control station (SCS) can be defined as stationary or transportable devices intended to monitor, command and control the unmanned vessel. The crucial functionalities of the shore control station are [2]: vehicle control – a capability to effectively control the USV during its mission, payload control – ability to operate payload sensors from the shore, mission planning – functionality that aids USV's operator in planning the mission providing required knowledge inputs concerning capabilities and USV's limitations, payload data analysis and dissemination – capability to disseminate the data from payload to eventual users, system/surface vehicle diagnostics – automatic test facility for USV and SCS effective maintenance and deployment, operator training – facility to train the surface vehicle operator in handling the vessel, practicing mission plans and emergency procedures, post-mission analysis – capability to store mission data and payload data and to analyze it after the flight mission.

AUTONOMOUS VERSUS AUTOMATIC MODE

Within autonomous vehicles group, the term "autonomous" is sometimes incorrectly used for defining fully automatic unmanned systems. As an adjective "automatic" means capable to operate without external control or intervention. It means that the vehicle is capable of following a programmed scenario or situation and all its reactions are already assigned in advance and implemented into vehicle's processor (mission controller) by the developer. "Autonomous" stands for self-governing , intelligent, sentient, self-aware, thinking, feeling, governing independently, and in application to a vehicle or robot means that it not only performs one or more task automatically, but is able to perform decision-making process independently , i.e. without operator's inputs and, the most important, in a complex situation not previously assigned. The autonomous decision is made on the basis of previous knowledge and experience collected by the vehicle. The autonomous vehicles are able to act in complicated, real-world environment, while automatic vehicles are not. Automatic vehicle will always need a human aid to realize decision -making process. The remotely controlled vehicles base on human control inputs, and are not able to perform any tasks without such control. It is important to notice, that for safety reason, any autonomous or automatic vehicles are to be equipped with remote control. The remote control should be considered as a safety pilot in case of any unpredictable behaviour of machine. The semi-autonomous vehicles perform some tasks independently, and some are to be acknowledged by the human operator.

According to the range of autonomy, unmanned vehicles can be divided into several levels (Fig.16):

Level 1: remote control mode (manual mode); on this level the unit is able to perform commands received form operators station (remote control). This is the lowest level in which any navigation or anti-collision system or sensors are engaged. It can be used for manual docking operation or in

case of malfunction of any sensor. Remote control (manual control) is strongly recommended for every autonomous system in order to have the possibility to overwrite the higher level commands – in this case remote control acts as a safety pilot. Every command generated by a mission control module or autonomous module can be overwritten in any time by a operator's manual command.

Level 2: automatic mode (steering, auto, return to home, smart return modes); on this level the unit uses internal navigation sensors and navigation algorithms to direct the unit. This level requires PID controllers (proportional–integral–derivative controller) to be tuned and for navigation sensors readings. The unit uses a compass (9 magnetometers), GNSS receiver to perform basic commands (steering mode), a mission plan to perform automatic mission (auto mode), home location (dock location) to perform return to home port (dock) task, and saving the path to perform smart return to home mission.

Level 3 : semi-autonomous mode– covering full level 2 functionality (automatic) with autonomous system advice. All anti-collision additional sensors are active (i.e. two depth echo sounders, omnidirectional lidar, front and back sector lidars, front anti-collision radar) and anti-collision module calculates the manoeuvres, analyzes situation and generates an advice. The navigation advice is displayed on the operator panel. Operator is able to acknowledge or reject the manoeuvre. This mode is perfect for autonomous system tuning and testing. The autonomous neural network support learning phase can be monitored and controlled. Laser scanner for autonomous navigation is quite popular and was presented in the literature [3,5,7,8,9,15,18, 24]. Radar sensor in not so popular like laser sensor but also was presented in some papers [4,10].

Level 4: autonomous mode – in which all navigation and anti-collision systems and sensors are active. The autonomous module directs its platform without operator attention, according to the mission plan and actual situation. In this mode remote controller is used only for safety reason.

In the case of the presented project, a system including software, hardware and overall architecture is developed to such extent as to be able to cover all autonomy levels, including its main assumptions, beginning form remote control and ending on autonomous task realization. All four autonomy levels have been achieved on every development stage of the project. It was assumed, that all hardware configurations have to be prepared to cover all autonomous requirements and be open to integration of new sensors in the future.

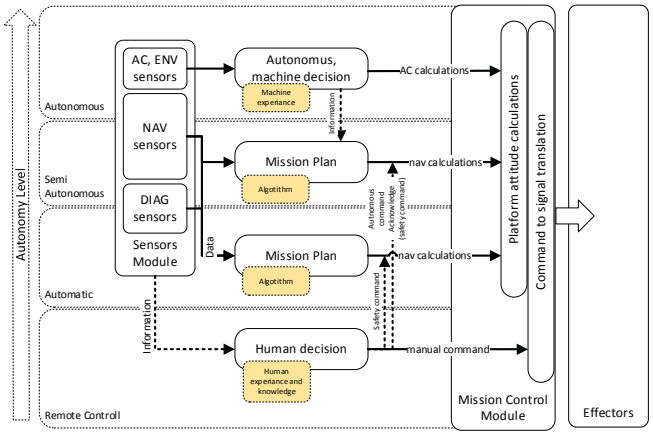

Fig. 16. Autonomy levels and minimally required modules (acc. these authors)

MULTIPURPOSE DESIGN CAPABILITIES

Multipurpose capabilities are achieved basing on a modular and open hardware and software architecture. All used algorithms, after proper tuning process, are able to operate on different hardware and direct any surface vessel different in type and size.

The automatic (mission control) algorithms are based on PID controller, what according to [6] was proved to be a sufficient method to control speed and course of surface vessel. The PID controller continuously attempts to minimize the error over time by adjustment of the control variable. The error value function is a difference between a desired set point and measured process variable PID controller function can be expressed as follows:

$$u(t) = K_p e(t) + \frac{1}{T_i}\int_0^t e(t)\,dt + T_d \frac{de(t)}{dt} \quad (1)$$

where K_p, K_i and K_d are non-negative quantities which denote the coefficients for the proportional, integral, and derivative terms, respectively. Depending on the vessel type, size and maneuvering parameters the PID coefficients are tuned in live tuning process. PID desired response and PID achieved response are monitored and displayed and the coefficients can be adjusted to achieve an appropriate object's response and stabilization of its parameters (course and speed).

The high level of calculation relies on Robot Operating System (ROS). The ROS provides libraries, tools, hardware abstraction, device drivers, visualizers, message-passing and package management necessary to form robot applications. The ROS is used for calculation of anti-collision sensor data. It is a flexible framework for writing any robot software. This enables to simplify the task of creating complex and robust vehicle behaviour. The ROS enables to implement new sensors and change the sensors configuration without changing main anti-collision method.

HARDWARE ARCHITECTURE

Hardware architecture and protocol integration scheme (Fig.17) is open to modifications, hardware changes and new sensors integration. The concept divides the hardware into a low- level and high- level hardware. The low- level hardware is responsible for automatic calculation, including safety actions. The low-level simple driver and controllers provide reliability to the system basic functions. The mission control module is based on 32bit STM32F427 Cortex-M4F core with FPU (floating-point unit), 168 MHz/ 252 MIPS, 256 KB RAM, 2 MB Flash (fully accessible) and 32bit STM32F103 failsafe co-processor (the additional processor only for trigger safety manoeuvre and system actions). The mission control module is supplied with redundant power inputs and automatic failover system (3 different power source).

The anti-collision module and payload storage module are assigned to the high level hardware and created based on two fan-less industrial commuters (Aplex ACS-2332). Potential malfunction of the high level hardware does not affect the low-level hardware. Each commuter is equipped with significant number of I/O ports (6 x USB, 4 serial RS-232/422/485, 3 display interfaces, GPIO and 4 x GbE LAN interfaces), what enables to connect a number of different sensors directly to the machine.

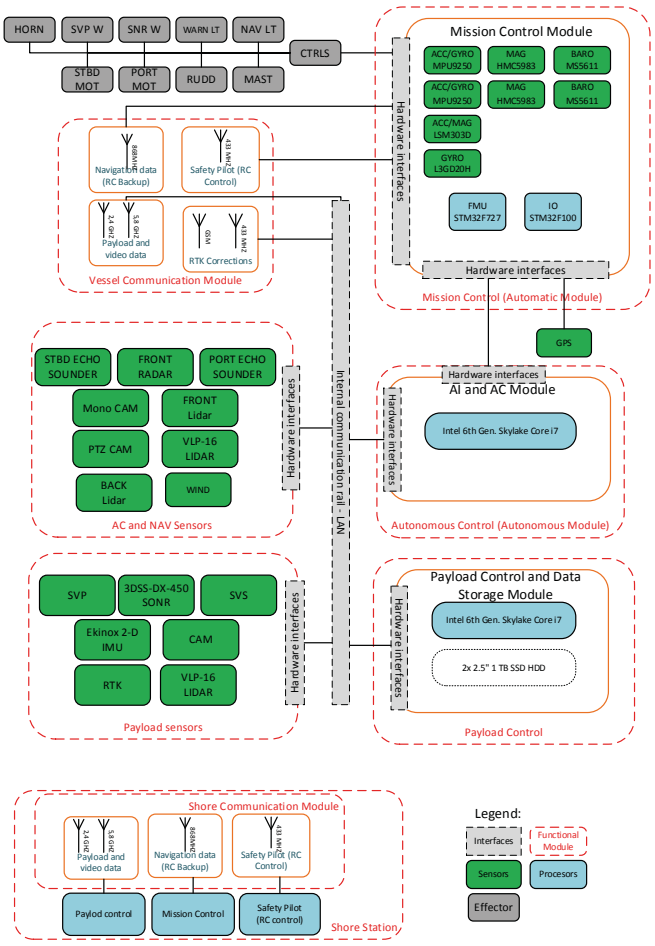

Fig. 17. Hardware architecture (acc. these authors)

NMEA (National Marine Electronics Association) communication based sensors are connected to the vessel internal network by means of the NMEA to LAN converter (MiniPlex-3E), and information is sent over the local network to all subscribers. All Ethernet- based sensors are integrated with internal LAN by means of two configurable switches (MikroTik). This concept allows to share all sensors information (including payload bathymetry sensors) within the system. The shared information is used by the anti-collision module and adaptive planning navigation system and recorded in the storage module for further analyses. Data from all sensors are broadcasted to the local network and can be used by the system modules as required. The vessel internal network is connected by means of wireless distribution system (WDS) to the shore station local network. Such connection enables to share sensor information to the shore station modules.

SOFTWARE ARCHITECTURE

The software architecture provides full sensor integration capabilities and is based on open- source application and software (except payload control software) (Fig.18).

The mission control module is based on NuttX operating system (NuttX is a real-time operating system (RTOS) with an emphasis put on standards compliance and small footprint, scalable from 8-bit to 32-bit microcontroller environments).

The collision avoidance module runs Linux Ubuntu software with ROS framework of modules having their own AI (artificial intelligence) and path-finding algorithms [13]. Different software implementations operate within different nodes.

In the nodes particular computations are performed . The presented USV control system comprises many nodes (for example, one node controls a laser range-finder, one node controls the radar computation, one performs path planning, one node provides a graphical view of the system, etc). The nodes produce topics – messages which are routed through a transport system with publish / subscribe semantics. A node sends out a message by publishing it to a given topic. A node that is interested in a certain kind of data will subscribe for an appropriate topic. Very important problem is multisensory data fusion; this issue was undertaken by several authors [11-13].

Payload control module runs Windows 10 and Hypack® software for full bathymetry payload control and hydrographic adaptive mission planning. The Hypack® provides hydrographic surveying packages with all the tools needed to design survey, collect data, process it, reduce it, and generate final products. The payload software is independent form other software used on the vessel. Additionally, the Hypack can creates adaptive survey grid based on the already measured data. The generated track are sent through internal LAN to the mission control module and the vessel can adjust current survey grid to the already collected bathymetric data.

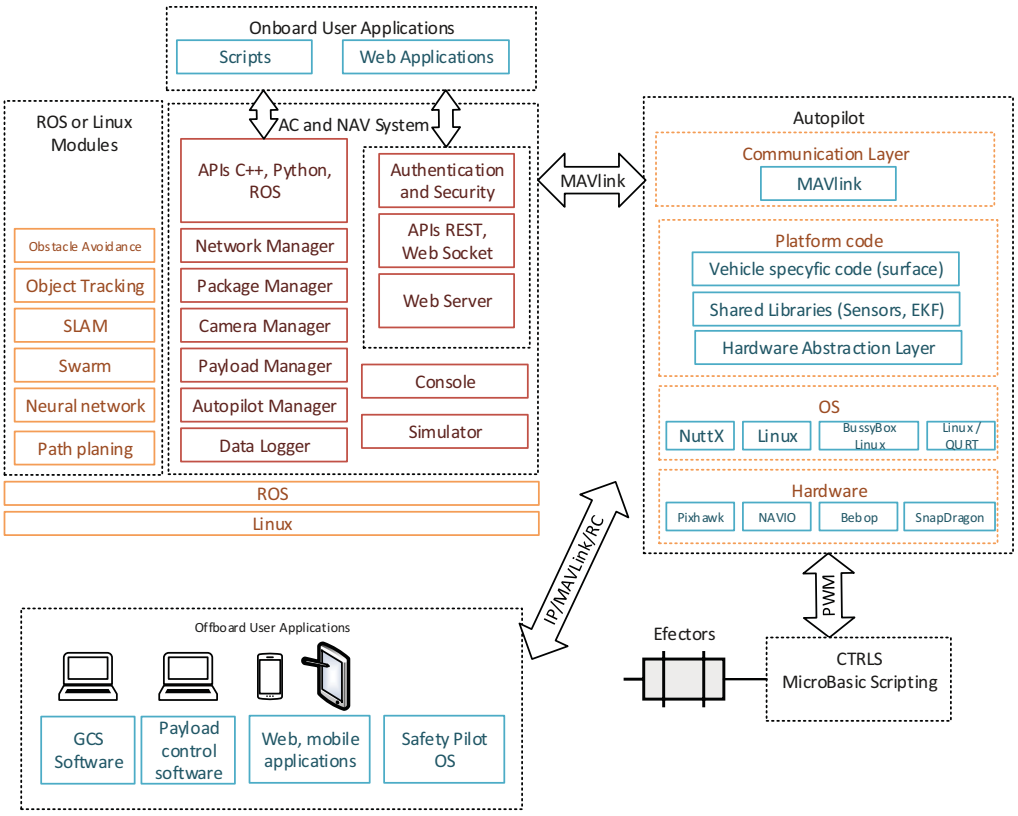

Fig. 18. Software architecture (acc. these authors)

COMMUNICATION CHANNELS

The communication and control link, in addition to the platform itself and the ground control station, is the most important module of the UVS and provides the necessary information exchange between the SCS and the proper platform systems. Communication with the USV is conducted in two directions : signals are sent towards the platform (uplink), and signals are received from the platform (downlink). The uplink consists of radio control signals for the payload and USV. The downlink provides telemetric data and sensors readings. In the presented application, the communication with the platform is conducted in radio bands and with transmission power that can be used without proper permission, i.e. in channels that have been allocated to the public (ISM Bands). According to the definition, the industrial, scientific and medical (ISM) radio bands are those intended to use radio frequency energy for industrial, scientific and medical purposes other than telecommunication. ISM bands allows to use transmitting devices without a radio license, within assigned frequencies and limited power. As a result, the frequency range and maximum power is strictly defined and manufacturers can build and market any radio devices that meet the conditions set out in the regulations, and users can use them without permission. In practice, this means that the released bands are very disrupted and there are many different radio devices working within the ISM bands.

For the presented project, three main communication channels have been chosen, prioritized and assigned in accordance with main function and range. The safety pilot (radio control) have the highest priority (should have the best range) and the lowest demands as for the channel width. The 433 MHz band has been assigned for the radio control application, with proven range up to 65 km. The RC (radio control) channel is only uplink. The telemetric data, uplink and downlink, are assigned to 868 MHz band. Two long-range radio modems are assigned for the telemetric data exchange between platform and shore station. The telemetric data allows to control and monitor vessel parameters, current state and position. It allows to operate beyond line of sight, with proven range up to 60 km. The most demanding channel, that for high-rate video data and payload control data , is assigned to 2,4/5,8 GHz band. The channel allows to transfer a live video feed form all cameras mounted on board, fully control commuters on board and transfer all raw sensors data from sensor module. The range of the link is proved to be up to 6 km. It should be mentioned, that payload is automatically controlled by the onboard commuter and its constant monitoring is not required. The camera live feed is not required during live operation over a long distance, while a unit operates on the open water. All anti-collision manoeuvres are carried out automatically, without operator attention taking for consideration international regulations. The problem of international regulations for autonomous surface vehicle was discussed in [18].

CONCLUSIONS

The universal autonomous control and management system for multipurpose unmanned surface vessel has been designed and implemented on the catamaran vessel tested and evaluated during the real environment trials on the lake (Fig.19).

The presented floating platform solution developed by the integrating of the unmanned vessel system with the optimizing of the platform drive and control and the use of real-time sensors constitutes a novelty not only in the Polish market, but also in a worldwide scale.

Fig. 19. Fully unmanned vessel system deployed for trials (first plane: shore station, safety pilot, hydrographic console; second plane: shore communication module; third plane: HydroDron unit afloat)

An important feature of the HydroDron is the ability to use it also for tasks other than hydrographic measurements, such as monitoring rivers, lakes and other water areas, environmental quality testing etc.

The possibility to replace sensors in modular kits and apply a universal control software designed for the use with different devices provides the ability to use a selected device in multiple variations.

ACKNOWLEDGMENTS

The presented work was financed from the European Regional Development Fund under the 2014-2020 Operational Programme Smart Growth. Project entitled „Developing of autonomous/remote operated surface platform dedicated to hydrographic measurements on restricted reservoirs" implemented as a part of the National Centre for Research and Development competition „INNOSBZ".

BIBLIOGRAPHY

1. Barton A., Volna E.: *Control of Autonomous Robot using Neural Networks*. Proceedings of the International Conference on Numerical Analysis and Applied Mathematics 2016 (ICNAAM-2016), vol. 1863, Rhodes, Greece 2016.

2. Burdziakowski P., Szulwic J.: *A commercial of the shelf components for a unmanned air vehicle photogrammetry,* 16th International Multidisciplinary Scientific GeoConference SGEM 2016, Albena, Bulgaria, 2016

3. Droeschel D., Schwarz M. Behnke S.: *Continuous mapping and localization for autonomous navigation in rough terrain using a 3D laser scanner*, Robotics and Autonomous Systems, vol. 88, pp. 104-115, 2017.

4. Guan R.P., Ristic B., Wang L.P. et al.: *Feature-based robot navigation using a Doppler-azimuth radar*, International Journal of Control, vol. 90, issue 4, pp. 888-900, 2017.

5. Guerrero J.A., Jaud M., Lenain R. et al.: *Towards LIDAR-RADAR based Terrain Mapping*, 2015 IEEE International Workshop on Advanced Robotics and its Social Impacts (ARSO), Lyon, France , 2015.

6. Guo W., Wang S., Dun W.: *The Design of a Control System for an Unmanned Surface Vehicle*, Open Autom. Control Syst. J., vol. 7, pp. 150–156, 2015.

7. Hollinger J., Kutscher B. Close B.: *Fusion of Lidar and Radar for detection of partially obscured objects*. Unmanned Systems Technology XVII, Baltimore, MD, vol. 9468 , 2015.

8. Huang L., Chen S., Zhang J. et al.: *Real-Time Motion Tracking for Indoor Moving Sphere Objects with a LiDAR Sensor*, Sensors, vol. 17, issue 9 , 2017.

9. Jeon H.C., Park Y.B., Park C.G.: *Robust Performance of Terrain Referenced Navigation Using Flash Lidar*, Proceedings of the 2016 IEEE/Ion Position, Location and Navigation Symposium (PLANS), pp. 970-975, Savannah, GA, 2016

10. Jiang Z., Wang J., Song Q.et al.: *Off-road obstacle sensing using synthetic aperture radar interferometry*, Journal of Applied Remote Sensing, vol. 11, 2017.

11. Jo J., Tsunoda Y., Stantic B. et al.: *A Likelihood-Based Data Fusion Model for the Integration of Multiple Sensor Data: A Case Study with Vision and Lidar Sensors*. Robot Intelligence Technology And Applications 4, vol. 447, pp. 489-500, 2017.

12. Jooho L., Joohyun W., Nakwan K.: *Obstacle Avoidance and Target Search of an Autonomous Surface Vehicle for 2016 Maritime RobotX Challenge*. IEEE OES International Symposium on Underwater Technology (UT), Busan, South Korea , 2017.

13. Kazimierski, W., Stateczny, A.: *Fusion of Data from AIS and Tracking Radar for the Needs of ECDIS*. Book Group Author(s): IEEE Conference: Signal Processing Symposium (SPS), Jachranka, Poland , 2013.

14. Ko B., Choi H.J., Hong C. et al.: *Neural Network-based Autonomous Navigation for a Homecare Mobile Robot*. 2017 IEEE International Conference On Big Data And Smart Computing (BIGCOMP), pp. 403-406, Jeju, South Korea , 2017.

15. Lil J., Bao H., Han X. et al.: *Real-time self-driving car navigation and obstacle avoidance using mobile 3D laser*

scanner and GNSS. Multimedia Tools and Applications, vol. 76, pp. 23017-23039, part B, 2016.

16. Lisowski J: *Optimization-supported decision-making in the marine game environment*. Mechatronic Systems, Mechanics And Materials II, Book Series: Solid State Phenomena, vol. 210, pp. 215-222, 2014.

17. Lisowski J: *The optimal and safe ship trajectories for different forms of neural state constraints*. Mechanics and Materials II, Book Series: Solid State Phenomena, vol.180, pp. 64-69 , 2012.

18. Mei J.H., Arshad M.R.: *COLREGs Based Navigation of Riverine Autonomous Surface Vehicle*. IEEE 6TH International Conference on Underwater System Technology, pp.145-149, Malaysia, 2016.

19. Mikhail M., Carmack N.: *Navigation Software System Development for a Mobile Robot to Avoid Obstacles in a Dynamic Environment using Laser Sensor*, SOUTHEASTCON 2017, Charlotte, NC, 2017.

20. Praczyk T.: *Neural anti-collision system for Autonomous Surface Vehicle*, Neurocomputing, vol. 149, pp. 559-572 , 2015.

21. Specht C, Weintrit A., Specht M.: *Determination of the territorial sea baseline - Aspect of Using Unmanned Hydrographic Vessels, Transnav-International Journal on Marine Navigation and Safety of Sea Transportation, vol. 10, pp. 649-654, 2016.*

22. Specht C. Switalski E., Specht M.: *Application of an Autonomous /Unmanned Survey Vessel (ASV/USV) in bathymetric measurements, Polish Maritime Research, No. 24, pp.36-44 , 2017.*

23. Stateczny A., Gronska D., Motyl W.: *Hydrodron - New Step for Professional Hydrography for Restricted Waters*, 2018 Baltic Geodetic Congress (BGC Geomatics), pp. 226–230, Olsztyn, Poland, 2018.

24. Williams G.M.: *Optimization of eye-safe avalanche photodiode lidar for automobile safety and autonomous navigation systems*, Optical Engineering, vol. 56, issue 3, 2017.

CONTACT WITH THE AUTHORS

Andrzej Stateczny
e-mail: a.stateczny@marinetechnology.pl

Marine Technology Ltd.
Cyfrowa 6, B.3.04a
71-441 Szczecin
Poland

Pawel Burdziakowski
e-mail: pawel.burdziakowski@pg.edu.pl

Gdansk University of Technology
Faculty of Civil and Environmental Engineering
Narutowicza 11/12
80-233 Gdansk
Poland

sciendo

POLISH MARITIME RESEARCH 1 (101) 2019 Vol. 26; pp. 40-48
10.2478/pomr-2019-0005

SPECTRAL DYNAMIC ANALYSIS OF A STATIONARY JACK-UP PLATFORM

Bogdan Rozmarynowski
Gdańsk University of Technology, Poland

ABSTRACT

The paper refers to the dynamic short-term response analysis of the Baltic steel drilling platform (see Fig.2) in a random sea-state represented by one-dimensional wave spectrum proposed by Striekalov and Massel, which is recommended for the Baltic Sea area. The Baltic drilling platform is a jack-up type platform for the exploration and exploitation of oil under the Baltic Sea. The presented analysis deals with the stationary phase of the platform life when its legs are fixed in the sea bottom. The submerged elements of jack-up platforms are relatively slender, thus to assess the in-line wave forces a modified Morison equation is justified. The application of frequency transfer functions to offshore vibration systems leads to structural response spectra whose input is defined by the wave elevation and wind velocity spectra. The analysis can be applied also to support structures for offshore wind turbines.

Keywords: offshore structures, random variables, structural reliability, simulation methods

INTRODUCTION

Offshore platforms are structural engineering systems designed and erected to withstand severe sea conditions including dynamic wave and wind loads. The paper follows the research of [4] and deals with dynamic analysis of a Baltic movable jack-up drilling platform. Stationary work phase of a jack-up platform assumes its fixed supporting in the seabed. The soil subsystem interacts both ways with the structure through the foundation, therefore a soil-structure interaction problem is analysed here. The analytical method is aimed at computing frequency transfer functions linked with the input wave elevation and wind fluctuation velocity spectra (see Fig. 7 and Fig. 8) in order to obtain structural response spectra. This concept of analyzing the offshore structural engineering systems assumes linearized relations between structural input and output. A general computational procedure aimed at response spectra (nodal displacements, cross-sectional forces, stresses) is presented in Fig. 6, Appendix 1.

The model of a jack-up platform assumes its support by submerged cylindrical members (see Fig. 2), too slender to significantly alter the incident wave field, thus application of the modified Morison equation is justified. The equation defines the wave force normal to the cylinder axis, collinear with the wave propagation direction. In a probabilistic approach the Morison function is affected by Gaussian wave particle kinematics [1].

In the case of slender cylindrical members subjected to sea waves action the wave-structure interaction problem is inherently nonlinear as shown in Fig. 1. The following relations hold: $H/D>1$, $D/L>0.2$ where H is the wave height, L is the wave length, D is the cylinder diameter (potential theory is applied, no diffractions effects).

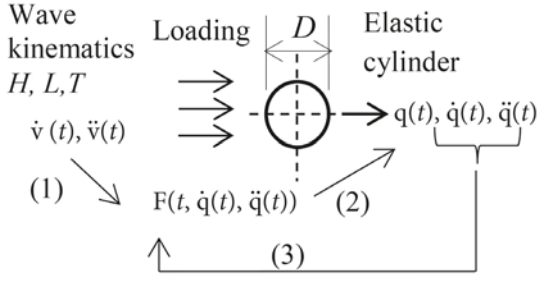

Fig. 1. Scheme of wave-structure interaction problem

The modified Morison equation (this version includes the relative wave kinematics due to moving cylinder), cf. [2], [3], [4]) reads:

$$\begin{aligned} d\mathbf{F}(s,t) &= d\mathbf{F}_p(s,t) + d\mathbf{F}_a(s,t) + d\mathbf{F}_d(s,t) = \\ &= \rho\frac{\pi D^2}{4}C'_M\frac{\partial \mathbf{v}_n(s,t)}{\partial t}ds + \\ &+\rho\frac{\pi D^2}{4}C''_M\left(\frac{\partial \mathbf{v}_n(s,t)}{\partial t}-\frac{\partial \dot{\mathbf{q}}_n(s,t)}{\partial t}\right)ds + \\ &+\frac{1}{2}\rho DC_D\left[\left(\mathbf{v}_n(s,t)-\dot{\mathbf{q}}_n(s,t)\right)\left|\mathbf{v}_n(s,t)-\dot{\mathbf{q}}_n(s,t)\right|\right]ds \end{aligned} \quad (1)$$

Here $d\mathbf{F}(s, t)$ is the differential wave force normal to the axis of the cylinder of the diameter D, co-linear with the direction of wave propagation on a length ds, s denotes the variable along the element length, ρ is the density of water, $\mathbf{v}_n(s, t)$ is the water particle velocity in the undisturbed wave process, subscript "n" denotes normal to the cylinder axis, C'_M, C''_M, C_D are empirical coefficients affected by the cross-sectional shapes, Reynolds and Keulegan-Carpenter Numbers and relative roughness ([5], 12]), $\mathbf{q}(s, t)$ is the cylinder response (displacement), $\partial(\bullet)/\partial t$ denotes the partial time derivative.

ASSUMPTIONS AND SOLUTION TECHNIQUES

The following assumptions with regard to two cases of the stochastic approach to the problem presented in Fig. 1, are considered:

I. Linear stochastic problem:

- deterministic soil-structure interaction which is represented by a system of springs and dash-pots connecting the legs of the structure and subsoil. The number of these connecting elements depends on the subsoil penetration depth of the structure leg ends,
- linearization of the velocity term in Eq. (1) is carried out by means of the least-square technique or stochastic averaging method (cf. [8], [10]),
- wave and wind loads are considered stationary Gaussian zero-mean ergodic processes, mutually independent,
- the equations of motion of the problem are solved in a reduced modal space.

II. Non-linear stochastic problem:

- non-deterministic soil-structure interaction problem is considered where the soil shear modulus G is a Gaussian random variable,
- the spring stiffnesses are linear functions of G, whereas the dash-pots are non-linear functions, it eventually yields non-Gaussian random variables [6],
- no vortex- induced oscillations are included in the analysis.

In the presented paper the following solution techniques are applied:

1. Modal transformation of the equation of motion:

$$\mathbf{M}\ddot{\mathbf{q}}(t) + \mathbf{C}\dot{\mathbf{q}}(t) + \mathbf{K}\mathbf{q}(t) = \mathbf{P}(t, \dot{\mathbf{q}}(t), \ddot{\mathbf{q}}(t)) \quad (2)$$

where $\mathbf{M}$, $\mathbf{C}$, $\mathbf{K}$ are the overall mass, damping and stiffness matrices $n\times n$, respectively, $\mathbf{q}(t)$ and $\mathbf{P}(t, \dot{\mathbf{q}}(t), \ddot{\mathbf{q}}(t))$ are the global displacement and applied force vectors $n\times 1$, $\mathbf{M} = \mathbf{M}_K + \mathbf{M}_S + \mathbf{M}_H$, $\mathbf{C} = \mathbf{C}_K + \mathbf{C}_S + \mathbf{C}^R_H$, $\mathbf{K} = \mathbf{K}_K + \mathbf{K}_S$, where $\mathbf{M}_K$, $\mathbf{C}_K$, $\mathbf{K}_K$ are the structural parts of matrices $\mathbf{M}_S$, $\mathbf{C}_S$, $\mathbf{K}_S$, show the soil impact $\mathbf{M}_H$, $\mathbf{C}^R_H$ denote hydrodynamic parts of matrices, an upper dot $\mathbf{P}(t, \dot{\mathbf{q}}(t), \ddot{\mathbf{q}}(t))$ denotes a time derivative, is the force vector due to hydrodynamic and wind loads:

$$\mathbf{P}(t, \dot{\mathbf{q}}(t), \ddot{\mathbf{q}}(t)) = \mathbf{F}(t, \dot{\mathbf{q}}(t), \ddot{\mathbf{q}}(t)) + \mathbf{W}(t, \dot{\mathbf{q}}(t)) \quad (3)$$

where: $\mathbf{F}$ and $\mathbf{W}$ are referred to wave and wind force vectors, respectively.

The eigenvalue problem is formulated by $\mathbf{K}\boldsymbol{\Phi}_i = \lambda_i\mathbf{M}\boldsymbol{\Phi}_i$, where $\lambda_i = \omega^2_{0i}$ is the *i-th* eigenvalue (squared natural frequency), $\boldsymbol{\Phi}_i$ is the *i-th* eigenvector, $(\omega_{01}, \boldsymbol{\Phi}_1), (\omega_{02}, \boldsymbol{\Phi}_2), \ldots, (\omega_{0n}, \boldsymbol{\Phi}_n)$ is the eigensolution with the orthogonality relation $\boldsymbol{\Phi}^T_i\mathbf{M}\boldsymbol{\Phi}_j = [\delta_{ij}] = \mathbf{I}$, where δ_{ij} is the Kronecker delta, $i, j = 1, 2\ldots, n$, is the $n\times n$ unit matrii.

Let $\boldsymbol{\Phi}_h = [\boldsymbol{\Phi}_1, \boldsymbol{\Phi}_2, \ldots \boldsymbol{\Phi}_h]$, $h \le n$ constitutes the reduction of the modal space and $\boldsymbol{\Phi}^T_h\mathbf{M}\boldsymbol{\Phi}_h = \mathbf{I}_h$, $\boldsymbol{\Phi}^T_h\mathbf{K}\boldsymbol{\Phi}_h = \boldsymbol{\Omega}^2_h = diag\{\omega^2_{01}, \omega^2_{02}\ldots \omega^2_{0h}\}$ where $\mathbf{I}_h$ is the $h\times h$ unit matrix.

2. Stochastic linearization method [7]:

The nonlinear (velocity) part of the Morison Eq. (1) is:

$$\mathbf{X}(\dot{\mathbf{x}}|\dot{\mathbf{x}}|) = (\mathbf{v}_n(s, t) - \dot{\mathbf{q}}_n(s, t))|\mathbf{v}_n(s, t) - \dot{\mathbf{q}}_n(s, t)| \quad (4)$$

This term may be linearized with a tendency to minimize the mean-square error:

$\mathbf{X}(\dot{\mathbf{x}}|\dot{\mathbf{x}}|) \rightarrow \mathbf{A}\dot{\mathbf{x}}$, where $\mathbf{e} = \mathbf{X}(\dot{\mathbf{x}}|\dot{\mathbf{x}}|)\mathbf{A}\dot{\mathbf{x}}$– and

$$e_i^2 = E\left[\left(\dot{x}_i|\dot{x}_i| - A_{ii}\dot{x}_i\right)^2\right] \rightarrow \min \quad (5)$$

The condition (5) gives the result:

$$\frac{\partial e_i^2}{\partial A_{ii}} = 0 \Rightarrow A_{ii} = \frac{E\left(\dot{x}_i^2|\dot{x}_i|\right)}{E\left(\dot{x}_i^2\right)} = \sqrt{\frac{8}{\pi}}\sigma_{\dot{x}_i} \quad (6)$$

The last term of the Morison equation (1) denotes the drag force. In view of the approximation (6) one gets the force equivalent to the drag force ([6], [8]) , given by:

$$d\tilde{\mathbf{F}}_d(s,t) = \frac{1}{2}\rho DC_D\sqrt{\frac{8}{\pi}}\cdot\sigma_{\mathbf{v}_n-\dot{\mathbf{q}}_n}\left(\mathbf{v}_n(s,t)-\dot{\mathbf{q}}_n(s,t)\right)ds \quad (7)$$

where: $\sigma_{\mathbf{v}_n-\dot{\mathbf{q}}_n}$ is a standard deviation of the relative velocity (assumed that $\sigma_{\mathbf{v}_n-\dot{\mathbf{q}}_n} \approx \sigma_{\mathbf{v}_n}$ if the condition $|\mathbf{v}_n(s, t)| >> |q_n(s, t)|$ is satisfied).

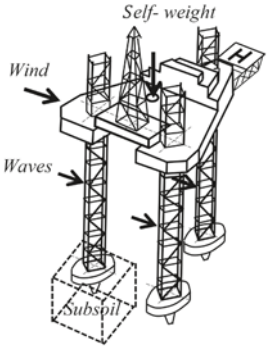

Fig. 2. General view of the platform

3. The perturbation method (cf [6], [9]):

Let the total mass, damping and stiffness matrices in Eq. (2) take the form:

$$\mathbf{M} = \mathbf{M}_0 + \varepsilon\mathbf{M}_1(\gamma),\ \mathbf{C} = \mathbf{C}_0 + \varepsilon\mathbf{C}_1(\gamma),\ \mathbf{K} = \mathbf{K}_0 + \varepsilon\mathbf{K}_1(\gamma),$$

$$\mathbf{q}(\gamma, t) = \mathbf{q}_0(\gamma, t) + \varepsilon\mathbf{q}_1(\gamma, t) \tag{8}$$

where: ε is the small parameter $|\varepsilon|<<1$, γ is an elementary event.

It yields the following set of equations:

$$\mathbf{M}_0\ddot{\mathbf{q}}_0(\gamma, t) + \mathbf{C}_0\dot{\mathbf{q}}_0(\gamma, t) + \mathbf{K}_0\mathbf{q}_0(\gamma, t) = \mathbf{P}(\gamma, t)$$

$$\mathbf{M}_0\ddot{\mathbf{q}}_1(\gamma, t) + \mathbf{C}_0\dot{\mathbf{q}}_1(\gamma, t) + \mathbf{K}_0\mathbf{q}_1(\gamma, t) =$$

$$-[\mathbf{M}_1(\gamma)\ddot{\mathbf{q}}_0(\gamma, t) + \mathbf{C}_1(\gamma)\dot{\mathbf{q}}_0(\gamma, t) + \mathbf{K}_1(\gamma)\mathbf{q}_0(\gamma, t)] =$$

$$\mathbf{Z}(\gamma, t) \tag{9}$$

where $\mathbf{M}_1(\gamma) = diag[M_{Sii}(\gamma)]$, $\mathbf{C}_1(\gamma) = diag[C_{Sii}(\gamma)]$, $\mathbf{K}_1(\gamma) = diag[K_{Sii}(\gamma)]$define diagonal elements of the mass, damping and stiffness matrices due to soil, $\mathbf{Z}(\gamma, t)$ is the vector of stochastic stationary process in the wide sense, ergodic in the mean but not in the correlation. The above given expressions are linear stochastic equations with deterministic parameters and stochastic excitations.

4. The stochastic averaging method:

A diffusion Markov vector process with stationary solution of the Itô stochastic differential equations with respect to the Wiener process (with orthogonal increments) is applied – cf. [8], [10]).

By transforming Eq. (2) into reduced modal space, the *i-th* equation of motion may be written as follows:

$$\ddot{y}_i(t) + \omega_{0i}^2\, y_i(t) = \varepsilon N_i[\dot{y}_i(t), v_n(t), t] \tag{10}$$

where: N_i is the *i-th* element of the vector $\mathbf{N}_h = \mathbf{R}_h - \boldsymbol{\beta}^R_h\dot{\mathbf{y}}_h - \boldsymbol{\beta}^F_h\dot{\mathbf{y}}_h$, $i = 1, 2,\ldots, h \le n$, ε is the small parameter, $\mathbf{R}_h = \boldsymbol{\Phi}^T_h[\mathbf{K}_M\dot{\mathbf{v}}_n + \mathbf{K}_D\mathbf{T}_1(v_n)]$, $\boldsymbol{\beta}^R_h = \boldsymbol{\Phi}^T_h(\mathbf{C}_K + \mathbf{C}^R_H)\,\boldsymbol{\Phi}_h$, $\boldsymbol{\beta}^F_h = \boldsymbol{\Phi}^T_h[2\mathbf{K}_D\mathbf{T}_2(v_n)]\,\boldsymbol{\Phi}_h$

$$\mathbf{T}_1(v_n) = diag\left\{|v_{nj}|\,v_{nj}\right\} =$$

$$= diag\left\{\sqrt{2/\pi}\sigma_{v_{nj}}v_{nj} + 1/3\,\sigma^{-1}_{v_{nj}}\sqrt{2/\pi}v^3_{nj}\right\},$$

$$\mathbf{T}_2(v_n) = diag\left\{1/2\,\sigma^{-1}_{v_{nj}}\sqrt{2/\pi}\left(v^2_{nj} - \sigma^2_{v_{nj}}\right)\right\},$$

$$\mathbf{C}^R_H = diag\left\{\sqrt{8/\pi}K_{Dj}\sigma_{v_{nj}}\right\},\ j = 1, 2..., n,$$

$$y_i \in \mathbf{y}_h = \boldsymbol{\Phi}^T_h\mathbf{q},$$

$\mathbf{K}_M = \rho C_M\mathbf{V}$, $C_M = C'_M + C''_M$, $\mathbf{K}_D = 1/2\,C_D\mathbf{A}$, $\mathbf{V}$ and $\mathbf{A}$ denote diagonal matrices of the volume and area of the submerged elements normal to the wave particle velocity.

Applying the Krylov – Bogolubov transformation of the joint response process $(y_i, \dot{y}_i)$ to a pair of slowly varying processesone (A_i, ϕ_i) gets:

$$y_i(t) = A_i(t)\cos\Theta_i(t),$$

$$\dot{y}_i(t) = A_i(t)\,\omega\sin\Theta_i(t) \tag{11}$$

where: $A_i(t)$ is the amplitude envelope process and $\Theta_i(t) = \omega_{0i}t + \varphi_i(t)$, $\varphi_i(t)$ indicates the phase process, provided that the condition $\dot{A}_i(t) = \dot{\varphi}_i(t)A_i(t)\sin\Theta_i(t)/\cos\Theta_i(t)$ is satisfied.

By substituting Eqs (11) into (10), the standard equations are:

$$\dot{A}_i(t) = \varepsilon G_i[A, \varphi, v_n(t), t]$$

$$\dot{\varphi}_i(t) = \varepsilon Z_i[A, \varphi, v_n(t), t] \tag{12}$$

where:

$$G_i\left[A, \varphi, v_n(t), t\right] =$$

$$= -\left(\frac{1}{\omega_{0i}}\right)N_i\left[-\omega_{0i}A_i\sin\Theta_i, v(t), t\right]\sin\Theta_i =$$

$$= G_{Ri}\left[A, \varphi, t\right] + G_{Fi}\left[A, \varphi, v_n(t), t\right]$$

$$Z_i\left[A, \varphi, v_n(t), t\right] =$$

$$= -\left(\frac{1}{\omega_{0i}A_i}\right)N_i\left[-\omega_{0i}A_i\sin\Theta_i, v(t), t\right]\cos\Theta_i =$$

$$= Z_{Ri}\left[A, \varphi, t\right] + Z_{Fi}\left[A, \varphi, v_n(t), t\right]$$

In the above given expressions G_{Ri} and Z_{Ri}, G_{Fi} and Z_{Fi} represent the regular and fluctuation parts of the corresponding functions, respectively.

The amplitudes A_i and phases φ_i are considered elements of a multi-dimensional function $\mathbf{X}(t) = [A_i(t), \varphi_i(t),\ldots, A_h(t), \varphi_h(t)]^T$.

It can be proved that the response of the Eq. (10) tends to a multi-dimensional diffusive Markov process if the conditions of the Khasminski limit theorem ([20]) are satisfied. The Itô stochastic differential equation is one of the methods for the analysis of Markov processes. In the case of a vector process $\mathbf{X}(t)$ it holds:

$$d\mathbf{X}(t) = \mathbf{m}[\mathbf{X}(t)]dt + \boldsymbol{\sigma}[\mathbf{X}(t)]d\mathbf{W}(t) \tag{13}$$

where $\mathbf{m}[\mathbf{X}(t)]$ is a drift coefficient, $\boldsymbol{\sigma}[\mathbf{X}(t)]$ a diffusion coefficient matrix, $\mathbf{W}(t)$ denotes the Wiener process (representing an independent Brownian motion process).

It can be proved that the equations for amplitudes are uncoupled from ones referring to phases (cf. [8], [19]). The set of Itô equations (13) takes the form:

$$dA_i(t) = m^A_i(A)dt + \sum_{j=1}^{h}\sigma^A_{ij}dW^A_j(t) \tag{14}$$

$$d\varphi_i(t) = m^\varphi_i(\varphi)dt + \sum_{j=1}^{h}\sigma^\varphi_{ij}dW^\varphi_j(t) \tag{15}$$

where W^A_j, W^φ_j are independent Wiener processes, m^A_i, m^φ_i and σ^A_{ij}, σ^φ_{ij} are drift and diffusion coefficients, respectively, $i = 1, 2,\ldots, h$.

The details related to the Khasminski limit theorem are fully developed in [8].

STRUCTURAL TRANSFER FUNCTION

This function can be derived directly from the dynamic equilibrium Eq.(2).

The force vector depends on structural kinematics, in this form the vector generates the nonlinear damping term in Eq. (1). For the linear case the equation can be written in frequency domain:

$$\frac{1}{2\pi}\int_{-\infty}^{\infty}\left(\mathbf{K}-\omega^2\mathbf{M}+i\omega\mathbf{C}\right)e^{i\omega t}d\bar{\mathbf{Q}}(\omega)= \\ =\frac{1}{2\pi}\int_{-\infty}^{\infty}e^{i\omega t}d\bar{\mathbf{P}}(\omega) \tag{16}$$

where the following transformations are defined:

$$\mathbf{q}(t)=\frac{1}{2\pi}\int_{-\infty}^{\infty}e^{i\omega t}d\bar{\mathbf{Q}}(\omega), \\ \mathbf{P}(t)=\frac{1}{2\pi}\int_{-\infty}^{\infty}e^{i\omega t}d\bar{\mathbf{P}}(\omega),\ i=\sqrt{-1} \tag{17}$$

The equation (16) can be stated in the form:

$$d\bar{\mathbf{Q}}(\omega)=\mathbf{H}_{QP}(\omega)d\bar{\mathbf{P}}(\omega) \tag{18}$$

in which $\mathbf{H}_{QP}(\omega)=(\mathbf{K}-\omega^2\mathbf{M}+i\omega\mathbf{C})^{-1}$ is the structural transfer function matrix ($n\times n$).

In the reduced modal space $Q\rightarrow Y$, the function $\mathbf{H}_{QP}(\omega)$ takes an approximate form:

$$\hat{\mathbf{H}}_{YP}(\omega)=\left[\mathbf{\Phi}_h^T\left(\mathbf{K}-\omega^2\mathbf{M}+i\omega\mathbf{C}\right)\mathbf{\Phi}_h\right]^{-1}= \\ =\sum_{r=1}^{h}H_r(\omega)\mathbf{\Phi}_{hr}\mathbf{\Phi}_{hr}^T \tag{19}$$

where: $H_r(\omega)=\frac{1}{k_r}\frac{\omega_{0r}^2}{\left(\omega_{0r}^2-\omega^2\right)+2i\xi_r\omega_{0r}\omega}$,

k_r is the generalized stiffness, ω_{0r}, ξ_r are the *r-th* natural frequency and the damping ratio, respectively, $h\le n$ denotes the number of modes $\mathbf{\Phi}_h$ in the reduced space.

WAVE TRANSFER FUNCTION

In the case o fsufficiently slender elements loaded by sea waves the Morison equation is applicable, it can be written in vector notation:

$$\mathbf{F}(t)=f(\beta)[\mathbf{K}_M\dot{\mathbf{v}}_n(t)+\mathbf{K}_D\mathbf{v}_n(t)] \tag{20}$$

where $\dot{\mathbf{v}}_n=\mathbf{a}_n$, is the acceleration vector,

$$\mathbf{K}_D=1/2\,\bar{C}_D\mathbf{A},\ \bar{C}_D=C_D\sqrt{\frac{8}{\pi}}\sigma_{\mathrm{v}_n},$$

σ_{v_n} is a standard deviation of horizontal velocity of water in the wave direction, $f(\beta)$ is a function of wave direction flow angle.

The force (20) can be stated in the frequency domain:

$$\mathbf{F}(\omega)=\mathbf{H}_{F\eta}(\omega)\,\eta(\omega) \tag{21}$$

where: $\eta(\omega)$ denotes water elevation considered the input function, $\mathbf{H}_{F\eta}(\omega)$ is the transfer function of the wave force (cf. [11]) according to the Morison equation:

$$\mathbf{H}_{F\eta}(\omega)=f(\beta)[\mathbf{K}_M+i\omega\mathbf{K}_D]\,\mathbf{H}_{v\eta}(\omega) \tag{22}$$

in which $\mathbf{H}_{v\eta}(\omega)$ is the transfer function vector between the normal water velocity and the water elevation.

The transfer function vector of the wave force given by Eq. (22) is defined in global coordinates for an entire structure after an assembly process of transfer functions of member forces. Given a particular element "*e*" whose length is l_e the wave force shows exponential distribution in vertical direction and harmonic in horizontal direction. The transfer functions of equivalent wave forces at member ends are calculated by assuming cubic polynomial functions to approximate member deformations ([12]). These transfer functions are given the following vector notation with respect to a member "*e*":

$$\mathbf{H}_{F\eta|e}^{L}(\omega)_e=\int_0^{l_e}\mathbf{N}_e^T\mathbf{H}_{F\eta}^{e}(\omega)dx \tag{23}$$

where: $\mathbf{N}_e$ describes shape function matrix of member deformations, l_e is the member length, x denotes a variable along the member axis, the superscript L indicates local coordinates. While an assembled system is considered this vector is transformed to global coordinates according to standard finite elements method (FEM) procedures.

RESPONSE SPECTRA

The response displacement spectral density function can be presented in the form:

$$\mathbf{S}_{yy}(\omega)=\hat{\mathbf{H}}_{YP}(\omega)\hat{\mathbf{S}}_{PP}(\omega)\left(\hat{\mathbf{H}}_{YP}^{*}(\omega)\right)^T \tag{24}$$

where: $\hat{\mathbf{H}}_{YP}$ is given by Eq. (19),

$$\hat{\mathbf{S}}_{PP}(\omega)=\mathbf{\Phi}_h^T\mathbf{S}_{PP}(\omega)\mathbf{\Phi}_h,\ \mathbf{S}_{PP}(\omega)=\mathbf{S}_{FF}(\omega)+\mathbf{S}_{WW}(\omega).$$

Here $\mathbf{S}_{FF}(\omega)$ and $\mathbf{S}_{WW}(\omega)$ correspond to waves and wind spectra, respectively.

The cross-spectral density of the wave load is:

$$\mathbf{S}_{F_mF_n}(\omega)=\mathbf{H}_{F\eta|m}^T(\omega)\mathbf{H}_{F\eta|n}(\omega)= \\ =\frac{\rho^2\pi^2D_m^2D_n^2C_{Mm}C_{Mn}}{16}\mathbf{S}_{v_mv_v}(\omega)+ \\ +\frac{\rho^2D_mD_n\bar{C}_{Dm}\bar{C}_{Dn}}{4}\mathbf{S}_{v_mv_n}(\omega)+ \\ +\frac{\rho^2\pi}{8}\left(C_{Mm}\bar{C}_{Dn}D_m^2D_n-C_{Mn}\bar{C}_{Dm}\right)\mathbf{S}_{v_mv_n}(\omega) \tag{25}$$

in which "*m*" and "*n*" are points of the structure with their global coordinates $\{x_m, y_m, z_m\}$ and $\{x_n, y_n, z_n\}$, respectively, D_m and D_n denote diameters of structural submerged members at these points,

$$\mathbf{S}_{v_m v_n}(\omega) = \mathbf{H}^T_{v\eta}(\omega)\mathbf{H}_{v\eta}(\omega) = \\ = \omega^2 S_{\eta\eta}(\omega)\mathbf{D}(k, z_m, z_n)\cdot \\ \cdot \exp\left[-ik\left(\Delta x\cos\beta + \Delta y \sin\beta\right)\right] \tag{26}$$

$$\mathbf{D}(k, z_m, z_n) = \mathbf{A}(k, z_m)\,\mathbf{A}^T(k, z_n) \tag{27}$$

$$\mathbf{A}(k,z) = \frac{1}{\sinh(kd)}\begin{Bmatrix}\cos\beta\cosh(kz)\\ \sin\beta\cosh(kz)\\ i\sinh(kz)\end{Bmatrix} \tag{28}$$

$$\mathbf{S}_{\dot v_m \dot v_n}(\omega) = \omega^2 \mathbf{S}_{v_m v_n}(\omega) \\ \mathbf{S}_{\dot v_m v_n}(\omega) = i\omega \mathbf{S}_{v_m v_n}(\omega) \tag{29}$$

where: $S_{\eta\eta}(\omega)$ in Eq. (26) denotes water elevation spectrum (e.g. the Massel-Striekalov spectrum [13], see Appendix 2, Fig. 4), k stands for the wave number, $k = 2\pi/L_w$, where L_w is the wave length, d is the water depth, β is long-crested – wave direction flow angle, $\Delta x = x_m - x_n$, $\Delta y = y_m - y_n$.

The cross-spectral density of the wind load can be written as follows:

$$S_{WmWn}(\omega) = \rho_A^2 C_{DAm} C_{DAn} A_m A_n \cdot \\ \cdot\left[|\overline{v}_m||\overline{v}_n| + \frac{1}{2\pi}\sigma_{v'_m v'_m}\sigma_{v'_n v'_n} + \sqrt{\frac{2}{\pi}}|\overline{v}_m|\sigma_{v'_n v'_n}\right] S_{v'_m v'_n} \tag{30}$$

where: ρ_A is the air density, C_{DAm}, C_{DAn}, A_m, A_n, $|\overline{v}_m|$, $|\overline{v}_n|$, $\sigma_{v'_n v'_n}$ and $\sigma_{v'_m v'_m}$ are the wind drag coefficients,windward areas, mean velocities, standard deviations at the points "m" and "n"lying in the vertical plane perpendicular to the mean-wind velocity, respectively, $S_{v'_m v'_n}$ is the cross-spectral density of the along-wind fluctuating velocity for the mentioned points:

$$S_{v_m v'_n}(\omega) = S^{RE}_{v'_m v'_n}(\omega) + iS^{IM}_{v'_m v'_n}(\omega) \tag{31}$$

where :

$$S^{RE}_{v'_m v'_n}(\omega) = \left|S^C_{v'_m v'_n}(\omega)\right|\sqrt{S_{v'_m v'_m}(\omega)S_{v'_n v'_n}(\omega)}\cos\theta_{v'_m v'_n}(\omega)$$

$$S^{IM}_{v'_m v'_n}(\omega) = \left|S^C_{v'_m v'_n}(\omega)\right|\sqrt{S_{v'_m v'_m}(\omega)S_{v'_n v'_n}(\omega)}\sin\theta_{v'_m v'_n}(\omega)$$

$$\theta_{v'_m v'_n}(\omega) = arctg\left[S^{IM}_{v'_m v'_n}(\omega)\Big/S^{RE}_{v'_m v'_n}(\omega)\right] = c\omega r_{mn}/\overline{v}$$

$$S^C_{v'_m v'_n}(\omega) = \exp\left[-\frac{ab\omega r_{mn}/\overline{v}}{\left(b^2\cos^2\beta_{mn} + a^2\sin^2\beta_{mn}\right)}\right]$$

$\overline{v}$ is the mean speed at the reference height, β_{mn} is the angle between the direction (m, n) and the horizontal, r_{mn} is the distance between the points m and n, a, b, c are empirical coefficients, $S_{v'_m v'_m}$ and $S_{v'_n v'_n}$ are spectral density functions (cf. (A2), Appendix 3) at two points m and n.

The calculation of transfer functions $\hat{\mathbf{H}}_{YP}$ is a time consuming process and the following relation is applied:

$$\hat{\mathbf{Z}}_{YP}(\omega)\hat{\mathbf{H}}_{YP}(\omega) = \mathbf{I}_h \tag{32}$$

here $\mathbf{I}_h$ is the unit matrix of $h \times h$ dimension.

Due to the above mentioned statement the matrices may be presented in the form:

$$\hat{\mathbf{Z}}_{YP}(\omega) = \mathbf{A} + i\mathbf{B}\,,\ \hat{\mathbf{H}}_{YP}(\omega) = \mathbf{D} + i\mathbf{E} \tag{33}$$

where: $\mathbf{A} = \mathbf{\Phi}^T_h(\mathbf{K} - \omega^2\mathbf{M})\,\mathbf{\Phi}_h$, $\mathbf{B} = \mathbf{\Phi}^T_h\omega\mathbf{C}\,\mathbf{\Phi}_h$, $\mathbf{D} = \mathrm{Re}\,\hat{\mathbf{H}}_{YP}(\omega)$, $\mathbf{E} = \mathrm{Im}\hat{\mathbf{H}}_{YP}(\omega)$

The set of equations (31), (32) in matrix form reads:

$$\begin{bmatrix}\mathbf{A} & -\mathbf{B}\\ -\mathbf{B} & -\mathbf{A}\end{bmatrix}\begin{bmatrix}\mathbf{D}\\ \mathbf{E}\end{bmatrix} = \begin{bmatrix}\mathbf{I}_h\\ \mathbf{0}\end{bmatrix} \tag{34}$$

where the right-hand side of (34) is composed of *2hx2h* vectors and the *m-th* vector can be stated as follows:

$$\left[\mathbf{I}^m_h, \mathbf{0}\right]^T = \left[(0, 0, ...1_m, 0, ...):\mathbf{0}\right]_{1\times 2h} \tag{35}$$

whileis 1_m unity located at the *m-th* place.

By introducing the following notations: $k_{ii} = \mathbf{\Phi}^T_h\mathbf{K}\mathbf{\Phi}_h$ and $m_{ii} = \mathbf{\Phi}^T_h\mathbf{M}\mathbf{\Phi}_h$, $c_{ii} = \mathbf{\Phi}^T_h\mathbf{C}\mathbf{\Phi}_h$ the solution of Eq. (32) can be stated as follows:

$$\mathrm{Re}\,H_{mi} = \frac{k_{ii} - \omega^2 m_{ii}}{\left(k_{ii} - \omega^2 m_{ii}\right)^2 + c^2_{ii}\omega^2} = \frac{\omega^2_{0i} - \omega^2}{\left(\omega^2_{0i} - \omega^2\right)^2 + 4\xi^2_i\omega^2_{0i}\omega^2} \\ \mathrm{Im}\,H_{mi} = \frac{-\omega c_{ii}}{\left(k_{ii} - \omega^2 m_{ii}\right)^2 + c^2_{ii}\omega^2} = \frac{-2\xi_i\omega_{0i}\omega}{\left(\omega^2_{0i} - \omega^2\right)^2 + 4\xi^2_i\omega^2_{0i}\omega^2} \tag{36}$$

in which m, $i = 1, 2, \ldots 2h$, ω and ω_{0i} denote spectrum frequency and *i-th* structural natural frequency, respectively.

THE SUBSOIL PROPERTIES

The subsoil parameters are assumed deterministic or random (cf. [4], [8], [16]), resulting in linear or non-linear stochastic problem (elements of stiffness and damping matrices are deterministic or random). In both variants the subsoil is assumed a homogeneous linear half-space defined by shear modulus G and Poisson's ratio ν. It is assumed that in the second variant of the subsoil model the shear modulus is random, whereas the Poisson's ratio is deterministic. The soil-structure interaction is simulated by a set of springs and dash-pots. The mean values and the variances of the spring stiffnesses are ([cf. 6], [16]):

$$\overline{K}_H = \frac{8r_0}{2-\nu}\overline{G}, \overline{K}_V = \frac{4r_0}{1-\nu}\overline{G}, \\ \overline{K}_R = \frac{8r^3_0}{3(1-\nu)}\overline{G}, \overline{K}_T = \frac{16r^3_0}{3}\overline{G} \\ \sigma^2_{K_H} = \frac{64r^2_0}{(2-\nu)^2}\sigma^2_G, \sigma^2_{K_V} = \frac{16r^2_0}{(1-\nu)^2}\sigma^2_G, \\ \sigma^2_{K_R} = \frac{7.11r^6_0}{(1-\nu)^2}\sigma^2_G, \sigma^2_{K_T} = 28.44r^6_0\sigma^2_G \tag{37}$$

where: the superscripts H, V, R and T denote horizontal, vertical, flexural and torsional components of the spring stiffnesses, r_0 is the radius of the foot circular plate, $\bar{G}$ is the mean value of shear modulus and σ^2_G denotes its variance.

Due to the dash-pot coefficients we denote (cf. [6], [16]):

$$\begin{aligned}
\bar{C}_V &= 3.58 r_0^2 \sqrt{\frac{\rho}{1-\nu}}\, E\{\sqrt{G}\},\\
\bar{C}_H &= 3.05 r_0^2 \sqrt{\frac{\rho}{2-\nu}}\, E\{\sqrt{G}\},\\
\bar{C}_M &= 0.77 r_0^4 \sqrt{\frac{\rho}{1-\nu}}\, E\{\sqrt{G}\},\\
\bar{C}_T &= 2.56 r_0^4 \sqrt{\rho E}\{\sqrt{G}\},\\
\sigma^2_{CV} &= \frac{12.82\rho r_0^4}{1-\nu}\bar{G} - (\bar{C}_V)^2,\\
\sigma^2_{CH} &= \frac{9.33\,\rho r_0^4}{2-\nu}\bar{G} - (\bar{C}_H)^2,\\
\sigma^2_{CM} &= \frac{0.59\,\rho r_0^8}{1-\nu}\bar{G} - (\bar{C}_M)^2,\\
\sigma^2_{CT} &= 6.57 r_0^8 \bar{G} - (\bar{C}_T)^2.
\end{aligned} \tag{38}$$

where : $$E\left\{\sqrt{G}\right\} = \left(\bar{G}\right)^{\frac{1}{2}}\left[1 - \frac{1}{8}\frac{\sigma_G^2}{\bar{G}^2} - \frac{15}{128}\frac{\left(\sigma_G^2\right)^2}{\bar{G}^4}\right]$$

is the approximate formula for the mathematical expectation of the shear modulus, assuming its Gaussian distribution.

NUMERICAL EXAMPLE

A numerical example concerns the existing structure, the Baltic drilling platform. The space beam model of the platform with 12 nodes and 12 beams is shown in Fig. 3 (cf. [4], [6]).

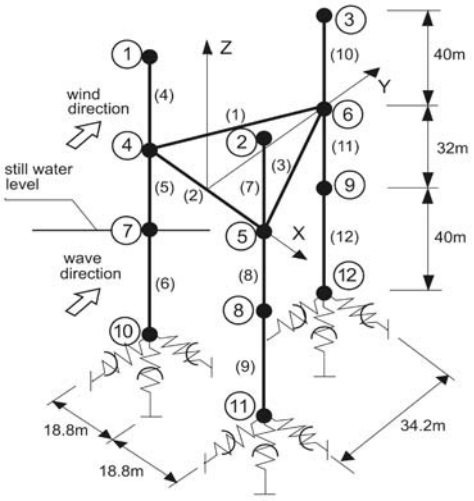

Fig. 3. Discrete model of the platform

Springs and dash-pots in Fig. 5 simulate elastic and damping properties of the subsoil. The platform is subjected to wind and wave loads which are treated as mutually independent stochastic processes.

Structural parameters are collected in Tab. 1 and 2.

Tab. 1. Element stiffnesses

Part	$EA[MN]$	$GJ_s[MNm^2]$	$EJ[MNm^2]$
Deck	$8.40 \cdot 10^5$	$1.94 \cdot 10^6$	$2.53 \cdot 10^6$
Legs	$0.79 \cdot 10^5$	$6.86 \cdot 10^5$	$8.93 \cdot 10^5$

Tab. 2. Lumped massess

Node	Mass [Mg]
1 (2, 3)	300
4 (5, 6)	1800
7 (8, 9)	310
10 (11, 12)	160
Total	2570x3=7710
Hydrodynamic masses	550
Deck exploitation mass	1700

Wave, wind and subsoil parameters assumed in the example are as follows:

wave parameters: $\bar{H} = 14m$, $\bar{T} = 10s$, $\bar{L} = 180m$, $C'_M = C''_M = C_D = 1$, where $\bar{H}$, $\bar{T}$, $\bar{L}$ are mean height, mean period and mean length for long-crested waves, respectively, C'_M, C''_M, C_D are empirical inertia and drag coefficients of the Morison equation [15],

wind parameters (see (A2), Appendix 3): $\bar{v}_{10} = 40m/s$, K = 0.005, $a = b = c = 1$where $\bar{v}_{10}$ is the mean wind speed at a height of 10m above the surface, K denotes the surface drag coefficient, a, b, c are empirical coefficients in the Davenport formula expressing the cross-spectral density of the along-wind fluctuating velocity [14],

subsoil parameters: $E = 60MPa$, $\nu = 0.4$, $\bar{G} = 21.4MPa$, $\sigma_G = 10{,}7MPa$ (i.e. 50 per cent of $\bar{G}$) where E is the Young's modulus, ν denotes the Poisson's ratio, $\bar{G}$ and σ_G are the mean value and standard deviation of the shear modulus.

The selected spectrum responses of the platform model, including the case when pin support of the legs simulate a connection of the structure to the subsoil, are shown in Figs. 4 and 5. The spectrum for the non-linear stochastic case is referred to as the mean values of the natural frequencies obtained from a linear stochastic solution.

CONCLUDING REMARKS

Based on the carried out analysis the following conclusions can be drawn:

1. The structural response is obtained in a frequency-domain by using a linearized form of drag forces, the subsoil stiffness and damping parameters are assumed deterministic

(a linear stochastic problem) or random variables (a non-linear stochastic problem).
2. Modal reduction of dynamic equations of motion performed to achieve a reasonable accuracy of structural response includes a few of the lowest modes.
3. The assumption that soil-structure interaction is modelled by pin supports leads to shifting the response spectrum to lower frequency values, compared to spring supports of the platform legs (Fig. 4).
4. The response spectra reveal two main peaks. The first one is related to the characteristic frequency of the wave ($\omega = 0.5\ rad/s$) whereas the second one is linked with the lowest natural frequencies of the structural system ($\omega_{01} = 1.561\ rad/s$ for $\beta = 0°$ and $\omega_{02} = 2.162\ rad/s$ for $\beta = 90°$).
5. There are series of zero points in the spectra due to those wavelengths which produce the forces on legs that are equal and of opposite sign (Fig. 4 and Fig. 5).
6. The wave load makes a major contribution to dynamic response in comparison to the wind load; the difference does not exceed 10% (cf. [6]).
7. For the non-linear stochastic case the peak in the response is about twice as great as that in the case of deterministic subsoil parameters. Thus the evaluation of the soil-structure interaction parameters is decisive in the response approximation.
8. In the case of relatively slender members of steel platforms major part of the damping forces of the vibrating system is produced by sea waves. When concrete gravity platforms are considered the subsoil contributes to total damping more significantly (cf. [2], [17], [18]).
9. The analysis presented in the paper refers to more general offshore engineering dynamic systems, thus it may be also applicable to structures supporting offshore wind turbines.

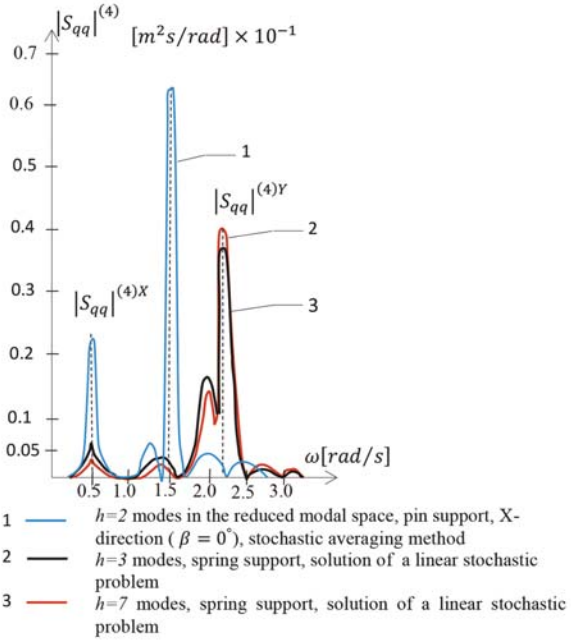

Fig. 4. Spectrum moduli of the displacement response at node (4) due to wave loads

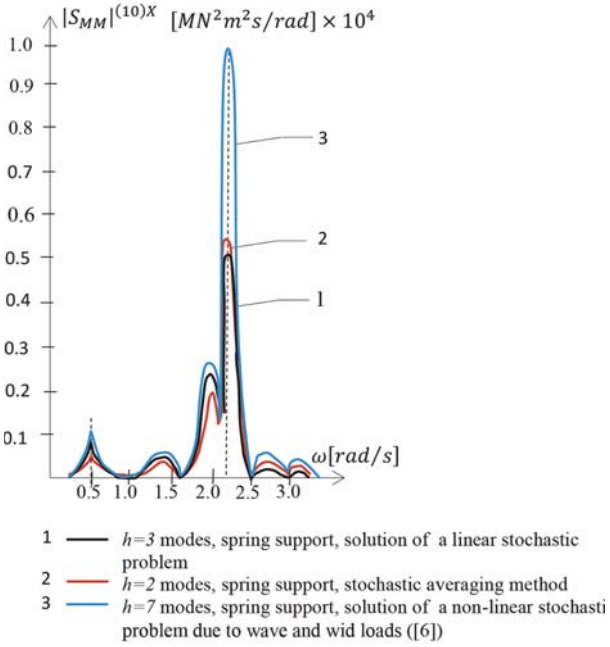

Fig. 5. Spectrum moduli of the response moment at the bottom at node 10 due to wave and wind loads

REFERENCES

1. Malhotra A.K.,Penzien J.: *Response of offshore structures to random wave forces*. Journal of the Structural Division, ASCE, 96, Nr ST10, 1970, pp. 2155–2173.

2. Clauss G., Lehmann E., Ostergaard C.: *Offshore structures*, Vol. ISpringer-Verlag, 1992, Vol. II, 1994.

3. Penzien J., Tseng S.: *Three-dimensional dynamic analysis of fixed offshore platforms*. Numerical Methods in Offshore Engineering, O.C. Zienkiewicz, R.W. Lewis and K.G. Stagg editors – Chapter 7, J. Wiley & Sons, New York, 1979

4. Rozmayrnowski B., Mikulski T.: *Selected problems of sensitivity and reliability of a jack-up platform*. Polish Maritime Research, 1 (97), Vol. 25, 2018, pp. 77–84.

5. DNV-OS-J101: Det Norske Veritas, *Design of offshore wind turbine structures*. May 2014.

6. Jesień W.: *Random Vibrations of the Baltic Drilling Platform Subjected to Wind Loads and Water Waves*. Earthquake Engineering and Structural Dynamics, 15, 1987, pp. 595–617.

7. Spanos P.D.: *Stochastic linearization in structural dynamics*. AMR, 34, No. 1, 1981.

8. Rozmarynowski B.: *Averaged Damping in Random Vibrations of the Baltic Drilling Platform*. Journal of Sound and Vibration 139(3), 1990, pp. 437–458.

9. Taylor E.R., Rajagopalan A.: *Dynamics of offshore structures, Part I: Perturbation analysis*. Journal of Sound and Vibration, No. 3, Vol. 83, 1982, pp. 417–431.

10. RajagopalanA.,Taylor E.R.: *Dynamics of offshore structures, Part II: Stochastic averaging analysis.* Journal of Sound and Vibration, No 3,Vol. 83, 1982, pp. 401–416.

11. Gierliński J.: *RASOS (Reliability Analysis System for Offshore Structures) – Theoretical manual*, Version Nov. WS-Atkins, UK, 1991.

12. Rozmarynowski B.: *Time-domain response of the Baltic drilling platform under regular sea wave excitation.* (in Polish). Archiwum Hydrotechniki, Nr XXXV/3-4, 1988, pp. 251–276

13. Massel St.: *Hydrodynamical issues of offshore structures* (in Polish), PWN, 1981.

14. Davenport A.G.: *The spectrum for horizontal gustiness near the ground in high winds*. Quarterly Journal of the Royal Meteorological Society , 87, 1961, pp.194–211..

15. Morison, J.R., O'Brien, M.P., Johnson, J.W. and Schast, S.A.: *The forces excerted by surface waves on piles*. PetroleumTrans., ASME, 189, 1950, pp. 149–154.

16. Clough R.W. and Penzien J.: *Dynamics of Structures*. McGraw-Hill, New York, 1975.

17. Barltrop N.D.P., Adams A.J.: *Dynamics of fixed marine structures*. Butterworth Heinemann, 1991.

18. Wilson J.F. (Editor): *Dynamics of offshore structures*. John Wiley& Sons, 2003.

19. Spanos P.D.: *Stochastic analysis of oscillators with non-linear damping.* Int. Journal of Non-linear Mechanics, 13, 1978, pp. 249–259.

20. Khas'minskii R.Z.: *A limit theorem for the solution of differential equations with random right-hand sides*. Theory of Probability and its Applications, 1966, Vol. 11, No. 3, pp. 390-406.

APPENDIX 1

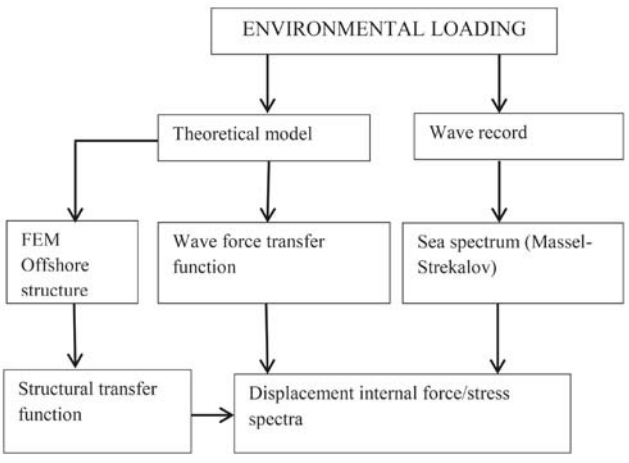

Fig. 6. Calculation flow chart of an internal force and stress spectra

APPENDIX 2

The Massel-Striekalov spectrum takes the form [13]:

$$S_{\eta\eta}(\omega)=\frac{\bar{H}^2}{\bar{\omega}}\left\{0.38\exp\left[-35\left(\frac{\omega}{\bar{\omega}}-0.8\right)^2\right]+0.22\left(\frac{\omega}{\bar{\omega}}\right)^{-5}\exp\left[-1.34\left(\frac{\omega}{\bar{\omega}_p}\right)^{-8}\right]\right\} \tag{A1}$$

with parameters $\bar{H}$, $\bar{\omega}$ indicating the mean wave height and frequency of the wave field.

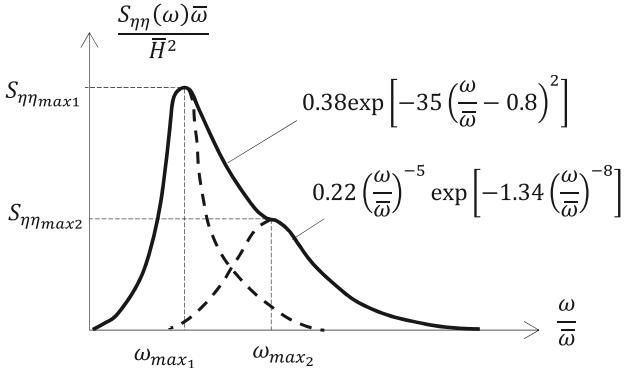

Fig. 7. One-dimensional wave spectrum defined by Striekalov and Massel [13]

APPENDIX 3

A spectral density function of the wind velocity fluctuations considered a one-dimensional stationary Gaussian process with zero mean value is given by Davenport [14]:

$$S_{v'v'}(\omega)=\frac{2KL^2\omega}{\pi\left[1+\left(\frac{\omega L}{2\pi\bar{v}_{10}}\right)^2\right]^{4/3}} \tag{A2}$$

where K is the surface drag coefficient for open sea areas, L is the length scale of turbulence ($L = 1200m$ according to Davenport), $\bar{v}_{10}$ represents the mean speed at a height of 10m above the surface, ω is the frequency. The graph of Eq. (A2) is presented in Fig. 8.

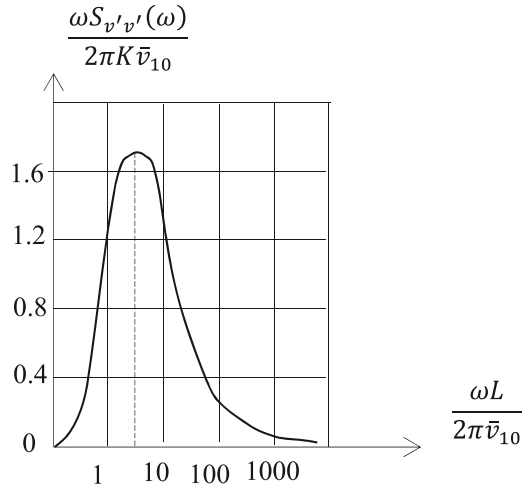

Fig. 8. The Davenport spectrum [14]

CONTACT WITH THE AUTHOR

Bogdan Rozmarynowski
e-mail: bogrozma@pg.edu.pl

Gdańsk University of Technology
11/12 Narutowicza St.
80-233 Gdańsk
Poland

sciendo

POLISH MARITIME RESEARCH 1 (101) 2019 Vol. 26; pp. 49-54
10.2478/pomr-2019-0006

THE APPLICATION OF PHENOMENOLOGICAL METHODOLOGY FOR DESIGNING PILE FOUNDATION IN PORT STRUCTURES

Paweł Więcławski
Gdańsk University of Technology, Faculty of Civil and Environmental Engineering, Poland

ABSTRACT

It is of utmost importance in the design process that a suitable, safe and concurrently economic solution be chosen. Issues connected with foundations require adopting a special approach. Soil is a composite medium, and it is essential to describe as precisely as possible the interaction taking place between the subgrade and the structure. There are many design methods of pile foundation that are based on in-situ test of soils. As a result of incessant development of the pile installation technology, the results obtained with design methods used to date do not assure the required accuracy, and consequently the values of pile load capacity are not sufficiently accurate. A partial solution to this problem may be applying the observation method. Based on assumptions of phenomenology as a science that enable cognition of natural and mathematical phenomena, a procedure has been developed for projecting loading-settlement dependencies for Vibro piles installed in port areas in Poland. Those areas are characterised by similar soil and water conditions, as well as soil genesis and parameters. This procedure enables estimating the limit of load capacity values with much better accuracy than the hitherto used direct methods. The full range of the s(Q) function also enables the possibility of designing structures allowing for stringent criteria of admissible settlements having a specified value.

Keywords: phenomenology, observation method, pile foundation, Eurocode 7, limit load capacity

INTRODUCTION

The development of port infrastructure depends to a large extent on the development of maritime navigation and transport. Major difficulties in this respect include significant implementation costs and lack of certainty related to safe building of structures. Variable elements are environmental impacts, such as waves, wind and water, and soil conditions. If the soil contains organic layers, mud, or silt, pile foundations need to be adopted [2,7,9]. The design methods comprise in the first place the method of limit states, in which the ultimate limit state (ULS) and the serviceability limit state (SLS)[14] are assessed. When commencing designs of pile foundations, firstly the in-depth analysis of relevant parameters related both to the soil, and to the characteristic features of the piles should be performed. As regards the subgrade, we should have at our disposal a complete identification of conditions in which the construction is to be founded. Attention should be drawn to: soil types, groundwater tables, natural state of stresses, filtration properties, and strength parameters. As for pile parameters, the elements which should be determined include: quality of the concrete mix, pile installation method, possibility of occurrence of deviations caused by the occurrence of soil layers of considerable compressibility,

and roughness and rigidity of the pile [5,. Allowing for those aspects is not simple if we have at our disposal only simplified analytical approaches. To quote K. Terzaghi [3]: "*Unfortunately, soils are made by nature and not by man, and the products of nature are always complex… As soon as we pass from steel and concrete to earth, the omnipotence of theory ceases to exist. Natural soil is never uniform. Its properties change from point to point while our knowledge of its properties is limited to those few spots at which the samples have been collected. In soil mechanics the accuracy of computed results never exceeds that of a crude estimate, and the principal function of theory consists in teaching us what and how to observe in the field*". The obtained results should be considered to be "crude estimate". To obtain more accurate results, the standard PN-EN 1997-1:2008 allows the possibility of adapting the observation method called "active designing" according to [8, 15]:"*...is a continuous, managed, integrated, process of design, construction control, monitoring and review, which enables previously defined modifications to be incorporated during or after construction as appropriate. All these aspects have to be demonstrably robust. The objective is to achieve greater overall economy without compromising safety*". This method is a combination of tests and analyses of the building structure and the soil with ongoing measurements of the behaviour of the building structure and the subgrade not only during the execution of construction works, but also during operation. The projection executed in this way, when limited to local conditions of soils with the same genesis, physical properties and strength parameters, enables achieving a more accurate reflection of the actual state. The paper presents a methodology for projecting the functioning of piles on the areas of Szczecin and Gdynia ports. Pursuant to rules of precise, economic and safe designing, a correlation has been defined between in-situ parameters of the soil and pile behaviour under the impact of vertical loads. The defined empirical dependencies enable the determination of the full settlement-load curve for the analysed pile based on the cone resistance q_c obtained from CPT probing. The option of assessing the full range of pile settlement provides the opportunity to make complex use of designing conditions based on stringent criteria of admissible settlements. The process of universalisation and the nature of interdependencies arise from observations and analyses of variating particular parameters comprised by the analysis. Due to the existence of a common part of each of the parameter configurations, it is possible to devise an outline of the phenomenon and to work out universal and practical correlations. Thus it is consistent with the assumptions of the observation method and, concurrently, of the phenomenological approach.

SOIL CONDITIONS OF RESEARCH FIELDS

The analysis was performed for Vibro piles situated on the areas of port facilities. The research fields were on the premises of the Szczecin and Gdynia ports (Fig.1).

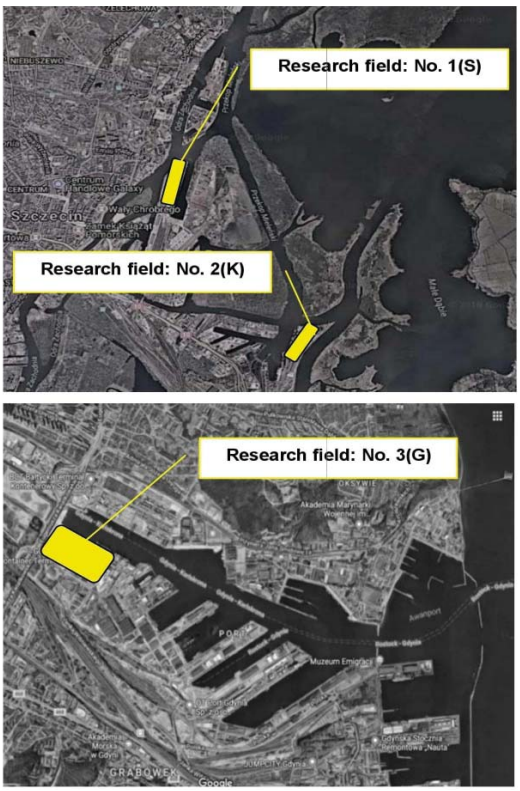

Fig.1. Situation of research fields in Port of Szczecin (up) and Port of Gdynia (down)

The testing scope comprised: geological boreholes, static CPT probing of the soil, and static pile load tests (SPLT). The analysis covered 36 Vibro piles, 9 CPT tests, and 8 geological boreholes (Fig. 2).

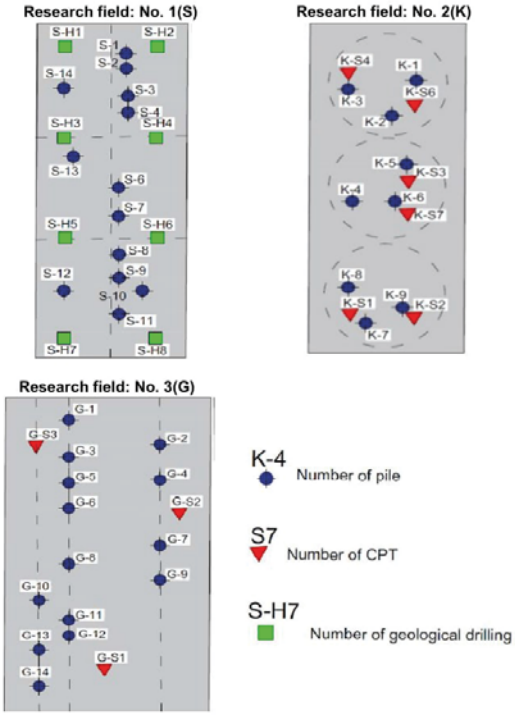

Fig.2. Distribution of research points

Research field No. 1(S). Field investigations enabled ascertaining that the soil contains Quaternary and Pleistocene formations. Subsoils are covered by a layer of uncontrolled embankments formed as a result of land management. These are predominantly sandy embankments, locally of mud with an admixture of concrete, gravel and stones. Their maximum thickness is 2.7m. At a depth ranging from 8.0 to 12.0 m occur riverine sands covered by series of mud with peat layers. The thickness of the entire organic deposit series ranges from 4.0 to 8.0 m. Below lies a series of deposits consisting of medium and fine sand in uncompacted state and medium dense state. The oldest deposits ascertained in the soil are Pleistocene water glacial formations, and medium and fine sand in compacted state (Fig.3). The bases of the planned Vibro piles have been founded in this layer.

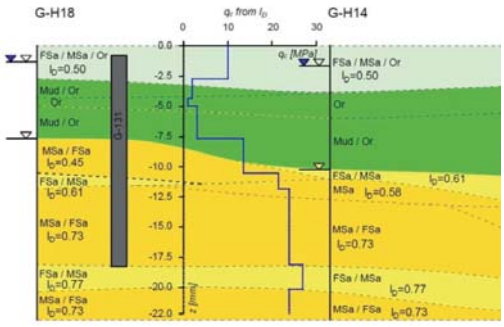

Fig.3. Characteristic geological section of the area of Research field No. 1(S)

Research field No. 2(K). The conducted tests of the soil and CPT (Fig. 4) have shown that directly under the surface lies a layer of embankments predominantly consisting of slag with admixture of debris and mineral soils. Under the embankments, fine sand has been ascertained. Sandy soil is in medium dense state. Deeper, there is a series of mud deposits, formed as silt, aggradate mud, and peat. Such soils lie as a rule 10.0 m below the land surface. Underneath is a series of non-cohesive soils, fine sand, where pile bases are founded.

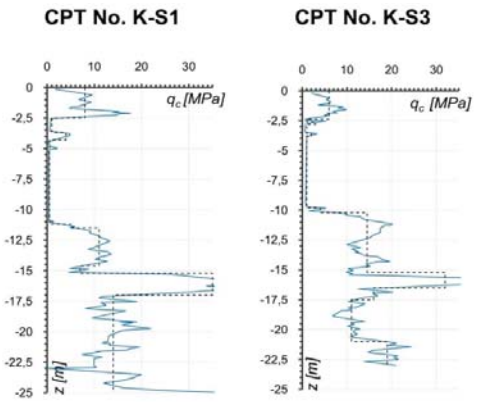

Fig.4. Characteristic results of CPT testing on the area of Research field No. 2(K)

Research field No. 3(G). Ground investigations and CPT probing (Fig.4) have shown that the surface part is made up of embankments consisting of fine sand with organic admixtures. Locally under the embankment layer lie organic soils such as peats and mud of maximum thickness of 1.0 m. The subsoil consists of Quaternary deposits, such as fine sand, either compacted or of medium compaction and compacted, with layers of medium sand.

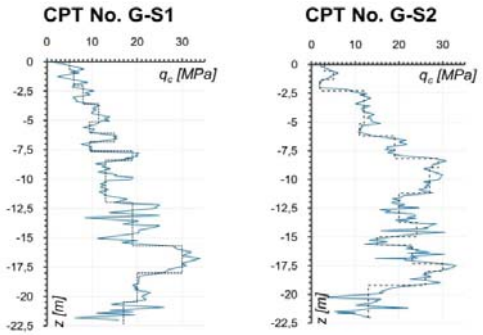

Fig.5. Characteristic results of CPT testing on the area of Research field No. 3(G)

A common element for the analysed areas is the genesis of soil conditions. The soil structure is a consequence of the accumulation of Quaternary sand materials, caused by the Northern Polish glaciation and the development of the Baltic Sea coastal zone. Weak layers comprise organic soils, such as mud and peats.

PHENOMENOLOGY AS VERIFICATION METHOD OF SETTLEMENT AND DESIGNING OF FOUNDATION PILES

Phenomenology is a direction of deliberations and analyses; in Greek the word *phainomenon* means "*anything that manifests itself*". The phenomenological method is an observation and descriptive method with emphasis on observation, and its elements comprise values of direct experience and intuition. It is a method of a specific nature that provides direct knowledge concerning "the substance of things". The method consists of seeking solutions by way of applying free conceptual variation and intentionality, i.e. a trend, which in each individual case is oriented towards something. According to E. Husserl, the author of the phenomenological approach, the accuracy of the analysed case may be achieved by implementing the postulate of the so-called theoretically uninvolved description. The concept is comprised of three basic elements: (1) adoption of an objectivistic approach, focused entirely on the studied structure, (2) exclusion or reduction of any knowledge that could originate from the existing scientific theories, and (3) ruling out convictions originating from tradition [6]. Its central thesis on cognition of a phenomenon by its specific values is adopted for the needs of mathematical and natural cognition. The conducted analysis is based on the above guidelines and its objective is to define the interaction of the soil medium with the axially loaded pile. This interaction is depicted by the load - settlement (Q-s) dependence obtained on the basis of the static load test (SPLT)[12].

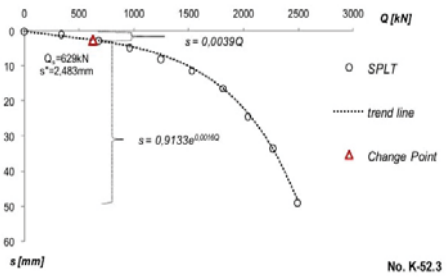

Fig. 6. Mathematical description of Q-s dependence

When analysing a set of curves, attention has been drawn to changes taking place in the nature and course of the Q-s dependence in specific soil conditions. A characteristic feature is the two-phase nature of the function. Each of the curves may be presented as consisting of the linear part and the exponential part, with the Change Point as a specific element in the mathematical description of phases (Fig. 6). Coordinates of the Change Point (Q_s, s") depend on pile geometry and soil parameters, represented in the analysis by cone resistance q_c on the CPT probe (Fig. 7.). Based on this assumption, correlations have been defined that enable determination of the theoretical curve Q-s (Fig. 8. - Fig. 10.)

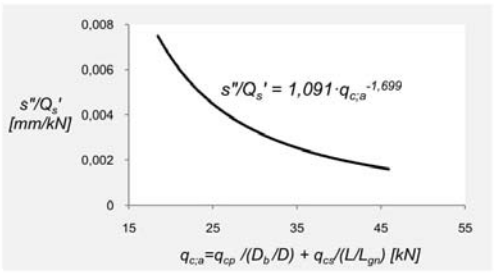

$q_{c;a}$ – average value of resistance q_c;
q_{cp} – average value of resistance q_c under pile base to the depth equal to pile diameter;
q_{cs} – average weighted value of resistance q_c along the pile side surface;
D – diameter of pile;
D_b – diameter of pile base;
L – total pile length;
L_{gn} – pile length in bearing soil (q_c>5 MPa)
Q_s' - abscissa, abscissa of Change Point;
s" - ordinate, coordinate of Change Point;

Fig. 7. Correlation of soil parameters and directional coefficient of settlement curve

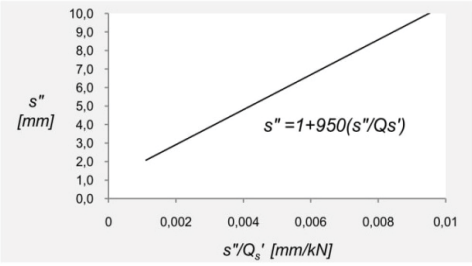

Fig. 8. Relation between Change Point coordinates

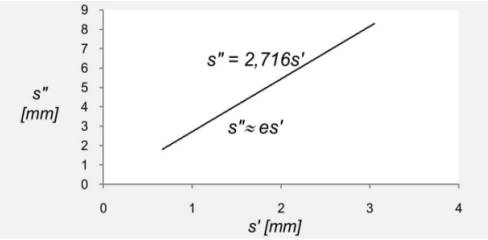

s'- basis of exponential function

Fig. 9. Relation between the basis of exponential function and the Change Point ordinate

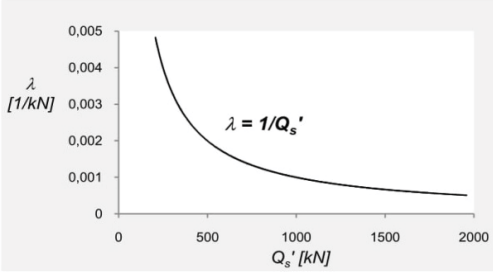

λ - exponent of exponential function

Fig. 10. Relation between the exponent of exponential function and the Change Point abscissa

Based on the correlations shown in Figs. 7 through 10, the linear phase equations (I-II) and the exponential phase (III-IV) should be determined for the s(Q) function. Before generating Q-s characteristics, the value of load Q' (also Q_s') must be reduced by adopting the correction coefficient, which depends on the averaged value of cone resistance $q_{c;a}$ (Table 1.)

Table 1. Values of correction coefficient

Value of averaged resistance- $q_{c;a}$	Correction coefficient - F_c
< 30 MPa	1.1
≥ 30 MPa	1.2

ASSESSING THE INTERACTION OF PILE FOOTING WITH SOIL

Geotechnical designing of piles includes the selection of the type, length and diameter of the pile for the analysed soil conditions. It is necessary that the condition of the ultimate limit state be met, i.e. the bearing capacity of the pile in the soil be greater than the calculated impact effect. The bearing capacity of the pile is delimited by dividing the characteristic load by the safety coefficient γ_t, the value of which is assumed depending on the adopted design approach. The characteristic load capacity is delimited on the basis of the ultimate bearing capacity and should enable the determination of the characteristic load capacity with a likelihood of p=0.95. In practical terms, we do not have at our disposal a sufficient number of delimited ultimate bearing capacity values to perform statistical analysis. Use is being made of correlation coefficients x, which depict directly the

distribution functions considered as appropriate for pile load capacity determination methods specified in standard PN-EN 1997-1:2008 [4,14] (Fig. 11.). The developed procedure enables determination of the value of the ultimate load capacity.

Table 2. Examples of determination of Q-s curve

Input data						
Pile No.	D	D_b	L	L_{gn}	q_{cp}	q_{cs}
K-4	m	m	m	m	MPa	MPa
	0,457	0,520	18,5	11,0	19,0	13,5

Output data						
$q_{c;a}$	s''/Q_s	s'	s''	Q_s'	λ	F_C
MPa	mm/kN	mm	mm	kN	1/kN	-
24,73	0,00469	2,006	4,45	1163	0,00086	1,1

Function s(Q)			
Linear stage	Change point		Nonlinear stage
$s_{(I-II)} = 0{,}00469 \cdot Q$	1163/1,1=1057kN	4,45mm	$s_{(III-IV)} = 2{,}006 \cdot e^{0{,}00086 \cdot Q}$

Q'	Q = Q'/F_C	s
kN	kN	mm
0	0	0
1163	1057	4,45
1588	1443	7,85
2041	1855	11,59
2722	2474	20,81
3400	3090	37,28
3645	3313	45,70

Q-s curve

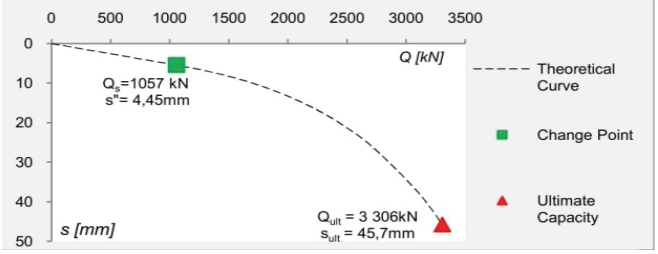

Pursuant to PN-EN 1997-1:2008, it has been assumed in the presented examples that the ultimate limit state occurs for the settlement equal to 10% of pile diameter [14] (Table 2.). In accordance with PN-EN 1997-1:2008, the testing should be repeated until it becomes possible to define the limiting bearing capacity of the pile. Based on an analysis for Vibro piles it has been ascertained that for this particular technology, the interpretation of the static load test (SPLT) according to the hitherto traditions has clearly become insufficient. The scope of loading from SPLT does not enable the determination of the value of the pile ultimate load capacity, and this in turn hinders verification of design methods and the execution of the proper statistical analysis. The convergence of the calculated and measured bearing capacity values was studied for loads conforming to maximum settlement from static load test.

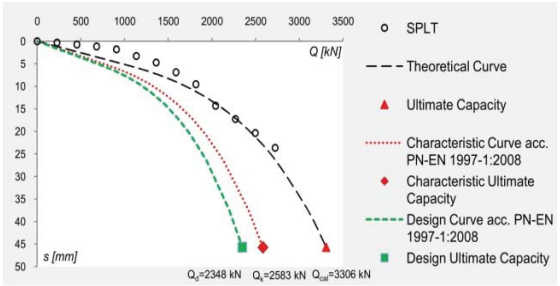

Fig.11. Values of ultimate bearing capacity pursuant to PN-EN 1997-1:2008

The statistical analysis comprises a trial that included 36 piles. It has been found that the load capacity values calculated for 22% of piles have been overestimated in relation to the measured values (Fig. 12.). By adopting the procedure specified in standard PN-EN 1997-1:2008 for calculating design values for all the piles, it was possible to obtain a safe load bearing value. The minimum safety reserve is 10% (Fig. 12.).

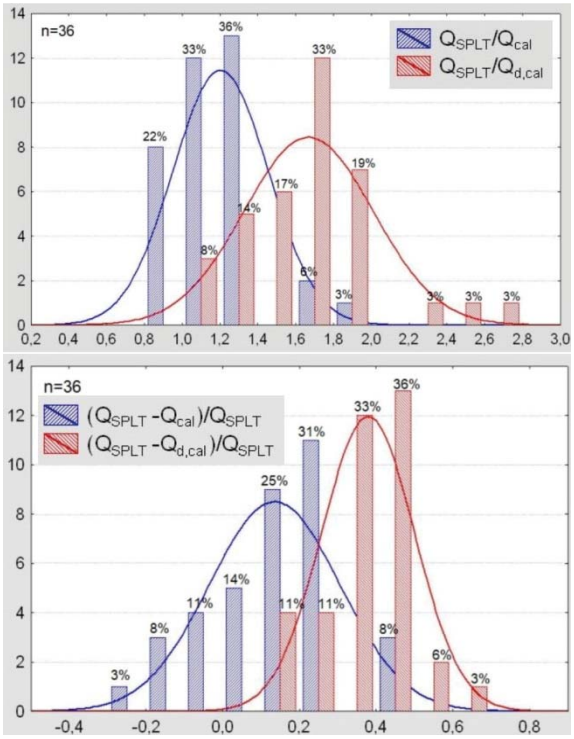

Fig. 12. Relation between calculated and measured load capacity values

SUMMARY AND CONCLUSIONS

The advantage of applying Eurocode 7 [14] is the possibility of making use, both for design and verification needs, of an arbitrary method based on any domestic practise in use to date [5]. The method discussed in this paper is of an empirical nature and has been based on assumptions of phenomenology. An element of particular importance is the Change Point in the interaction of an axially loaded pile with the subgrade, defined on the basis of CPT results. A unique feature of the procedure is clear and simple possibility of completing the determination of the s(Q) function. This enables a more accurate assessment of theoretical pile load capacity as compared to other direct methods based on results of CPT. Comparing the limit load capacity values calculated with methods of LPCP, Gwizdała-Stęczniewski [10,11,13], or according to PN-EN 1997-2:2008 [14,15], enabled reaching the conclusion that the values based on the developed procedure are closer to actual ones. This conclusion continues to apply even after the adoption of standard safety coefficients. In popular methods use is made of high coefficients of global safety. For

methods used in Europe, the value of coefficients ranges from 1.5 even to 3.5 [1,11], depending on soil conditions, applied piles, or type of construction. The results obtained based on phenomenological dependences are similar to the values obtained from the static load test. This has a considerable impact on the economic and optimal designing of pile foundations. If the full Q-s curve is available, it is possible to adopt for design needs the values of critical loading or limit loading and settlements which correspond to strictly defined required interaction criteria of the foundations and the entire facility. These requirements constitute a crucial aspect in designing port infrastructure, including foundations for specialist technical structures such as tanks, silos, or gantry cranes.

BIBLIOGRAPHY

1. Bustamante M., Gianeselli L.: *Pile Bearing Capacity Prediction by Means of Static Penetration CPT.* Proceedings of 2nd European Symposium on Penetration Testing, Amsterdam, 1982.

2. DeRuiter J., Beringen F. L.:. Pile Foundations for Large North Sea Structures. Marine Geotechnology, 1979.

3. Goodman R. E.: *Karl Terzaghi: The Engineer As Artist*. Amer Society of Civil Engineers**,** 1998.

4. Gwizdała K., Brzozowski T., Więcławski P.: *Calculation aspects used in Eurocode 7 for pile foundation. From Research to Design in European Practice*. Bratislava, Slovak Republic, June 2 – 4, 2010.

5. Gwizdała K., Więcławski P.: *Polish experience in the assessment of pile bearing capacity and settlement of the pile foundation.* Baltic Piling Days, Estonia, Talin, September 3 – 5, 2012

6. Husserl E.: *The Crisis of European Sciences and Transcendental Phenomenology*. Northwestern University Press, 1970.

7. McClelland J.: *Design of deep penetration piles for ocean structures*. J. Geotech. Eng. 1974.

8. Nicholson D., Tse C., Penny C.: The *Observational Method in ground engineering–principles and applications.* Report 185, CIRIA, London, 1999.

9. Randolph M. F., *Design consideration for offshore piles*. Proc. Of the Conference on Geotechnical Practice in Offshore Eng., ASCE, 1983.

10. Salgado, R.; Lee, J., *Pile Design on Cone Penetration Test Results*. Final Report, FHWA/IN/JTRP-99/8, 1999.

11. Tomlinson M.J., *Pile Design and Construction Practice*. Wyd. E&FN SPON, Londyn, 1994.

12. Więcławski P. *Methodology for estimating settlement of Vibro piles based on CPT*. Gdansk University of Technology 2016.

13. Wroth C.P., *The Interpretation of in situ Soil Tests*. Geotechnique, Vol. 34, No 4, 1984.

14. PN-EN 1997-1:2008: *Geotechnical design, part 1. General rules.* Eurocode 7, Brussels, 2008.

15. PN-EN 1997-2:2008: *Geotechnical design, part 2. Ground investigation and testing.* Eurocode 7, Brussels, 2008.

CONTACT WITH THE AUTHORS

Paweł Więcławski
e-mail: pawwiecl@pg.edu.pl

Gdańsk University of Technology
Faculty of Civil and Environmental Engineering
Gabriela Narutowicza 11/12
80-233 Gdańsk
Poland

sciendo

POLISH MARITIME RESEARCH 1 (101) 2019 Vol. 26; pp. 55-64
10.2478/pomr-2019-0007

FUZZY IDENTIFICATION OF THE RELIABILITY STATE OF THE MINE DETECTING SHIP PROPULSION SYSTEM

Michał Pająk[1]
Łukasz Muślewski[2]
Bogdan Landowski[2]
Andrzej Grządziela[3]
[1] University of Technology and Humanities, Radom, Poland
[2] University of Science and Technology, Bydgoszcz, Poland
[3] Polish Naval Academy, Poland

ABSTRACT

The study presents the evaluation and comparative analysis of engine shaft line performance in maritime transport ships of the same type. During its operation, a technical system performs functions for which it was designed. It goes through different states. Dynamic state changes of a rotational system can be identified by means of its vibration measurement. For this purpose, a research was carried out which involved recording vibrations of the analysed rotational systems. The recordings were used for calculating selected characteristics in the time-domain, where one of the most unique is the value of the normalized mutual correlation function. On the basis of the concentration values, the characteristics which unambiguously determine the ability state were selected for further studies. Then an identification method for rotational system non-coaxiality was proposed. The method involves using fuzzy clustering. According to this method the values of input signal characteristics were used to formulate fuzzy clusters of system ability and inability states. The method can be used for identifying the current state of the system. The study presents the results of the application of this method in engine turbine shaft lines of minesweepers, with the rotational system selected as an example. It needs to be noted that the efficiency of identifying the operating state of the system with this method is higher than with other methods described in the literature by authors who deal with this issue. The research results have a significant impact on the evaluation of mechanical properties of the studied objects and directly affect operational states of mechanical systems, including those installed in minesweepers, thus determining their reliability.

Keywords: ships, rotational system, mutual correlation, non-coaxiality, fuzzy clusters

INTRODUCTION

Rotating machinery is widely used in energy transformation and power transmission industries. Malfunctioning of the rotational system is most commonly caused by the impact of external forces, fatigue corrosion, aging, and poor working conditions. This leads to unexpected downtime and economic losses. Therefore, monitoring the technical state of a machine system is becoming an important issue of the engineering and academic research. The vibration signal analysis based fault detection and rotor system diagnosis is one of the principal maintenance tools [17]. From the point of system operation damageability, reliability, and safety, vibrations are the primary diagnostic symptoms [25, 26, 47, 48, 59].

Vibrations and noise generated by rotational subsystems occur, practically, in all mechanical systems of transport means including ships. Vibrations can be generated by shafts, axes and fans, depending on the type of transport means or device.

According to literature, it is possible to carry out the research on the basis of correlation analysis, and to identify early symptoms of rotational system dynamic changes, especially its misalignment, through measurement of its vibrations [8, 10-12, 16]. The Fourier transformation [1, 20] and the wavelet transformation [37, 38] have been widely applied in recognizing fault feature frequencies of machinery equipment. Wavelet packet decomposition is utilized to analyse acoustic emission of signals and thus to identify the failure of a tribological system [2]. It is also applied to

provide temporal-frequency information and capture the energy features [5], and to denoise non-stationary signals [49]. Although the wavelet analysis is widely used in vibration signal processing, there are certain problems concerning its application, such as difficulties in finding the best threshold and selecting the proper wavelet basis.

Vibration signals of the rotating machinery can have nonlinear and non-stationary characteristics when the mechanical transmission system fails to operate properly. Empirical mode decomposition (EMD) has been proved to be the proper method for dealing with nonlinear and non-stationary signals. In this method, any complex information can be adaptively decomposed into a number of individual, mono-component signals described by intrinsic mode functions. However, EMD has some problems, such as endpoint effect or modal aliasing. To cope with EMD disadvantages its some extensions have been developed. One of them is ensemble EMD (EEMD) [44]. Ensemble empirical mode decomposition has many advantages and has been applied in many scientific fields [50, 52]. Another extension of EMD is variational mode decomposition (VMD). Through adaptive quasi-orthogonal signal decomposition, VMD decomposes the multi-component signal into several single-component signals, thus solving the problem of mode aliasing of EMD. Simultaneously, VMD makes use of Wiener filtering and has good noise robustness [23].

The EMD method and its extensions are often used in hybrid solutions, where these methods are combined with other types of signal processing. Here, the HHT method can be considered as an example. This is an adaptive time-frequency signal processing method which was applied in the past to water wave analysis, EEG signal feature extraction, and vibration signal processing [40]. In [34], a method of extracting shock energy-associated features from the background of intense noise interference is proposed. The energy weighting method starts with raw vibration signal decomposition using EEMD and time-frequency mapping by Hilbert transformation. Subsequently, the time-frequency map is considered as a set of time series of energy values for each particular frequency and each signal, and is analysed to check if impulsive energy exists. Finally, each binary spectrum is converted into weights of particular energy compounds to total weight of energy, and a characteristic frequency corresponding to a specific fault is revealed.

For monitoring the condition of a rotor system when the vibration signals produce an impulsive signature, the Spectral Kurtosis (SK) method is used. [39, 46]. With this method, it is possible to extract a part of the signal with the highest level of impulsiveness. The SK method has been already applied successfully by many researchers in monitoring the condition of rotating machinery and fault diagnosing [45]. In [51], a new method combining the advantages of EEMD and SK for rotor bearing system multi-fault diagnosis is proposed.

As far as the rotor system multi-fault diagnosis is concerned, the faulty signal is often intermixed with vibrations or noise emitted by other sources [22, 56]. A similar situation occurs in diagnosing the rotor system operation under transient conditions, when the vibration signal is affected by the speed change and the transmission path [21]. If the traditional Fast Fourier Transform is adopted, it will lead to frequency aliasing. Order Tracking (OT) is the most direct and effective method to deal with the fault diagnosis under variable conditions [4, 6]. Non-stationary signals are converted into stationary signals by equal angle resampling. There are two types of OT: Hardware Order Tracking (HOT) and Computed Order Tracking (COT). The HOT performs equal angle sampling of the vibration signal with the analogue device [57]. The hardware devices are expensive and complex, which limits the range of application of this method. In the COT, the vibration signal and the key phase signal of the machine are collected synchronously in the equal time interval sampling mode. Then, the equal angle sampling sequence in the angle domain is obtained by the interpolation algorithm. COT has been applied to feature extraction and fault diagnosis of internal combustion engines [55]. In [14], a hybrid method based on order tracking, EEMD, and 1.5 dimension spectrum is proposed for extracting the rolling bearing fault feature, under variable conditions.

However, the feature frequency cannot always be detected due to difficulties in obtaining the value of rotating frequency or the values of operational parameters of mechanical parts, which limits its implementation. In such a case, the classification-based fault diagnosis is used as another method of vibration analysis to avoid calculation of fault feature frequencies. The classification methods which are frequently used in the field of fault diagnosis include linear discriminant analysis (LDA) [13], artificial neural network (ANN) [36], support vector machine (SVM) [58], and sparse representation based classification (SRC) [7].

LDA, as a basic Fisher discriminant classifier, pursues a low degree of coupling between classes and a high degree of polymerization within a class. ANN provides nonlinear mapping between symptoms and faults. SVM is a machine learning method based on the statistical learning theory, and produces a favourable generalization performance. The basic principle of SRC is to sparse code a test sample over a dictionary and then to perform the classification based on the reconstruction error. SRC and its variants have been widely applied in face recognition, EEG signal classification, and music genre classification, or to reduce the dimension of original vibration signals. In [53], on the basis of SRC, a classification method for machinery vibration signals, named Transform Domain Sparse Representation-based Classification (TDSRC), is proposed. In TDSRC, the dictionary for sparse representation is not constructed with raw samples, but with their transformation coefficients.

The authors also focused on vibration signal time-domain analysis. In works [10, 11, 18, 27], the best characteristics of vibration signals in terms of reliability state identification were selected. Subsequently, they were used to formulate the functional space in which the ability state and inability state clusters of signals were specified. Thanks to the proposed methods implementation, it was possible to correctly identify the ability state in 65% and the inability state in 94%. Despite pretty high efficiency of the inability state identification, the

study was performed in order to increase the ability state identification. As a result, a fuzzy classification of vibration signals in the time-domain was proposed. A detailed description of the method in presented in Chapter 4. In order to facilitate understanding of the idea and to present its genesis, a short description of the performed operational tests (Chapter 2) and the elements of former works (Chapter 3) are also enclosed. The results of the method application in the considered naval vessels are discussed in Chapter 5. The paper is summed up by some conclusions formulated in Chapter 6.

OPERATIONAL TESTS OF MINE DETECTING SHIPS

The study deals with selected types of ships, specifically with their propulsion systems. These ships are used by the Navy and their main task is to detect marine mines Fig. 1.

Fig. 1. Mine detecting ship 207P

Vibrations of the main engine shaft were recorded at 6 measuring points of the considered propeller systems. These points were located on: main engine bed plate, power consumer facing engine shaft end, hydrokinetic coupling, bearings at reversing reduction gear input and output, and thrust bearing, as shown in Fig. 2.

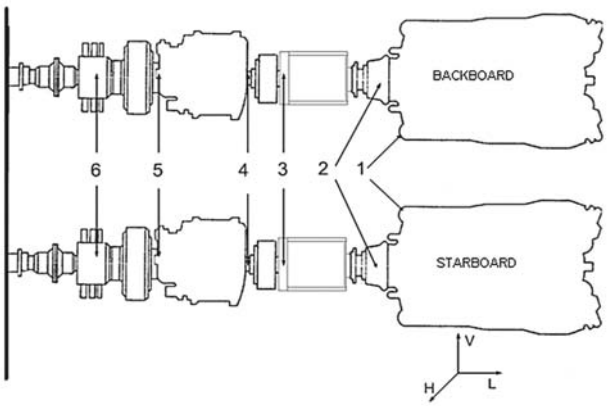

Fig. 2. Arrangement of measuring points on the analysed propulsion systems; 1-engine bed plate; 2-power consumer facing engine shaft end; 3-hydrokinetic coupling; 4-bearing at input of reversing reduction gear; 5-bearing at output of the gear; 6-thrust bearing

Each system is characterized by: nominal rotational speed equal to 1550 rpm, nominal power of 736kW, hydro-kinetic coupling with nominal slide 2% and skid control range 2-98%, reversing reduction gear with coefficient 3.5:1, and thrust bearing (equipped with three ball bearings).

The vibration accelerations were recorded in four vessels: on two drive shaft lines in three vessels and on one shaft line in the remaining one. Six measurement points were situated on each shaft line. A sample vibration acceleration time-history recorded during the measurement is shown in Fig. 3.

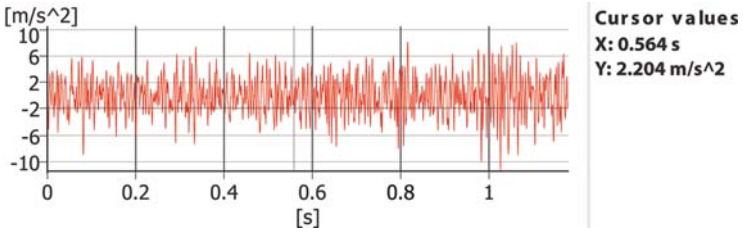

Fig. 3. Fragment of vibration acceleration time-history recorded during measurements

The operational tests were performed during normal ship operation when the wind did not exceed 2°B, as otherwise, waves hitting the ship body would affect excessively the recorded vibrations. The temperature in the powerhouse compartment was nearly 40°C. As already mentioned, the main engine shaft vibrations were measured at 6 points (for each drive shaft).

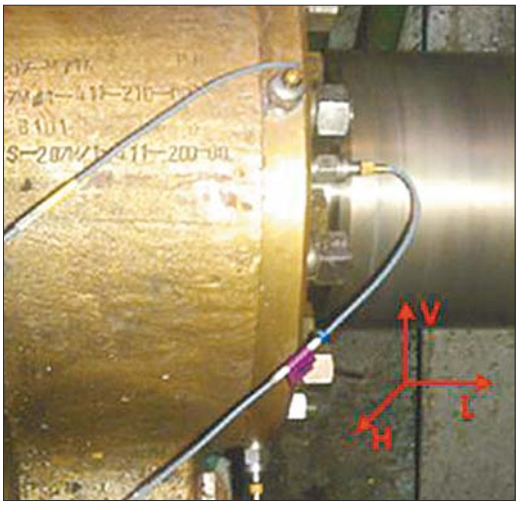

Fig. 4. Places on the resistance-carrier bearing where accelerometers were fixed, with marking of measurement directions

Three identical speedometers were used (B&K 4514B) for this purpose. They were mounted on three mutually perpendicular axes. Since there was no possibility to use a threaded mutually perpendicular joint, converters were fixed with glue to the tested elements of the propulsion system.

After taking the measurements, the measurement paths were calibrated. All the recorded signals were synchronized by means of a four-channel gauge [3]. The vibration values were recorded within 3.2 kHz band, at the sampling frequency equal to 8192Hz.

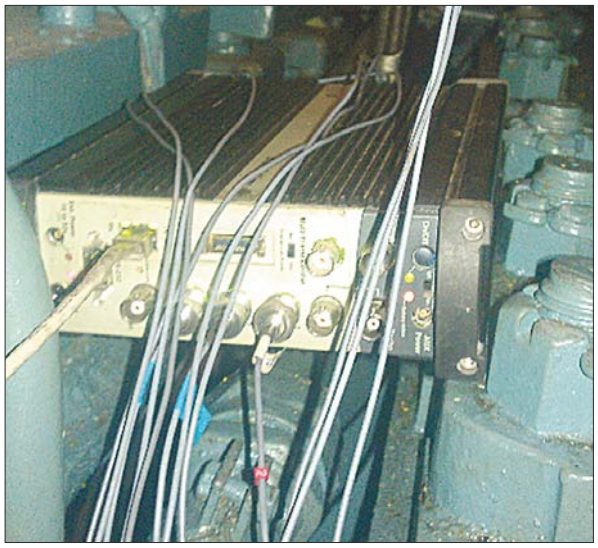

Fig. 5. Device used for measurements in B&K 3560-B-120

Vibrations were recorded in three mutually perpendicular directions for 4 rotational speeds: 850rpm, 1100rpm, 1300rpm, and 1500rpm. The recorded results were stored in csv files. Each file included the vibration values for a given shaft system, measuring point, and rotational speed [11,27]. After recording, the files were divided into groups in such a way that each file in one group included 1024 measured values. However, after a preliminary analysis of the obtained files it turned out that the last file in each group contained only 1011 measurements. These files were excluded from further analysis. In this way, 252 files were obtained for shaft lines being in ability state, and 68 files for shaft lines being in inability state for each measurement point-vibration axis-rotational speed (PAS) combination. Each file contained the same number of measurements.

VIBRATION SIGNAL TIME-DOMAIN ANALYSIS

The time-histories of the recorded vibrations were treated as discrete signals expressed in the time domain. For each signal (vsi), the following characteristics (*CH(vsi)*) were calculated [27, 41, 42]: integral, mean value, energy, average power (rms square), I order moment, II order moment, I order central moment, II order central moment, I order normalized moment, II order normalized moment, I order normalized central moment, II order normalized central moment, abscissa of the signal square gravity centre, the signal square variance, and the signal equivalent mean.

It was also established that the considered signals take non-zero values only within a finite interval, thus, they are impulse signals [59]. Having calculated the energy of signals according to Eq. (1), it was stated that these are impulse signals with limited energy [15]:

$$E = \int_{t_0}^{t_k} vs^2(t)dt \tag{1}$$

where E is the energy of the signal time-history, vs is the signal value, and t_0 and t_k are the times of interval beginning and end, respectively.

Thus, the signals can be considered as points of the $L^2(t_0, t_k)$ function space, where time t_0 corresponds to the first measurement in the file and time tk to the last one. This space is a space of impulse signals with limited energy [42]. It is composed of a set of impulse signals with limited energy VS and the metrics expressed by Eq. (2).

$$\rho(vs_i\Big|_{t_0}^{t_k}, vs_j\Big|_{t_0}^{t_k}) = \sqrt{\int_0^{\max(t_k)} \left| vs_i(t)\Big|_{t_0}^{t_k} - vs_j(t)\Big|_{t_0}^{t_k} \right|^2 dt} \quad \wedge \quad \mathrm{vs}_i, vs_j \in VS \tag{2}$$

where $\rho(vs_i\Big|_{t_0}^{t_k}, vs_j\Big|_{t_0}^{t_k})$ is the functional such that $VS \times VS \to \Re^+ \cup \{0\}$, $max(t_k)$, $max(t_k)$ is the maximum time of the interval end, vs_i is the time-history of i-th signal $i = 1,2,...$, lvs, vsj is the time-history of j-th signal $j = 1,2,...$, lvs, lvs is the number of signal time-histories, $\left| vs_i(t)\Big|_{t_0}^{t_k} - vs_j(t)\Big|_{t_0}^{t_k} \right|$ is the distance between the time-histories of i-th signal j-th signal, and VS is the set of signal time-histories.

Extension of the space with scalar addition, multiplication, and norm Eq. (3), constitutes the normalized linear Hilbert space [9]:

$$\| vs \|_{L^2} = \sqrt{\int_0^{\max(t_k)} \left| vs(t) \right|^2 dt} \tag{3}$$

where is the norm of L^2 space.

The time-histories of vibration values are real signals. For such signals, the adjugated signal is equal to the primary signal. Thus, the normalized function of mutual correlation of the recorded vibration time-histories can be expressed as [10]

$$\alpha'_{vs_i, vs_j}(\tau) = \frac{\left(\int_0^{\max(t_k)} vs_i(t)\Big|_{t_0}^{t_k} \cdot vs_j(t-\tau)\Big|_{t_0}^{t_k} dt \right)^2}{\int_0^{\max(t_k)} vs_i(t)\Big|_{t_0}^{t_k}{}^2 dt \cdot \int_0^{\max(t_k)} vs_j(t)\Big|_{t_0}^{t_k}{}^2 dt} \tag{4}$$

Above, the measure of signal similarity defines the distance in L^2 space between the time-histories depending on their relative shift along the time axis. The aim of the analysis of the recorded time-histories is to define a measure of their distance in space L^2. However, this measure should increase along with an increase in the distance of signals. For this reason, expression (5) was accepted as a measure of the distance [33].

$$\delta(vs_i, vs_j) = 1 - \max(\alpha'_{vs_i, vs_j}(\tau \in [-t_k, t_k])) \tag{5}$$

where $\delta(vs_i, vs_j)$ is the distance between signals vs_i and vs_j in space L^2, and α'_{vs_i,vs_j} is the normalized mutual correlation function.

Randomly selecting one signal from each *PAS* subgroup to be the reference signal, the normalized mutual correlation function was calculated according to Eqs. (4, 5) as an additional characteristic of the recorded vibration time-histories.

According to the theory presented in [10], the characteristics were analysed in terms of concentration and unambiguity, using the following formulas:

$$CH_{CON} \Leftrightarrow \sigma_{CH(PAS)} \leq \overline{CH}(PAS) \cdot 0.15 \quad (6)$$

where CH_{CON} is the concentrated characteristic, $\sigma_{CH(PAS)}$ is the standard deviation of the characteristic *CH*, and $\overline{CH}_{(PAS)}$ is the mean value of the characteristic *CH* calculated from PAS group of signals.

$$CH_{UE} \Leftrightarrow \{CH \in CH_{CON} \wedge \sigma_{CH(PAS_{IA})} + \sigma_{CH(PAS_A)} \leq \left|\overline{CH}(PAS_{IA}) - \overline{CH}(PAS_A)\right|\} \quad (7)$$

where CH_{UE} is the unambiguous characteristic, CH_{CON} is the concentrated characteristic, $\sigma_{CH(PAS)}$ is the standard deviation of the characteristic *CH* calculated from *PAS* group of signals, $\overline{CH}_{(PAS)}$ is the mean value of the characteristic *CH* calculated from *PAS* group of signals, PAS_{IA} is the *PAS* group of signals recorded on rotational systems being in inability state, and PAS_A is the *PAS* group of signals recorded on rotational systems being in ability state.

The deviation from the mean value in Eq. (6) was equal to 0.15. This value was obtained as a result of the studies conducted by the authors and described in detail in [10] and [27]. For this value, the highest efficiency of inability state identification was achieved.

Tab. 1. Results of concentration analysis of the normalized mutual signal correlation function

Measurement point	01	02	03	04	05	06
PAS groups – ability state	12	12	12	8	12	12
Concentrated PAS groups – ability state	10	11	12	8	10	10
PAS groups – inability state	12	12	12	8	12	12
Concentrated PAS groups – inability state	10	11	12	8	10	10
Concentrated PAS groups – total	83%	92%	100%	100%	83%	83%

The further analysis includes characteristics which meet the concentration and unambiguity condition to a relatively high degree. These were: signal energy, average power of signal, abscissa of the signal square gravity centre, signal square variance, and normalized mutual signal correlation function. In the case of the normalized mutual signal correlation function, an additional description should be made. Table 1 presents the results of the concentration analysis for the considered characteristic. It was established that the distance of signals, determined according to the value of the normalized mutual correlation function of the recorded vibration time-histories, meets the requirements of concentrated characteristics in more than 90% of the analysed cases. Therefore, despite the fact that the unambiguity condition is not fulfilled, this characteristic is also taken into further considerations.

FUZZY CLASSIFICATION OF VIBRATION SIGNALS

The selected characteristics determine a five-dimensional space, where each signal is expressed as a point and its coordinates are the values of the characteristics [26, 47, 48]. Detailed theoretical considerations about space formulation and industrial applications of the proposed approach can be found in the literature [28-32]. Although only concentrated and unambiguous characteristics were used as dimensions of the space of signals recorded during the industrial research, they form a cloud of points in space. In the cloud, regions of points related to the ability and inability states can be observed. In order to eliminate the problems arising from irregular and discontinuous distribution of the measured points in the space, elements of the theory of fuzzy sets are widely used [33, 35, 54]. Moreover, it was noticed that identification of regions is a similar issue to image recognition, where the fuzzy clustering implementation brings very good results [19, 24]. Therefore, the regions were considered fuzzy clusters and identified according to the fuzzy c-means (FCM) method [35].

Having analysed the signals, it was found that the dimension ranges of the formulated space varied significantly. Therefore, prior to identification of clusters, the maximum and minimum values were calculated for each dimension and on this basis the values of coordinates of each signal were normalized according to Eq. (8):

$$CH(vs_i) = \frac{CH(vs_i)}{\max(CH(VS)) - \min(CH(VS))} \quad (8)$$

where *VS* is the set of vibration signals, $max(CH(VS))$ and $min(CH(VS))$ are the maximum and minimum values of the characteristic *CH* of *VS*, respectively, vs_i is the vibration signal No. *i*, and $CH(vs_i)$ is the value of the characteristic *CH* of the vibration signal vs_i.

Due to normalization of coordinates, each dimension in the space has the same impact on the clustering process. In the first step of identification, the signals were divided into two groups. The first group consisted of 17792 signals recorded on systems being in ability state and 2854 signals recorded on systems being in inability state. This group, referred to as the learning set, was used in the cluster identification process. The second group consisted of 5670 signals collected on rotational systems being in ability state and 1386 signals on systems being in inability state. This group, called the testing set, was used to examine the quality of the misalignment identification method.

Next, the *FCM* method was performed using the learning set. This method requires three starting parameters to be set: the number of clusters (*cno*), the procedure termination condition parameter (ε), and the cluster fuzzifier (*q*), which is the parameter that controls how fuzzy the clusters will be. The higher it is, the fuzzier the clusters will be in the end. A large *q* results in smaller membership values, and hence, fuzzier clusters. In the limit $q = 1$, the memberships converge to 0 or 1, which implies a crisp partitioning. In the beginning, initial random values of the membership matrix were generated. This matrix defines the membership degree of each signal to a given cluster. Then, central points of the clusters are calculated according to Eq. (9):

$$c_{j,k} = \frac{\sum_{i=1}^{lvs} \mu_{i,j} \cdot CH_k(vs_i)}{\sum_{i=1}^{I} \mu_{i,j}} \tag{9}$$

where $c_{j,k}$ is the k-th dimension of cluster No. *j*, *lvs* is the number of signals *vs*, $\mu_{i,j}$ is the membership degree of *i*-th signal to cluster No. *j*, $CH_k(vs_i)$ is the value of *k*-th characteristic of the vibration signal vs_i, and vs_i is the vibration signal No. *i*.

Subsequently, the membership matrix values are recalculated according to formula Eq. (10):

$$\mu_{i,js} = \frac{1}{\sum_{j=1}^{cno} \left[\frac{\sqrt{\sum_{k=1}^{chno} (c_{js,k} - CH_k(vs_i))^2}}{\sqrt{\sum_{k=1}^{chno} (c_{j,k} - CH_k(vs_i))^2}} \right]^{\frac{2}{q-1}}} \tag{10}$$

where $\mu_{i,js}$ is the membership degree of *i*-th signal to cluster No. *js*, cno is the number of clusters, *chno* is the number of dimensions, *q* is the coefficient which defines the fuzziness of the cluster membership function, $c_{j,k}$ is the *k*-th dimension of cluster No. *j*, $CH_k(vs_i)$ is the value of *k*-th characteristic of the vibration signal vs_i, and vs_i is the *i*-th vibration signal.

Calculations were performed until the termination condition, described by formula (11), was fulfilled:

$$\sum_{j=1}^{cno} \sum_{i=1}^{lvs} \left| \mu_{i,j}(t) - \mu_{i,j}(t-1) \right| < \varepsilon \tag{11}$$

where $\mu_{i,j}$ is the membership degree of *i*-th signal to cluster No. *j*, *cno* is the number of clusters, *lvs* is the number of signals *vs*, *t* is the iteration number, and ε is the procedure termination condition parameter.

The termination condition parameter ε can have a value between 0 and 1. In the case of very complicated issues (coloured image processing) the used values range within 0.01–0.03. However, applications of higher values can be found in the literature as well [43]. Therefore, in order to decrease the calculation time, 10% of the maximal value of the termination condition parameter was used in the conducted research.

Tab. 2. Parameters of the cluster identification process

Signals collected on systems:	Number of clusters *cno*	Fuzziness coefficient of the cluster membership function *q*	Procedure termination condition parameter ε
in ability state	2	3	0.1
in inability state	2	2	0.1

Tab. 3. Cardinality and coordinates of the identified clusters

	Cardinality	Coordinates
Signals collected on system in ability state	8084.79	0.068;0.067;0.479;0.451;0.934
	9707.2	0.025;0.024;0.481;0.457;0.956
Signals collected on rotational systems in inability state	1026.88	0.176;0.175;0.484;0.459;0.979
	1827.12	0.078;0.077;0.482;0.458;0.983

Identification of clusters was performed a few times during the tests, with the use of different values of cluster numbers and different fuzziness coefficients of the membership function, in order to define the noise of signals and their spatial arrangement. The identification process parameters were accepted only when the cardinality of the weakest detected cluster was not lower than 30% of the cardinality of the strongest one:

$$\forall c_j \in C_{ident} : card(c_j) \geq 0.3 \cdot \max(card(C_{ident}))$$
$$card(c_j) = \sum_{i=1}^{lvs} \mu_{i,j} \tag{12}$$

where c_j is the cluster No. *j*, C_{ident} is the set of the identified clusters, $card(c_j)$ is the cardinality of cluster No. *j*, $max(card(C_{ident}))$ is the maximum value of the cardinality among the clusters from set C_{ident}, *lvs* is the number of signals *vs*, and $\mu_{i,j}$ is the membership degree of i-th signal to cluster No. *j*.

The values of starting parameters in the identification procedure are given in Table 2. They were used in the process of cluster determination in the learning set of signals. The cardinality values and coordinates of the obtained clusters are presented in Table 3.

IDENTIFICATION OF RELIABILITY STATES OF SHIPS

Finally, one cluster was identified for each *PAS* subgroup from the test set of signals, according to the *FCM* method. The identification procedure was identical to that described in the previous section by Eqs. (9-11). To fulfil the requirement that the identification process should be independent from the data under consideration, the termination condition

parameter ε and the cluster fuzzifiers q were equal to the values given in Table 2. The number of clusters *cno* for each *PAS* subgroup was set equal to one.

Next, the obtained clusters were analysed. The distance from the clusters identified for the set of signals collected on rotational systems being in ability state and the distance from the clusters identified for the set of signals collected on rotational systems being in inability state were calculated according to Eqs. (13,14).

$$d_{as}(ctst_{ls}) = \sum_{j=1}^{cano} \sqrt{\sum_{k=1}^{chno} (ca_{j,k} - ctst_{ls,k})^2} \tag{13}$$

where $ctst_{ls}$ is the cluster identified for the test set No. *ls*, das is the distance from clusters identified for signals collected on rotational systems in ability state, *cano* is the number of clusters identified for signals collected on rotational systems in ability state, *chno* is the number of dimensions, $ca_{j,k}$ is the *k*-th dimension of the ability state cluster No. *j*, and $ctst_{j,k}$ is the *k*-th dimension of the test cluster No. *j*.

$$d_{ins}(ctst_{ls}) = \sum_{j=1}^{cinno} \sqrt{\sum_{k=1}^{chno} (cin_{j,k} - ctst_{ls,k})^2} \tag{14}$$

where $ctst_{ls}$ is the cluster identified for the test set No. *ls*, *dins* is the distance from clusters identified for signals collected on rotational systems in inability state, *cinno* is the number of clusters identified for signals collected on rotational systems in inability state, *chno* is the number of dimensions, $cin_{j,k}$ is the *k*-th dimension of the inability state cluster No. *j*, and $ctst_{j,k}$ is the *k*-th dimension of the test cluster No. *j*.

If the distance between the test cluster and the ability state clusters was larger than that between the test cluster and the inability state clusters, then the signals of the analysed test cluster were interpreted as signals of a rotational system being in inability state:

$$d_{as}(ctst_{ls}) > d_{ins}(ctst_{ls}) \tag{15}$$

where $ctst_{ls}$ is the cluster identified for the test set No. *ls*, and d_{ins} and d_{as} are the distances from clusters identified for signals collected on rotational systems in inability or ability state, respectively.

Otherwise, they were interpreted as signals of the rotational system being in ability state. Table 4 collates the results of the testing set analysis. The presented results indicate that the efficiency of the analysed method is higher for signals collected from rotational systems being in ability state rather than for those which are in inability state. Comparing the efficiency of the proposed method with earlier works by the authors [10, 11, 18, 27], it can be observed that the efficiency of ability state identification is slightly lower but still relatively high (higher than 90%), whereas the efficiency of inability state identification is significantly higher. The overall efficiency of identification of rotational system non-coaxiality is higher than 82%.

Tab. 4. Results of the testing set analysis

Signals collected on rotational systems:	Number of signals tested	Number of signals identified as signals collected on rotational systems being in ability state	Number of signals identified as signals collected on rotational systems being in inability state
in ability state	5670	4536 (80%)	1134 (20%)
in inability state	1386	126 (9%)	1260 (91%)

CONCLUSIONS

On the basis of the carried out tests it can be concluded that the distance of signals determined according to the normalized mutual correlation function and the recorded time-histories can be considered as a feature which unambiguously identifies the reliability state of a drive shaft line. The identification of rotational system non-coaxiality with the use of fuzzy clustering makes it possible to formulate a conclusion that the application of signal energy, signal mean power, abscissa of the signal square gravity centre, signal square variance, and normalized mutual signal correlation function for this purpose is justified, which has been proved by using the analysed method. Its efficiency is 80% for signals collected from rotational systems being in ability state, and 91% for systems being in inability state.

The novelty of the presented work involves developing a new vibration signal measurement method belonging to a relatively small group of methods which do not require fault feature frequency calculations. The method is a new approach to the considered issue, where the implementation of artificial intelligence techniques in the form of elements of the theory of fuzzy sets brings pretty high efficiency of ability state identification.

The proposed method can become a universal tool to be used for analysing propeller system vibrations. Nevertheless, further research in this area is planned. One of its directions will be analysing the influence of the cluster membership function shape on the efficiency of ability state identification.

Finally, it needs to be highlighted that mechanical properties of the propulsion system of a given vessel largely affect its operational state and, subsequently, the ability to perform reliable, timely, safe and efficient operational tasks.

REFERENCES

1. Antoni J.: *Cyclic spectral analysis of rolling-element bearing signals: Facts and fictions*. Journal of Sound and Vibration 2007 (304), pp. 497–529.

2. Bianchi D., Mayrhofer E., Groeschl M., Betz G., Vernes A.: *Wavelet packet transform for detection of single events in acoustic emission signals*. Mechanical Systems and Signal Processing 2015, Vol. 64-65, p. 441–451.

3. Bielawski, P.: *Diagnostics of marine propeller shafts*. Journal of Polish CIMAC, 2011 Vol. 6 No. 2, pp. 31-40.

4. Borghesani P., Pennacchi P., Chatterton S., Ricci R.: *The velocity synchronous discrete Fourier transform for order tracking in the field of rotating machinery*. Mechanical Systems and Signal Processing 2014, 44, pp. 118-133.

5. Castejon C., Gomez M., Garcia-Prada J., Ordonez A., Rubio H.: *Automatic Selection of the WPT Decomposition Level for Condition Monitoring of Rotor Elements Based on the Sensitivity Analysis of the Wavelet Energy*. International Journal of Acoustic Vibration 2015, Vol. 20, Issue 2, pp. 95–100.

6. Coats M.D., Randall R.B.: *Single and multi-stage phase demodulation based order-tracking*. Mechanical Systems and Signal Processing 2014, 44, pp. 86–117.

7. Gang Tang, QinYang, Hua-Qing Wang, Gang-gang Luo, Jian-wei Ma: *Sparse classification of rotating machinery faults based on compressive sensing strategy*. Mechatronics 2015, Volume 31, pp. 60–67.

8. Girtler J.: *The semi-Markov model of the process of appearance of sea-going ship propulsion system ability and inability states in application to determining the reliability of these systems*. Polish Maritime Research 4(80) 2013, Vol 20, pp. 18–24.

9. Górniewicz I., Roman S.: *Mathematical Analysis for Physicians. Scientific*. Publishing Office of Nicolaus Copernicus University of Torun, Torun 2000.

10. Grządziela A., Musiał J., Muślewski Ł., Pająk M.: *A method for identification of non-coaxiality in engine shaft lines of a selected type of naval ships*. Polish Maritime Research 2015, 1(85) Vol. 22, pp. 65–71.

11. Grządziela A. Muślewski Ł.: *High quality simulation of the effects of underwater detonation impact*. Journal of Vibroengineering, 2013, Issue 1, Volume 15.

12. Gurr C., Rulfs H.: *Influence of transient operating conditions on propeller shaft bearings*. Journal of Marine Engineering and Technology, No. 12/2008, pp. 3–7.

13. Haining Liu, Chengliang Liu, Yixiang Huang: *Adaptive feature extraction using sparse coding for machinery fault diagnosis*. Mechanical Systems and Signal Processing 2011, 25 pp. 558–574.

14. Hongkai Jiang, Qiushi Cai, Huiwei Zhao, Zhiyong Meng: *Rolling bearing fault feature extraction under variable conditions using hybrid order tracking and EEMD*. Journal of Vibroengineering 2016, Vol. 18, Issue 7, pp. 4449–4457.

15. Izydorczyk J., Pionka G., Tyma G.: *Theory of Signals. Introduction*. II corrected and completed edition. HELION, Gliwice 2006.

16. Kostek R., Landowski B., Muślewski Ł.: *Simulation of rolling Bering vibration in diagnostics*. Journal of Vibroengineering, 2015, Issue 8, Volume 17.

17. Lal M., Riwari R.: *Multi-fault identification in simple rotor-bearing-coupling systems based on forced response measurements*. Mechanism and Machine Theory 2012, Vol. 51, pp. 87–109.

18. Landowski B, Pająk M, Żółtowski B, Muślewski Ł.: *Method of building a model of operational changes for the marine combustion engine describing the impact of the damages of this engine on the characteristics of its operation process*. Polish Maritime Research, 2017 no 4 (96), vol. 24, pp. 67–76.

19. Leski J. M.: *Fuzzy c-ordered-means clustering*. Fuzzy Sets and Systems 2016, 286, pp. 114–133.

20. Li B., Mo-Yuen C., Yodyium T., et al.: *Neural-network-based motor rolling bearing fault diagnosis*. IEEE Transactions on industrial electronics, 2000, 47(5): pp. 1060–1069.

21. Lin J., Zhao M.: *Dynamic signal analysis for speed-varying machinery: A review*. Scientia Sinica 2015, Vol. 45, Issue 7, pp. 669.

22. Liu Z.W., Wei G., Hu J.H., Ma W.S.: *A hybrid intelligent multi-fault detection method for rotating machinery based on RSGWPT*. KPCA and Twin SCM 2017, Vol. 66, pp. 249–261.

23. Liu Y., Yang G., Li M., et al.: *Variational mode decomposition denoising combined the detrended fluctuation analysis*. Signal Processing 2016, Vol. 125, Issue C, pp. 349–364.

24. Miin-Shen Y., Nataliania Y.: *Robust-learning fuzzy c-means clustering algorithm with unknown number of clusters*. Pattern Recognition 2017, 71, pp. 45–59.

25. Molland A.F.: *The Maritime Engineering Reference Book, A Guide to Ship Design, Construction and Operation*, Butterworth-Heinemann Oct. 13, 2011.

26. Muślewski Ł.: *Evaluation Method of Transport Systems Operation Quality*. Polish Journal of Environmental Studies, Vol. 18, No. 2A, Hard Olsztyn 2009.

27. Muślewski Ł., Pająk M., Grządziela A., Musiał J.: *Analysis of vibration time histories in the time domain for propulsion systems of minesweepers*. Journal of Vibroengineering, 2015 Issue 3, Volume 17, pp. 1309–1316.

28. Muślewski Ł., Pająk M., Landowski B., Żółtowski B.: *A method for determining the usability potential of ship steam boilers*. Polish Maritime Research 4(92) 2016 Vol. 23, pp. 105–112.

29. Pająk M.: *The space of a feature of a complex technical system*. Scientific Problems of Machines Operation and Maintenance, 2/2010, ITeE Radom 2010, pp. 31–41.

30. Pająk M.: *Types of the states space of complex technical systems*. Journal of KONES vol. 18 No. 3, Warsaw 2011, pp. 323–331.

31. Pająk M.: *The technical states' space in the modelling process of operation tasks of a complex technical system*. Maintenance Problems, 1/2014, ITeE Radom 2014, pp. 15–33.

32. Pająk M.: *Operation and service processes expressed in the technical states space of a system.* Maintenance Problems, 1/2016, ITeE Radom 2016, pp. 65–81.

33. Pająk M.: *Identification of the operating parameters of a complex technical system important from the operational potential point of view*. Institution of Mechanical Engineers Part I: Journal of Systems and Control Engineering, 2018 Issue 1, Volume 232 pp. 62–78.

34. Peng Wang , Taiyong Wang: *Energy weighting method and its application to fault diagnosis of rolling bearing*. Journal of Vibroengineering 2017, Vol. 19, Issue 1, pp. 223–236.

35. Piegat A.: *Fuzzy modelling and control*. EXIT, Warszawa 1999.

36. Rafiee J., Tse P.W., Harifi A., et al.: *A novel technique for selecting mother wavelet function using an intelligent fault diagnosis system*. Expert Systems with Applications 2009, 36, pp. 4862–4875.

37. Qiu H., Lee J., Lin J., et al.: *Wavelet filter-based weak signature detection method and its application on rolling element bearing prognostics*. Journal of Sound and Vibration, 2006 (289), pp. 1066–1090.

38. Ruqiang Yan R., Gao R.X., Chen X.: *Wavelets for fault diagnosis of rotary machines: A review with applications*. Signal Processing, 2014 (96), pp. 1–15.

39. Saidi L., Ali J. B., Bechhoefer E., Benbouzid M.: *Wind turbine high-speed shaft bearings health prognosis through a spectral Kurtosis-derived indices and SVR*. Applied Acoustics 2017, Vol. 120, pp. 1–8.

40. Shih M., Doctor F., Fan S., Jen K., Shieh J.: *Instantaneous 3D EEG Signal Analysis Based on Empirical Mode Decomposition and the Hilbert-Huang Transform Applied to Depth of Anaesthesia*. Entropy 2015, Vol. 17, Issue 3, pp. 928–949.

41. Stefański T.: *Steering Theory. Discrete Systems, Nonlinear Stochastic Processes, Static and Dynamic Optimization*. Kielce University of Technology, Tom II, Kielce 2001.

42. Szabatin J.: *Basics of Theory of Signals*. WKŁ, Warszawa 2007.

43. Taria L., Barala Ch., Kimab S.: *Fuzzy c-means clustering with prior biological knowledge*. Journal of Biomedical Informatics 2009, Volume 42, Issue 1, pp. 74–81.

44. Wang H.C., Chen J., Dong G.M.: *Feature extraction of rolling bearing's early weak fault based on EEMD and tuneable Q-factor wavelet transform*. Mechanical Systems and Signal Processing 2014, Vol. 48, pp. 103–119.

45. Wang T.Y., Chu F.L., Han Q.K., Kong Y.: *Compound faults detection in gearbox via meshing resonance and spectral kurtosis methods*. Journal of Sound and Vibration 2017, Vol. 392, pp. 367–381.

46. Wang Y.X., Xiang J.W., Markert R., Liang M.: *Spectral kurtosis for fault detection, diagnosis and prognostics of rotating machines: A review with applications*. Mechanical Systems and Signal Processing 2016, Vol. 66–67, pp. 679–698.

47. Woropay M., Landowski B., Neubauer A.: *Controlling reliability in the transport systems*. B.P.E.-WIEM, Bydgoszcz–Radom 2004.

48. Woropay M., Muślewski Ł.: Quality in a systemic approach. ITeE, Radom 2005.

49. Wu G. W., Wang C. M., Bao J. D., et al.: *A wavelet threshold de-noising algorithm based on adaptive threshold function*. Journal of Electronics & Information Technology 2014, Vol. 36, Issue 6, pp. 1340–1347.

50. Xiaoming Xue, Jianzhong Zhou, Yanhe Xu, Wenlong Zhu, Chaoshun Li: *An adaptively fast ensemble empirical mode decomposition method and its applications to rolling element bearing fault diagnosis*. Mechanical Systems and Signal Processing 2015, 62–63, pp. 444–459.

51. Xiaoyun Gong, Wenliao Du, Anthimos Georgiadis, Baowei Zhao: *Identification of multi-faults in rotor-bearing system using spectral kurtosis and EEMD*. Journal of Vibroengineering 2017, Vol. 19 Issue 7, pp. 5036–5046.

52. Xi-hui Chen, Gang Cheng, Xian-lei Shan, Xiao Hu, Qiang Guo, Hou-guang Liu: *Research of weak fault feature information extraction of planetary gear based on ensemble empirical mode decomposition and adaptive stochastic resonance*. Measurement 2015, 73, pp. 55–67.

53. Yu Fajun, Fan Fuling, Wang Shuanghong, Zhou Fengxing: *Transform-domain sparse representation based classification for machinery vibration signals*. Journal of Vibroengineering 2018, Vol. 20, Issue 2, pp. 979–987.

54. Zerroukia A.A., Aifac T., Baddaria, K.: *Prediction of natural fracture porosity from well log data by means of fuzzy ranking and an artificial neural network in Hassi Messaoud oil field Algeria*. Journal of Petroleum Science and Engineering 2014, 115, pp. 78–89.

55. Zhang L. L., Zeng R.L., Jia J.D., et al.: *Engine fault diagnosis based on work-cycle order tracking spectrum and fuzzy c-mean clustering*. Automotive Engineering 2014, Vol. 36, Issue 8, pp. 1024–1028.

56. Zhang D.C., Yu D.J.: *Multi-fault diagnosis of gearbox based on resonance-based signal sparse decomposition and comb filter*. Measurement 2017, Vol. 103, pp. 361–369.

57. Zhao M., Lin J., Wang X., et al.: *A tacho-less order tracking technique for large speed variations*. Mechanical Systems & Signal Processing 2013, Issue 1, pp. 76–90.

58. Zhiquan Qi, Yingjie Tian, Yong Shi: *Robust twin support vector machine for pattern classification*. Pattern Recognition 2013, 46, pp. 305–316.

59. Zieliński T.P.: *Digital Processing of Signals. From theory to practice*. WKŁ, Warszawa 2009.

CONTACT WITH THE AUTHORS

Michał Pająk
e-mail: m.pajak@uthrad.pl

University of Technology and Humanities
Stasieckiego 54
26-600 Radom
Poland

Łukasz Muślewski
e-mail: l.muslewski@wp.pl

University of Science and Technology
Kaliskiego 7
85-796 Bydgoszcz
Poland

Bogdan Landowski
e-mail: bogdan.landowski@utp.edu.pl

University of Science and Technology
Kaliskiego 7
85-796 Bydgoszcz
Poland

Andrzej Grządziela
e-mail: A.Grzadziela@amw.gdynia.pl

Polish Naval Academy
Śmidowicza 69
81-103 Gdynia
Poland

sciendo

POLISH MARITIME RESEARCH 1 (101) 2019 Vol. 26; pp. 65-71
10.2478/pomr-2019-0008

THERMAL DEGRADATION PROCESS OF SEMI-SYNTHETIC FUELS FOR GAS TURBINE ENGINES IN NON-AERONAUTICAL APPLICATIONS

Jarosław Sarnecki
Tomasz Białecki
Bartosz Gawron
Jadwiga Głąb
Jarosław Kamiński
Andrzej Kulczycki
Katarzyna Romanyk
Air Force Institute of Technology, Warsaw, Poland

ABSTRACT

This article concerns the issue of thermal degradation process of fuels, important from the perspective of the operation of turbine engines, especially in the context of new fuels/bio-fuels and their implementation. The studies of the kerosene-based jet fuel (Jet A-1) and its blends with synthetic components manufactured according to HEFA and ATJ technology, were presented. Both technologies are currently approved by ASTM D7566 to produce components to be added to turbine fuels. Test rig investigations were carried out according to specific methodology which reflects the phenomena taking place in fuel systems of turbine engines. The mechanism of thermal degradation process was assessed on the basis of test results for selected properties, IR spectroscopy and calculation of activation energy. The results show that with the increase of the applied temperature there is an increment of the content of solid contaminants, water and acid for all tested fuels. Thermal degradation process is different for conventional jet fuel when compared to blends, but also semi-synthetic fuels distinguished by different thermal stability depending on a given manufacturing technology.

Keywords: gas turbine engine, thermal stability, bio-fuels, thermal degradation process

INTRODUCTION

Gas turbine engines are currently used in many transport fields. Most commonly they are used to power modern aircraft, i.e. passenger and jet aircraft as well as helicopters. In spite of the broad application in aviation, they can be used as propulsion for power generating sets or stationary peak power plants. Besides, gas turbines become an alternative to conventional engines used in ships. Merchant ships are usually equipped with self-ignition engines and their important drawback is considerable size and mass. Gas turbines are characterized by high power in relation to their mass and have the possibility to operate with different types of fuels. Thus, this kind of propulsion is frequently applied in high-speed military ships (chasers, destroyers, motor torpedo boats) and luxurious cruise ships [1].

Current data show that worldwide there are used approximately 700 ships powered with gas turbines [2], and most of them are military ships. In the Polish Navy, only two ships are provided with such drive units: the patrol ship ORP 'Ślązak' and rocket frigate ORP 'Gen. K.Pułaski' (FFG 7).

The principle of a single - fuel policy (introduced by NATO countries) assumes use of one fuel (F-34, kerosene-based jet fuel) by aircraft, vehicles and military ground equipment during warfare [3]. As the same principle can be applied in the navy (single naval fuel), the studies were performed [4] to define potential problems.

The engines used in land, maritime and air transport from decades are designed to burn conventional fuels, i.e. hydrocarbon. In the last decades however a substantial development of bio-fuels (fuels produced from biomass) can be observed. The reason is necessity to reduce the emission

of carbon dioxide (global warming). Previously, bio-fuels were dedicated only to automotive, but constant growth of air transport, observed in the last decade, led to the intensification of works to introduce bio-fuels in aviation. Additionally, the Regulations On Energy Efficiency for Ships in MARPOL Annex VI implemented in 2013 resulted in intensified search for alternative energy sources also in this transport branch [5].

Conventional fuels, including fuels for turbine aircraft engines, are in fact a blend of different (above 1000) hydrocarbons. Physicochemical and operational properties of fuels are not only due to the properties of particular hydrocarbons, but the relations of their concentrations and mutual impacts. It was observed that when small amount of new hydrocarbons is added to conventional fuel (10–50% (V/V)), it significantly disturbs these relations and consequently leads to the change of many operational properties of composed fuel. It was found that the chemical composition of synthetic hydrocarbon components has a significant influence on the properties of fuels, determining the failure-free operation of engine supply systems. Chemical composition and the properties of synthetic components of fuels depend on manufacturing technology. Feedstock from which these components are produced affects chemical composition and consequently also properties of final synthetic blends.

Currently, fuels containing synthetic hydrocarbons are approved for application in turbine aircraft engines. ASTM D7566 [6] allows to add up to 50% synthetic components to conventional fuel to supply turbine engines. The procedure and certification path of new fuels for aviation are described in [7].

The results from tests of different technologies of biofuels and their application in turbine engines, especially to be used in the aviation sector as well as maritime industry, can be found in many publications [8-13].

One of the essential aspects in the context of operation of turbine engines is thermal degradation of fuels. It occurs in the hot section of the fuel supply system and in combustion chamber. Deposits formed in fuel pipelines, injectors and combustion chamber [14] affect stability and kinetics of combustion process, which may cause failures in the engine's hot section, especially the combustor region. To sum up, the forming of deposits negatively affects operation process of turbine engines and thermal conductivity in aircraft systems.

Current large engines maximize the available heat sink capacity of the fuel system. Increased thermal loads, in connection with currently used fuel, cause different operational problems and reduce life and reliability. In order to absorb additional heat produced by future VHBR engine, acceptable temperatures of fuel system have to be increased and future fuel must be thermally optimized to increase its heat sink potential.

The reason of thermal stability importance is that actually used gas turbine engines as well as those planned for production in the future use jet fuel as their primary heat sink. Commercial jet aircraft uses fuel as a heat sink for cooling avionic and hydraulic systems. After absorbing heat, only a fraction of the fuel is burnt, and the rest is recycled back into the fuel tanks to undergo the heat exchange processes. As jet fuel during aircraft operation is subjected to high heat loads (very low temperatures in wing fuel tanks and fuel pipelines, high temperatures in heat exchangers, very high temperatures in fuel nozzles), it undergoes thermal stress and degrades. Actually more and more aircraft systems require intensive cooling, so the need to increase jet fuel "thermal capacity" is a critical factor.

The objective of the studies was to analyze the effects of changes of a hydrocarbon composition of fuel for turbine engines (by adding bio-components) on the mechanism and intensity of thermal degradation of these fuels.

FUEL SAMPLES

For the tests blends of jet fuel and synthetic hydrocarbons approved to be used in aviation turbine engines were used. To prepare those blends, necessary components were selected in compliance with the ASTM D7566. The major component of each blend was a commercial jet fuel (kerosene type Jet A-1) from Merox technology. The other components were synthetic hydrocarbons obtained from hydro-processed esters and fatty acids (HEFA) and alcohol-to-jet (ATJ) technologies. The quantitative selection of components for the preparation of blends involved the usage of maximum allowable contents of synthetic hydrocarbons in jet fuel. The composition of tested fuels is presented in Tab. 1.

Tab.1. Composition of tested fuels

Fuel	Composition [%(V/V)]		
	Jet A-1	HEFA	ATJ
Jet	100	–	–
Jet/HEFA	50	50	–
Jet/ATJ	50	–	50

TEST RIG AND PROCEDURE

To conduct a simulated thermal degradation process of fuels, a specially built test rig was used, which was worked-out as a part of the research project No. DEC-2011/01/D/ST8/06567 funded by the National Science Centre. The project of the non-standard test rig was developed to be a tool for studying thermal degradation of fuels, due to the emerging problem of correlation between the results collected by using the ASTM D3241 method dedicated for this purpose [15], and direct observation in operation.

On this test rig, oxidation and thermal degradation processes occur under certain conditions during the flow of fuel through the system. The fuel sample is re-pumped through subsequent component parts of the set, moving through its fundamental part, a sand bath with precisely controlled working temperature. The intensity of destruction processes depends on the value of the selected temperature

in the sand bath and the duration of its influence on fuel. Exposure time (presence of the portion of fuel in hot section) is controlled by changing the fuel flow speed.

The general view of the test rig is shown in Fig. 1, and its more detailed description is provided in [16].

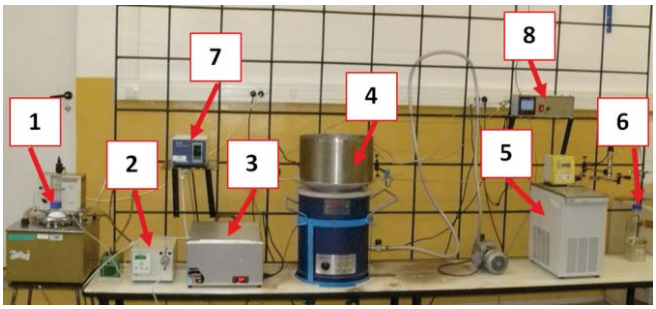

Fig. 1. General view of the test rig: 1. vessel with the tested sample, 2. fuel pump, 3. water bath, 4. sand bath, 5. cooling thermostat, 6. vessel for the tested sample, 7. temperature controller in the sand bath, 8. recorder

To conduct the thermal degradation process of the samples of fuels the following conditions were established:

1. Constant pressure value in test rig : 3.5 MPa – such pressure value occurs in fuel systems of modern aircraft.
2. Temperatures of the sand bath: 300°C and 500°C – the values reflect the thermal degradation of fuel (Fig. 2).
3. Constant value of the fuel flow rate: 3.0 ml/min – it ensures the identical thermal impact on the fuel under investigation.

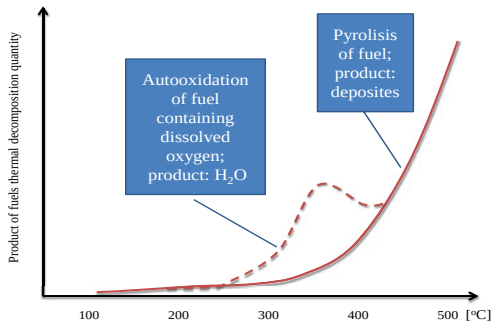

Fig. 2. Thermal degradation process of aviation fuels

As the first step, all fuel samples were prepared by filtering them through 0.8 µm membrane filters to remove contaminants. Then they were thermally stressed on the test rig (Fig. 1), and after that selected properties were checked, according to Tab. 2.

Tab. 2. Selected properties and test methods

Property	Test method
Solid contaminants	ASTM D 5452
Water content	PN-EN ISO 12937
Acid number	ASTM D 3242

The principal sign of thermal degradation of fuel is the formation of solid contaminants (products from the degradation process) and the increase of acid number. As a result, increased water content (a product of oxidation reaction derived from the dehydrogenation of hydrocarbons) can be observed. The analysis of the above mentioned parameters allows to evaluate changes in the fuel, resulting from the thermal stressing.

The IR (infrared) spectrometry was applied to monitor changes of chemical composition caused by fuel thermal stressing. For this purpose FT-IR Nicolet iS10 spectrometer was used. IR spectra were obtained with transmission method by using a variable path-length cell (VPL). The range of the spectrum was 4000-400 cm^{-1}. The spectral research was conducted with samples before and after the thermal stressing process in given experimental conditions.

RESULTS AND DISCUSSION

The influence of thermal stressing conditions on selected properties of investigated fuels is presented in Tab. 3.

Tab. 3. Conditions for bench tests and results of fuel tests

Property	Fuel								
	Jet			Jet/HEFA			Jet/ATJ		
	not stressed	thermally stressed		not stressed	thermally stressed		not stressed	thermally stressed	
Conditions during bench tests									
Test temperature, [°C]	–	300	500	–	300	500	–	300	500
Flow speed, [ml/min]	–	3.0	3.0	–	3.0	3.0	–	3.0	3.0
Pressure, [MPa]	–	3.5	3.5	–	3.5	3.5	–	3.5	3.5
Selected test results									
Solid contaminants, [mg/l]	0.30	5.05	6.98	0.40	3.82	4.39	1.06	5.36	7.48
Water content, [mg/kg]	71.3	126.1	162.1	66.3	95.8	160.5	68.6	88.6	149.0
Acid number, [mg KOH/g]	0.002	0.007	0.020	0.001	0.007	0.009	0.002	0.008	0.018

The analysis of the obtained results clearly shows that there are differences in the thermal degradation process between conventional jet fuel (Jet) and semi-synthetic fuels (Jet/HEFA and Jet/ATJ). For all tested fuels thermal impact causes the same direction of changes in selected properties, i.e. with the increase of the test temperature, there is an increase of the content of solid contaminants, water and acid number. However, the intensity of the changes is different for neat kerosene-based fuel and semi-synthetic fuels. Besides, by analyzing the results only for semi-synthetic fuels, the discrepancies are visible in the course of thermal degradation process depending on the selected technology for manufacturing a synthetic component (different results for different blend).

The above observation allows to formulate a conclusion that though all investigated fuels are approved for use in turbine engines, depending on the technology of bio-component production, thermal impact leads to the degradation of fuel with different intensity. Thermal degradation process is dependent on the chemical composition and properties of a given fuel. This process may be different and have various effects in the current operation of turbine engines depending on the type of applied fuel.

The studies with IR spectroscopy method started with making spectra of neat components, i.e. Jet, HEFA and ATJ. Among the mixture of various hydrocarbons found in Jet, the infrared analysis showed n-paraffins and aromates, HEFA was defined as n-paraffins and ATJ as iso-paraffins. Next, spectra of the tested fuel blends were recorded before and after passing through the test stand. Analyzing the obtained spectra, three bands were identified, where changes indicating the progressing thermal degradation process were visible. Band 1641 cm^{-1} is characteristic for stretching vibrations C=C in alkenes, band 1607 cm^{-1} appears as a result of skeletal vibrations causing the extension of bond C=C inside the ring in aromatic hydrocarbons, and band 909 cm^{-1} originates from wagging vibrations =C–H in alkenes with the double bond at the end of the molecule. For the mentioned bands, qualitative changes were depicted in the form of spectra and quantitative changes, as surface areas below the peak before and after the studies. The surface area was calculated with the integration method, limited by a baseline and absorption curve.

The emergence of bands typical for alkenes indicates that as a result of thermal stressing, hydrocarbon chains are broken, and double bonds are formed. Besides, the accumulated results confirm that in all cases there is an increase of intensity for a band with maximum by 1607 cm^{-1} derived from aromates. For bands derived from alkenes, significant and observable changes in IR spectra occur only at 500°C, where the reactions of thermal decomposition (pyrolysis) took place, but the changes detected for the band derived from aromates, developed equally intensively already in the first stage (Fig. 3 and Fig. 4). The observed changes are not significant, but they show the trend of destruction processes, the intensity of which is significantly dependent on the added components.

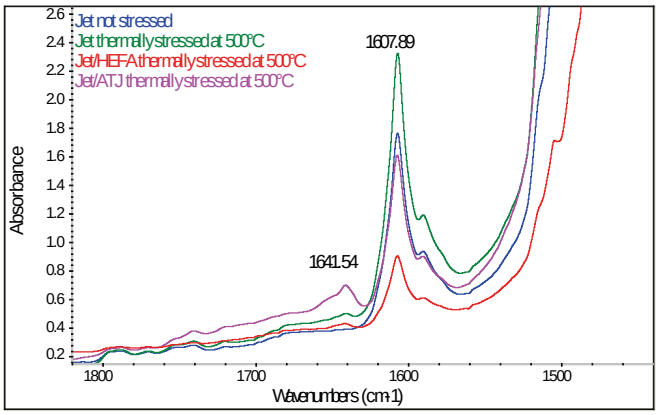

Fig. 3. IR spectra in the range 1800-1450 cm^{-1} for the tested mixtures after the thermal degradation process at 500 ° C and the IR Jet A-1 spectrum before the test

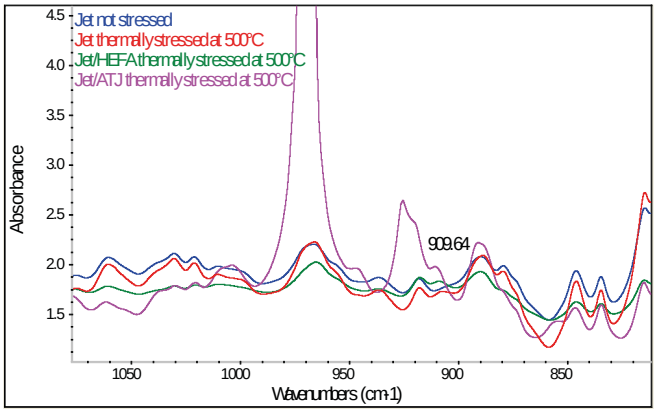

Fig. 4. IR spectra in the range 1100- 800 cm^{-1} for the tested mixtures after the thermal degradation process at 500 ° C and the IR Jet A-1 spectrum before the test

The research outcomes of IR spectra prove that engine fuels are susceptible to degradation to a varying degree, depending on their chemical composition. It is due to the general mechanism of chemical reactions that contribute to the formation of solid contaminants [17, 18, 19, 20, 21].

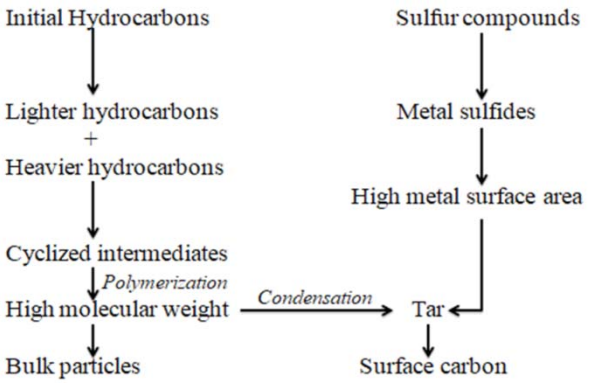

Fig. 5. Diagram of thermal degradation reaction chains, acc.[17]

In high temperature (>350°C), two processes are dominant: distribution of hydrocarbons which are broken down to

carbon and hydrogen or polymerization/condensation of hydrocarbons which are broken down to poly-nuclear aromatic hydrocarbons, from which carbonated deposits are created.

The first of the processes is catalyzed by the surfaces of metals, with which the fuel comes in contact within the hot section of the supply system. The second mechanism, polymerization, is usually a non-catalytic reaction.

The analysis of results compiled in Tab. 4 enables to observe that the changes occurred with different speed depending on the content of the fuel, what was also discovered based on physicochemical studies. The band characteristic for stretching vibrations C=C in alkenes (1641 cm^{-1}) for Jet/ATJ is noticed as post-production impurity already prior to subjecting it to the degradation process. The surface area of this peak for Jet/ATJ after the process in 500°C is ten times bigger comparing to Jet. From the analysis of the spectra, it can be stated that the most stable sample was Jet. For its strongest resistance to thermal degradation are responsible hydrocarbon chains that are n-paraffins and the increased amount of aromates, when compared to the other two blends. Jet/ATJ blend turned out to be the least stable due to presence of iso-paraffins derived from synthetic component.

Tab. 4. Surface area under the peak for bands, where changes were noticed after the thermal degradation processes, for tested fuels.

Fuel	Surface area under the peak		
	1641 cm^{-1} band	1607 cm^{-1} band	909 cm^{-1} band
Jet not stressed	0	24.67	0
Jet thermally stressed at 300 °C	0	28.46	0
Jet thermally stressed at 500 °C	0.26	33.07	0.19
Jet/HEFA not stressed	0	7.20	0
Jet /HEFA thermally stressed at 300 °C	0	11.33	0
Jet/HEFA thermally stressed at 500 °C	0.33	8.40	0.21
Jet/ATJ not stressed	0.16	15.75	0
Jet /ATJ thermally stressed at 300 °C	0.17	15.90	0
Jet /ATJ thermally stressed at 500 °C	2.62	17.79	0.60

On the basis of the research results presented in Tab. 4 it can be stated that:

- water is the oxidation product of hydrogen removed during the formation of olefins from saturated hydrocarbons (n-paraffins and iso-paraffins); these reactions occur at temperature above 300°C and belong to reactions catalyzed by conduits' surfaces, through which the fuel is pumped;
- solid contaminants are products of non-catalytic reactions of condensation of hydrocarbons broken down to poly-nuclear aromatic hydrocarbons.

For all examined samples the dependence was observed between the surface area of the peak 1607 cm^{-1} and the content of solid contaminants. It enables to link the increase of the number of aromatic rings in fuels after thermal degradation with the amount of solid contaminants formed during degradation. This regularity was observed both for the process conducted at the temperature of 300°C as well as at 500°C. It allowed to state that for all examined fuels the mechanism of reaction of thermal degradation is the same at the temperature of 300°C and 500°C. As per the results of the measurement of the amount of deposits, the value of the activation energy of reaction leading to the formation of solid contaminants can be calculated.

Assuming that reactions of thermal destruction of fuel are first-order reactions relative to the final product, the kinetic equation of the thermal destruction process of fuel takes the following form:

$$V_{product} = d\,c_{product}/dt \quad (1)$$

$$V_{product} = k\,c_{product} \quad (2)$$

where: $V_{product}$ – reaction rate, $c_{product}$ – concentration of reactions product, k – reaction rate constant, t – time.

After the integration between c_0 and c_t, and assuming that $t_0 = 0$ and $t = V/v_w$, where:
V – volume of the pumped fuel,
v_w – speed of fuel flow,
$c_{product}$ – concentration of the product.

$$k = [(\ln c_{product}) - (\ln c_{product0})]v_w/V \quad (3)$$

Applying relation (3) and introducing $c_{product}$ as the acid value, the amount of deposits and the water content, the values of the rate constant of thermal degradation reaction was calculated for the investigated fuels.

These values were calculated for both temperatures under which the thermal degradation process was carried out: 500°C and 300°C. Using the Arrhenius equation:

$$k = A\exp(-E_a/RT) \quad (4)$$

where: E_a - activation energy, R – gas constant, T – temperature.

And the values of the rate constant of reactions for the reaction of thermal degradation of fuel at temperature of 500°C and 300°C, the E_a values were calculated for each of the examined fuels, as follows:

$$\ln k = \ln A - Ea/RT \quad (5)$$

$$\ln k_{500} - \ln k_{300} = E_a/R(-1/773+1/573) \quad (6)$$

$$E_a = R(\ln k_{500} - \ln k_{300})/(-1/773+1/573) \quad (7)$$

The results were shown in Tab. 5. It is worth to highlight that the obtained absolute values of activation energy shall not be analyzed: the content of solid contaminants is not expressed in units of concentration. Thus, the results illustrated in Tab.5 are indicative, enabling to compare the mechanism of thermal degradation of fuel containing different synthetic components.

Tab. 5. Activation energy of thermal degradation reactions for tested fuels based on solid contaminants

Fuel	Activation energy [kJ/mol]
Jet	1.7
Jet/HEFA	1.3
Jet/ATJ	4.1

The presented results indicate that the introduction of synthetic hydrocarbon in the amount of 50 % (V/V) into conventional jet fuel results in the change of mechanism of reactions constituting a thermal degradation. The hydrocarbons obtained by HEFA technology do not substantially alter the mechanism of thermal degradation reaction when compared to the thermal degradation of Jet. ATJ hydrocarbons, however, significantly change the thermal degradation mechanism.

CONCLUSIONS

This work considered the intensity of the thermal degradation process of fuels used in turbine engines, containing synthetic components from HEFA and ATJ technology. The research results are summarized as follows:

1. For all tested fuels the thermal impact causes the same direction of changes of selected properties, associated with the products of the thermal degradation process. With the increase of the applied temperature, there is an increment of the content of solid contaminants, water and acid value. Nonetheless, the intensity of these changes is different for neat kerosene-based fuel and semi-synthetic fuels. There are also differences in the course of the thermal degradation depending on the selected technology of manufacturing a synthetic component.
2. Analysis with IR spectroscopy method confirmed the results for selected properties. The formation of bands characteristic for alkenes reflects the amount of formed water, and bands for aromates correspond to the amount of solid contaminants.
3. Calculated activation energy of reactions as a result of which solid contaminants are formed indicates the change of its mechanism due to the change of hydrocarbon composition of fuel.
4. Thermal degradation process is contingent upon the chemical composition and properties of a given fuel. It can proceed differently and exert various effects in the current operation of turbine engines depending on the used fuel.

The project has been funded by National Science Centre granted acc. the decision No. DEC-2011/01/D/ST8/06567

BIBLIOGRAPHY

1. Pawlak M., Kuźniar M.: *Determination of emission of noxious compounds in exhaust gas from naval gas turbine on the basis of emission characteristics of aircraft engine* (in Polish), Autobusy, No.12, pp. 345-350, 2017.
2. GE, *Building on a Marine Power Legacy*, 2017.
3. *NATO Logistics Handbook,* NATO Headquarters, Brussels, 2012.
4. Giannini R.M., Martin C.J., Strucko R.: *Single naval fuel at sea feasibility study – phase one. Naval Air Systems Command Fuels and Lubricants Division*, NAVAIRSYSCOM Report 445/02-004, 2002.
5. Cengiz D., Burak Z.: *Environmental and Economical Assessment of Alternative Marine Fuels*, Journal of Cleaner Production Vol. 113, No. 02, pp. 438-449, 2016.
6. ASTM D7566 *Standard Specification for Aviation Turbine Fuel Containing Synthesized Hydrocarbons,* 2018.
7. ASTM D 4054 *Standard Practice for Evaluation of New Aviation Turbine Fuels and Fuel Additives,* 2017.
8. Gawron B., T. Białecki T.: *Impact of a Jet A-1/HEFA blend on the performance and emission characteristics of a miniature turbojet engine,* International Journal of Environmental Science and Technology, Vol. 15, No. 7, pp. 1501-1508, 2018.
9. El Gohary M., Ammar N.R.: *Thermodynamic Analysis of Alternative Marine Fuels for Marine Gas Turbine Power Plants*, J. Marine Sci. Appl. Vol. 15, No. 1, pp. 95-103, 2016.
10. Chiong M. C., Chong C. T., Ng J.-H., Lam S. S., Tran M.-V., Chong W.W.F, Mohd Jaafar M.N., Valera-Medina A.,: *Liquid biofuels production and emissions performance in gas turbines: A review*, Energy Conversion and Management, Vol. 173, pp. 640-658, 2018.
11. Kołwzan K., Narewski M.: *Study on alternative fuels for marine applications*. Latvian Journal of Chemistry, Vol. 51, No. 4, pp. 398-406, 2012.
12. Hashimoto N., Nishida H., Ozawa Y.: *Fundamental combustion characteristics of Jatropha oil as alternative fuel for gas turb*ines, Fuel, Vol. 126, pp. 194-201, 2014.
13. Seljak T., Sirok B., Katrasnik T.: *Advanced fuels for gas turbines: Fuel system corrosion, hot path deposit formation and emissions*, Energy Conversion and Management, Vol. 125, pp. 40-50, 2016.

14. Spychała J., Kułaszka A., Giewoń J.: *Report No. 1/ AŁ-21F3/34/2011.*

15. ASTM D 3241 *Standard Test Method for Thermal Oxidation Stability of Aviation Turbine Fuels,* 2018.

16. Sarnecki J., Gawron B.: *A method of assessing the tendency of aviation fuels to generate thermal degradation products under the influence of high temperatures*, Journal of KONES, Vol. 24, No. 4, pp. 377-384, 2017.

17. Altin O., Eser S.: *Carbon deposit formation from thermal stressing of petroleum fuels;* Am. Chem. Soc., Div. Fuel Chem., Vol. 49, No. 2, pp. 764-766, 2004.

18. Carlisle H. W., Frew R. W., Mills J. R., Aradi A. A., Avery N. L.: *The effect of fuel composition and additive content on injector deposits and performance of an air-assisted direct injection spark ignition (DISI) research engine*. SAE paper, No. 2001-01-2030, 2001.

19. Osgood E., Mansker K.: *Performance Enhancing Diesel Additives,* Fuel Marketer News Magazine, pp. 24-26, 2014.

20. Stępień Z. - *Intake valve and combustion chamber deposits formation – the engine and fuel related factors that impact their growth*; NAFTA-GAZ, No. 4, pp. 236-242, 2014.

21. Pedley J. F., Hiley R. W., Solly R. K.: *Storage stability of petroleum-derived diesel fuel: 4. Synthesis of sediment precursor compounds and simulation of sediment formation using model systems; Fuel*, Vol. 68, No. 1, pp. 27-31, 1989.

CONTACT WITH THE AUTHORS

Jarosław Sarnecki
e-mail: jaroslaw.sarnecki@itwl.pl

Tomasz Białecki
e-mail: tomasz.bialecki@itwl.pl

Bartosz Gawron
e-mail: bartosz.gawron@itwl.pl

Jadwiga Głąb
e-mail: jadwiga.glab@itwl.pl

Jarosław Kamiński
e-mail: jaroslaw.kaminski@gmail.com

Andrzej Kulczycki
e-mail: andrzej.kulczycki@itwl.pl

Katarzyna Romanyk
e-mail: katarzyna.romanyk@itwl.pl

Air Force Institute of Technology
Księcia Bolesława 6
01-494 Warsaw
Poland

sciendo

POLISH MARITIME RESEARCH 1 (101) 2019 Vol. 26; pp. 72-81
10.2478/pomr-2019-0009

THE CFD METHOD-BASED RESEARCH ON DAMAGED SHIP'S FLOODING PROCESS IN TIME-DOMAIN

Hu Li-Fen[1]
Qi Huibo[1]
Li Yuemeng[2]
Li Wubin[1]
Chen Shude[1]
[1] Communications of Institute, Ludong University, Yantai, China
[2] Ulsan Ship and Ocean College, Ludong University, Yantai, China

ABSTRACT

The flooding process is one of the main concerns of damaged ship stability. This paper combines the volume of fluid (VOF) method incorporated in the Navier-Stokes (NS) solver with dynamic mesh techniques to simulate the flooding of a damaged ship. The VOF method is used to capture the fluid interface, while the dynamic mesh techniques are applied to update the mesh as a result of transient ship motions. The time-domain flooding processes of a damaged barge and a rectangular cabin model are carried out based on the abovementioned method, and the computational results appear compatible with the experimental data. During the flooding process, the motion of the flooding flow at different stages is observed and compared with that observed in real conditions. The time-domain research of the flooding process is the starting point for subsequent establishment of damaged ship's roll movement and capsizing the mechanism of dead ship condition in wave.

Keywords: flooding process; Bernoulli equation; time domain calculation; damaged ship

INTRODUCTION

Nowadays, ship damages caused by collision and grounding provide serious threat to their life and safety, and even to the environment. When the ship is damaged, water starts to flow through the created opening to the ship hull. Sometimes, the progressive course of flooding may take a very long time, and the intermediate flooding stages can be more dangerous than the final equilibrium state. Nowadays, the International Maritime Organization (IMO) has also requirements concerning the damaged ship stability during intermediate flooding stages (IMO, 2008). In this context, the simulation of the intermediate flooding process is of utmost importance for ship stability.

The time-domain based flooding simulation tools have been significantly developed during recent years (Santos, 2002; Vassalos, 2004; Ruponen, 2007&2012; Lee, 2007; Tiago, 2008&2009; Ypma, 2010; Schreuder, 2011; Lemoine, 2013). The available flooding investigation methods include: model test, quasi-static method based on Bernoulli equation, meshless method, Computational Fluid Dynamics (CFD) simulation based on Navier-Stokes equations, etc. The increased calculating capacity has made the time-domain simulation possible even for complex damage stability analyses (Ruponen, 2017; Manderbacka, 2015&2016).

This paper carries out the flooding simulation research based on Navier-Stokes equations and CFD technology. The magnitude and phase of the dynamic roll moment caused by the water in the compartment are investigated employing the six degrees of freedom motion solution and the dynamic mesh strategy. In the reported study, a solver which combines the NS equations with the Volume of Fluid (VOF) model was adopted to simulate the coupled motion of the damaged ship and floodwater. The progressive course of flooding is predicted using the time-domain flooding simulation method described in the article. The applied method is based on the law of conservation of mass and the Bernoulli equation. To test the applied method, the developed solver was used to investigate

the flooding process of a damaged barge and a rectangular cabin model. The numerical results were compared with the experimental data, and this comparison has proved that the adopted method can successfully simulate the interactive dynamics between the ship and floodwater, as well as predict the ship's floating position. All simulations were conducted on a core-processor (Intel Core2, 3.0GHz) server.

MATHEMATICAL MODEL

GOVERNING EQUATIONS OF FLUID MOTION

The incompressible flow of two different fluids (water and air) (Li, 2016) is considered. Based on this assumption, the differential forms of the NS equation and the continuity equation are as follows:

Continuity equation:

$$\frac{\partial \overline{u_i}}{\partial \overline{x_i}} = 0 \tag{1}$$

RANS equation:

$$\rho \frac{\partial \overline{u_i}}{\partial t} + \rho \overline{u_j} \frac{\partial \overline{u_i}}{\partial x_j} = -\frac{\partial \overline{p}}{\partial x_i} + \mu \frac{\partial^2 \overline{u_i}}{\partial x_j \partial x_j} - \rho \frac{\partial \overline{u_i' u_j'}}{\partial x_j} + \rho \overline{f_i} \tag{2}$$

In these equations, $\overline{u}_i$ is the dynamic viscosity $\rho \overline{u_i' u_j'}$, is the Reynolds stress, ρ is the density of fluid, v is the fluid viscosity, p is the pressure, $\rho=\alpha\rho_1+(1-\alpha)\rho_2$ is the effective density, ρ_1 and ρ_2 are the densities of water and air, respectively, $v=\alpha\mu_1+(1-\alpha)\mu_2$ is the effective viscosity, μ_1 and μ_2 are the viscosity of water and air, respectively, and α is the fluid volume fraction. Both fluids: water and air, are considered incompressible.

FREE SURFACE CAPTURING METHOD

The VOF (Gao, 2010) method is used to capture the free surface. This method is a surface tracking method fixed under the Euler grid. It simulates the multiphase flow model by solving the momentum equation and the volume fraction of one or more fluids. Within each control volume, the sum of the volume fractions of all the phases is 1. As to Phase q, its equation is:

$$\frac{\partial a_q}{\partial t} + \frac{\partial (u a_q)}{\partial x} + \frac{\partial (v a_q)}{\partial y} + \frac{\partial (w a_q)}{\partial z} = 0 \tag{3}$$

where a_1 and a_2 are, respectively, the volume fractions of air and water, and $a_q = 0.5$ is the air/water interface. q=0 means that the unit is filled with water, while q=1 means that the unit is filled with air. In the present study, the turbulence effect on the flows is not considered, and the laminar flow model is adopted in the simulations which will be discussed in Section 4.1.

GOVERNING EQUATIONS OF RIGID BODY MOTION

The rigid body motion can be evaluated from the following equations:

$$\frac{dP}{dt} = F$$
$$\frac{d\pi}{dt} = m \tag{4}$$

These equations explain that for a rigid body undergoing translation and rotation, the rate of change of the linear and angular momentum of the rigid body, P and π respectively, is equal to the applied force F and torque m acting on the body.

EQUATION OF PROGRESSIVE FLOODING

During the past decades, the time-domain flooding simulations have mainly been based on a hydraulic model, using the Bernoulli equation and conservation of mass. Nowadays, the simulation is already a well-established approach to study the details of a damage case and a valuable tool for accident investigations.

In the majority of damaged model investigations, the simple hydraulic model referred to as the orifice equation is used. This model can be drawn from the Bernoulli equation for steady flow (Lyu, 2015). For a streamline from point A in the damaged tank to point B in the outlet of the cross-duct, the Bernoulli equation can be written as:

$$\frac{1}{2g} v_1^2 + \frac{p_1}{\rho g} + h_1 = \frac{1}{2g} v_2^2 + \frac{p_2}{\rho g} + h_2 \tag{5}$$

Considering conservation of energy, the flow velocity at the damaged opening is:

$$v_2 = \sqrt{2g(h_1 - h_2)} \tag{6}$$

where v_2 is the flow velocity at the damaged opening, h_1 is the vertical distance between the extra waterline and the centerline of the damaged opening, h_2 is the vertical distance between the cabin waterline and the centerline of the damaged opening, and g is the acceleration due to gravity.

Considering the flooding process in the time domain, the volumetric flow through the opening with area A is:

$$t_{a11} = \int_0^v \frac{1}{C_d A \sqrt{2g(h_1 - h_2)}} dV \tag{7}$$

$$dV = Q \cdot dt = C_d A \sqrt{2g(h_1 - h_2)}\, dt \tag{8}$$

$$V = \sum dV \tag{9}$$

where Q is the flow rate through the opening at a given time, A is the area of the damaged opening, V is the volume of the flooding water, $t_{a||}$ is the summation of each time step, and C_d is the discharge coefficient which takes into consideration

waves, sloshing, etc. The flow rate Q is obtained by integration over the area of the opening.

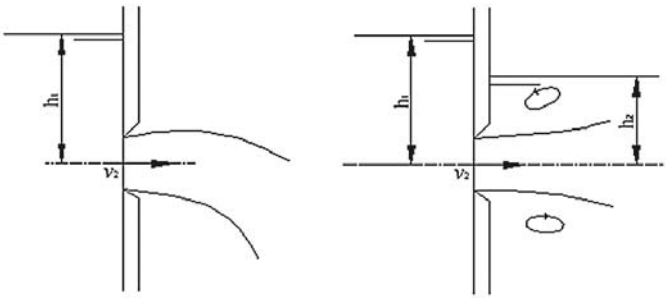

Fig. 1. Flow through the orifice

At each time step, the water levels in the flooded rooms are solved iteratively to satisfy the conservation of mass, and the flow velocities in the openings are solved by applying the Bernoulli theorem. A constant discharge coefficient 0.6 is used for all openings. The sea is assumed to be calm and the ship motions are considered to be fully quasi-stationary.

NUMERICAL METHOD

The equations (1)-(3) are analyzed using the finite volume method to simulate the fluid field. The SIMPLE algorithm is employed in the pressure-based solver, which is mainly used for incompressible fluid fields. For the coupling movement during the flooding process, this paper adopts a six degrees of freedom solver and the dynamic mesh strategy with rigid boundaries.

DYNAMIC MESH STRATEGY

As the surface is part of the boundary of the fluid, it is necessary to dynamically update the grid according to the geometric change of the fluid domain caused by the body motion during the calculation process. In the paper, the dynamic mesh strategy is applied to update the mesh. By means of this strategy, the mesh is automatically deformed, including changes of the region boundary geometry, at the same time keeping its topology constant. The computational domain contains floodable compartments and the external flow region near the damaged section of the ship, as shown in Fig. 2. The computational domain is divided into three regions, labelled as region 1, region 2 and region 3. Region 1 experiences the same translational and rotational motion as the body, and, consequently, the mesh of this region could be shifted without geometrical and topological changes, which includes ship hull and adjacent hull part. Using this strategy, the optimum mesh quality is maintained during the calculation. Region 2 is the buffer, in which the mesh is automatically deformed following the change of the region boundary geometry, while keeping its topology constant. Region 3 is the fixed region, in which the mesh is kept static throughout the simulation. This approach makes it easier to meet specific boundary conditions along the outer boundaries.

CONVERGENCE JUDGEMENT

The time step adopted in this paper is assumed to meet the cell Courant number C (Li, 2016) within a limit value of 10.

$$C = \Delta t \Big/ \min(\Delta x / u) \leq C_{\lim} \tag{10}$$

where: Δt is the time step, Δx is the mesh spacing, u is the inflow velocity, and C is the cell Courant number, which is used here to coordinate the mesh size and the time step. When C is larger than 10, the calculation is easy to diverge and fail to provide a result. That is why the values of the mesh size and the time step have to be selected in a proper manner suitable for the calculation to be performed.

The time step is adjusted according to $C_{\lim}$. Three different $C_{\lim}$ values: 0.25, 0.5, 0.75 were investigated in terms of their influence on the flooding problem. The flooding profiles obtained from these calculations are compared in Fig. 3.

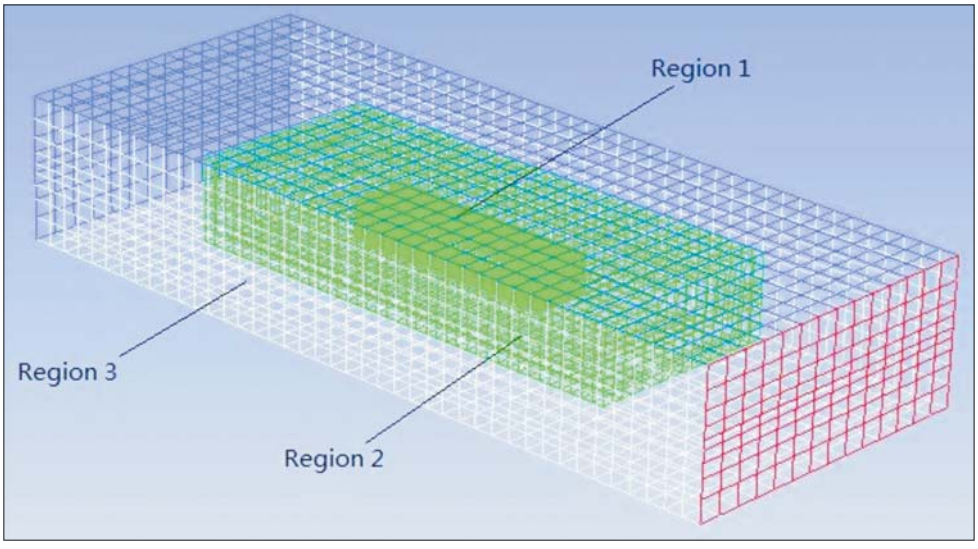

Fig. 2. Diagram of the computational domain

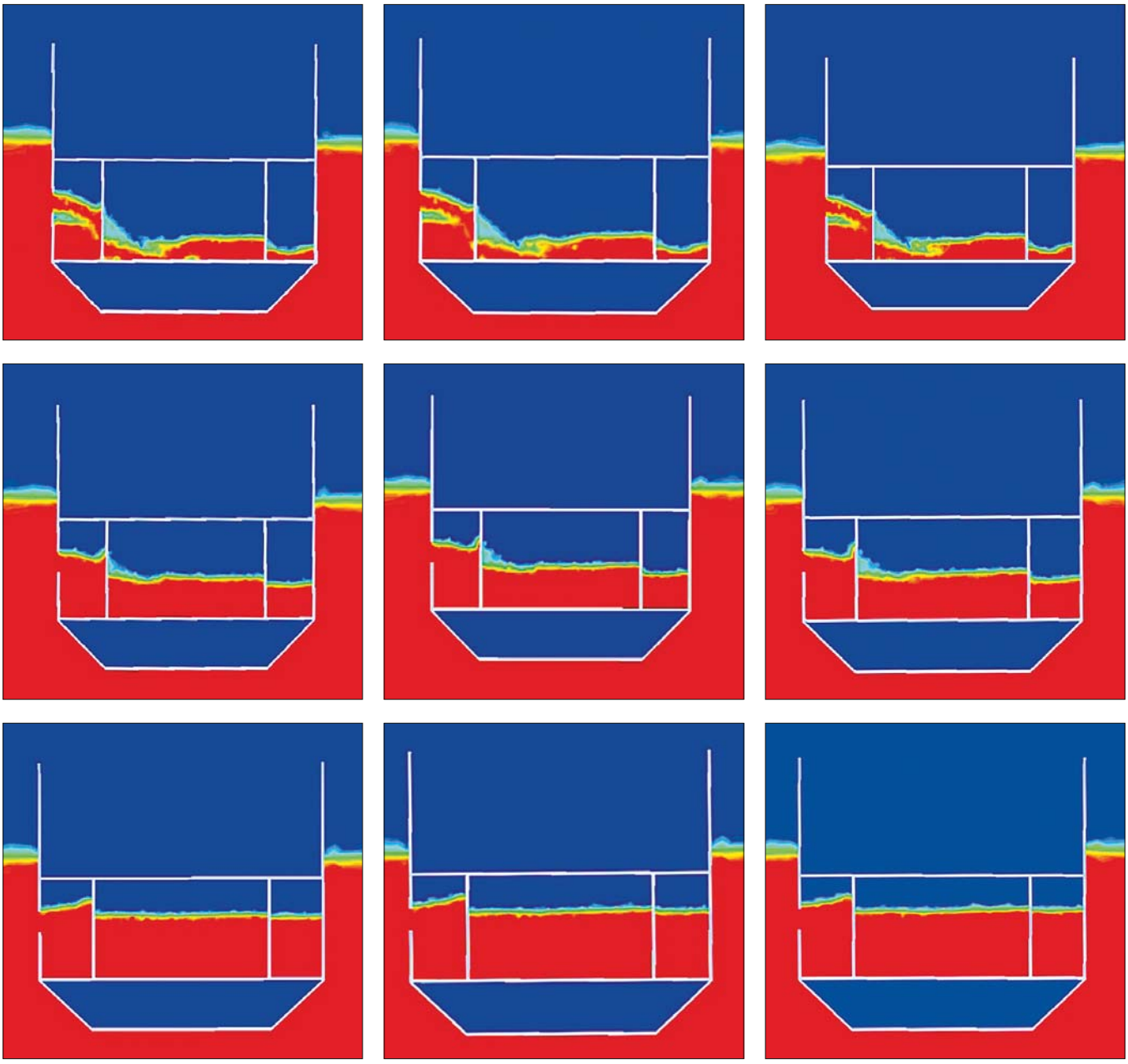

Fig. 3. Flooding process (t=5s, 10s, 15s) with different C_{lim} values (left: 0.25, mid: 0.5, right: 0.75)

When the floodwater reaches the opposite side of the compartment, the flow becomes violent. However, even in that case, there is still good consistency in the motion of floodwater for these three C_{lim} values. The results show that the case C_{lim}=0.5 consumes relatively little computational resources, while still ensuring feasible numerical accuracy. Therefore, the limiting cell Courant number equal to 0.5 will be used throughout the simulation.

Normally, time steps between 0.001s and 5s are used in flooding simulations (Gao, 2012&2013; Ruponen, 2014), to coordinate with the mesh size. This paper adopts the time step of 0.005s to minimize the computation time, while preserving an acceptable accuracy. The flow calculation chart is shown in Fig. 4.

NUMERICAL RESULTS

FLOATING BARGE FLOODING CASE

This paper adopts the box-shaped barge model to verify the model test results of the flooding process. Ruponen (Ruponen, 2006) analyzed experimentally a series of model tests for a damaged barge in calm water, in order to provide experimental data for verification of numerical tools. The arrangement of the compartments in the barge is shown in Fig. 5, and its main particulars are provided in Table 1. The connection hole dimensions are listed in Table 2.

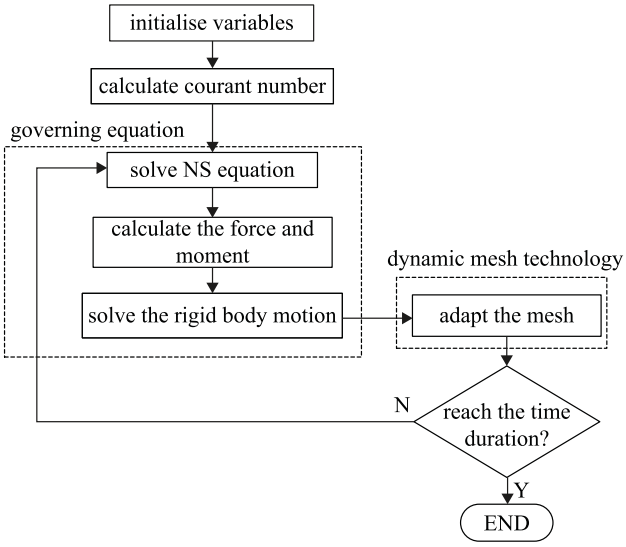

Fig. 4. Flow calculation chart

Tab. 1. Main data of the barge

Parameter	Dimension
Length of all (Loa) (m)	4.00
Breadth (B) (m)	0.80
Depth (D) (m)	0.80
Draft (T) (m)	0.50
Center of gravity above base line (KG) (m)	0.278
Displacement (Δ) (m)	1447.39
Length of tank (m)	0.7
Breadth of tank (m)	0.8
Height of tank (m)	0.8
Moment of inertia along x-axis(Ixx) (kg m^2)	176.0
Moment of inertia along y-axis(Iyy) (kg m^2)	2235.3
Moment of inertia along z-axis(Izz) (kg m^2)	2209.4

In Table 2, DB1-DB2 means the hole between tanks DB1 and DB2. The hole is round, and its diameter is 20mm. DB2-R21 means the hole connecting tanks DB2 and R21. It is rectangular, and its dimensions are 60*40. The following expressions are similar. The floodwater motion in the compartment is the key to the flooding process. The prediction accuracy significantly depends on the number of grid elements. In this paper, the appropriate size of mesh enables to keep the Courant number below the limit of 10. The number of elements is listed in Table 3.

Considering the oscillation of the real flow field, in order to compare changes of the mass flux at the damaged opening during the initial flooding stage, three models: the standard k -ε model, the RNG k-ε model, and a simple laminar model have been adopted. Fig. 6 shows the time-history of mass flux change at the damaged opening. At the initial stage, the mass flux at the damaged opening increases quickly, and the tendency of changes presented by the three investigated models is similar. Compared with the other two models, the use of the simple laminar model can ensure

Tab. 2. Main particulars of the barge model

Location of tank	Connection hole dimension (mm)
DB1-DB2	D=20 (round hole)
DB2-R21	60*40
R21-R21S	20*200
R21-R21P	20*200
R21-R11	D=20 (round hole)
R21-R22	100*100
R11-R12	100*100
R12-R22	80*200

Tab. 3. Number of grid elements in different domains

location	region 1			region 2	region 3
	eight cabins	enclosed cabin	adjacent hull		
number	556489	125623	934562	236320	95782

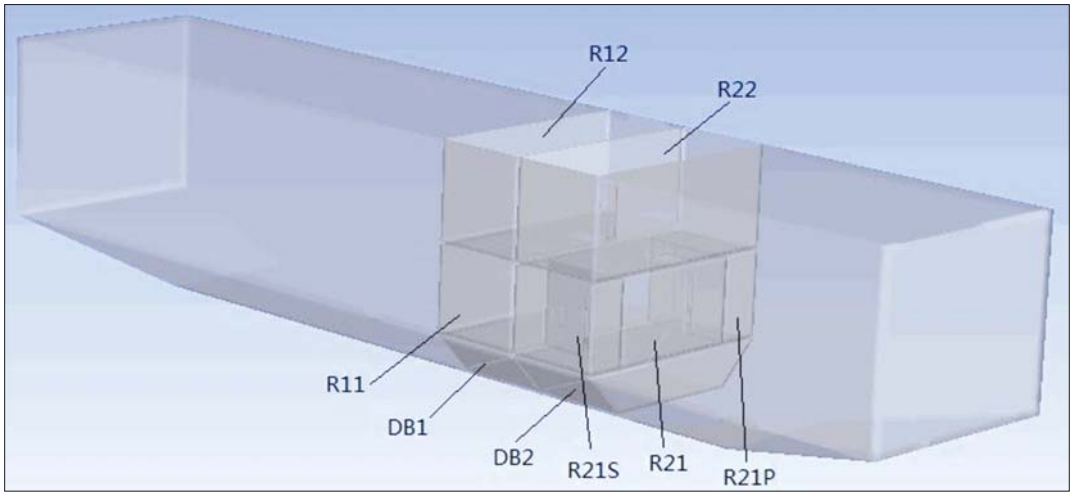

Fig. 5. Diagram of the damage barge model

acceptable numerical accuracy while consuming relatively little computational resource. Thus, this paper adopts the laminar model to conduct the simulation.

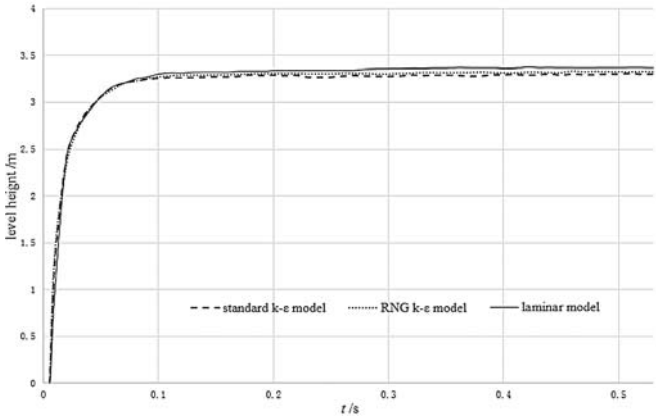

Fig. 6. Time-history of mass flux change at damaged opening

The simulation process ends at 180s. It uses 600 CPU hours for the flooding. The flooding water in the compartments is shown in Fig. 7. In general, the computed floodwater characteristics are in accordance with the experimental results. During the initial several seconds, the flooding is asymmetrical with respect to the central axis, but the entire flooding process appears to be symmetrical about the central axis. The external water floods into R21S violently via the damaged opening and its level increases rapidly in the compartment. The floodwater sprays straightly into R21 and spreads throughout the compartment promptly, as the damaged opening is collinear with the internal opening that connects R21S with R21. As the internal openings connecting the compartments are large, the floodwater flows through R21, R21P and R21S without obvious blockage. The water height in these compartments rises rapidly. After 15s, the flooding process seems to become almost symmetrical.

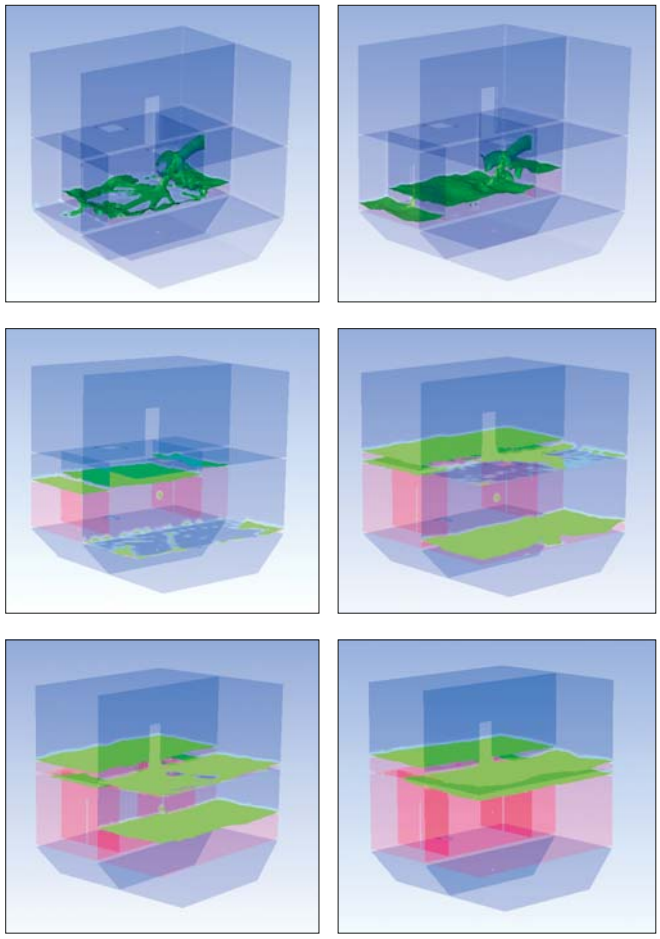

Fig. 7. Internal water motion at different stages (t=1s, 4s, 15s, 32, 52s, 84s)

Figs. 8–10 compare the water levels obtained in the numerical simulation (Gao, 2011) and the experiment (Ruponen, 2006). Since the difference between the internal and external water heights decreases, the water level initially rises rapidly and then slows down. The difference between the results of the numerical simulation and the experiment decreases at the final flooding stage. When the water level in the compartments is approximately the same as that outside the barge, the flooding process terminates at almost 180s.

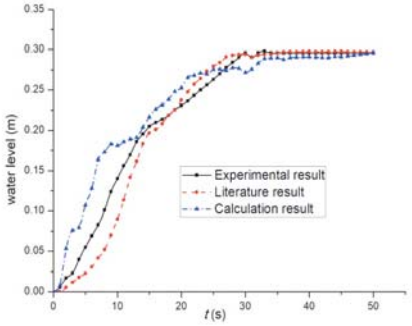

Fig. 8. Comparing time-histories of water level change in R21S

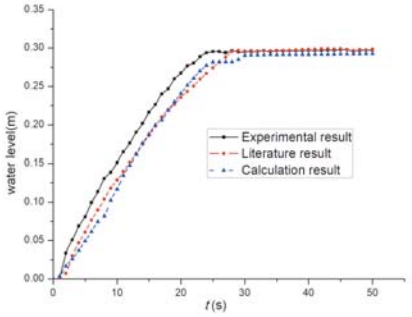

Fig. 9. Comparing time-histories of water level change in R21

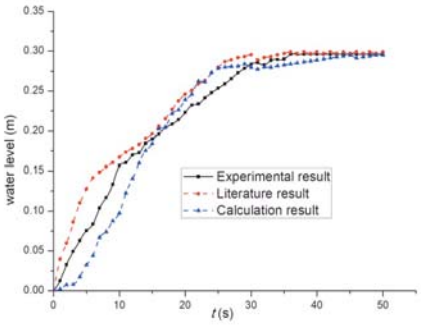

Fig. 10. Comparing time-histories of water level change in R21P

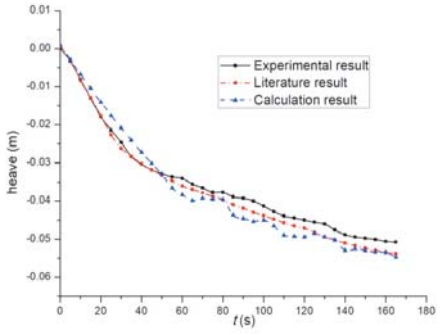

Fig. 11. Time histories of heave motion of the barge

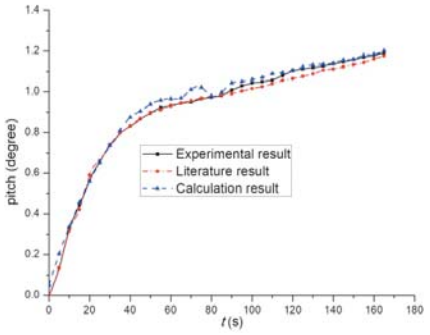

Fig. 12. Time-histories of pitch motion of the barge

The barge motions are shown in Figs. 11–12. The calculated results are compared with the experiment and the data available in the literature (Ruponen, 2006; Gao, 2011). Firstly, the barge sinks rapidly due to drastic water entry. Once the tanks R21, R21P and R21S are fully filled, the sinking of the barge becomes slower. The comparison indicates that the computed results are in accordance with the experiment.

This simulation calculation assumes six degrees of freedom of the ship, and the model test is performed for the fully free floating state. The flooding process is initially violent, then the barge is forced to sink and roll rapidly. In the final stages, the flooding water moves smoothly, and the barge becomes quasi-static. According to the reference (Ruponen, 2007), the roll motion of the barge model during the flooding process can be neglected, which is validated in this simulation and omitted in the result. The elevations of the liquid level in the abovementioned three compartments coincide well, which shows that the heaving motion of the ship has little influence on the flooding process of these three compartments. Judging from comparison with the available data, the results of the CFD technology based simulation turn out accurate, and the acceptable simulation accuracy level is obtained, which proves that the selected setting options and mesh parameters are feasible.

RECTANGULAR CABIN MODEL FLOODING CASE

The rectangular cabin model is shown in Fig. 13, and its dimensions are given in Table 4.

Tab. 4. Main particulars of the rectangular cabin model

Parameter	Dimension (mm)
Length	L=350 (mm)
Width	B=170 (mm)
Height	H=130 (mm)
Damaged opening	D=90 (mm)
Thickness	10 (mm)
Mass	3.225 (kg)

Fig. 14 compares the simulation results recorded at different times (t=0.14s, 0.4s, 0.54s), with those presented for 3DSPH in reference (Cao, 2013). The model experiences the heaving motion, mainly at the initial flooding stage, when a large amount of water floods into the model clapboard. After 0.14s, the buoyancy is increased during the falling process, and the baffles around the damaged opening block the water inflow into the model. At 0.4s, the model starts to rise, and the water begins to enter into the model. At 0.55s, both sides of the baffles are flooded, and the model continues to fall. It is noteworthy that the same trends can be found in the numerical and experimental results.

Changes of vertical center of gravity and vertical velocity acquired from the simulation and the experiment are compared in Fig. 15 and Fig. 16, which illustrate the coupling movement of the damaged model and flooding water within

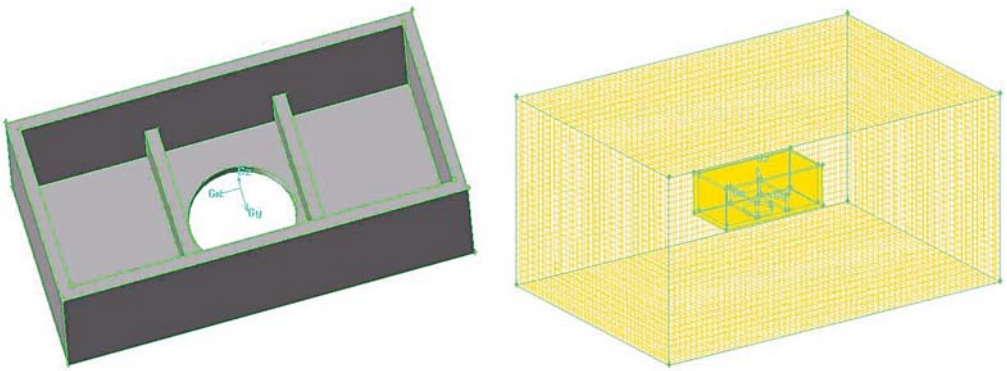

Fig. 13. Model diagram (left: cabin model, right: mesh)

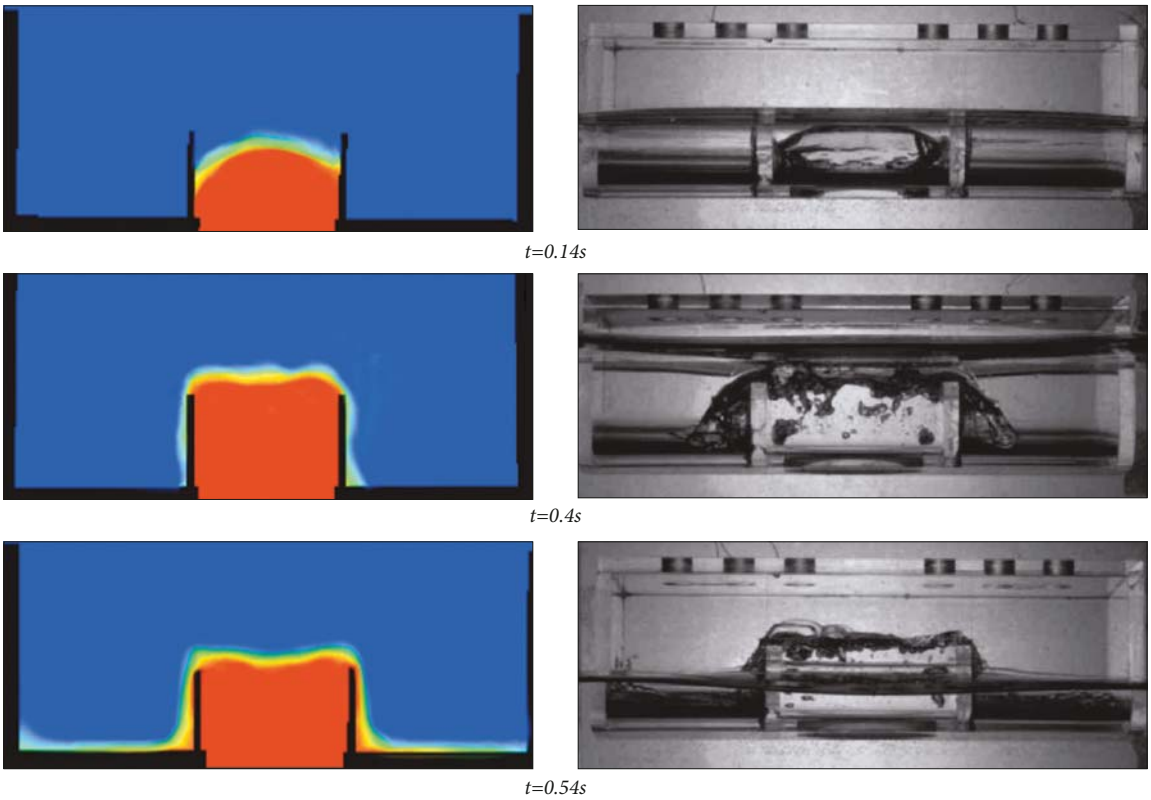

Fig. 14. Flooding process stages at different times (left: numerical simulation, right: experiment)

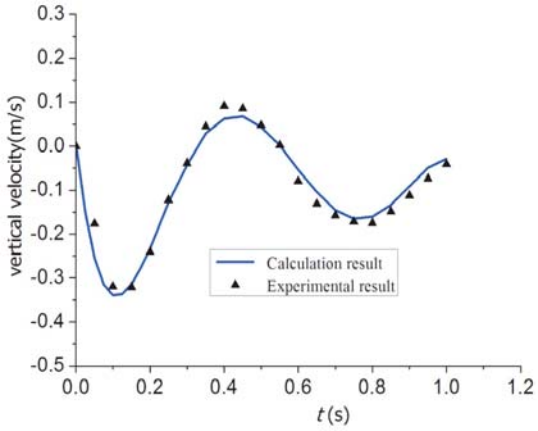

Fig. 15. Time-history of vertical velocity change

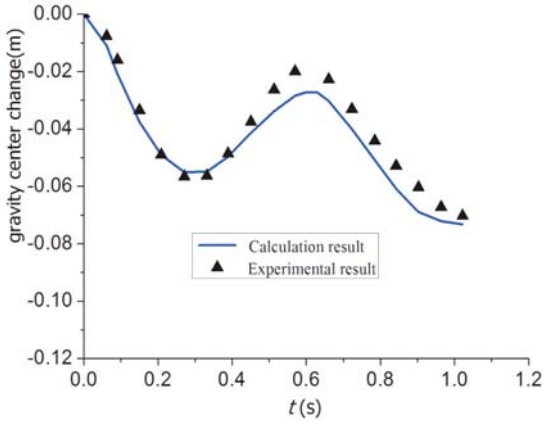

Fig. 16. Time-history of gravity center change

1 second. This comparison reveals that the results obtained using the above two methods coincide well with each other, and the discrepancies between them during the flooding process are small. Thus, the numerical results obtained using the present mesh for the examined case can be considered satisfactory and useful as both the reference for ship's flooding process forecasting, and a tool in rescue actions.

CONCLUSION

This paper has adopted the NS solver with the VOF model to simulate the flooding of a box-shaped barge. To validate its performance, the flooding study of a rectangular cabin model was also carried out. The research has shown that the developed method is effective in predicting the coupled dynamic characteristics of the ship with floodwater. The VOF method is feasible for capturing the free surface during the flooding process. The dynamic mesh strategy is introduced to consider the motions of the ship. For the floating barge, the flooding process is violent during the initial stage, while in the intermediate and final stages the barge becomes quasi-static and the flooding flow moves smoothly. For the rectangular model, the simulation results are in good accordance with the experiment, which provides some guidance for ship flooding. Also, on the basis of this validation, the numerical research of flooding of a certain damaged warship in beam wind and wave conditions will be carried out in the time-domain.

ACKNOWLEDGEMENTS

This paper was supported by the National Natural Science Foundation of China (51509124, 51681340360) and the Natural Science Fund of Shandong Province (ZR2015PE010), within the framework of the Hi Tech ship project of the Ministry of industry and technology entitled: "Study on second generation intact stability criteria and direct assessment technique of pure loss of stability 2016" [26]. The authors would like to extend their sincere gratitude to the above organizations.

REFERENCES

1. Cao X Y, Ming R F, Zhang A M. *Flooding characteristic simulation study of damaged ship based on 3D SPH method.* 16th Academic Symposium on China's marine (Shore) Engineering, 2013, Dalian, China.

2. D.K. Lee, S.Y. Hong, G.-J. Lee. *Theoretical and experimental study on dynamic behavior of a damaged ship in wave.* Ocean Engineering, 2007, 34: 21-31.

3. Gao Z L, Vassalos D, Gao Q X. *Numerical simulation of water flooding into a damaged vessel's compartment by the volume of fluid method.* Ocean Engineering, 2010, 37: 1428-1442.

4. Gao Q X, Vassalos D. *Numerical study of damage ship hydrodynamics.* Ocean Engineering, 2012, 55: 199-205.

5. Gao Z L, Gao Q X, Vassalos D. *Numerical study of a damaged ship flooding in beam seas.* Ocean Engineering, 2013, 61: 77-87.

6. Gao Z L, Gao Q X, Vassalos D. *Numerical simulation of flooding of a damaged ship.* Ocean Engineering, 2011, 38: 1649-1662.

7. IMO. *Explanatory Notes to the SOLAS Chapter II-1 Subdivision and Damage Stability Regulations*, Resolution MSC. 2008, 281(85).

8. Lemoine, L., Mahé, F., Morisset, N., Bertin, R. *Interpretation and design implications of probabilistic damage stability regulation*, Proceedings of the 13th International Ship Stability Workshop, 2013: 214–227, Brest, France.

9. Li Y M, Duan W Y, Jin Y L et al. *Flooding Process of Damaged Ship Based on CFD.* Shipbuilding of China, 2016, 57(2): 149-163.

10. Lyu Z W, Ma K, Liu F. *Military ship's subdivision optimization for reinforcement of anti-wind capacity after damage.* Journal of Marine Science and Technology, 2015, 20: 579-589.

11. Manderbacka, T., Mikkola, T., Ruponen, P., Matusiak, J. *Transient response of a ship to an abrupt flooding accounting for the momentum flux.* Journal of Fluids Structure, 2015, 57: 108–126.

12. Manderbacka, T., Ruponen, P. *The impact of the inflow momentum on the transient roll response of a damaged ship.* Ocean Engineering, 2016, 120: 346–352.

13. Ruponen, P., Queutey, P., Kraskowski, M., Jalonen, R., Guilmineau, E. *On the calculation of cross-flooding time.* Ocean Engineering, 2012, 40: 27–39.

14. Ruponen, P., Pulkkinen, A., Laaksonen, J. *A method for breach assessment onboard a damaged passenger ship.* Applied Ocean Research, 2017, 64: 236-248.

15. Ruponen, P. *On the effects of non-watertight doors on progressive flooding in a damaged passenger ship.* Ocean Engineering, 2017, 130: 115-125.

16. Ruponen, P. *Adaptive time step in simulation of progressive flooding.* Ocean Engineering, 2014, 78: 35–44.

17. Ruponen, P. *Model tests for the progressive flooding of a box-shaped barge.* Helsinki University of Technology, Ship Laboratory Report M-292, 2006.

18. Ruponen, P. *Progressive flooding of a damaged passenger ship.* Helsinki University of Technology, Helsinki, Finland, 2007.

19. Ruponen, P., Sundell, T., Larmela, M. *Validation of a simulation method for progressive flooding.* International Shipbuilding Progress, 2007, 54: 305-321.

20. Santos, T.A., Winkle, I.E., Guedes Soares, C. *Time domain modelling of the transient asymmetric flooding of Ro-Ro ships.* Ocean Engineer. 2002, 29: 667–688.

21. Schreuder, M., Hogström, P., Ringsberg, J.W., Johnson, E., Janson, C.-E. *A method for assessment of the survival time of a ship damaged by collision.* Journal of Ship Research, 2011, 55 (2): 86–99.

22. Tiago A. Santos, C. Guedes Saores. *Study of damaged ship motions taking into account floodwater dynamics.* Journal of Marine Science and Technology, 2008, 13(3): 291-307.

23. Tiago A. Santos, C. Guedes Saores. *Numerical assessment of factors affecting the survivability of damaged ro-ro ships in waves.* Ocean Engineering, 2009, 36(11): 797-809.

24. Vassalos, D., Ikeda, Y., Jasionowski, A., Kuroda, T. *Transient Flooding on Large Passenger Ships.* Proceedings of the 7th International Ship Stability Workshop, 2004, Shanghai, China.

25. Ypma, E., Turner, T. *An approach to the validation of ship flooding simulation models.* Proceedings of the 11th International Ship Stability Workshop, 2010, Wageningen, The Netherlands.

CONTACT WITH THE AUTHORS

Hu Li-Fen
e-mail: hlfgffff2008@aliyun.com

Qi Huibo
e-mail: 499427729@qq.com

Li Wubin
e-mail: 277481485@qq.com

Chen Shude
e-mail: 759817781@qq.com

Ludong University, Transporation School
HONGQI Middle Road
264025 Yantai
China

Li Yuemeng
e-mail: 421022889@qq.com

Ludong University, Ulsan Ship and Ocean College
HONGQI Middle Road
264025 Yantai
China

sciendo

POLISH MARITIME RESEARCH 1 (101) 2019 Vol. 26; pp. 82-94
10.2478/pomr-2019-0010

REGRESSION FORMULAS FOR THE ESTIMATION OF ENGINE TOTAL POWER FOR TANKERS, CONTAINER SHIPS AND BULK CARRIERS ON THE BASIS OF CARGO CAPACITY AND DESIGN SPEED

Tomasz Cepowski
Maritime University of Szczecin, Poland

ABSTRACT

This article presents regression formulas for the preliminary design of tankers, bulk carriers and container vessels, based on the data of ships built from 2000 to 2018. The formulas could have practical application for the estimation of total engine power by using ship's deadweight or TEU capacity and speed.
The regressions presented in this article are based on the most recent data and were developed for individual sub-types of tankers, bulk carriers and container ships. The presented regressions comply with trends found in the literature and offer greater accuracy for characteristics of new-built ships.

Keywords: preliminary design,total power,regression,bulk carrier,tanker,container vessel

INTRODUCTION

Ship designing is a multistage process which proceeds through preliminary, contract and detailed design stage. At the preliminary design stage major design issues such as the initial body lines, general arrangement and propulsion system are conceptualized. This early design phase consists of parametric and geometric design periods.

The main purpose of parametric design is, among others, to select main ship dimensions and estimate main propulsion and powering parameters.

As noted by Papanikolaou [9] an exact estimate of the required propulsion power for achieving design speed is not required at the preliminary design stage. This design problem can be solved by the selection of propeller and rudder in relation to other hydrodynamic ship characteristics. Papanikolaou argues that at the preliminary design, an appraisal of design power is needed to estimate:

- total ship weight, including weight of machinery and propulsion system installation,
- the required volume of engine room,
- ship fuel consumption and fuel weight.

Total ship power may also be used to pre-estimate the building price of the ship, which includes, among others, ship propulsion system parameters.

Celik et al. [1] argued that ship engine power is required to estimate tanker engine weight and cost at the preliminary design stage. Schneekluth and Bertram [12] noted that weight of engine foundation, engine plant and gearbox, as well as other engine weights such as pumps, pipes, sound absorbers and others are functions of propulsion power.

Lin and Shaw [7] suggested that container ship propulsion power is required to estimate stern frame, rudder, power generator, propeller and shaft weight and finally the total cost.

As noted by Papanikolaou [9] the following methods are commonly used for main engine power approximation at the preliminary design stage:

- geometrically similar ship methods based on the British Admiralty coefficient $C_{N:}$

$$D_N = \frac{D^{2/3}V^3}{P} \tag{1}$$

where:
C_N – coefficient, V – speed, P – installed power

- use of technical diagrams, for example MAN B&W Diesel diagrams [8]

Computational multi-criteria optimization methods are often used for preliminary design. To apply such methods simple mathematic equations mapping the design characteristic relationships are required. For this purpose, the geometrically similar ship methods and technical diagrams could have limited application for a main engine total power estimation. In this case a set of regression equations based on ship databases may be more practical.

The number of scientific publications dealing with propulsion power estimation at the preliminary design stage is rather small. Historically, one of the first set of regression analyses was presented by Piko [10] in 1980. Characteristics such as length, breadth, draught, gross and net registered ton capacities, as well as power and speed have been regressed each against deadweight and speed. The Lloyd's Register of Shipping database including 10334 ships was used in the publication. The main disadvantage of this form of study is the outdated nature of the database.

Żelazny [15] presented regression equations to estimate the propulsion power for container ships, tankers and bulk carriers. But the regressions were developed by using a relatively small database which only included 41 bulk carriers, 53 container ships and 32 tankers, moreover, the author did not take into account ship capacity parameters.

Ekinci et al. [3], through different computational intelligence techniques, determined principal parameters of contemporary oil/chemical tankers, also including main engine power. These authors took only into account length between perpendiculars instead of using a deadweight to engine power assessment. In the study, data from 114 oil/chemical tankers obtained from the website of Turkish Shipbuilders Association , were used. The tankers had lengths from 53 to182 m. A Levenberg–Marquardt Neural Network was applied to estimate engine total power. A problem in this method is that the mathematical models of neural networks are extremely complicated and the network presented in Ekinci paper can only be used applying computer techniques.

The engine power technical diagrams developed by engine manufacturers are often used for design analysis at the early design stage. An example propulsion power diagram published by MAN [8] is shown in Fig. 1. A drawback of this method is that the technical diagrams include nominal values and require corrections through sea trial data.

Besides the above design issues, engine power has been used to calculate the EEDI (Energy Efficiency Design Index). The EEDI was implemented as an amendment to the MARPOL Annex VI for new ships and aimed to use the most energy – efficient and low – polluting equipment and engines. The EEDI index is used to measure CO^2 emission from ships. Hence, propulsion power design methods are vitally important for this purpose as the main ship power may be used to estimate the EEDI index and also energy consumption in shipbuilding and shipping industry as a whole. Key ship characteristics optimization with regard to energy efficiency is the most effective method at the preliminary design stage.

THE AIM OF RESEARCH

The main aim of this research was to develop a set of regression formulas for such ships as tankers, bulk carriers and container ships and their sub-types.

In the parametric design phase, the key design characteristics are determined based on the most important functions of the ship. Chadzynski and Papanikolau [2, 9] categorized ship types by key design characteristics, as follows:

- deadweight carriers where deadweight capacity is a decisive design characteristic; tankers and bulk carriers are typical representatives of this ship category,
- volume carriers where the most significant design characteristic is hold volume capacity; RO-RO cargo ships, car carriers, container vessels are typical for this category.

This shows that deadweight capacity may be a key design parameter for tankers and bulk carriers, and TEU container

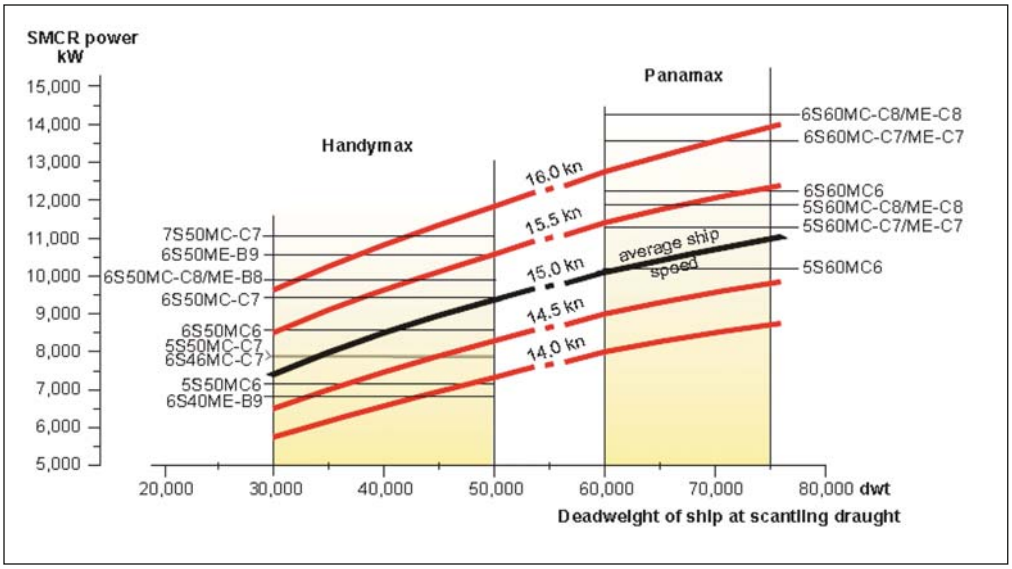

Fig. 1. The propulsion SMRC power demands of Handymax and Panamax tankers presented by MAN [8]

capacity is a key design parameter for container ships. Chądzynski, Papanikolaou, and Watson [2, 9, 14] argued that key design characteristics required to estimate the total power of ship main engines are deadweight or TEU capacity and design speed.

Therefore, in this study the above mentioned ship design parameters were taken into account and selected as independent variables for the estimation of main engine power, namely :

- maximum possible deadweight tonnage which corresponds to fully loaded deadweight at full summer saltwater draught (normally of 1,025 t/m^3 density), for tankers and bulk carriers,
- a maximum number of TEU containers that could be carried by a container ship,
- design speed of a tanker, bulk carrier and container ship.

Conversely, in this study the engine power is represented by Maximum Continuous Rating (MCR). MCR is the maximum power output of engine that can be produced while running continuously at safe limits and conditions.

Therefore, the main aim of this research was to develop a set of regression formulas to estimate Maximum Continuous Rating MCR, based on the deadweight DWT or TEU capacity, as well as the design speed V:

$$MCR = f(DWT/TEU, V) \quad (2)$$

where:
MCR – main engine total power,
DWT – deadweight capacity,
TEU – number of containers,
V – design speed,
f – a function (design formula) to calculate main engine power.

The regression functions were developed in two ways:

- for all sub-types of tankers, bulk carriers and container ships,
- for each individual ship sub-type such as:
  - Handysize, Handymax, Panamax, Aframax, Suezmax and VLCC tanker type,
  - Handysize, Handymax, Panamax, Capesize, Large Capesize and VLBC bulk carrier type,
  - Small Feeder, Feeder, Panamax, Post Panamax and ULCS container ship type.

The source of data used in this study was Sea-web Ships 2018 [5]. This database consists of the technical characteristics of over 200 000 ships and is considered an up-to-date document of the world fleet.

From this database, technical data dealing with the recent tankers, bulk carriers and container vessels built in the years from 2000 to 2018 , were used in this research.

When using a regression method the implemented data should be of the utmost quality and clearly representative. Bad quality data lead to incorrect statistical analysis and regression coefficient values. The Sea-web Ships database contains a data set of all ships, including sister ships which have identical or similar characteristics. In this study, the ship database was fully verified. Tanker sample sizes which remained after the verification are presented in Fig 2 . The total sample sizes were as follows:

- 1710 tankers,
- 1248 bulk carriers,
- 442 container ships.

In this study, tankers were the largest group, the smallest – container ships. As shown in Fig. 2 :

- The Handysize sub-type dominated the tanker group,
- The Capesize sub-type dominated the bulk carrier group
- The Feeder sub-type is the most common class in the container vessel group.

In contrast, the number of Panamax tankers, Large Capesize and VLBC bulk carriers, as well as ULCV container ships is the lowest in the ship database. The range and mean values of total engine power, deadweight, TEU capacity and design speed for particular types of ships are shown in Tab. 1–3. It is interesting that as tanker, bulk carrier and container ship capacity increased, average design speed also generally increased. This trend is noted through the use of MAN analysis data presented in 2007,

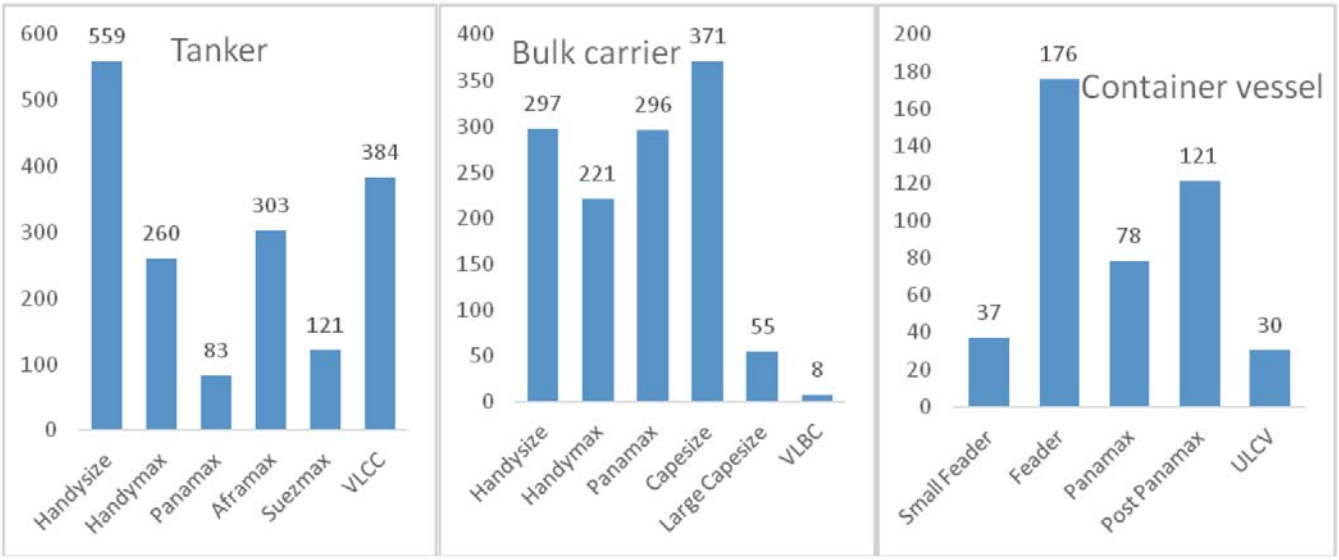

Fig. 2. The ship sample sizes used in this research

Tab. 1. Mean, minimum and maximum values of parameters of tanker sub-types, where : MCR – total engine power, DWT – deadweight, V – speed

		MCR [kW]	DWT [t]	V [knots]
Handysize	Mean	5456	16925	13.95
	Min	2301	10000	10
	Max	11700	26961	16.5
Handymax	Mean	8447	39548	14.59
	Min	5180	27000	12
	Max	13365	50571	16.2
Panamax	Mean	11524	72293	14.87
	Min	7500	56168	14
	Max	13650	79905	16
Aframax	Mean	13100	108562	14.77
	Min	10599	81305	12
	Max	16630	122018	16
Suezmax	Mean	17015	157529	15.06
	Min	14300	146270	14
	Max	19620	167282	16
VLCC	Mean	27174	307139	15.58
	Min	20800	279989	13
	Max	33627	323182	17.4

Tab. 2. Mean, minimum and maximum values of parameters of bulk carrier sub-types, where : MCR – total engine power, DWT – deadweight, V – speed

		MCR [kW]	DWT [t]	V [knots]
Handysize	Mean	5765	26378	13.53
	Min	2400	10034	10
	Max	9488	34961	15.1
Handymax	Mean	7854	44071	14.28
	Min	5640	35009	12.8
	Max	9960	55000	15.75
Panamax	Mean	9447	65329	14.44
	Min	6780	55060	13.8
	Max	14350	79964	15.3
Capesize	Mean	13896	123488	14.47
	Min	8740	80013	13.8
	Max	21840	186300	16.8
Large Capesize	Mean	19355	226242	14.59
	Min	16040	203024	14
	Max	28260	299688	15.55
VLBC	Mean	28500	353398	14.99
	Min	25200	313049	14.6
	Max	31640	403627	15.9

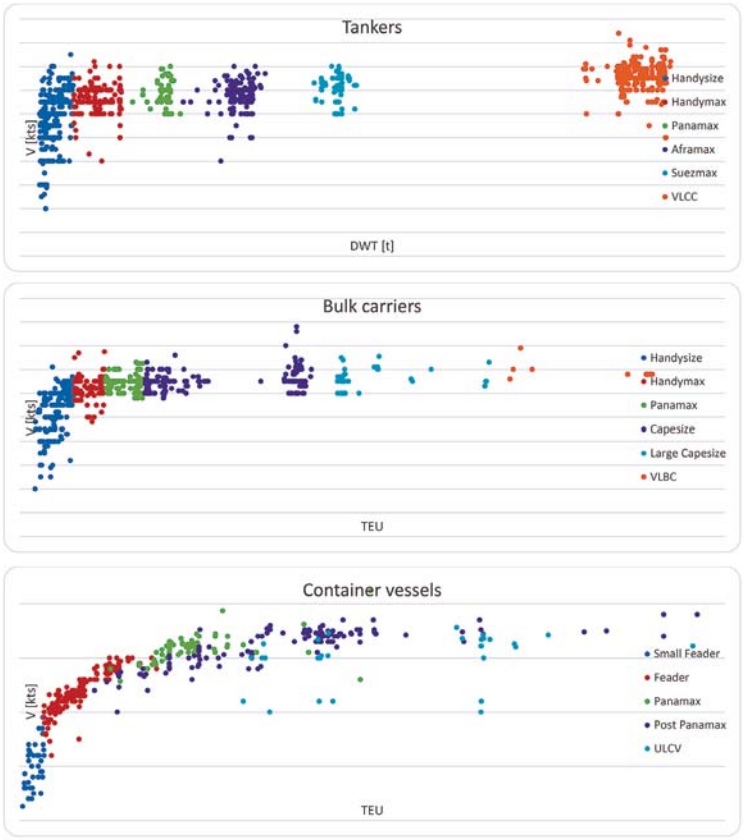

Fig. 3. Ship data used in this research

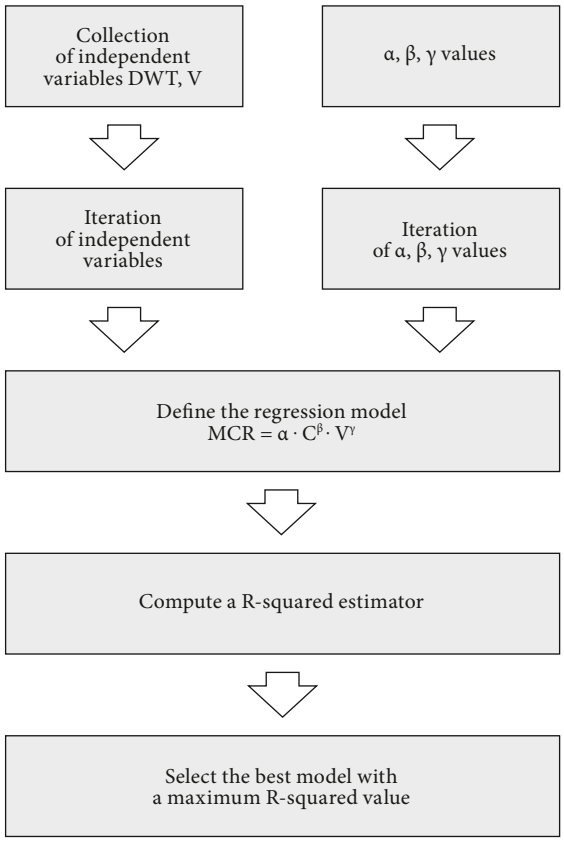

Fig. 4. A general algorithm scheme, where: MCR is main engine total power, C–DWT or TEU capacity, V–speed, α, β, γ are coefficients

Tab. 3. Mean, minimum and maximum values of parameters of container carrier sub-types, where : MCR – total engine power, DWT – deadweight, V – speed

		MCR [kW]	TEU	V [knots]
Small Feeder	Mean	2764	424	13.04
	Min	894	90	9.30
	Max	4400	698	17.50
Feeder	Mean	14357	1649	19.69
	Min	6930	704	14.00
	Max	28887	3889	23.00
Panamax	Mean	38616	4889	23.80
	Min	21735	2588	20.85
	Max	68640	9954	29.20
Post Panamax	Mean	52942	7595	24.05
	Min	19620	2127	18.00
	Max	81254	19224	27.00
ULCV	Mean	65295	10944	23.03
	Min	46620	6350	18.00
	Max	80905	19100	25.80

2008 and 2010. But Aframax tankers and VLBC container ships are an exception from this apparent rule.

Fig. 3 shows the design speed V against DWT and TEU capacity for tanker, bulk carrier and container ships, which is used in this study.

RESEARCH METHOD

Nonlinear regression analysis was applied to estimate any relationship between main engine total power, deadweight or TEU capacity and design speed. The following general regression model was assumed in this work:

$$MCR = \alpha \cdot C^{\beta} \cdot V^{\gamma} \quad (3)$$

where:
MCR – main engine total power,
C – DWT or TEU capacity,
V – design speed,
α, β, γ – regression model coefficients.

An ordinary least square approach was used in the presented regression analysis.

On the basis of the method this Author developed an algorithm to find α, β, γ values. The values of α, β, γ were iteratively searched through all their possible combinations by using this algorithm. The general algorithm scheme is shown in Fig. 4.

NdCurveMaster software (Version 3.1, SigmaLab, 2017) was used to develop regression equations presented in this paper. The regressions containing the calculated values of α, β, γ coefficients for the estimation of engine total power are presented in the next part of the article.

Tab. 4. Values of the regression coefficients (α, β, γ), standard deviation SE and R-square error relating to the model (4) for tankers

Tanker type	α	β	γ	SE [kW]	R-square error
All tanker types	2.66	0.6	0.6	1662	0.988
All tanker types	Piko (1980)			2044	0.983
All tanker types	Żelazny (2015)			1738	0.988
Handysize	0.364	1/2	1.8	868	0.974
Handymax	17.033	1/3	1	1285	0.977
Panamax	0.1	0.8	1	1134	0.990
Aframax	18.59	1/3	1	1332	0.989
Suezmax	2.894	1/2	1	1180	0.995
VLCC	3.2E-06	1/7	1/2	1922	0.995

RESULTS

The following models were fitted to ship data:

- for tankers and bulk carriers:

$$MCR = \alpha \cdot DWT^{\beta} \cdot V^{\gamma} \quad (4)$$

- for container ships:

$$MCR = \alpha \cdot TEU^{\beta} \cdot V^{\gamma} \quad (5)$$

where:
MCR – main engine total power [kW],
DWT – deadweight capacity [t],
TEU – number of containers [-],
α, β, γ – regression model coefficients,
V – design speed [knots].

Regression coefficient values (α, β, γ), standard (SE) and the R-squared errors relating to the worked-out regressions (4) and (5) for each ship type are given in Tab. 4, 5, 6. The tables also show the standard deviations SE and the R-squared errors relating to the methods of Piko and Żelazny with regard to the Sea-web Ships database. Fig. 5–8 show the relationship between deadweight, number of containers, speed and main engine total power for each ship type, calculated by using the regressions (4) and (5).

Fig. 5 shows the total power plotted against deadweight and TEU capacity for each ship type by using the methods of Żelazny and Piko. In Żelazny's regressions the waterline area AWL and speed V are taken into account as follows:

$$MCR_T = (7E{-}07 \cdot A_{WL}{}^2 + 0.1737 \cdot A_{WL} + 321.58) \cdot V \quad (6)$$

$$MCR_C = (7E{-}07 \cdot A_{WL}{}^2 + 0.1737 \cdot A_{WL} + 321.58) \cdot V \quad (7)$$

$$MCR_B = (7E{-}07 \cdot A_{WL}{}^2 + 0.1737 \cdot A_{WL} + 321.58) \cdot V \quad (8)$$

where:
MCR_T – tanker main engine total power [kW],
MCR_C – container ship main engine total power [kW],
MCR_B – bulk carrier main engine total power [kW],
A_{WL} – waterline area [m^2],
V – speed [m/s].

Tab. 5. Values of the regression coefficients (α, β, γ), standard deviation SE and R-square error relating to the model (4) for bulk carriers

Bulk carrier type	α	β	γ	SE [kW]	R-square error
All bulk carrier types	4.297	0.6	0.4	1167	0.989
All bulk carrier types	Piko (1980)			2202	0.964
All bulk carrier types	Żelazny (2015)			1363	0.986
Handysize	0.731	0.6	1.1	765	0.983
Handymax	0.691	0.6	1.1	785	0.990
Panamax	16.277	1/3	1	1120	0.986
Capesize	0.858	0.6	1	1267	0.992
Large Capesize	1.81E-02	0.8	1.5	1788	0.991
VLCC	1.58E-03	0.8	2.4	1041	0.998

In order to compare the engine power calculated by the Żelazny method to the regressions (4) and (5), the relationship between the DWT or TEU capacity and waterline area AWL were determined as follows:
for tankers:

$$A_{WL} = -617.39 + 9.158 \cdot DWT^{0.6}, \quad (9)$$

for bulk carriers:

$$A_{WL} = 1497.6 + 0.658 \cdot DWT^{0.8}, \quad (10)$$

for container ships:

$$A_{WL} = -5412.3 + 1003.1 \cdot TEU^{0.3}. \quad (11)$$

Fig.9 shows the relationship between the DWT or TEU capacity and waterline area AWL calculated by using the equations (9) – (11). The values of the standard deviation SE and the R-squared error relating to the equations are given in Tab. 7.

DISCUSSION OF RESULTS

The correlation between coefficients presented in Tab. 4, 5, 6 was high due to the use of a regression model with no intercept term. When a regression without any constant in the model is used it can lead to an unnatural increase in a sum of squares (residual and total) and an increase in R-square error values. Therefore, in this case the standard deviation SE may be a more reliable estimator.

Tab. 4,5,6 show the accuracy of the worked – out regressions for all types of ships than when compared to the SeaWeb database, which was higher than for the equations published by Piko and Zelazny. Though it should be noted that the accuracy of Piko regression was the lowest.

Żelazny equations that were developed (2015) for tankers and bulk carriers are reasonably accurate.

Tab. 6. Values of the regression coefficients (α, β, γ), standard deviation SE and R-square error relating to the model (5) for container ships

Container ship type	α	β	γ	SE [kW]	R-square error
All container ship types	10.13	0.6	1	4210	0.987
All container ship types	Piko (1980)			7673	0.959
All container ship types	Żelazny (2015)			7104	0.965
Small Feeder	11.634	0.8	1/4	215	0.995
Feeder	4.08	0.7	1	846	0.997
Panamax	8.885	0.8	1/2	2183	0.997
Post Panamax	25.593	1/2	1	4397	0.993
ULCV	560.695	0.4	1/3	3317	0.999

Tab. 7. The values of the standard deviation SE and the R-square error relating to the worked-out regressions (9), (10), (11)

Equation number	SE [m²]	R-square
(9)	308	0.995
(10)	376	0.983
(11)	656	0.949

However, the author's equations developed for container ship power resulted in the halving of the power estimates in standard deviation SE, compared to the Piko and Zelazny regressions.

Tab. 4, 5, 6 show that the standard deviation for the estimation of ship engine total power for tankers, bulk carriers and container ships is generally higher than that for the estimation of the engine power of their sub-types.

The exception are the regressions for VLCC tankers, Capesize, Large Capesize and VLBC bulk carriers and Post Panamax container ships. The engine power estimate standard deviation for these ships' sub-types is higher than that for the main ship types. As Tab. 1, 2, 3 show, this high value of standard deviation results from a much higher value of engine power range in case of the ships' sub-types. In addition, correlation coefficient values for the estimate of engine power of sub-types' ship are much higher than the correlation coefficient for the estimate of engine power of tanker, bulk carrier and container ship. This means that the accuracy of engine power estimation equations for ship sub-types is higher than for other main types.

An analysis of Tab. 4–6 and Fig. 5–8 shows that the effect of DWT and TEU capacity on main engine power is non-linear.

In the equations (4) and (5) the power exponent coefficient β reaches values lower than 1 . However, the tables and figures in question show that the speed has a linear (or almost linear) effect on total engine power. The exponential coefficient γ takes values from 1 to 1.1 in the equations (4) and (5).

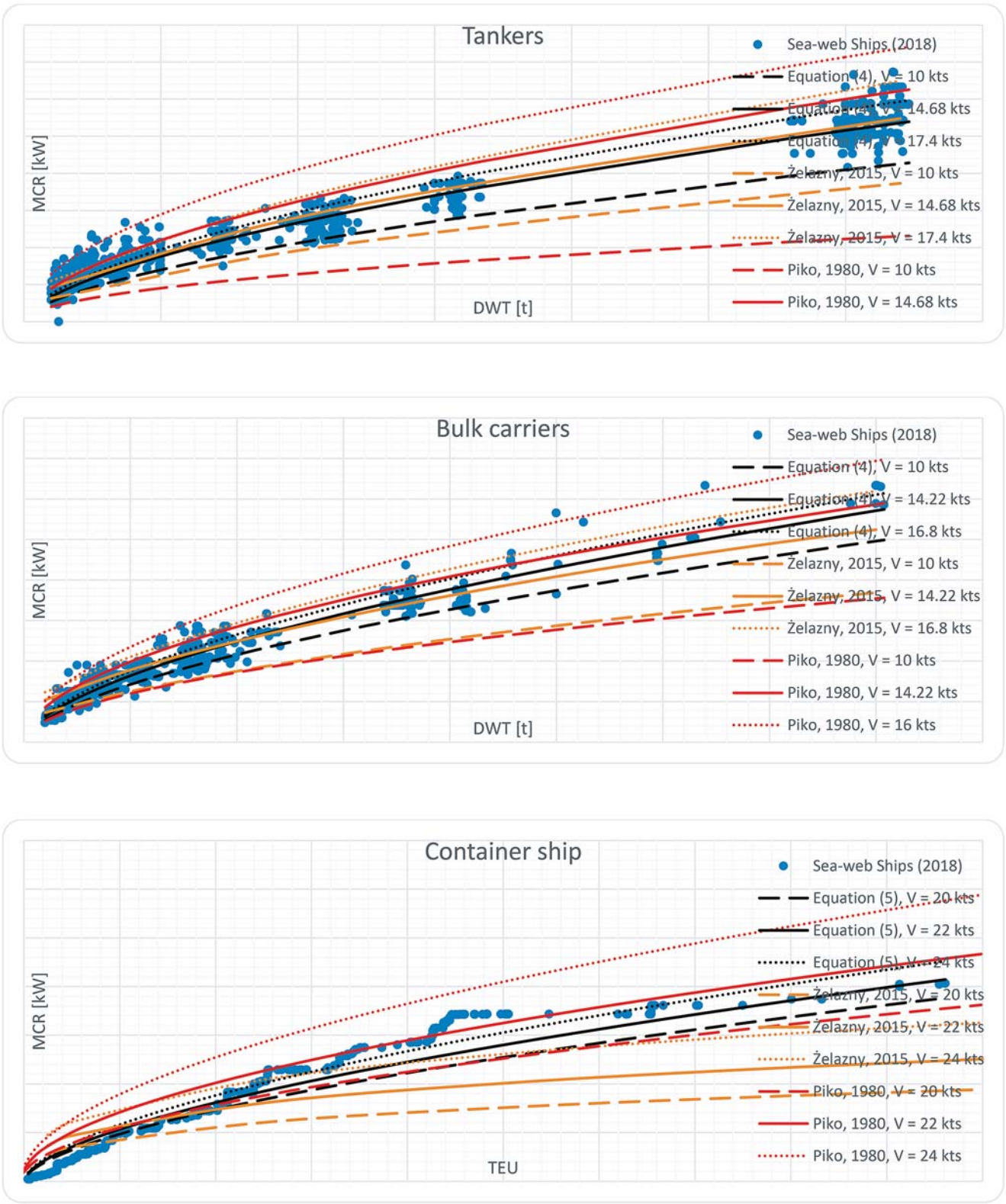

Fig. 5. The main engine total power MCR in function of DWT or TEU capacity

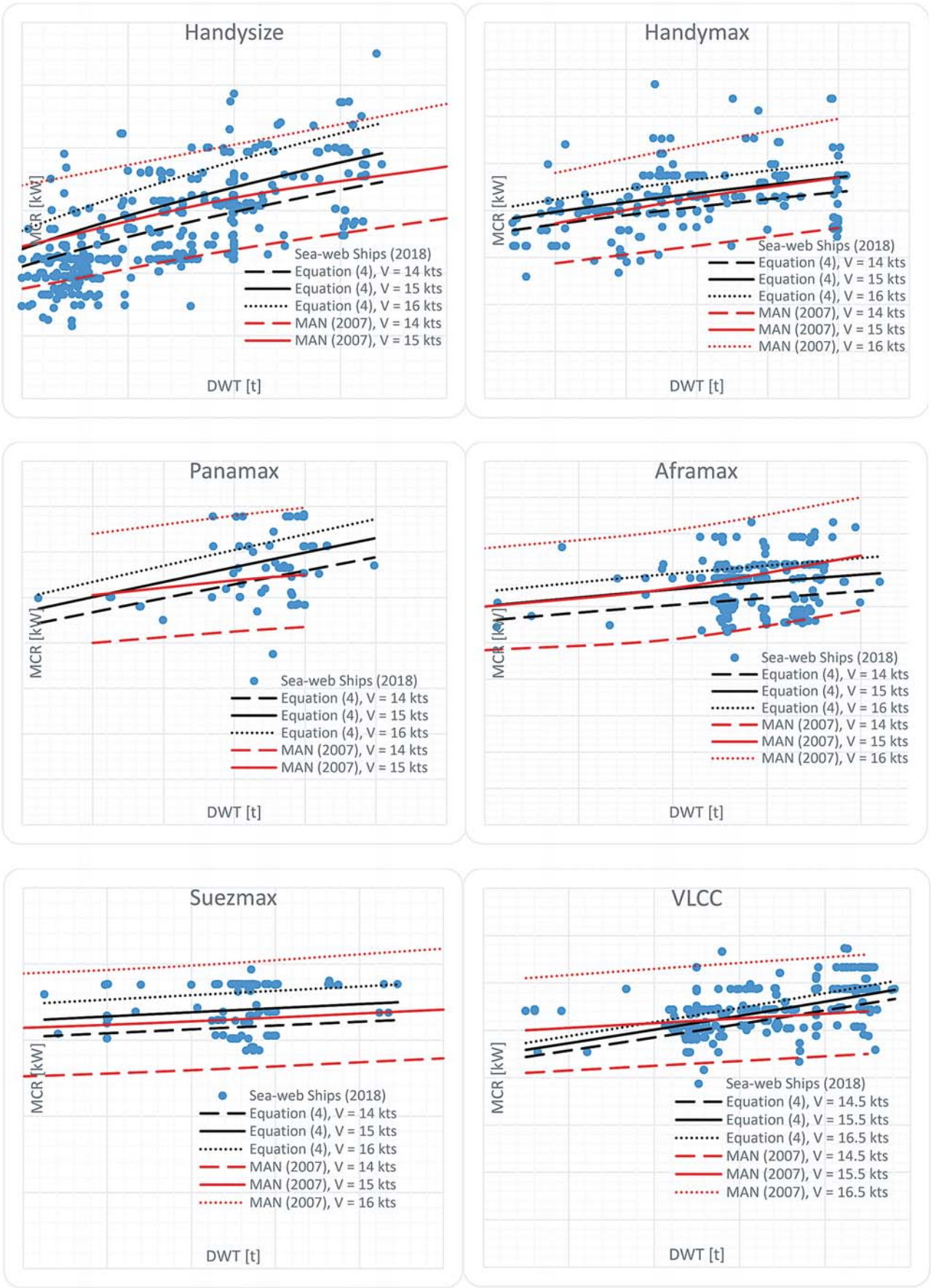

Fig. 6. The main engine total power MCR in function of DWT capacity, for tankers

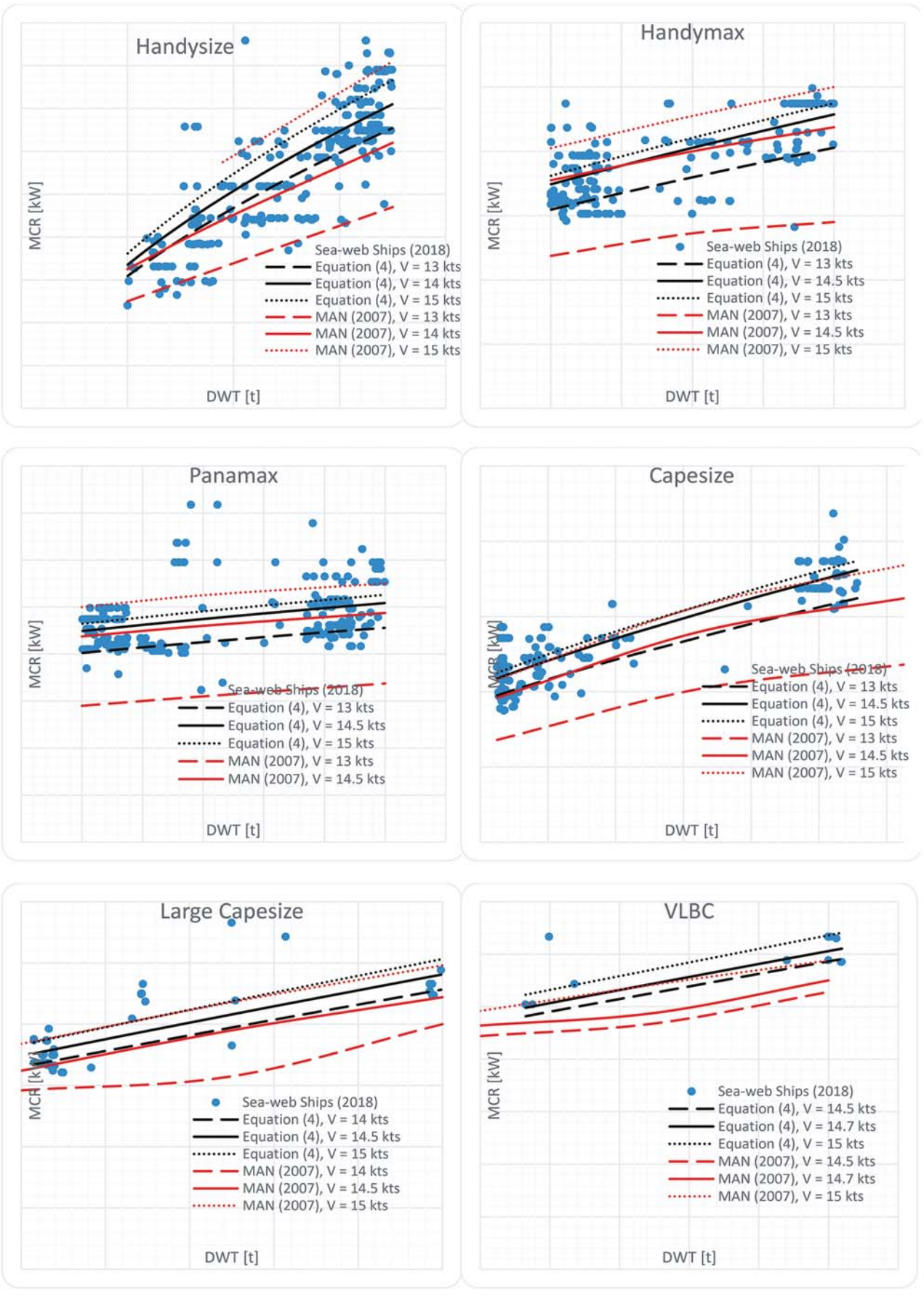

Fig. 7. The main engine total power MCR in function of DWT capacity, for bulk carriers

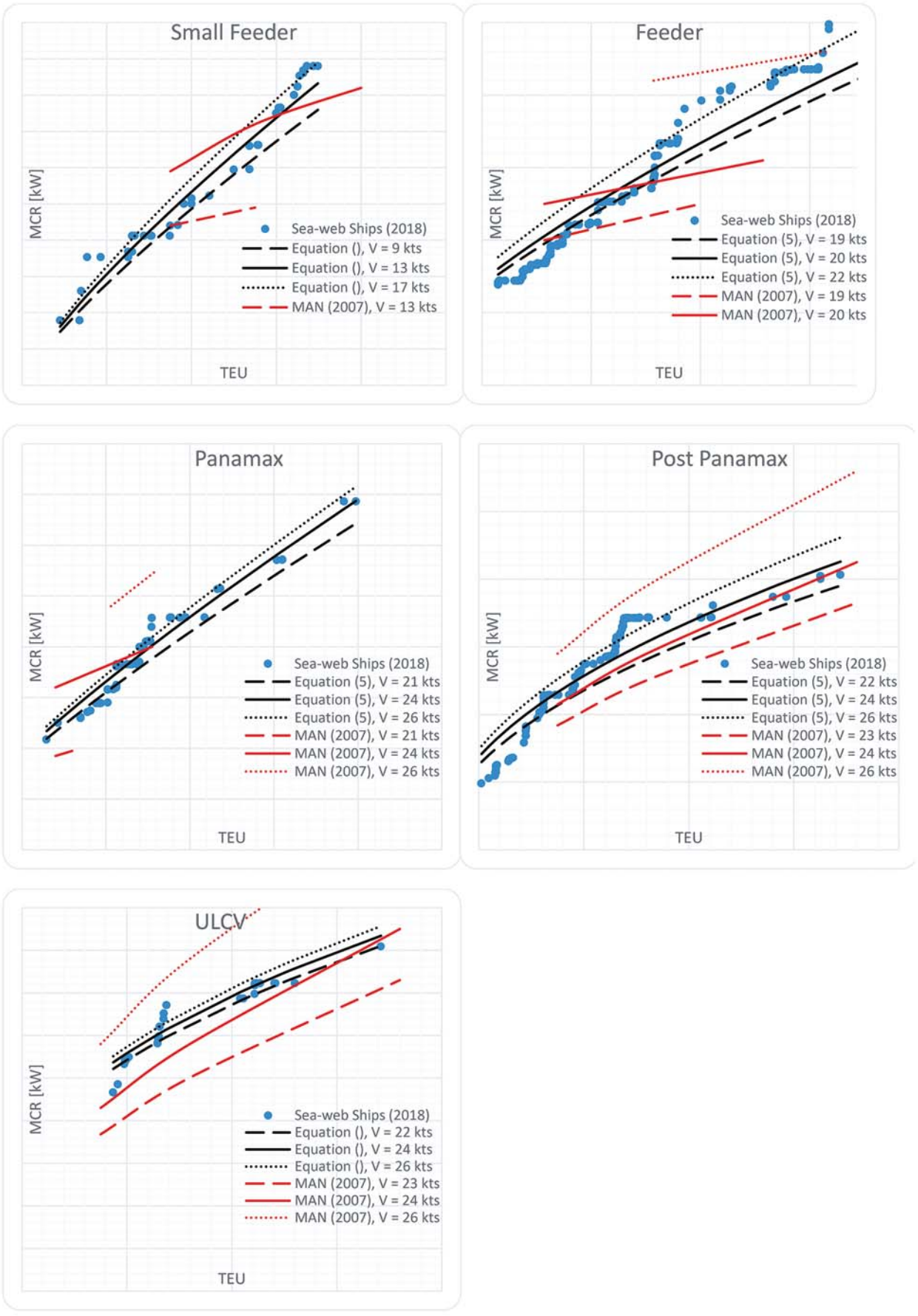

Fig. 8. The main engine total power MCR in function of TU capacity, for container ships

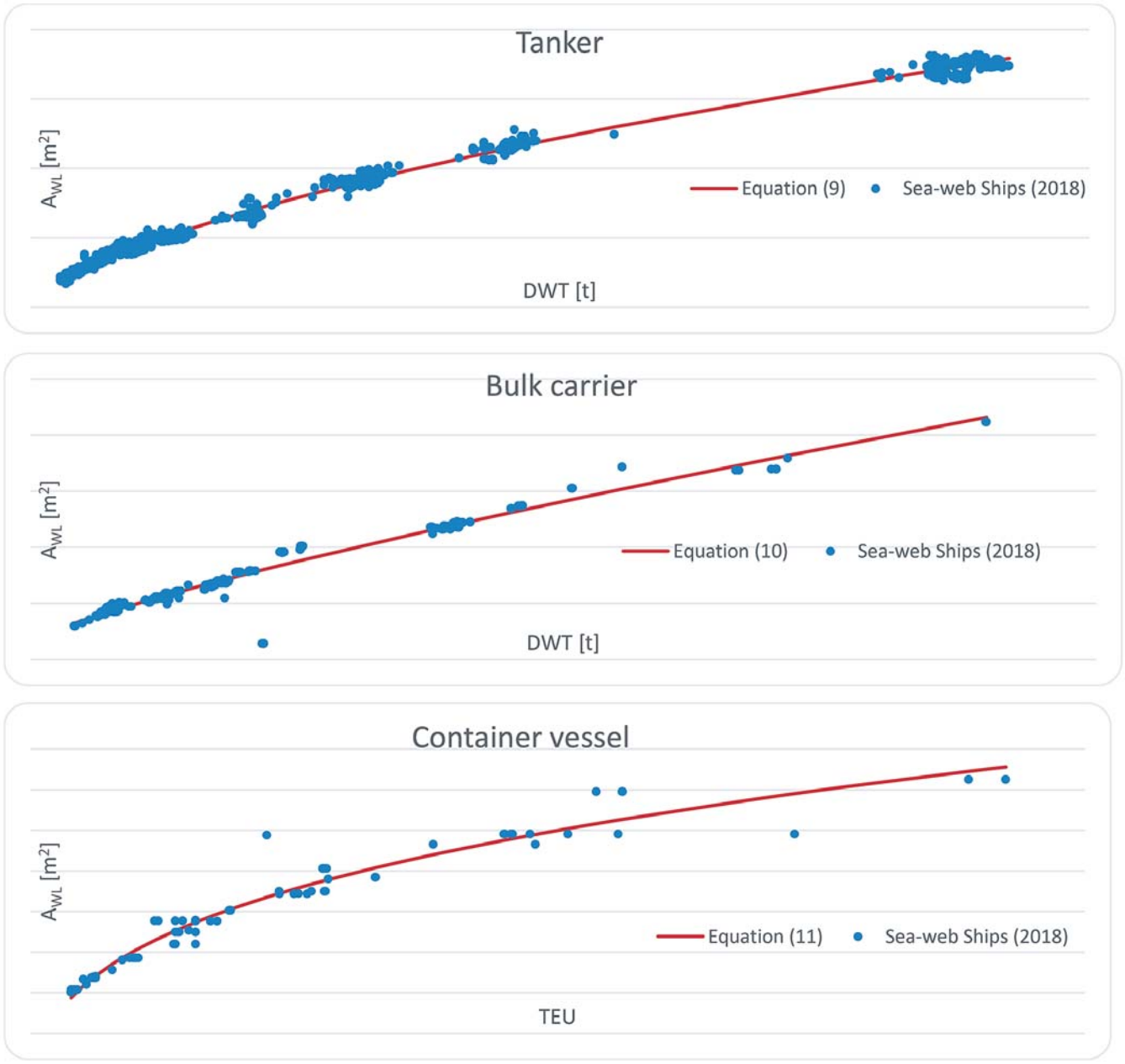

Fig. 9. The waterline area AWL in function of DWT or TEU capacity

But for some sub-types, the speed has a clearly nonlinear effect on engine power. The exponential coefficient γ reaches the value of 1.8 for Handysize tankers and the value of 2.4 for VLBC bulk carriers. In contrast, the speed of VLCC tankers, Small Feeder, Panamax and ULCV container ships has a smaller influence on each individual engine power than in case of the other ship types.

Fig. 5 shows that the worked-out regressions (4) and (5) are generally well matched to SeaWeb data. However, the regressions developed by Piko and Żelazny are worse matched to the reference data. Significant inaccuracies occur in extreme speed values in case of using the Piko and Żelazny methods. These regressions erroneously assess the influence of speed on engine power; Żelazny regressions applied to container ships appeared the least accurate. Low accuracy of Pico equation may result from an out-of-date ship database that was used for developing the regressions.

Fig. 6–8 compare regressions used with the SeaWeb data and MAN nominal diagrams. The figures show that the MAN nominal diagrams are well matched to SeaWeb data only in the case of average speed values. For extreme speeds, power estimated by using MAN diagrams significantly exceeds the ship power values in the SeaWeb database. In particular, speed values which are lower than the given ship sub-type average speed mean that the estimated power is lower than SeaWeb ship power. Similarly, for ship speed greater than the average speed of a given ship type, the estimated power is much greater than the engine power of new- built ships. Perhaps this is due

to the fact that nominal diagrams do not sufficiently take sea trials tests into account.

The equations presented in this article can be used only in the ranges of deadweight and speed values shown in Tab. 1–3 for each of the ship sub-types. For example, according to Tab. 1, the equation (4) for engine power estimate of Handysize bulk carrier can only be used for:

- fdeadweight – from 10 034 to 34 961 t,
- fspeed – from 10 to 15.1 knots.

The formulas presented in this article estimate total ship engine power depending on two independent variables simultaneously: DWT or TEU capacity and speed. However, it is possible to transform the formulas into a simpler form based on one independent variable, i.e. either deadweight capacity, TEU capacity or speed. To do this, the regression coefficients presented in Tab. 4–6 should be converted by using average values shown in Tab. 1–3. For example, the equation (4) can be transformed to a simpler form by using:

– fthe average value of Handysize bulk carrier speed V = 13.53 knots, as follows:

$$MCR = 0.731 \cdot DWT^{0.6} \cdot 13.53^{1.1} = 12.833 \cdot DWT^{0.6} \quad (12)$$

– or the average value of Handysize bulk carrier deadweight DWT = 26,378 t, as follows:

$$MCR = 0.731 \cdot 26378^{0.6} \cdot V^{1.1} = 328.6 \cdot V^{0.6} \quad (13)$$

It is important to remember that the simplification of the equation (4) to the equation (12) or (13) reduces its accuracy.

CONCLUSIONS

This article presents a set of simple regression functions for the estimation of total engine power of tankers, bulk carriers and container ships depending on deadweight or TEU capacity and speed, for new-built ship sub-types. The article also presents total power estimation equations for ship sub-types.

The relationships between engine total power, DWT or TEU capacity and speed presented in the article offer similar trends that can be found in relationships presented by Piko (1980), Żelazny (2015) and MAN. The comparisons presented in this study clearly show that the regression formulas by Piko , Żelazny and MAN are accurate for the design of modern ships only in the case of medium-size ships. In the speed range of remaining ships, estimated engine power values obtained with the use of the methods by Piko, Żelazny and MAN incorrectly match new-built ship characteristics.

Accuracy of the regressions developed in this article for full ship capacity range is higher than in the case of the corresponding Piko and Żelazny regressions.

The nominal engine power diagrams presented by MAN are often used for ship engine power estimates in ship design practice. This study shows that using the nominal diagrams for engine power estimates for extreme speed values (in relation to the average speed value) may result in inaccurate estimations and lead to design errors.

For a ship speed much lower or higher than the average speed of a given ship type, estimated engine power may be incorrect, and this would lead to over- or under- estimated propulsion mass, mass of stores and ship building costs . The analyses presented in this article show that the accuracy of regressions worked-out by this author is higher, over full design speed range of ship sub-types , than that resulted from MAN diagrams in regard to the ships' statistical data published in the Sea-web database.

The analyzes show that the regressions developed for tanker, bulk carrier and container ship sub-types are characterized by a higher accuracy than the regressions developed for their main types. The regressions represent an improvement over other modern preliminary design methods.

All equations presented in this paper refer to the most contemporary ships and may find practical application at the preliminary ship design stage and contribute to ship design theory development.

The research confirms that DWT and TEU capacity has a non-linear effect on total engine power. However, speed of tanker, bulk carrier and container ships , correlated with DWT and TEU capacity, usually affects total engine power in a linear way.

REFERENCES

1. Celik F., Erturk I, Turan E.: *Investigation of main particulars subject to minimum building cost for chemical tankers*. Ocean Engineering 73 (2013) , pp. 32–37.
2. Chądzyński W.: *Elements of contemporary design methods of floating objects* (in Polish). Scientific Reports of Szczecin University of Technology (2001), Department of Ocean Engineering and Marine System Design.
3. Ekincia S., Celebia U.B., Bala M., Amasyalia M.F., Boyacia K.: *Predictions of oil/chemical tanker main design parameters using computational intelligence techniques*. Applied Soft Computing 11 (2011), pp. 2356–2366.
4. Elvekrok D.R.: *Concurrent Engineering in Ship Design*. Journal of Ship Production, (1997) Vol. 13, No. 4, pp. 258–269.
5. Sea-web Ships (2018) [Online]. Available from: https://maritime.ihs.com [Accessed: 10. Feb. 2018]
6. Kristensen H.O.: *Determination of Regression Formulas for Main Dimensions of Tankers and Bulk Carriers based on IHS Fairplay data*. Project no. 2010–56, Emissionsbeslutningsstøttesystem. Work Package 2, Report No. 02. (2012), Technical University of Denmark.
7. Lin C., Shaw H.: *Feature-based estimation of preliminary costs in shipbuilding*. Ocean Engineering 144 (2017), pp. 305–319.

8. MAN Diesel AS: *Propulsion trends in tankers* (2007).

9. Papanikolaou A.: *Ship Design: Methodologies of Preliminary Design*. Springer , Dordrecht (2014).

10. Piko G. P.: *Regression Analysis of Ship Characteristics*. C. J. Thompson Commonwealth Government Printer, Canberra (1980).

11. Rawson K.J. and Tupper E.C.: *Basic Ship Theory. Ship Dynamics and Design. Volume 2*. Fifth edition. Butterworth-Heinemann, (2001).

12. Schneekluth H., Bertram V.: *Ship Design for Efficiency and Economy*. Second edition. Butterworth-Heinemann, (1998).

13. SigmaLab (2017) ndCurveMaster [Computer software] Available from: www.ndcurvemaster.com [Accessed: 4 Dec. 2017]. Szczecin, Poland.

14. Watson D.G.M.: *Practical Ship Design*. Volume 1. Elsevier Science, (1998).

15. Żelazny K.: *Method for determination of service speed useful in the initial design of cargo vessels under statistical weather conditions occurring on shipping route* (in Polish). West Pomeranian University of Technology, Publishing House, Szczecin, (2015).

CONTACT WITH THE AUTHOR

Tomasz Cepowski
e-mail: t.cepowski@am.szczecin.pl

Maritime University of Szczecin
ul. W. Chrobrego 1-2
70-500 Szczecin
Poland

sciendo

POLISH MARITIME RESEARCH 1 (101) 2019 Vol. 26; pp. 95-106
10.2478/pomr-2019-0011

SIMULATION AND MEASUREMENT STUDIES OF THE VDES SYSTEM'S TERRESTRIAL COMPONENT

Krzysztof Bronk
Patryk Koncicki
Adam Lipka
Dominik Rutkowski
Błażej Wereszko
National Institute of Telecommunications, Wireless Systems and Networks Department, Gdansk, Poland

ABSTRACT

In the paper, the measurement and simulation results of the VDES (VHF Data Exchange System) terrestrial component are discussed. It is anticipated that VDES will be one of the major solutions for maritime communications in the VHF band and its performance will be sufficient to fulfill the requirements of the e-navigation applications. The process of the VDES standardization (ITU R, IALA) has not been officially completed yet, but substantial amount of technical information about the future system's terrestrial component (VDE-TER) is already available. The paper is divided into three general parts: (a) theoretical presentation of the system's physical layer and the radio channels applicable to VDES, (b) simulation results (BER, BLER, channel delay between two propagation paths and its influence on bit rates) and (c) measurement results (useful ranges, BER). It turned out that in real maritime conditions, the VDES system can offer ranges between 25 and 38 km for the configurations assumed during the measurement campaign. Those results are generally compliant with the theoretical data in the line-of-sight conditions. In the NLOS scenarios, where fading becomes the dominant phenomenon, the discrepancies between the measurements and the theoretical results were more significant. The obtained results confirmed that VDES provides a large coding gain, which significantly improves the performance of data transmission and increases the bit rate compared to the existing maritime radiocommunication solutions. It should be noted that the results presented in the article were used by the IALA while developing the current version of the VDES specification.

Keywords: Maritime radiocommunications, E-navigation, VHF Data Exchange System, VDE-TER, Maritime VHF channels

INTRODUCTION

NoIn recent years, a significant growth in data transmission systems using maritime radio equipment has become a global trend [9]. Such systems are utilized for many reasons: to improve communications between ships and ports, to increase maritime safety, to protect the natural environment, and also to provide means for the novel concept of so-called e-navigation. One of the projects that deals with the enavigation is EfficienSea2 [4], which is aimed at the development of a hybrid communication system for maritime applications including a new standard of wireless data transmission referred to as VDES (VHF Data Exchange System).

The VDES system is being developed not only to increase the achievable transmission rate but also to improve the availability of data transmission services at sea. To a certain degree, the system is an extension of the existing AIS standard (Automatic Identification System) which was mainly created to ensure an efficient and smooth exchange of navigation data between ships and between ships and coastal entities [10].

In accordance with the ITU-R Recommendation [12], the VDES system should provide an access to the radio link, taking into account the existence of the AIS system and effective utilization of its own spectral resources, and users' needs as well. For this reason, the considered standard will have a lower service priority than the AIS.

In general, three segments of the VDES system have been defined: terrestrial segment, satellite segment for uplink, and satellite segment for downlink. The following paper is dedicated to the physical layer of the terrestrial part, which is often referred to as VDE-TER.

For the new maritime data exchange standard, the following transmission channels have been assigned:

- Channels 2027 and 2028 for the ASM system (Application Specific Messages),
- Channels 24, 84, 25, 85 with 100 kHz band each for the VDE-TER segment.

In the VDES system, three modulation and coding schemes (MCS) have been defined. The assumed MCSs and three available transmission bandwidths (25 kHz, 50 kHz and 100 kHz) fully define the capabilities of the VDE-TER; their parameters are included in Table 1 [12].

During the work carried out within the framework of the EfficienSea2 project, software implementation of the physical layer for a VDES system's terrestrial component has been developed and the simulation studies based on that software have been executed. As the next step, measurement tests in the maritime environment have been performed to verify the obtained simulation results. It was one of the first ever measurement campaigns of the VDES physical layer (terrestrial component), conducted in its target conditions (i.e. at sea). The findings of both simulation and measurement activities are summarized in the next sections.

The novelty of the paper can be accentuated by the fact that the results discussed below were presented at the IALA forum and had an impact on the current version of the VDES technical specification [12].

Tab. 1. Achievable throughput in the VDE-TER segment

Modulation and Coding Scheme (MCS)	Throughput (kb/s) per bandwidth (RAW[1]/NET[2])		
	25 kHz	50 kHz	100 kHz
MCS-1 (π/4 QPSK, CR[3]=½)	38.4/15	76.8/32	153.6/66
MCS-3 (8PSK, CR=¾)	57.6/35	115.2/74	230.4/150
MCS-5 (16QAM, CR=¾)	76.8/47	153.6/100	307.3/200

[1] RAW– raw bit rate, [2] NET– net bit rate, [3] CR– code rate *

PHYSICAL LAYER OF VDE-TER SEGMENT

The physical layer of the VDE-TER segment is responsible for transmission and reception of the bit data stream, including channel coding, modulation, symbol shaping, as well as signal filtering and synchronization [12].

For each band, the structure of the frame has been defined (Fig. 1). The frame duration is the same for every bandwidth and equals 26.667 ms. On the other hand, the number of symbols transmitted in a single frame varies depending on the bandwidth: in the case of 25 kHz there are 512 symbols per frame, in the case of 50 kHz – 1024 symbols, and in the case of 100 kHz – 2048 symbols.

As we can see, the frame comprises five blocks:

- The initial block is responsible for power detector's activation,
- The training sequence is composed of the bit '1' concatenated with two orthogonal Barker codes (1+Barker13+Inversed Barker13, so the actual sequence is: *1 1111100110101 0000011001010*). The Barker codes have very good autocorrelation properties, which makes the detection of subsequent frames simple and reliable.
- The third block contains the basic information about the MCS and it is comprised of four bits which are encoded using the Hamming (7,4) code. The resulting sequence is 7 bit long.
- The data block carries the encoded user data based on cyclic and correction code.
- A buffer appended to the frame acts as a time reserve to eliminate the influence of transmission delays caused by the varying distance between the transmit and receive stations.

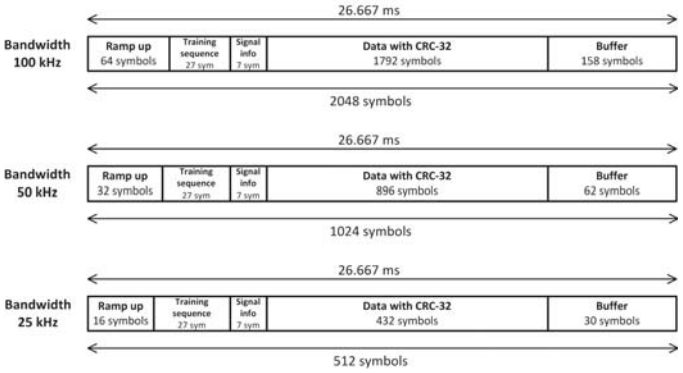

Fig. 1. Single frame structure for the VDE-TER

Figs. 2 and 3 show simplified block diagrams of the VDE-TER transmitter and receiver, respectively.

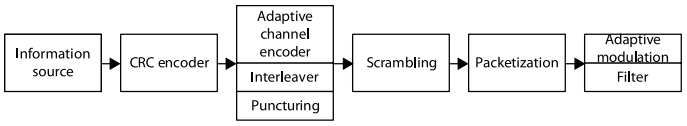

Fig. 2. Simplified VDE-TER transmitter block diagram

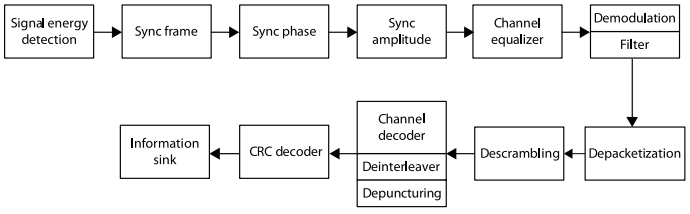

Fig. 3. Simplified VDE-TER receiver block diagram

The first step of the signal transmission process is source data generation. The information sequence prepared in this way is then fed into the CRC32 cyclic encoder, where the 32bit

* The code rate *k/n* is the ratio of the *k-bit* information sequence and the corresponding *n-bit* code word sequence.

checksum is appended. In the next stage, channel encoding is performed using a turbocoder. After that, the processed data is fed into the scrambler and randomized. The resulting data sequence is then packetized, modulated and filtered, and finally it is transmitted over the radio channel.

The first step of the reception procedure is signal detection. It is performed using a power detector. The subsequent stages execute time synchronization, phase and frequency synchronization, and amplitude scaling [18]. After that, the coefficients of the channel equalizer's filter are calculated [7]. Next, filtering and demodulation of the received signal is carried out. Then, the bits are fed into the depacketizer block which selects only those bits that belong to a data block. Each received block is descrambled and turbodecoded. The data reconstructed after turbodecoding is validated (using the CRC32 cyclic decoder) and finally the estimation of the source information is produced.

Turbocoding is a method to detect and correct errors. It is the most significant way to ensure high reliability of digital transmission. The turbocoding (based on the 3GPP2 turbocode) in the VDES system is performed using an interleaver, two identical systematic encoders of the convolutional code, and a puncturing block. The same turbocoder is used for each MCS, but the interleavers and puncturing algorithms vary depending on a scheme that is being utilized. Generally, the standard [12] defines nine versions of the interleaver (one for every possible combination of MCS/bandwidth) and two versions of puncturing (either to obtain CR=1/2 or CR=3/4, see Table 1). The turbodecoder, on the other hand, is comprised of two convolutional code decoders, and interleaver and deinterleaver blocks. The decoding process is performed using a soft-decision Viterbi algorithm SOVA (Soft Output Viterbi Algorithm), in which the metrics are calculated using soft decisions produced by two decoders which "support" each other in subsequent turbodecoding iterations [20].

In the VDE-TER system, three modulation schemes have been defined: π/4 QPSK, 8PSK, and 16QAM. It is assumed that the preamble block (including training sequence and "signal info" field) and the buffer are always modulated using the π/4 QPSK modulation in order to ensure reliable time synchronization (in case of user data, each of the three possible modulation schemes can be used depending on the channel quality). Additionally, to enable soft turbodecoding, each of the analyzed demodulators is equipped with a soft-output decision-making block.

The Root Raised Cosine filter (RRC), with Roll-off factor=0.3, is applied both in the modulator and demodulator. It is used to reduce the modulated signal bandwidth and to minimize the intersymbol interference (ISI).

The essential units in the VDE-TER segment are those responsible for synchronization and reception of signals. The receiving process starts in the signal power detector, which checks whether the average received signal power is above the designated threshold. When the receiver detects a signal, it is necessary to determine the position of the transmitted frame. As soon as there are enough samples of the signal in the receiver's memory, the time synchronization algorithm initiates its operation. The received signal is correlated with the known reference signal (this is possible due to the training sequence placed in the frame structure). The training sequence is composed of two Barker codes (see the description above) which have very good autocorrelation properties. Once the frame's position has been determined and the sufficient amount of data accumulated, the signal phase needs to be evaluated. Phase synchronization consists in comparing the received training symbol positions with their reference positions. Based on the known signal constellation, the amplitude of the received signal is also determined.

In the VDE-TER segment, the system self-adjusts to the condition of the radio channel. It is assumed that on the basis of the MER parameter (Modulation Error Ratio [5]), the system adapts itself to the most suitable modulation and coding scheme (when the transmitter obtains the feedback information from the receiver).

The value of this parameter depends on the level and type of noise that interferes with the signal. Generally, the MER should be interpreted as a distance from the total signal fading and it can be calculated using the following equation [3]:

$$MER(dB) = 10\,log_{10}\left(\frac{P_{signal}}{P_{error}}\right) \quad (1)$$

where:

P_{signal} – RMS (Root Mean Square) power of the 'perfect' signal,

P_{error} – RMS power of the very strongly distorted signal.

The implemented simulator allows to enter the MER value at which the system should change its current MCS scheme.

It is of crucial importance to correctly determine which modulation and coding scheme has been used by the transmitter. On the basis of this information, the receiver selects the appropriate demodulator. The MCS information encoded by the Hamming code is placed in the frame field "signal info" and modulated using the π/4 QPSK modulation. Consequently, to obtain the information about MCS it is necessary to demodulate the received signal and decode the relevant field in the frame. In order to improve the signal-to-noise ratio and to increase the detection probability of the "signal info" field, the following mapping applies to the training and signal information:

- "1" is mapped to π/4 QPSK symbol 3 (1, 1)
- "0" is mapped to π/4 QPSK symbol 0 (0, 0).

By utilizing various MCS schemes and the measured MER, the system can work adaptively, i.e. it can adapt itself to radio channel conditions, thus maximizing the throughput and transmission quality.

In order to minimize the way in which fadings might affect the transmitted signal, a ZF (Zero Forcing) channel equalizer [14], [15], [16] has been introduced. The task of this module is to determine the filter coefficients on the basis of the synchronization signal and the known reference signal.

This module is necessary to minimize the influence of fadings that exist in the maritime radio channel – especially when a ship is in close proximity to the shore, and signal reflection and heavy attenuation can occur.

The last stage of signal processing in the receiver is its filtering and demodulation. Three demodulators have been implemented in the VDE-TER software simulator: π/4 QPSK, 8PSK, and 16QAM. The decision-making blocks are different for each demodulator. Additionally, for the needs of turbodecoding, each of the analyzed demodulators is equipped with a soft-output decision-making module.

TRANSMISSION CHANNELS

In the VDE-TER simulator, three transmission channels have been implemented:

- AWGN (Additive White Gaussian Noise) channel,
- Rayleigh channel – Rayleigh fading channel with additive white Gaussian noise,
- Two-path AWGN channel – two-path maritime channel with additive white Gaussian noise and slow fading.

The first two channels are commonly known and frequently utilized in simulations and analyses of radiocommunication systems (see e.g. [19]), so only the third channel will be introduced here in a more detailed way.

MARITIME RADIO CHANNEL

To facilitate the analysis of a new wireless data transmission system at sea, a novel maritime radio channel model in the VHF band has been defined by IALA. It was observed that in maritime conditions, two channel cases can be distinguished:

- The case where the ship is out at sea, and the multipath propagation is virtually nonexistent (the observations have shown that the delay of the second propagation path on the high seas is a few nanoseconds). Consequently, the only transmission channel in this case is practically an AWGN channel.
- The case where the ship is in the harbor or its vicinity. In this scenario, the multipath effect is significant, and consequently, after investigations, it is recommended. This special scenario should be modelled as a two-tap AWGN channel in which the second path attenuation varies depending on the ship location and the number of reflecting objects in the harbor [6].

In both scenarios mentioned above, it is assumed that due to small speed of ships and other objects nearby, the Doppler offset is small and almost constant. Consequently, the Rayleigh fading effect is virtually nonexistent.

Therefore, three variants of the maritime radio channel have been proposed, with their parameters listed below:

- Delay of the second path in relation to the main path is 10 μs,
- Attenuation of the second path (second tap) with respect to the first one depends on the severity of the multipath phenomenon and might be equal to: 3 dB, 6 dB or 10 dB,
- Doppler shift is almost constant and does not exceed 5 Hz at 160 MHz.

SIMULATION RESULTS

The simulation research has been carried out using the software developed by the authors in the C++ language. The transceiver and radio channel blocks have been implemented in software. In each simulation, the number of transmitted frames (sufficient to reliably obtain the BER equal to 10^{-6}) and the appropriate MCS scheme for a given bandwidth were indicated. Phase synchronization, amplitude estimation, and scrambler (descrambler) and turbocoder (turbodecoder) blocks were also included. Furthermore, the simulations were performed for two transmission channels (AWGN and the maritime radio channel).

CHARACTERISTICS OF BER AND BLER FOR VARIOUS MCSS

The characteristics of bit error rate (BER) vs. E_b/N_0 and block error rate (BLER) vs. E_s/N_0 for MCS-1, MCS3 and MCS-5 in the AWGN channel are presented in Figs. 4, 5 and 6. In each case, the results have been obtained for three channel bandwidths: 25 kHz, 50 kHz, and 100 kHz. The bit error rate characteristics have been compared to the theoretical curves for QPSK (MCS-1), 8PSK (MCS-3) and 16QAM (MCS5).

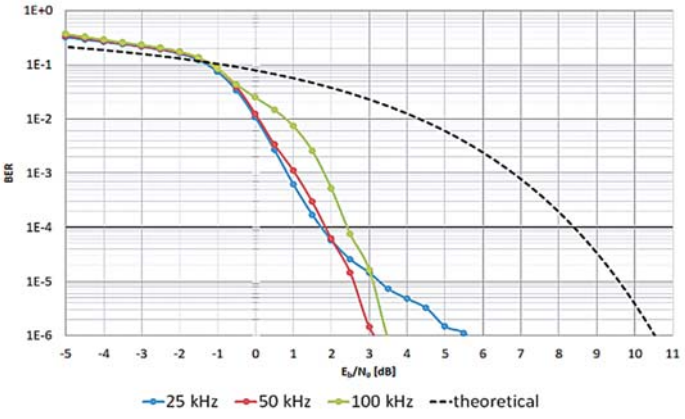

Fig. 4. BER vs. E_b/N_0 for MCS-1 in the AWGN channel

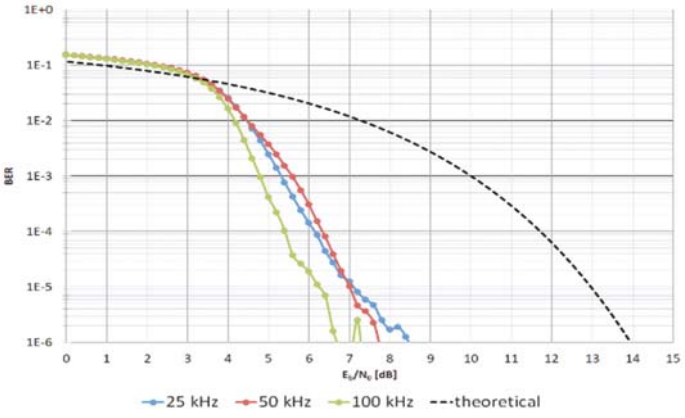

Fig. 5. BER vs. E_b/N_0 for MCS-3 in the AWGN channel

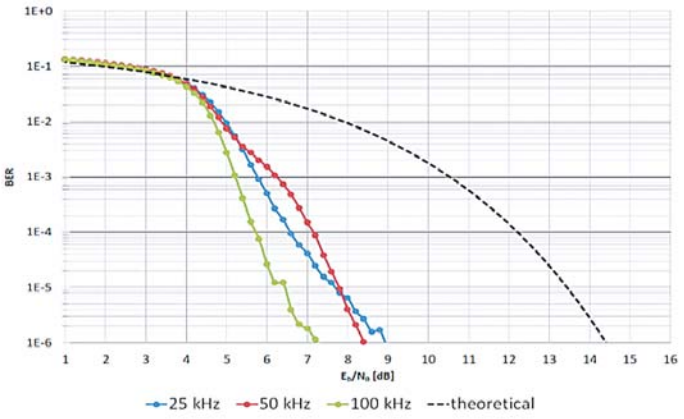

Fig. 6. BER vs. E_b/N_0 for MCS-5 in the AWGN channel

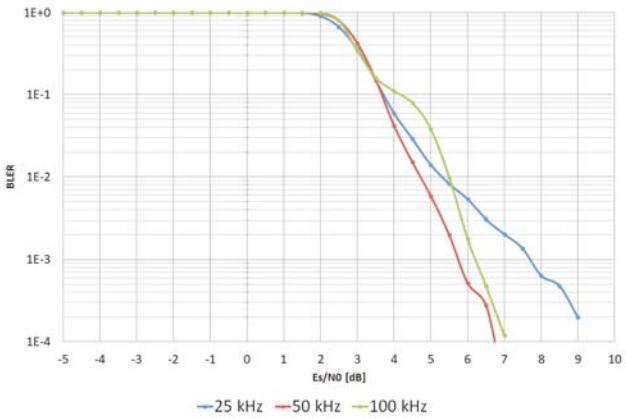

Fig. 7. BLER vs. E_s/N_0 for MCS-1 in the AWGN channel

Table 2 collates coding gains observed for each of the analyzed MCS schemes. The gain values have been calculated with respect to the theoretical BER curves, for BER value of 10^{-6}.

Tab. 2. Coding gains for BER=10^{-6}

Modulation and coding scheme (MCS)	Coding gain [dB]		
	25 kHz	50 kHz	100 kHz
MCS-1	5	7	7.5
MCS-3	5.5	6	6
MCS-5	7.5	7.5	7.3

As we can see, the largest coding gain can generally be achieved for the 100 kHz bandwidth, because in this case the data blocks are the longest, which improves the turbodecoding quality. On the other hand, the 100 kHz bandwidth requires highly reliable time synchronization, as one symbol contains 4 signal samples. Consequently, any synchronization error (e.g. shift by one sample on the time scale) might result in a transmission error. This issue is much less significant in the 50 kHz and 25 kHz bandwidths, because in these cases one symbol is comprised of 8 and 16 samples, respectively.

The block error rate characteristics indicate the E_s/N_0 values at which at least one block of data on the average can be received correctly. As we can see in Figs. 7–9, in the case of MCS-1 not even one block can be sent successfully if E_s/N_0 is less than 2.5 dB. In the cases of MCS-3 and MCS-5, the respective E_s/N_0 threshold values are 9 dB and 11 dB.

Table 3 presents the simulation results obtained for three radio channel models (AWGN and two versions of the maritime radio channel) and for selected E_b/N_0 values. These results indicate that the first version of the maritime channel (delay=30 μs, attenuation=20 dB) has slightly worse BER characteristics compared to the AWGN channel. On the other hand, the utilization of the other maritime channel (delay=10 μs, attenuation=3 dB) results in substantial degradation of the reception quality (BER increases by several orders of magnitude).

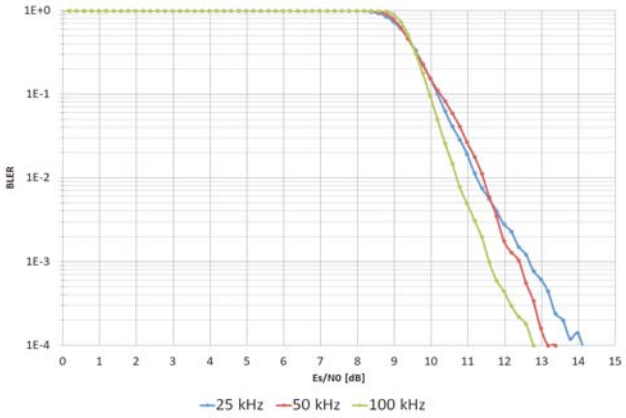

Fig. 8. BLER vs. E_s/N_0 for MCS-3 in the AWGN channel

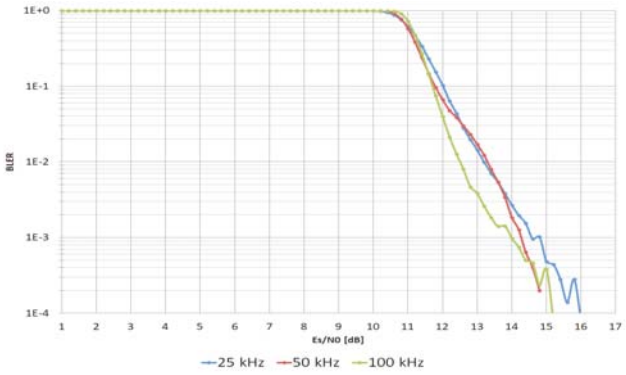

Fig. 9. BLER vs. E_s/N_0 for MCS-5 in the AWGN channel

Tab. 3. BER for three different radio channels (without equalizer)

	Bandwidth	AWGN channel	Maritime channel	
			delay=30μs att.=20dB	delay=10μs att.=3dB
MCS-1	25 kHz (E_b/N_0=5,5dB)	1,1 E-6	6,0 E-7	8,8 E-7
	50 kHz (E_b/N_0=3dB)	1,4 E-6	2,5 E-6	3,5 E-5
	100 kHz (E_b/N_0=3,5dB)	8,5 E-7	1,1 E-5	1,1 E-2

	Bandwidth	AWGN channel	Maritime channel	
			delay=30μs att.=20dB	delay=10μs att.=3dB
MCS-3	25 kHz (E_b/N_0=8,4dB)	1,3 E-6	1,2 E-6	3,1 E-6
	50 kHz (E_b/N_0=7,8dB)	6,7 E-7	6,7 E-7	1,1 E-3
	100 kHz (E_b/N_0=6,8dB)	6,7 E-7	1,4 E-6	1,5 E-1
MCS-5	25 kHz (E_b/N_0=9dB)	7,7 E-7	1,1 E-6	6,9 E-6
	50 kHz (E_b/N_0=8,4dB)	1,0 E-6	6,7 E-7	2,3 E-2
	100 kHz (E_b/N_0=7dB)	1,8 E-6	2,2 E-6	1,7 E-1

THE INFLUENCE OF SYNCHRONIZATION ERROR ON TRANSMISSION QUALITY

Figure 10 shows the characteristics of the following three parameters as functions of E_s/N_0:

- Time synchronization error rate (denoted as 'sync time error' in the figure),
- Error of "signal info" field reception (denoted as 'signal info error') – the "signal info" field carries the information about the current MCS scheme, so the erroneous reception of this field may result in incorrect signal demodulation,
- Block error rate (BLER).

These curves have been drawn for MCS-1.

Figure 10 illustrates how the synchronization error and errors of "signal info" field reception affect the transmission quality.

In the perfect scenario, there shouldn't be any sync and signal info errors when E_s/N_0 is large enough to send at least one block correctly (i.e. when BLER is less than 1). As was mentioned in the previous subsection, this threshold value of E_s/N_0 is approx. 2.5 dB (for MCS-1).

In the case of MCS-1, this perfect scenario is not achieved, but the results are still satisfactory. As we can observe, at E_s/N_0=2.5 dB, the signal info error is less than 10^{-2} and the sync error is less than 10^{-4}. Practically, it is assumed that the transmission is correct when BLER is less than 10^{-1}, and this condition is satisfied in the discussed figure.

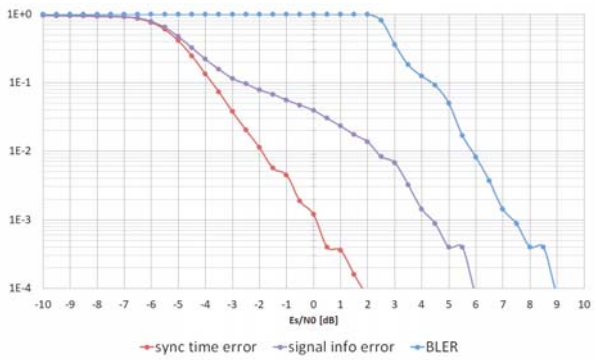

Fig. 10. Synchronization error rate, "signal info" field reception error, and BLER for MCS-1

THE EFFICIENCY OF THE ZERO-FORCING CHANNEL EQUALIZER

Figure 11 shows the 8PSK modulation constellation (MCS-3) for the AWGN channel (a), maritime radio channel without equalizer (b), and maritime radio channel with equalizer (c).

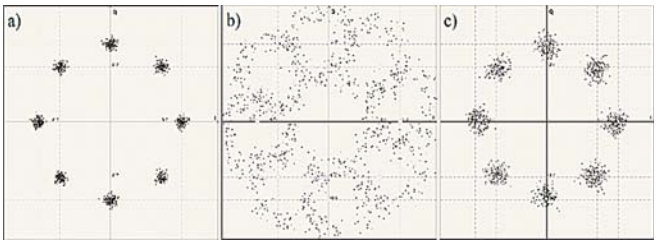

Fig. 11. MCS-3 signal constellation for: a) AWGN channel without equalizer, b) maritime channel without equalizer, c) maritime channel with equalizer

This figure mainly demonstrates the efficiency of the zero-forcing channel equalizer when used in the VDES system. In the discussed scenario, the ZF equalizer is used in the presence of selective frequency fadings. New characteristics of the filter are calculated for every subsequent training sequence, i.e. for every frame. If the equalization is not used, the fading and intersymbol interference (ISI) strongly affect the transmitted signal and make correct transmission almost impossible (see fig. 11b). Obviously, this issue is becoming more serious when higher-order modulations are utilized. On the other hand, the signal constellations show that the influence of ISI is substantially reduced when the equalizer is used (theoretically, the ZF equalizer is perfect, i.e. removes all ISI in a fully noiseless channel). At the same time, we might also observe that using the equalizer will result in noise amplification; it is a drawback of this solution, but it is consistent with the general theory of the zero-forcing equalizer.

It should be mentioned here that for the purpose of the discussed simulations, a slightly modified version of the ZF equalizer was implemented, which assumed adding a type of a limiter. Theoretically, in the presence of deep fading, the filer's coefficients for some frequencies would be enormous and the filter characteristics would approach infinity, which would be impossible to implement. To avoid such situations, the filter coefficients whose values were above the threshold were simply limited ("truncated") by the algorithm.

THE INFLUENCE OF CHANNEL INFORMATION DELAY ON THE ACHIEVABLE BIT RATES

Figures 12–14 illustrate the influence of the auxiliary information about the channel state on the transmission rate. Since the VDES system utilizes adaptive modulation, the timely information about the current state of the radio channel is of paramount importance and the lack of such data significantly degrades the efficiency and performance of the system.

The characteristics in Figs. 12–14 represent the bit rate vs. E_b/N_0 in the AWGN channel and have been obtained for three bandwidths: 25 kHz, 50 kHz and 100 kHz. Two cases of channel information delay have been considered: no delay (red bars) and 3 frames delay (blue bars).

Obviously, as the E_b/N_0 increases, so does the bit rate, which is mainly due to the adaptive modulation and coding algorithms. The better the channel quality, the better the MCS and, consequently, the higher the bit rate.

At the same time, we can observe that the channel state info delay negatively affects the bit rate for E_b/N_0 from 5 dB to 9 dB. For other E_b/N_0 values, the resulting bit rates are almost identical and do not seem to be affected by the discussed delay. The above observation is true for every analyzed bandwidth.

These results have shown that in the future stages of VDES development, a new MCS scheme should be introduced to increase the achievable bit rates.

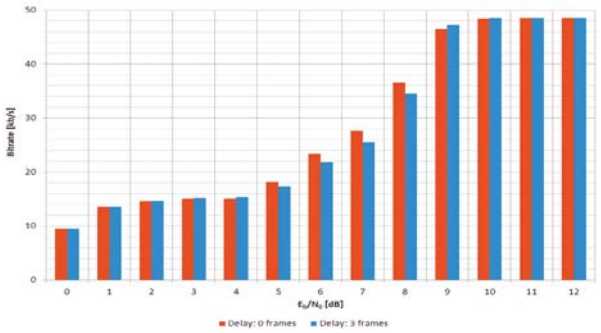

Fig. 12. Bit rate vs. E_b/N_0 for 25 kHz AWGN channel

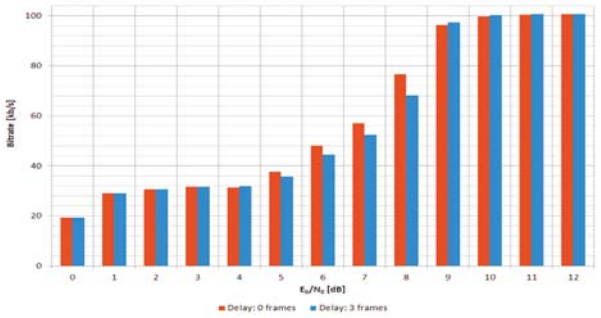

Fig. 13. Bit rate vs. E_b/N_0 for 50 kHz AWGN channel

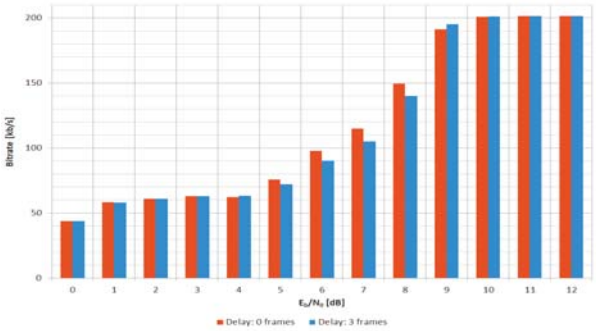

Fig. 14. Bit rate vs. E_b/N_0 for 100 kHz AWGN channel

MEASUREMENT RESULTS

In the period between 23 March 2017 and 6 April 2017, a measurement campaign of the VDES physical layer was carried out as part of the EfficienSea 2.0 project. As a result, roughly 6 terabytes of measurement data were collected and subsequently subjected to further, more thorough, analysis. The main goal of this analysis and processing was to obtain the bit error rate characteristics that could serve as a basis for some conclusions regarding the performance of the system. Most importantly, it allowed to compare the results obtained during the simulation analysis with the actual measurement data. For the purpose of this measurement campaign, the receiver part of the VDES simulator was utilized [1]. Additionally, a software interface has been developed which allowed to process data samples collected during the measurements at sea.

Figure 15 presents the general idea of the measurements. As it can be seen, during the campaign, one VDES transmitter and two VDES receivers were utilized. The transmitter was located in the Gedser Havn port (Denmark), whereas one of the receivers was aboard the Scandlines Ferry M/F Berlin, and the other one was aboard the Scandlines Ferry M/F Copenhagen. To make the measurements as realistic as possible, the installation aboard those vessels took advantage of the existing VHF installation. To verify how antenna height affects the propagation, the antennas on the two vessels were installed at different heights (M/F Berlin: 18 m and M/F Copenhagen: 23 m). The entire route length from Gedser to Rostock was about 48 km (one-way). It should be mentioned that when the ferries were at the maximum possible distance away from the transmitter, they were partly in the inland area, which made the measurement results even more valuable, since in that case the level of interference was higher and the propagation conditions – much tougher.

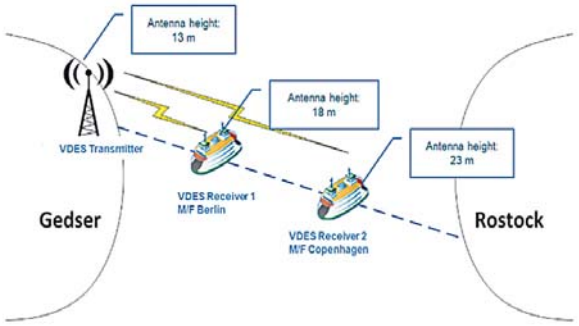

Fig. 15. General concept of the measurement campaign at sea

The technical parameters of the transmitter and two receivers used during the campaign are listed below.

Technical parameters of the transmitter:

- Height of the antenna above ground: 13 m,
- Height of the ground in the transmitter's location: 2 m a.s.l.,
- Frequency band: 160 MHz,
- Distance between the antenna's location and the shore: 0 m at the ferry landing bridge,
- Transmitter power: 6.3 W (π/4-QPSK) or 4 W (16QAM),
- Antenna gain: 3 dBi,
- Antenna cable length and type: 12 m, RG 214.

Technical parameters of the receivers:

- Height of the antenna: M/F Berlin: 18 m, M/F Copenhagen: 23 m,

- Location description: one ship: top of the wheel house, the other one: top of the radar mast,
- Receiver sensitivity: -110 dBm (π/4-QPSK) or -96 dBm (16-QAM),
- Antenna gain: 3 dBi,
- Antenna cable length and type: 17 m, RG 214.

A hardware platform used during the measurements was a proprietary solution comprised of a digital signal processor and a FPGA module on which the transmission and receive channels were implemented. A digital-to-analog converter and an analog-to-digital converter were also part of the setup, as well as the DR 200 broadband power amplifier (version D) made by Prana. The bits were processed separately in the I and Q channels (that includes filtering and mixing). The receive data rate of the FPGA was 19.66 Mbps, and the sampling rate was 4.9152 MHz.

DATA SEQUENCE UTILIZED DURING THE MEASUREMENT CAMPAIGN

During the measurement campaign, a predefined data sequence (lasting 20 seconds in total) was employed. That sequence was transmitted in a defined order and that order was strictly followed throughout the entire campaign. The transmitter located in the Gedser port transmitted the data in the following sequence:

- First, the data was transmitted in the 25 kHz bandwidth in the following order: MCS-1, MCS-3, MCS-5,
- Then, the data was transmitted in the 50 kHz bandwidth in the following order: MCS-1, MCS-3, MCS-5,
- After that, the data was transmitted in the 100 kHz bandwidth in the following order: MCS1, MCS-3, MCS-5,
- No transmission took place during the periods of switching between different bandwidths. During those periods the slots could be occupied by noise or other interference signals.

The transmitted data sequence spans across a number of time slots assigned to specific modulation schemes. Table 4 contains the information regarding the number of slots available for a given MCS. Additionally, a total duration of the time slot series which depends on the utilized modulation scheme is included.

As it can be seen, it takes exactly 20 seconds to transmit the entire sequence. At this point it should be mentioned that one measurement file covers 60 seconds of data (i.e. three transmitted sequences – a total of 2250 time slots).

During the time slots when no data is sent, the transition from one available bandwidth to another is being performed. That approach has been chosen to facilitate smooth filter passband change. Eight slots with noise located at the end of the transmitted sequence allowed for the measurements of noise power and distortion in the receiver.

It should be noted that it was intentional to assign different numbers of slots to different MCSs. The respective number of slots was selected in such a way that the number of user bits was similar for each case (i.e. for each MCS and bandwidth), as discussed in the next subsection. Consequently, the resulting BER characteristics could be reliably compared to one another.

Tab. 4. Number of time slots and their total duration in the transmitted data sequence

		25 kHz	50 kHz	100 kHz
MCS-1	Slots	250	116	57
	duration [s]	6.67	3.09	1.52
MCS-3	Slots	106	50	25
	duration [s]	2.83	1.33	0.67
MCS-5	Slots	79	38	19
	duration [s]	2.11	1.01	0.51
NO TRANSMISSION	Slots	10		
	duration [s]	0.27		
TOTAL	Slots	750		
	duration [s]	20		

ATTENUATION IN THE RECORDED DATA

The data format used during the measurement campaign contained the information about time periods when additional attenuation was inserted into the analog receiver's path and the receiver did not operate at its maximum sensitivity. Generally, this occurred in two situations:

- The first situation is caused by the VDES signal itself and in the case of the campaign discussed in this document, it occurred when the measurements were conducted close to Gedser (approx. at the distance of 2-3 km),
- The second situation was related to the blocking typically caused by the ships' VHF equipment (AIS, VHF radio).

In Figure 16, the attenuation activity periods are shown as a function of ship's position. It illustrates – for the specific file number – the data percent for which the attenuation was actually active.

Both Fig. 16 and other obtained results confirm that the attenuation was mainly active when the ship was in the vicinity of the shore.

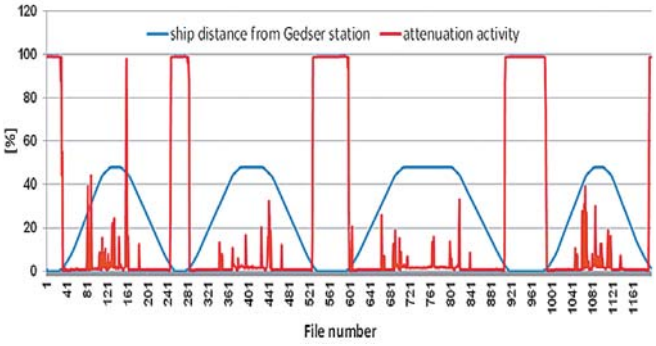

Fig. 16. Attenuation activity vs. file number (ship's distance from Gedser station is also indicated)

METHOD TO CALCULATE SIGNAL-TO-NOISE RATIO

In order to obtain correct bit error rate characteristics, it is first necessary to derive the signal-to-noise ratio (usually referred to as SNR) for the given system. This parameter indicates the ratio of the useful signal power to the noise power in the given bandwidth. The expressions (2) and (3) indicate how to calculate SNR and Es/N0 (i.e. the ratio of the energy per symbol to noise power spectrum density).

$$\frac{S}{N} = \frac{R_S \cdot E_S}{B_N \cdot N_0} = \frac{R_S \cdot E_S}{\frac{F_S \cdot N_0}{2}} = \frac{2 \cdot R_S \cdot E_S}{F_S \cdot N_0} \tag{2}$$

$$\frac{E_S}{N_0} = \frac{S \cdot F_S}{N \cdot 2 \cdot R_S} \tag{3}$$

The symbols used in formulas (2) – (3) represent: S – signal power, N – noise power, R_s – symbol rate, B_N – noise bandwidth, F_s – sampling frequency, E_s – energy per symbol, N_0 – noise power spectrum density (N_0=kTB, where k is the Boltzmann constant, T is the absolute temperature of the load, and B is the measurement bandwidth).

It should be noted that the preamble (see Fig. 17) is not used in the (S+N) calculations according to formulas (2) – (3). It is due to the fact that the preamble is always modulated using the same modulation scheme, i.e. π/4-QPSK.

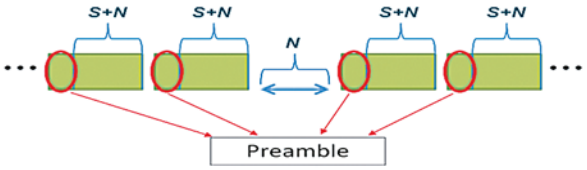

Fig. 17. Illustration of considerations for signal power to noise power determination

The symbol rates for various bandwidths which are necessary to be employed in the formulas considered above are presented in Table 5 [12].

THE ACHIEVABLE RANGE OF THE VDES SYSTEM

Depending on the modulation scheme and bandwidth, different ranges of the VDES system were recorded. In this case, the term "range" indicates a maximum distance at which the data frame could still be correctly received. The assumed BER threshold value is 10^{-5}.

The theoretical ranges of the VDES system were calculated using the ITU-R P.1546-5 [11] propagation model. These calculations have been made for two cases:

- Most robust scenario (best case): π/4-QPSK modulation and bandwidth of 25 kHz,
- Highest throughput scenario (worst case): 16QAM modulation and bandwidth of 100 kHz.

Figure 18 presents the maximum and minimum useful ranges for antenna height of 18 m.

Fig. 18. Maximum and minimum useful range for antenna height of 18 m

The theoretical calculations carried out on the basis of the ITU-R P.1546-5 propagation model indicate that the maximum useful range for the VDES system is about 62.9 km. Such a range is achievable for data reception using the π/4-QPSK modulation scheme, the 25 kHz bandwidth, and the receiving antenna height of 23 m. On the other hand, the shortest useful range has been determined for the 16-QAM modulation scheme and the bandwidth of 100 kHz. Assuming such a configuration, the achievable range did not exceed 30.9 km for the receiving antenna height of 18 m.

The measurements confirmed the results of the theoretical analysis realized earlier: the longest range was observed for the π/4-QPSK modulation scheme and the bandwidth of 25 kHz, whereas for the 16-QAM modulation and the bandwidth of 100 kHz, the achievable range was the shortest. Greater antenna height (23 m as opposed to 18 m) resulted in the range increase by approx. 3 km.

Figures 19 and 20 present the useful VDES ranges. The curves were drawn for two different antenna heights and for two different modulation schemes and bandwidths, represented here by the respective MCS.

In both figures, the line-of-sight distance is presented as the black dotted line. To calculate this parameter, it was first necessary to obtain the radio horizon distance, separately for the transmitter and the receiver. To do so, the following formula [2] was used:

$$d_{horizon}[km] \approx 4.12 \cdot \sqrt{h} \tag{4}$$

where h is the transmitter/receiver antenna height (in [m]), respectively.

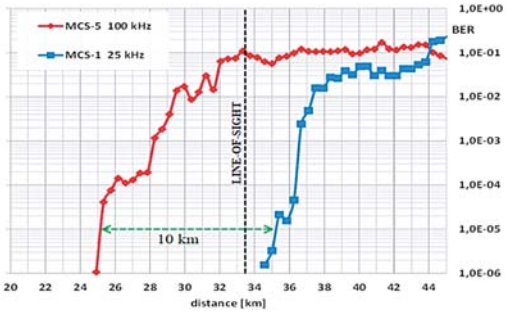

Fig. 19. Useful VDES ranges for MCS-1 and MCS-5 at antenna height of 18 m

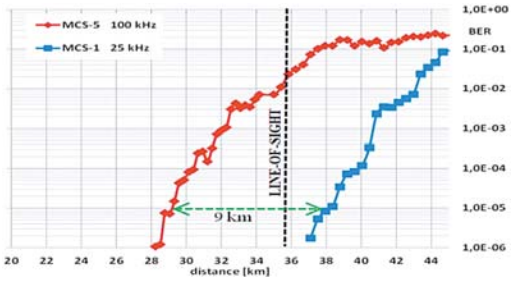

Fig. 20. Useful VDES ranges for MCS-1 and MCS-5 at antenna height of 23 m

Finally, the line-of-sight distance was calculated as the sum of radio horizon distances for the transmitter and the receiver:

$$d_{LOS} = d_{horizon_{transmitter}} + d_{horizon_{receiver}} = \\ = 4.12 \cdot (\sqrt{h_{transmitter}} + \sqrt{h_{receiver}}) \quad (5)$$

For the case shown in Fig. 19, where $h_{transmitter}$ = 15 m and $h_{receiver}$ = 18 m, $d_{LOS} \approx$ 33.44 km, while for that shown in Fig. 20, where $h_{transmitter}$ = 15 m and $h_{receiver}$ = 23 m, $d_{LOS} \approx$ 35.72 km.

It can be observed that in the cases of LOS (line-of-sight) scenarios, the measured useful ranges were generally consistent with the theoretical results obtained using the ITU-R P.1546-5 propagation model [11]. In LOS, the range of the system is mainly limited by the receiver's sensitivity and the AWGN noise.

For the NLOS scenarios (i.e. after crossing the radio horizon line), the consistency between the theoretical and measured data was no longer observed. The ITU-R P.1546-5 model only covers the attenuation increase due to crossing the radio horizon, but it does not include other significant effects that occur in the NLOS situation. The most important factor that limits the actual range in NLOS is signal fading, and this particular phenomenon cannot be analyzed using the ITU-R P.1546 model.

BIT ERROR RATE CHARACTERISTICS OF THE SYSTEM

The results obtained in the VDES receiver's simulator included bit error rate (BER) characteristics. To calculate them, it was necessary to divide the number of erroneous bits (those with an incorrect checksum or those that could not be decoded due to synchronization errors) by the total number of all transmitted bits.

Such an approach allowed to analyze how the bit error rate actually depends on the signal power for various scenarios, including three modulation schemes and three bandwidths. Table 6 collates the values of E_s/N_0 for which BER = 10^{-6}.

Figs. 21 and 22 show the selected bit error rate characteristics of the VDES system.

The analysis of these characteristics shows that the smallest value of E_s/N_0 for BER=10-6 is achieved for the π/4-QPSK modulation and the bandwidth of 25 kHz, with the antenna height of 23 m. Generally, narrower bandwidths resulted in better bit error rate characteristics. For higher modulation and coding schemes (e.g. MCS-5), substantial degradation of the BER can be observed. This is caused by the fact that higher order modulations (like 16-QAM) – while providing higher throughput and allowing for more efficient use of the spectrum – are much more vulnerable to any interference or distortions than the basic modulation schemes (QPSK).

Tab. 6. The values of E_s/N_0 [dB] for BER = 10^{-6}

	Antenna height=18 m			Antenna height=23 m		
	MCS-1	MCS-3	MCS-5	MCS-1	MCS-3	MCS-5
25 kHz	6.25	10	13.25	5.5	8.75	11.75
50 kHz	8.75	11.75	14	7.75	10.5	13.5
100 kHz	10.5	13.5	15	9.25	11.75	14

CONCLUSIONS

The VHF Data Exchange System is one of the key solutions that will influence the development of maritime communications. According to IMO or IALA assumptions [8], VDES will be one of the essential "platforms" for future e-navigation services and applications, and as such it will also be a crucial system from the safety of navigation point of view.

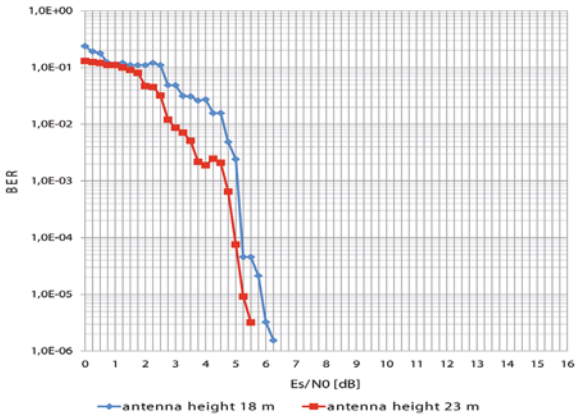

Fig. 21. BER vs. E_s/N_0 for MCS-1 and bandwidth 25 kHz

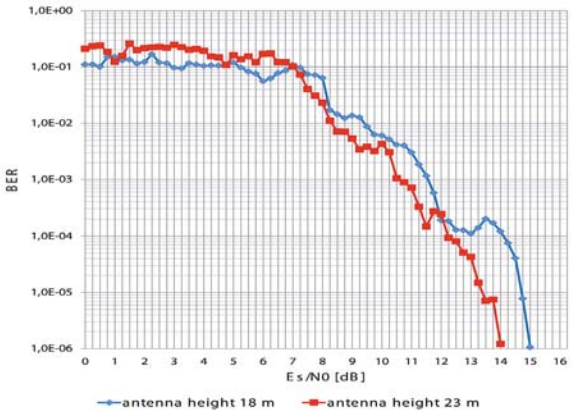

Fig. 22. BER vs. E_s/N_0 for MCS-5 and bandwidth 100 kHz

One of the main tasks assigned to the National Institute of Telecommunications in the EfficienSea 2.0 project was participation in technical standardization of the VDES system (mainly through cooperation with IALA). All the results presented in the paper were obtained as part of this cooperation, therefore it can be emphasized that they substantially influenced the present form of the VDES standard.

The results presented in the article clearly show that the VDE-TER ensures a large coding gain, which significantly improves the quality of data transmission and increases the bit rate. The VDE-TER provides the useful data rates of up to 200 kb/s, which is an important improvement, compared to the currently existing systems (e.g. AIS).

It should be noted that, during the measurements, a zero-bit error rate for each MCS and bandwidth considered was achieved.

In the case of LOS (line-of-sight) scenarios, i.e. before crossing the radio horizon, the measured useful ranges were generally consistent with the theoretical results obtained using the ITU-R P.1546-5 propagation model. Small discrepancies between the theoretical and measured data in this case could be due to:

- man-made noise (ITU-R P.372-8) [13],
- interference with the legacy systems onboard the ships.

In the LOS scenarios, the range of the system is mainly limited by the receiver's sensitivity and the AWGN noise. After crossing the horizon line, the NLOS (non-line-of-sight) becomes the main mechanism and in this case, the observed differences between the theoretical and measured data were much more substantial than for the LOS.

In the NLOS case, the range is mainly limited by the fading (it is not AWGN any more). This is the major reason of significant discrepancies observed between the theoretical and actual ranges. Even though the propagation model ITU-R P.1546-5 takes into account the increased attenuation due to crossing the horizon line, it does not include inevitable signal fadings that occur in the NLOS environment.

It should also be observed that in the NLOS case, the MCS-5 cannot be utilized any more, and the MCS-1 remains the only option.

Generally, the obtained results fall into „the area" between the theoretical results for the AWGN channel and the Rayleigh channel.

At this point, it should also be recalled, that VDES – in its final version – should also include a satellite segment [17]. At this point however, the issue of frequency allocations for that purpose is a source of controversy in many countries. Thus, any decisions in that respect have been postponed until the World Radiocommunication Conference WRC-19 which will take place in autumn 2019 in Sharm El Sheikh, Egypt.

REFERENCES

1. Bronk K., Mazurowski M., Rutkowski D., Wereszko B.: *Simulation Investigations of the Physical Layer for a VDES System's Terrestrial Component* (in Polish). Przegląd Telekomunikacyjny i Wiadomości Telekomunikacyjne, No. 6/2016, pp. 467-470.
2. Busi R.: *High Altitude VHF and UHF Broadcasting Stations*. Technical Monograph, p. 3108-1967, 1967.
3. Chen Q., Song Y., Hu F., Cai C.: *A Novel Method for Adjusting Digital Predistortion with Modulation Error Ratio in OFDM System*. 9th International Congress on Image and Signal Processing, BioMedical Engineering and Informatics (CISP-BMEI), 2016.
4. EfficienSea 2 project official website: *http://www.efficiensea2.org/*.
5. ETSI Technical Report ETR 290: *Digital Video Broadcasting (DVB); Measurement guidelines for DVB systems*, 1997.
6. General Lighthouse Authorities, Report No: RPT-09-JSa-14: *VDES Channel Sounding Campaign*, Safar Jan, 2015.
7. Gong M., Chen F., Yu H., Lu Z., and Hu L.: *Normalized adaptive channel equalizer based on minimal symbol-error-rate*, IEEE Transactions on Communications, vol. 61, no. 4, pp. 1374–1383, 2013.
8. IALA Guideline G1139: *The Technical Specification of VDES*, Edition 1.0, December 2017.
9. IMO, Report MSC 85/26/Add.1 Annex 20: *Strategy for the Development and Implementation of enavigation*, 2008.
10. ITU-R Recommendation M.1371-5: *Technical characteristics for an automatic identification system using time division multiple access in the VHF maritime mobile frequency band*, 2014.
11. ITU-R Recommendation ITU-R P.1546-5: *Method for point-to-area predictions for terrestrial services in the frequency range 30 MHz to 3000 MHz. Radiowave propagation*, 2013.
12. ITU-R Recommendation M.2092-0:*Technical characteristics for a VHF data exchange system in the VHF maritime mobile band*, 2015.
13. ITU-R Recommendation P.372-8: *Radio noise. Radiowave propagation*, 2003.
14. Mark J. W., Zhuang W.: *Wireless Communications and Networking*. Pearson, 2003.
15. Molisch A. F.: *Wireless Communications*, Wiley, 2005
16. Proakis J.: *Digital Communications*, McGraw Hill, 2000
17. Raulefs R., Stenbock T. A., Dammann A., Plass S.: *Physical Layer Design Towards VHF Data Exchange (VDE)*

Link, German Aerospace Center (DLR), Institute of Communications and Navigation.

18. Robertson P.: *Optimal Frame Synchronization for Continuous and Packet Data Transmission*. Dissertation, 1995.

19. Seybold J.S.: *Introduction to RF Propagation*, Wiley, 2005

20. Woodard J. P., Hanzo L.: *Comparative Study of Turbo Decoding Techniques: An Overview*, IEEE Transactions on Vehicular Technology, vol. 49, no. 6, November 2000.

CONTACT WITH THE AUTHORS

Krzysztof Bronk
e-mail: K.Bronk@itl.waw.pl

National Institute of Telecommunications
Wireless Systems and Networks Department
Jaskowa Dolina 15
80-252 Gdansk
Poland

sciendo

POLISH MARITIME RESEARCH 1 (101) 2019 Vol. 26; pp. 107-116
10.2478/pomr-2019-0012

MOTION CONTROL AND COLLISION AVOIDANCE ALGORITHMS FOR UNMANNED SURFACE VEHICLE SWARM IN PRACTICAL MARITIME ENVIRONMENT

Jiayuan Zhuang[1]
Lei Zhang[1]
Zihe Qin[2]
Hanbing Sun[1]
Bo Wang[1]
Jian Cao[1]
[1] College of Shipbuilding Engineering, Harbin Engineering University, China
[2] Zhuhai Yunzhou Intelligence Technology Ltd., China

ABSTRACT

The issue of controlling a swarm of autonomous unmanned surface vehicles (USVs) in a practical maritime environment is studied in this paper. A hierarchical control framework associated with control algorithms for the USV swarm is proposed. In order to implement the distributed control of the autonomous swarm, the control framework is divided into three task layers. The first layer is the tele-operated task layer, which delivers the human operator's command to the remote USV swarm. The second layer deals with autonomous tasks (i.e. swarm dispersion, or avoidance of obstacles and/or inner-USV collisions), which are defined by specific mathematical functions. The third layer is the control allocation layer, in which the control inputs are designed by applying the sliding mode control method. The motion controller is proved asymptotically stable by using the Lyapunov method. Numerical simulation of USV swarm motion is used to verify the effectiveness of the control framework.

Keywords: USV; swarm control; collision avoidance; sliding mode; artificial potential field.

INTRODUCTION

In recent years, the concept of marine ranching has become a research hotspot. However, in a real case, it is a high risk that the marine ranching may get stolen, and more than ten thousand dollars can be lost in a single night. Thus, the surveillance and observation performed by a number of cooperating USVs is of great practical significance. Beside the surveillance task and patrolling the growth environment of marine creatures, it is also sometimes necessary to achieve the roundup of thieving ships.

The USV motion control has received high attention from control communities in the past decades, and the research topics about USVs were focused on path planning, path following, and formation keeping [1-3]. Recently, there are two significant trends in research focused on USV motion control. One is to equip the control system with intelligence, or in other words to achieve autonomous control of USV, while the other one is to extend the autonomous control from a single vessel to a number of cooperating vessels.

So far, studies on multi-agents are mainly about formation keeping, obstacle avoidance, and connectivity maintaining [4-6]. For the formation keeping, extensive studies have been made, and the study objects include satellites, aircrafts, vessels, and underwater vehicles. During the research progress, three dominating methods for formation control have been universally acknowledged, i.e. the leader-follower method [7], the virtual structure method [8-9], and the behavior based

method [10]. The formation control can preserve the desired formation well, but the controller is centralized, and the members are not endowed with the capability of decision-making. Thus, when dealing with some problems, for instance avoiding obstacles and/or collisions with other fleet's members, the controller might get unstable [11].

It is worth mentioning that the concept of swarm control has become a focus recently. It aims to achieve automatic control of a multi-agent system [12-13]. Being superior to the formation control, the swarm control focuses on attaching robotics with intelligence. Much of the inspiration for artificial swarms stems from the study of biological swarms, and most of the earlier investigations that focus on this general theme of artificial swarm consider a homogenous swarm [14, 15]. In Cepeda-Gomez et al. [14], a robust sliding mode control strategy is implemented on two competing multi-agent swarms, called pursuers and evaders. The proposed control achieves the stability and the ability to capture the evaders by the pursuers despite the uncertainties in the evaders' behavior. Liu et al. [16] have studied the problem of bilateral human-swarm interaction, which enables a human operator to simultaneously interact with a group of swarm robots in a remote environment. The authors have developed a task-oriented control framework for 2-DOF robots.

So far, swarm research is mainly about ground robots and unmanned aerial vehicles. In general, USV swarm is the object of research in the aspects of obstacle avoidance, formation control, and collision avoidance.

In this paper, the swarm control problem of a group of autonomous USVs is studied, and a hierarchical control framework is proposed. The underactuated property is considered in the controller design, and control allocation is then supplemented. According to different functions of tele-operated task, autonomous tasks, and control allocation, the designed controller has three layers. The controller is proved asymptotically stable by using the Lyapunov method. Numerical simulation is also provided to illustrate the validity and effectiveness of the proposed method.

USV DYNAMICS

In motion control of ships in the horizontal plane, it is conventional to ignore heave, pitch, and roll motions, and only consider such motions as surge, sway and yaw. Assume that the swarm is composed of n USVs, and for the *i*th USV, the mathematical equations of kinematics and kinetics are defined as follows [17]:

$$\begin{aligned} \dot{\boldsymbol{\eta}}_i &= \boldsymbol{J}_i(\psi_i)\boldsymbol{v}_i \\ \boldsymbol{M}_i\dot{\boldsymbol{v}}_i &= -\boldsymbol{C}(\boldsymbol{v}_i)\boldsymbol{v}_i - \boldsymbol{D}_i\boldsymbol{v}_i + \boldsymbol{\tau}_i \end{aligned} \tag{1}$$

where $\boldsymbol{\eta}_i = (x_i, y_i, \psi_i)^T$ denotes the earth-fixed coordinate frame coordinates and the yaw angle of *i*th USV, and $\boldsymbol{v}_i = (u_i, v_i, r_i)^T$ denotes the body fixed velocities for $i = 1, 2, \cdots, n$. $\boldsymbol{J}_i(\psi_i)$ denotes the rotation matrix of the ship from body-fixed frame to earth-fixed frame. The frame transformation is presented in Fig. 1, where the *X*-axis points to the north and the *Y*-axis points to the east.

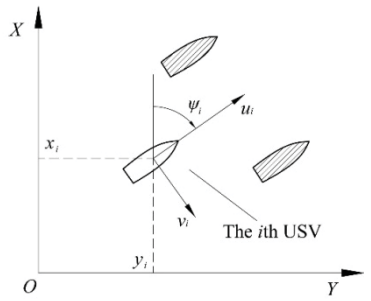

Fig. 1. Frame transformation in horizontal plane

$\boldsymbol{M}_i$ is the inertia matrix considered with hydrodynamic added inertia. $\boldsymbol{C}(\boldsymbol{v}_i)$ denotes the Coriolis and centripetal matrix, which is caused by the rotation. $\boldsymbol{D}_i$ denotes the damping matrix, which is composed of damping coefficients in the surge, sway, and yaw axis directions. $\boldsymbol{\tau} = (\tau_u, 0, \tau_r)^T$ is the control input, which consists of surge thrust and yaw moment. It should be pointed out that $\boldsymbol{M}_i$ and $\boldsymbol{D}_i$ are both positive definite, and they are assumed to be constant. The abovementioned matrixes have the following forms:

$$\boldsymbol{M}_i = \begin{bmatrix} m_{11i} & 0 & 0 \\ 0 & m_{22i} & 0 \\ 0 & 0 & m_{33i} \end{bmatrix},\ \boldsymbol{C}(\boldsymbol{v}_i) = \begin{bmatrix} 0 & 0 & -m_{22i}v_i \\ 0 & 0 & m_{11i}u_i \\ m_{22i}v_i & -m_{11i}u_i & 0 \end{bmatrix},$$

$$\boldsymbol{D}_i = \begin{bmatrix} d_{ui} & 0 & 0 \\ 0 & d_{vi} & 0 \\ 0 & 0 & d_{ri} \end{bmatrix},\ \boldsymbol{J}_i(\psi_i) = \begin{bmatrix} \cos\psi_i & -\sin\psi_i & 0 \\ \sin\psi_i & \cos\psi_i & 0 \\ 0 & 0 & 1 \end{bmatrix}$$

Based on the motion model of each individual, the integral dynamics of the swarm can be defined as:

$$\begin{aligned} \dot{\boldsymbol{\eta}} &= \boldsymbol{J}(\psi)\boldsymbol{v} \\ \boldsymbol{M}\dot{\boldsymbol{v}} &= -\boldsymbol{C}(\boldsymbol{v})\boldsymbol{v} - \boldsymbol{D}\boldsymbol{v} + \boldsymbol{\tau} \end{aligned} \tag{2}$$

where the symbols in Eq. (2) have the following form:

$$\boldsymbol{\eta} = [\boldsymbol{\eta}_1^T, \boldsymbol{\eta}_2^T, \cdots, \boldsymbol{\eta}_n^T]^T,\ \boldsymbol{v} = [\boldsymbol{v}_1^T, \boldsymbol{v}_2^T, \cdots, \boldsymbol{v}_n^T]^T,\ \boldsymbol{\tau} = [\boldsymbol{\tau}_1^T, \boldsymbol{\tau}_2^T, \cdots, \boldsymbol{\tau}_n^T]^T,$$

$$\boldsymbol{J} = diag\{\boldsymbol{J}_1, \boldsymbol{J}_2, \cdots, \boldsymbol{J}_n\},\ \boldsymbol{M} = diag\{\boldsymbol{M}_1, \boldsymbol{M}_2, \cdots, \boldsymbol{M}_n\},$$

$$\boldsymbol{C}(\boldsymbol{v}) = diag\{\boldsymbol{C}(\boldsymbol{v}_1), \boldsymbol{C}(\boldsymbol{v}_2), \cdots, \boldsymbol{C}(\boldsymbol{v}_n)\}\boldsymbol{D} = diag\{\boldsymbol{D}_1, \boldsymbol{D}_2, \cdots, \boldsymbol{D}_n\}.$$

FRAMEWORK DESIGN FOR SWARM CONTROL

In order to achieve the autonomous motion control of USV swarm, the controller is bilaterally designed according to different goals. It is composed of three layers, the supreme of which is the tele-operated task layer. In this layer, the center

position of the swarm and the average distance between USVs and the center position are remotely controlled by a human operator. The second layer is the autonomous task design, in which some autonomous tasks are defined to solve specific problems in practical navigation, and it is essential for these tasks to meet the demand of the tele-operation layer. The bottom layer is the control allocation design. In this layer, the underactuated feature of USVs is considered, and the control input is re-designed to fit the drive appliances.

TELE-OPERATED TASK LAYER

In this layer, an individual position of each USV is not directly controlled. The human operator only controls the center position and the average distance, the desired values of which are delivered to each USV. In order to express these orders in a mathematical way, the desired position function is defined as follows:

$$\boldsymbol{X}_h = [\overline{x}_d, \overline{y}_d, \sigma_d]^T \tag{3}$$

where $(\overline{x}_d, \overline{y}_d)$ denotes the desired value of the center position and σ_d denotes the desired distance variance.

According to the form of Eq. (3), the position function of the swarm is defined as:

$$\boldsymbol{X}_s = [\overline{x}, \overline{y}, \sigma]^T \tag{4}$$

where $(\overline{x}, \overline{y})$ denotes the desired value of the center position, and σ denotes the desired distance variance, which can be written as follows:

$$\begin{aligned} \overline{x} &= \frac{1}{n}\sum_{i=1}^{n} x_i, \quad \overline{y} = \frac{1}{n}\sum_{i=1}^{n} y_i \\ \sigma &= \frac{1}{n^2}\left(\sum_{i=1}^{n}[(x_i - \overline{x})^2 + (y_i - \overline{y})^2]\right) \end{aligned} \tag{5}$$

The tele-operated task error $\boldsymbol{e}_h$ is further defined as:

$$\boldsymbol{e}_h = \boldsymbol{X}_s - \boldsymbol{X}_h = [e_1, e_2, e_3]^T \tag{6}$$

where e_1, e_2, and e_3 denote the components of $\boldsymbol{e}_h$.

The control framework with the task layer design and the sequence of information transfer is shown in Fig. 2. Some symbols shown in the figure, such as $\boldsymbol{\eta}$ and $\boldsymbol{\tau}'$, will be explained later in the article.

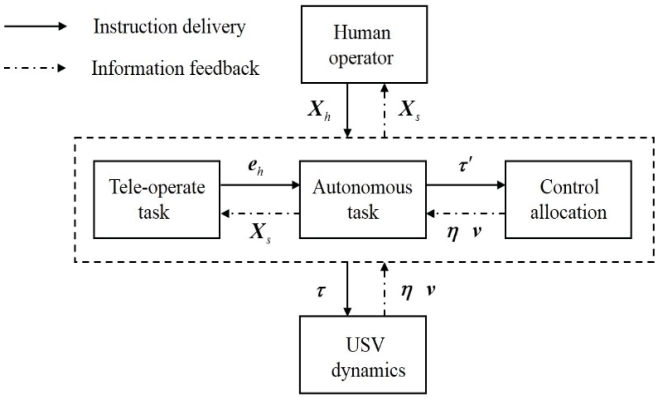

Fig. 2. Framework of the closed-loop control system

Differentiating Eq. (4) we get

$$\dot{\boldsymbol{X}}_s = \boldsymbol{J}_s(\boldsymbol{\eta})\dot{\boldsymbol{\eta}} \tag{7}$$

where $\boldsymbol{J}_s$ is the Jacobian matrix having the following form:

$$\boldsymbol{J}_s(\boldsymbol{\eta}) = \frac{\partial \boldsymbol{X}_s}{\partial \boldsymbol{\eta}} = \left[\frac{\partial \boldsymbol{X}_{s1}}{\partial \boldsymbol{\eta}}^T, \frac{\partial \boldsymbol{X}_{s2}}{\partial \boldsymbol{\eta}}^T, \frac{\partial \boldsymbol{X}_{s3}}{\partial \boldsymbol{\eta}}^T\right]^T \in R^{3\times 3n} \tag{8}$$

Notice that $\boldsymbol{J}_s$ is not a square matrix, and the pseudo-inverse of $\boldsymbol{J}_s$ is defined as $\boldsymbol{J}_s^+ = \boldsymbol{J}_s^T(\boldsymbol{J}_s\boldsymbol{J}_s^T)$, which satisfies the condition of $\boldsymbol{J}_s\boldsymbol{J}_s^+ = I_3$ [18].

AUTONOMOUS TASK LAYER

During the autonomous navigation of USV swarm, many autonomous tasks may need to be conducted simultaneously, and controlled solely by USVs instead of the human operator. To simplify the research, only 3 typical cases have been selected as autonomous tasks, which are: obstacle avoidance, inner USV collision avoidance, and swarm dispersion. The autonomous tasks are designed by making use of potential functions. By defining a specific mathematical function for each task, the corresponding purposes can be achieved.

Obstacle avoidance

In this task the obstacles are assumed to be known, and the collision avoidance algorithm presented by Stipanović et al. [19] for a multi-agent system is used for the USV swarm. Then the obstacle avoidance task function Φ_{oj} is given by

$$\Phi_{oj} = \sum_{i=1}^{n}\{\min(0, \frac{d(i,o_j)^2 - R_o^2}{d(i,o_j)^2 - r_o^2})\}^2 \tag{9}$$

where $d(i,o_j)$ is the distance between the ith USV and the jth obstacle, whose position in the remote environment is

denoted by η_{oj} and given by the operator. R_o is the avoidance distance, and r_o is the shortest safe distance. As for Eq. (9), it can be used to avoid both static and moving obstacles. Thus, the avoidance of sailing ships can be achieved as well.

The partial derivative of Φ_{oj} for η has the following form

$$\frac{\partial \Phi_{oj}}{\partial \boldsymbol{\eta}} = 4\frac{(R_o^2 - r_o^2)(d(i,o_j)^2 - R_o^2)}{(d(i,o_j)^2 - r_o^2)^3}(\boldsymbol{\eta}_s - \boldsymbol{\eta}_{oj})^T \text{ , if } \quad r_o < d(i,o_j) < R_o \tag{10}$$

where $\boldsymbol{\eta}_s = [x_1, y_1, 0, \cdots, x_n, y_n, 0,]^T$ denotes the position of USVs, $\boldsymbol{\eta}_{oj} = [ox_j, oy_j, 0, \cdots, ox_j, oy_j, 0]^T$ is the obstacle vector, and $\boldsymbol{\eta}_s, \boldsymbol{\eta}_{oj} \in R^{3n}$.

The auxiliary control function φ_o is further defined as:

$$\boldsymbol{\varphi}_o = -\sum_{j=1}^{m}(\partial \Phi_{oj} / \partial \boldsymbol{\eta})^T \tag{11}$$

Inner USV collision avoidance

This task aims to keep a safe distance between each pair of USVs to avoid collision between them. Similarly to Eq. (9), the inner USV collision avoidance can be achieved by defining the following function:

$$\Phi_{rj} = \sum_{i=1}^{n}\{\min(0, \frac{d(i,j)^2 - R_r^2}{d(i,j)^2 - r_r^2})\}^2 \tag{12}$$

where $d(i,j)$ is the distance between the ith USV and the jth USV, R_r is the avoidance distance, and r_r is the smallest safe distance between two USVs.

Taking the partial derivative of Φ_r for η we get the following equation:

$$\frac{\partial \Phi_{rj}}{\partial \boldsymbol{\eta}} = 4\frac{(R_r^2 - r_r^2)(d(i,j)^2 - R_r^2)}{(d(i,j)^2 - r_r^2)^3}(\boldsymbol{\eta}_s - \boldsymbol{\eta}_{rj})^T, \text{ if } \quad r_r < d(i,j) < R_r \tag{13}$$

where $\boldsymbol{\eta}_{rj} = [x_j, y_j, 0, \cdots, x_j, y_j, 0]^T$ is the position vector for the ith USV, and $\boldsymbol{\eta}_{rj} \in R^{3n}$

The auxiliary control function φ_{rj} is further defined as:

$$\boldsymbol{\varphi}_r = -\sum_{j=1}^{m}(\partial \Phi_{rj} / \partial \boldsymbol{\eta})^T \tag{14}$$

Swarm dispersion

USVs might gather together into several small groups while achieving the tele-operated task. However, in applications such as coverage control of a mobile robot network, increasing the coverage area is necessary to improve the swarm performance in the cases of surface search or seabed detection [20]. The swarm dispersion task is considered to maximize the inter-member distance and thus to enlarge the area of coverage. The task function is given as

$$\Phi_d = -\sum_{i=1}^{n-1}\sum_{j=i+1}^{n} d(i,j)^2 \tag{15}$$

The auxiliary control function φ_{rj} is further defined as

$$\boldsymbol{\varphi}_d = -(\partial \Phi_d / \partial \boldsymbol{\eta})^T = \sum_{j=1}^{n}(\boldsymbol{\eta}_s - \boldsymbol{\eta}_{rj})^T \tag{16}$$

Remark 1. In the autonomous task layer, the abovementioned tasks should be considered simultaneously. The autonomous task functions can be combined to generate the auxiliary function, for example $\Phi = k_1\Phi_{oj} + k_2\Phi_{rj} + k_3\Phi_d$. Then the total auxiliary control function is given as $\boldsymbol{\varphi} = k_1\boldsymbol{\varphi}_o + k_2\boldsymbol{\varphi}_r + k_3\boldsymbol{\varphi}_d$, where k_1, k_2 and k_3 are proper gains for each task.

As for parameters k_1, k_2 and k_3, they are proportional to relevant virtual forces, and they can be chosen according to task priority. The obstacle avoidance task has higher priority than inner USV collision avoidance, and swarm dispersion is the last task needed to fulfill. In addition, virtual repulsive forces for each USV should be large enough to achieve the goal of collision avoidance, but also should not be excessively large to avoid unstable operation of the controller system. Combining the above factors, k_1 and k_2 were assumed to be large constants, and k_3 to be a large constant at the beginning. Then multiple simulation tests were conducted, after which the final values of parameters were selected as k_1=20, k_2=5, k_3=0.1.

Preliminary design of control input

To accomplish the tele-operated task and autonomous task, the following Lyapunov function is defined:

$$V_1 = \frac{1}{2}\boldsymbol{e}_h{}^T\boldsymbol{e}_h + \Phi \tag{17}$$

Differentiating both sides of Eq. (17), we get

$$\begin{aligned}\dot{V}_1 &= \boldsymbol{e}_h{}^T\dot{\boldsymbol{e}}_h - \lambda\boldsymbol{\varphi}^T\dot{\boldsymbol{\eta}} = \boldsymbol{e}_h{}^T(\boldsymbol{J}_s\dot{\boldsymbol{\eta}} - \dot{\boldsymbol{X}}_h) - \boldsymbol{\varphi}^T\dot{\boldsymbol{\eta}} \\ &= (\boldsymbol{e}_h{}^T\boldsymbol{J}_s - \boldsymbol{\varphi}^T)\dot{\boldsymbol{\eta}} - \boldsymbol{e}_h{}^T\dot{\boldsymbol{X}}_h\end{aligned} \tag{18}$$

According to Eq. (18), we define a virtual control item to make V_1 converged, which is designed as follows:

$$\dot{\boldsymbol{\eta}}^{\alpha} = -k_4(\boldsymbol{J}_s{}^T\boldsymbol{e}_h - \boldsymbol{\varphi}) \tag{19}$$

where $\dot{\boldsymbol{\eta}}^{\alpha}$ is the desired value of $\dot{\boldsymbol{\eta}}$, and k_4 is a positive constant coefficient. Then we define another error variable as: $\boldsymbol{\xi} = \dot{\boldsymbol{\eta}} - \dot{\boldsymbol{\eta}}^{\alpha}$.

In the task design, it is convenient to set $\boldsymbol{X}_h$ constant over a certain period of time, as a result of which $\dot{\boldsymbol{X}}_h = 0$. By substituting Eq. (19) into Eq. (18), $\dot{V}_1$ can be rewritten as:

$$\begin{aligned}\dot{V}_1 &= (\boldsymbol{e}_h{}^T\boldsymbol{J}_s - \boldsymbol{\varphi}^T)(\dot{\boldsymbol{\eta}}^{\alpha} + \boldsymbol{\xi}) \\ &= -k_4(\boldsymbol{J}_s{}^T\boldsymbol{e}_h - \boldsymbol{\varphi})^T(\boldsymbol{J}_s{}^T\boldsymbol{e}_h - \boldsymbol{\varphi}) + (\boldsymbol{J}_s{}^T\boldsymbol{e}_h - \boldsymbol{\varphi})^T\boldsymbol{\xi}\end{aligned} \tag{19}$$

In the next step, another Lyapunov function V_2 is defined as

$$V_2 = V_1 + \frac{1}{2}\boldsymbol{\xi}^T\boldsymbol{\xi} \tag{20}$$

Taking the time derivative of V_2 along the solution of Eq. (19) and setting $\boldsymbol{J}\dot{\boldsymbol{v}} = -k_5\boldsymbol{\xi} - \dot{\boldsymbol{J}}\boldsymbol{v}$, where k_4 is also a positive coefficient, we get Eq. (21) as follows:

$$\begin{aligned}\dot{V}_2 = &-k_4(\boldsymbol{J}_s{}^T\boldsymbol{e}_h - \boldsymbol{\varphi})^T(\boldsymbol{J}_s{}^T\boldsymbol{e}_h - \boldsymbol{\varphi}) - k_5\boldsymbol{\xi}^T\boldsymbol{\xi} + \\ &(\boldsymbol{J}_s{}^T\boldsymbol{e}_h - \boldsymbol{\varphi})^T\boldsymbol{\xi} - \boldsymbol{\xi}^T\ddot{\boldsymbol{\eta}}^\alpha\end{aligned} \tag{21}$$

If the coefficients satisfy the condition of $k_5 = 1/(4k_4)$, then Eq. (21) can be transformed to the following form:

$$\dot{V}_2 = -k_4(\boldsymbol{J}_s{}^T\boldsymbol{e}_h - \boldsymbol{\varphi} - \boldsymbol{\xi})^T(\boldsymbol{J}_s{}^T\boldsymbol{e}_h - \boldsymbol{\varphi} - \boldsymbol{\xi}) - \boldsymbol{\xi}^T\ddot{\boldsymbol{\eta}}^\alpha \tag{22}$$

Since $\boldsymbol{\xi}$ and $\ddot{\boldsymbol{\eta}}^\alpha$ are bounded, then $\left|\boldsymbol{\xi}^T\ddot{\boldsymbol{\eta}}^\alpha\right| \le \Delta_1$ can be obtained, where Δ_1 is an arbitrary small positive constant. Then, Eq. (23) is obtained as:

$$\dot{V}_2 \le -k_4(\boldsymbol{J}_s{}^T\boldsymbol{e}_h - \boldsymbol{\varphi} - \boldsymbol{\xi})^T(\boldsymbol{J}_s{}^T\boldsymbol{e}_h - \boldsymbol{\varphi} - \boldsymbol{\xi}) + \Delta_1 \tag{23}$$

Thus, V_2 is asymptotically converged, and the same applies to ($\boldsymbol{e}_h$, φ, ξ).

Substituting Eq. (2) into $\boldsymbol{J}\dot{\boldsymbol{v}} = -k_5\boldsymbol{\xi} - \dot{\boldsymbol{J}}\boldsymbol{v}$, the initial form of control input τ is given as $\boldsymbol{\tau}'$:

$$\boldsymbol{\tau}' = -k_5\boldsymbol{M}\boldsymbol{J}^T\boldsymbol{\xi} - \boldsymbol{M}\boldsymbol{J}^T\dot{\boldsymbol{J}}\boldsymbol{v} + \boldsymbol{C}(\boldsymbol{v})\boldsymbol{v} + \boldsymbol{D}\boldsymbol{v} \tag{24}$$

where $\boldsymbol{\tau}' = [\tau'_{u1}, \tau'_{v1}, 0, \tau'_{u2}, \tau'_{v2}, 0, \cdots, \tau'_{un}, \tau'_{vn}, 0]^T$.

In the preliminary design of control input, the yaw angle of each USV is not designed, and the motion control mainly relies on τ'_u and τ'_v. Under the input of Eq. (24), the yaw rate acceleration is $\dot{r}_i = 0$ for each USV. In other words, USVs will sail without making a turn. However, this drive configuration and motion pattern do not accord with the practical situation. Therefore, the control input needs to be reshaped considering the underactuated feature of USVs, which is called the control allocation.

CONTROL ALLOCATION

The control allocation can be achieved by properly designing the yaw angle, as shown in Fig. 3. By defining the yaw angle error and applying the sliding-mode control method, the yaw moment τ_r is designed. In the control allocation layer, the surge thrust τ_u remains unchanged, i.e. $\tau_u = \tau'_u$, while the sway thrust τ_v is set equal to zero, and the yaw angle varies in real time to eliminate the demand of τ_v.

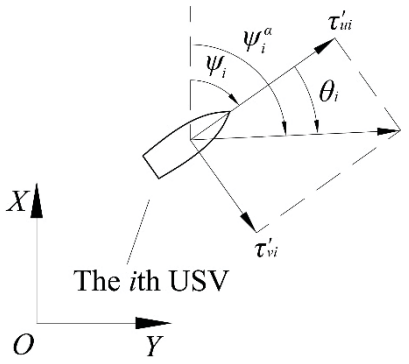

Fig. 3. Schematic of yaw angle designing

The yaw angle error of the *i*th USV is defined as

$$\tilde{\psi}_i = \psi_i - \psi_i^\alpha = -\theta_i \tag{25}$$

where ψ_i^α is the desired value of ψ_i, and $\theta_i = \text{atan}\,2(\tau'_{vi}, \tau'_{ui})$.

Then, in order to eliminate the yaw angle error, the following first-order sliding manifold is introduced:

$$S_i = \dot{\tilde{\psi}}_i + \lambda\tilde{\psi}_i = r_i - \dot{\psi}_i^\alpha - \lambda\theta_i \tag{26}$$

and the Lyapunov function V_3 is defined as

$$V_3 = \frac{1}{2}S_i{}^2 \tag{27}$$

Differentiating both sides of Eq. (27), and setting $\dot{r}_i$ as follows

$$\dot{r}_i = -\lambda r_i + (\lambda\dot{\psi}_i^\alpha + \ddot{\psi}_i^\alpha) - k_6\,\text{sgn}(S_i) \tag{28}$$

we get

$$\begin{aligned}\dot{V}_3 = S_i\dot{S}_i &= S_i[\dot{r}_i + \lambda_2 r_i - (\lambda\dot{\psi}_i^\alpha + \ddot{\psi}_i^\alpha)] \\ &= -k_6|S| \le 0\end{aligned} \tag{29}$$

Thus, the sliding surface S_i is asymptotically stable, and the same applies to $\tilde{\psi}_i$. Substituting Eq. (1) into Eq. (28), the yaw moment of the *i*th USV is obtained as follows:

$$\tau_{ri} = -k_6 m_{33i}\,\text{sgn}(S_i) + (d_{ri} - \lambda m_{33i})r_i - \frac{m_{11i} - m_{22i}}{m_{33i}}u_i v_i + (\lambda\dot{\psi}_i^\alpha + \ddot{\psi}_i^\alpha) \tag{30}$$

To avoid differentiating of ψ_i^α, the following second order filter is introduced to calculate $\dot{\psi}_i^\alpha$ and $\ddot{\psi}_i^\alpha$.

$$\ddot{\psi}_i^\alpha + \zeta\dot{\psi}_i^\alpha + \omega(\psi_i^\alpha - \psi_i - \theta_i) = 0 \tag{31}$$

where ζ and ω are filter gains, which are to be properly chosen.

NUMERICAL SIMULATION

To illustrate that the proposed methodology is effective, numerical simulations of USV swarm motion have been performed. The swarm comprises 6 homogeneous USVs. The total length of each USV is 13 meters, and the motion parameters of USVs are given as follows [9]: m_{11}=120×10^3 kg, m_{22}=177.9×10^3 kg, m_{33}=636×10^5 kg, d_u=215×10^2 kg·s^{-1}, d_v=147×10^3 kg·s^{-1}, d_r=802×10^4 kg·s^{-1}. In order to be consistent with the actual situation, the actuator saturation is taken into account and the saturation limits of control inputs for each USV are set as $|\tau_{ui}| \leq 1.0\times10^6$N and $|\tau_{ri}| \leq 1.0\times10^9$Nm.

The control parameters mentioned in the controller design are chosen as follows: k_1=20, k_2=5, k_3=0.1, k_4=0.5, k_6=2, λ=0.2, ζ=10, ω=20. While selecting parameters, some aspects need special attention. The collision avoidance task has higher priority than the tele-operated task and swarm dispersion, so it is advisable to set k_1 and k_2 relatively large, while k_3 only needs to be a small variable. Parameters k_4 and k_6 affect directly only the convergence rate of error variables, but if they are too large, the system response will also be affected. The distance parameters mentioned in the autonomous task have been chosen as follows: R_o=50m, r_o=25m, R_r=20m, r_r=10m.

SIMULATION 1: TARGET TRACKING WITH STATIC OBSTACLES IN THE VICINITY OF THE COURSE

In simulation 1, the USV swarm tracks a moving underwater target, and there are some static obstacles in the navigation area. The target position (x_t, y_t) is assumed always known, and the desired distance variance of the swarm is chosen equal to 80m^2, thus the desired position function is designed as $\boldsymbol{X}_h$=[x_t, y_t, 80m^2]. The target starts moving from point (40m, 180m) at time t=0s, and reaches points (250m, 450m), (150m, 650m), (-50m, 450m) at times t=30s, 55s, and 80s, respectively. Besides, since the target is under water, the USVs will not collide with the target. The initial velocities of all USVs are set equal to zero. The overall performance of the USV swarm is illustrated in Fig. 4 through Fig. 8.

Fig. 4 presents the sailing paths of USVs and moving target. The six colored lines denote the paths of six USVs, while the black dotted line denotes the target path. As we can see in the subfigures, the swarm has a good performance in target tracking, and each USV can automatically choose a proper route to avoid collisions when getting close to the obstacle. It is easily noticeable in Fig. 4(b) that when the obstacle is too close to the target, the six USVs choose to bypass the obstacle in different directions. Besides, during the navigation, each USV keeps a safe distance from other USVs, and collision between USVs does not happen.

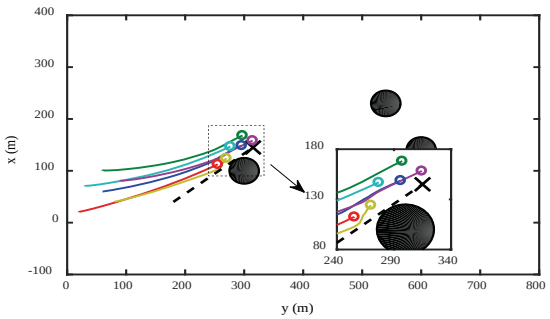

(a) Time t = 15s

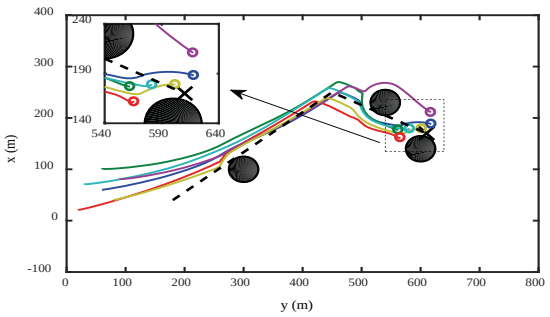

(b) Time t = 50s

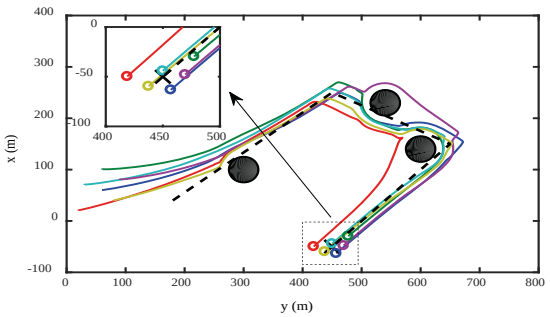

(c) Time t = 80s

Fig. 4. Sailing path of the USV swarm

Fig. 5 shows the error curves of the tele-operated task, where e_1 and e_2 denote the relative positions of the swarm center and the target, and e_3 denotes the error of desired distance variance. The most expected case is that e_1, e_2 and e_3 all converge to zero. However, in this simulation, due to the existence of obstacles, these error variables will not converge to zero until the swarm has sailed away from the obstacles. This phenomenon is explained by the fact that collision avoidance has higher priority than target tracking and formation keeping.

In order to see how each USV works, let us take USV 1 as an example. Fig. 6 shows the desired yaw angle error of USV 1, while Fig. 7 and Fig.8 show the input of thrust and yaw moment respectively. In Fig. 6, most of the time, the error of the desired yaw angle keeps equal to zero, while the large error values at times 30s and 55s are caused by surrounding obstacles. In Fig. 7 and Fig. 8, high frequency oscillations of control inputs are observed. These oscillations are due to the combined effect of tracking the desired position with virtual

repulsive forces from adjacent USVs and from the obstacle. After the obstacle avoidance is finished, the control inputs get stable. From the sailing paths shown in Fig. 4 we can find that these oscillations do not affect the performance of target tracking and obstacle avoidance. It is important to note that in practical applications, USVs may get a larger spacing than that assumed in the simulation, or smaller USVs may be used at the same spacing extent. In those situations the control inputs will be much smoother when adjusting position and orientation.

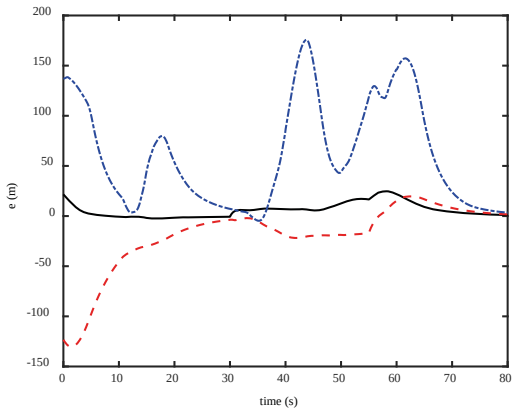

Fig. 5. Response curves of tele-operated task error

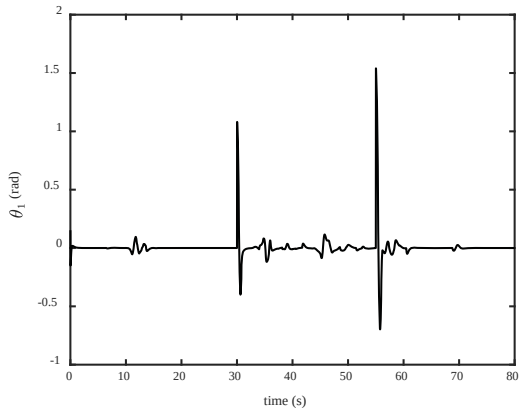

Fig. 6. Desired yaw angle error of USV 1

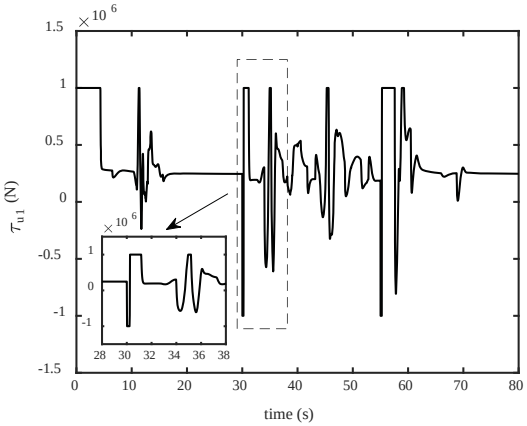

Fig. 7. Thrust input of USV 1

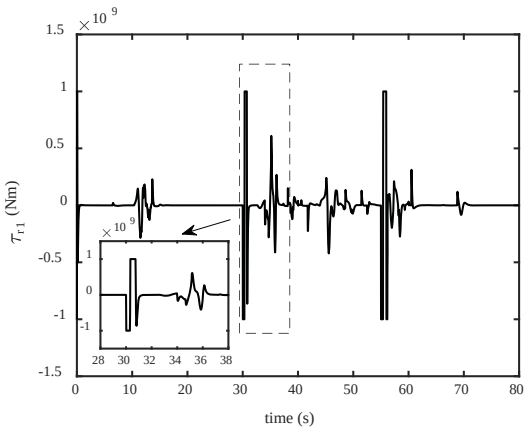

Fig. 8. Yaw moment input of USV 1

SIMULATION 2: TARGET TRACKING WITH MOVING OBSTACLES IN THE VICINITY OF THE COURSE

In simulation 2, the USV swarm tracks a moving underwater target, and there are three moving obstacles in the navigation area. The target position (x_t, y_t) is assumed always known, and the desired distance variance of the swarm is chosen equal to 80m^2, thus the desired position function is designed as $\boldsymbol{X}_h$=[x_t, y_t, 80m^2]. The target starts moving from point (40m, 180m) at time t=0s and moves at constant speed to reach points (250m, 500m), (440m, 590m), (585m, 725m) at times t=40s, 60s, and 80s, respectively. The initial velocities of all USVs are set equal to zero. The overall performance of the USV swarm is illustrated in Fig. 9 through Fig. 13.

Fig. 9 shows the sailing path of USV swarm at times t=20s, 34s and 80s. In the subfigures, the black polyline denotes the path of the moving target, while the six colored curves denote the tracking paths of six USVs. As we can see in Fig. 9(a) and Fig. 9(b), there are 3 ships sailing in the vicinity of the swarm, and they are equivalent to moving obstacles for the USVs. It is easily noticeable in the enlarged drawing fragments that USVs automatically avoid the obstacle ships. In this simulation, each USV tracks the moving target well with acceptable overshoot at turning points. Initially, the 6 USVs are far apart from each other, then they gather rapidly and form a relatively stable formation shape while tracking the target. During the auto navigation, the 6 USVs always keep a safe distance from each other, and no collision between USVs occurs.

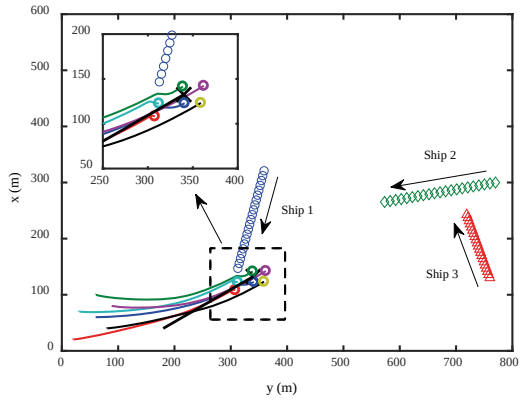

(a) Time t = 20s

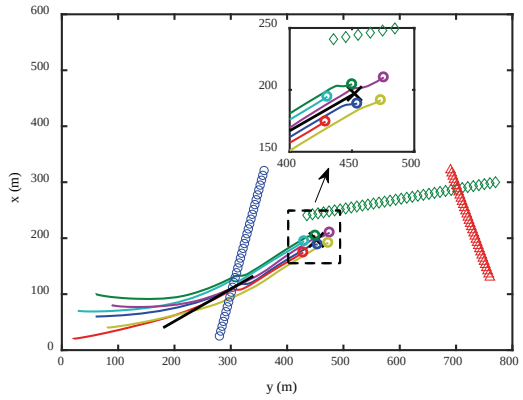

(b) Time t = 34s

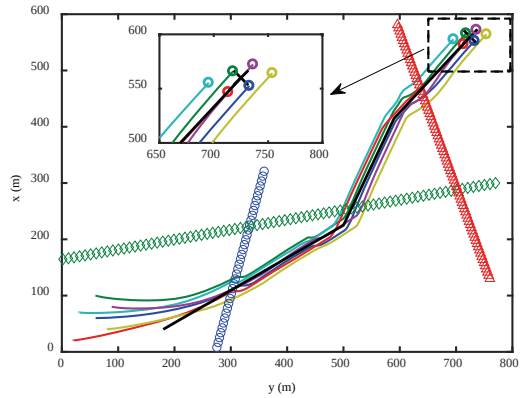

(c) Time t = 80s

Fig. 9. Sailing path of the USV swarm

Fig. 10 shows the error curves of the tele-operated task, and Fig. 11 shows the desired yaw angle error of USV 1. In Fig. 10, it is easy to notice that the initial errors are rapidly eliminated, which means that the swarm reaches the desired position and gets the desired distance variance gradually. As for the rebounds at times *t*=17s, 40s, and 65s, they are caused by the presence of the obstacles, as a result of which the USVs need to take time for making a turning. The underlying reason has been explained in detail in simulation 1.

Fig. 12 and Fig. 13 show the thrust and yaw moment input of USV 1. Combining with Fig. 11, we can see that the controller is running smoothly, except for the oscillations at times 17s, 40s, and 65s, generated while avoiding the sailing ships. Once the swarm sails away from the obstacle ships, the error variables converge to zero rapidly. We can conclude from the simulation results that the proposed USV swarm control method has a good performance in target tracking and obstacle avoidance.

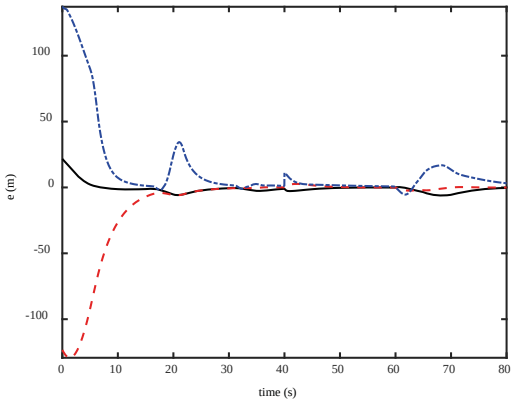

Fig. 10. Response curves of tele-operated task error

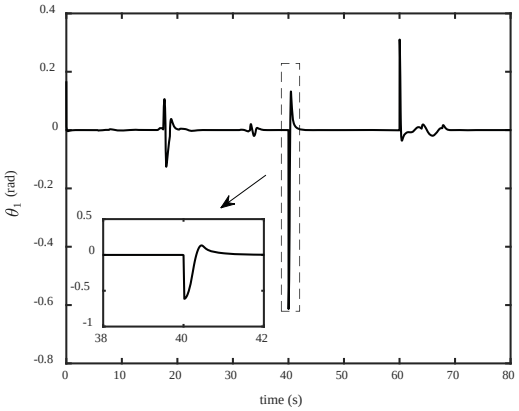

Fig. 11. Desired yaw angle error of USV 1

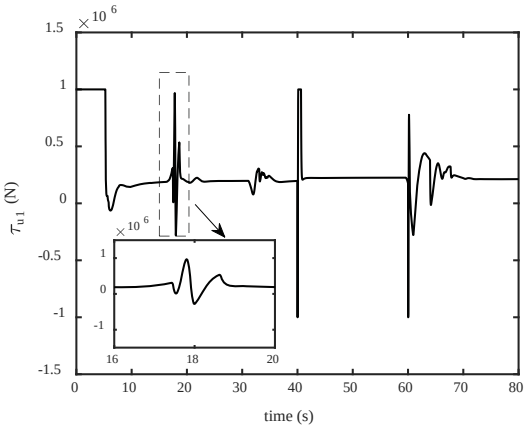

Fig. 12. Thrust input of USV 1

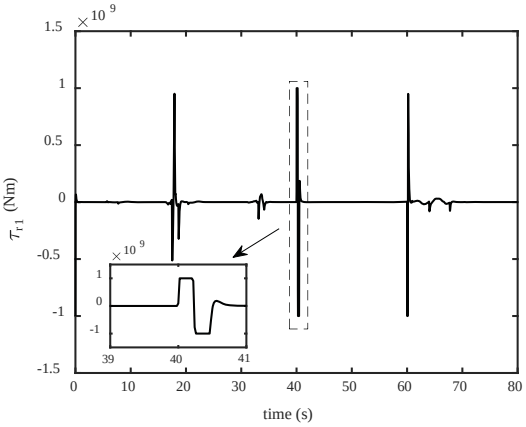

Fig. 13. Yaw moment input of USV 1

CONCLUSIONS

In the paper, a hierarchical control framework with relevant algorithms is proposed to achieve auto navigation of a USV swarm. This control enables the swarm to track autonomously the desired target, avoid obstacles, and avoid collisions between swarm members. Theoretical proof and numerical simulations are provided to demonstrate the efficiency and robustness of the overall control system.

It can be seen from the simulation results that the originally designed hierarchical swarm controller based on potential field method and individual control allocation design is suitable for the underactuated USV swarm. Besides, compared to other formation control methods, a fixed formation shape is not needed in the swarm control, and the swarm members are intelligent to a certain extent.

In the future study, the proposed USV swarm control method will be improved to facilitate its conversion into practical use. For example, an actual electronic chart will be pixelated and used for modeling external geographical information for USVs.

ACKNOWLEDGEMENTS

We would like to thank the associate editor and the reviewers for their helpful comments. We would also like to thank the National Natural Science Foundation of China (Grant No. 51409054), the Foundation Research Funds for the Central Universities (Grant No. HEUCF180101) and High-tech Ships Technology of Ministry of Industry and Information (Grant No. [2016]26) for their financial support of our research.

REFERENCES

1. Do K. D. Practical formation control of multiple underactuated ships with limited sensing ranges. Robotics and Autonomous Systems, 2011, 59(6): 457-471.
2. Zhuang J.Y., Su Y.M., Liao Y.L., Sun H. Unmanned surface vehicle local path planning based on marine radar. Journal of Shanghai Jiaotong University, 2012, 9: 006.
3. Shojaei K. Neural adaptive robust control of underactuated marine surface vehicles with input saturation. Applied Ocean Research, 2015, 53:267-279.
4. Wai R.J., Liu C.M., Lin Y.W. Design of switching path-planning control for obstacle avoidance of mobile robot. Journal of the Franklin Institute, 2011, 348(4): 718-737.
5. Cui R., Ge S.S., How B.V.E., Choo Y.S. Leader–follower formation control of underactuated autonomous underwater vehicles. Ocean Engineering, 2010, 37(17): 1491-1502.
6. Peng Z., Wang D., Chen Z., Hu X. Adaptive dynamic surface control for formations of autonomous surface vehicles with uncertain dynamics. IEEE Transactions on Control Systems Technology, 2013, 21(2): 513-520.
7. Ding L., Guo G. Formation control for ship fleet based on backstepping. Control and Decision, 2012, 27(2): 299-303.
8. Mehrjerdi H., Ghomman J., Saad M. Nonlinear coordination control for a group of mobile robots using a virtual structure. Mechatronics, 2011, 21(7): 1147-1155.
9. Do K.D. Formation control of underactuated ships with elliptical shape approximation and limited communication ranges. Automatica, 2012, 48: 1380-1388.
10. Glotzbach T., Schneider M., Otto P. Cooperative line of sight target tracking for heterogenous unmanned marine vehicle teams: From theory to practice. Robotics and Autonomous Systems, 2015, 67: 53-60.
11. Johnson J.T. A Brief Investigation of Swarm Theory and Applications. ASME 2009 International Design Engineering Technical Conferences and Computers and Information in Engineering Conference. American Society of Mechanical Engineers, 2009: 209-218.
12. Bae J., Kim Y. Adaptive controller design for spacecraft formation flying using sliding mode controller and neural networks. Journal of the Franklin Institute, 2012, 349(2): 578-603.
13. Wang H. Flocking of networked uncertain Euler–Lagrange systems on directed graphs. Automatica, 2013, 49(9): 2774-2779.
14. Cepeda-Gomez R., Olgac N., Sierra D.A. Application of sliding mode control to swarms under conflict. IET control theory & applications, 2011, 5(10): 1167-1175.

15. Franchi A., Secchi C., Son H.I., Bülthoff H.H. Bilateral teleoperation of groups of mobile robots with time-varying topology. IEEE Transactions on Robotics, 2012, 28(5): 1019-1033.

16. Liu Y.C. Task-space coordination control of bilateral human–swarm systems. Journal of the Franklin Institute, 2015, 352(1): 311-331.

17. Wan L., Dong Z.P., Li Y.M., He B. Global asymptotic stabilization control of incomplete symmetry underactuated USV. Journal of Huazhong University of Science and Technology, 2014, 8(42): 48-53.

18. Liu Y.C., Chopra N. Controlled synchronization of heterogeneous robotic manipulators in the task space. IEEE Transactions on Robotics, 2012, 28(1): 268-275.

19. Stipanović D.M., Hokayem P.F., Spong M.W., Siljak D. Cooperative avoidance control for multiagent systems. Journal of Dynamic Systems, Measurement, and Control, 2007, 129(5): 699-707.

20. Schwager M., Rus D., Slotine J.J. Decentralized, adaptive coverage control for networked robots. The International Journal of Robotics Research, 2009, 28(3): 357-375.

CONTACT WITH THE AUTHORS

Lei Zhang
e-mail: cheung103@163.com

Harbin Engineering University
Nantong Street
150001 Harbin
China

sciendo

POLISH MARITIME RESEARCH 1 (101) 2019 Vol. 26; pp. 117-124
10.2478/pomr-2019-0013

WATER ENTRY OF A WEDGE INTO WAVES IN THREE DEGREES OF FREEDOM

Shi Yan Sun
Jiangsu University of Science and Technology, China
Hai Long Chen
Harbin Engineering University, China
Gang Xu
Jiangsu University of Science and Technology, China

ABSTRACT

The hydrodynamic problem of a two-dimensional wedge entering into a nonlinear wave in three degrees of freedom is investigated based on the incompressible velocity potential theory. The problem is solved through the boundary element method in the time domain. To avoid numerical difficulties due to an extremely small contact area at the initial stage, a stretched coordinate system is used based on the ratio of the Cartesian system in the physical space to the distance travelled by the wedge in the vertical direction. The mutual dependence of body motion and wave loading is decoupled by using the auxiliary function method. Detailed results about body accelerations, velocities and displacements at different Froude numbers or different waves are provided, and the mutual effect between body motion and wave loading is analysed in depth.

Keywords: Water entry; nonlinear waves; three degrees of freedom; boundary element method; auxiliary function method.

INTRODUCTION

The impact between wave and structure occurs very often in violent sea conditions. When a ship advances in rough seas, the bow may emerge from the water and then re-enter into the wave with high speed. In those cases, the local area of hull surface would surfer a very large impact pressure, and a great risk would be imposed to the structure. The wave/structure impact can also be observed in problems of wave energy converters operating in rough seas, large waves hitting an offshore platform, and liquid sloshing in a tank. Those phenomena are dynamically equivalent to a wedge entering freely into a wave.

The past research often focused on the wedge entry into calm water. Wagner's theory was commonly used to analyse this problem, especially for bodies with small deadrise angles. Most popular works on the subject include those by: Howison et al. [1] for bodies with small deadrise angles, Faltinsen [2] on the wedge with finite deadrise angle, and Korobkin et al. [3] for the body with elastic deformation. In contrast to Wagner's theory, the fully nonlinear boundary element method is more accurate in simulating such a nonlinear process. Dobrovolskaya [4] and Zhao & Faltinsen [5] considered the vertical entry of a wedge into water. Semenov & Iafarati [6] solved the problem of vertical entry of an asymmetric wedge, while Xu et al. [7] investigated the case of oblique entry of an asymmetric wedge. The problem of twin wedges was analysed by Wu [8]. Wu et al. [9] considered the vertical entry of a wedge in free fall motion with a single degree of freedom, and Xu et al. [10] considered the free fall with three degrees of freedom, in which the vertical motion is coupled with the horizontal and rotational motion.

Wave slamming is a common phenomenon but rarely considered in the research. Faltinsen [11] was the first to investigate the slamming effect of a wedge advancing in waves. In his work, the slamming pressure of ship section is calculated based on Wagner's theory. Sun et al. [12] adopted the boundary element method to investigate the problem of a wedge entering into waves in a given motion. In that work, the mutual dependence between wave and body motion is not considered, however, this coupling effect plays a significant role in modelling the physical process of wedge entering into waves.

In this paper, the coupled process of a wedge entering into waves in free motion is investigated. The boundary element method is adopted, and the fully nonlinear boundary conditions are imposed on the free surface and the instantaneous body surface. Some analyses associated with the Froude number and wave effect are undertaken. On the one hand, unlike the calm water cases, the effect of Froude number is changed noticeably by the waves. The reason for this is that the fluid flow velocity distribution is altered in the wave field, and thus free surface profiles, pressure distributions and motions under different Froude numbers reveal some peculiar features. On the other hand, the effects of wave height and wave number which are closely related to wave effects are studied in depth. It should be noted that the reported investigations mainly focus on slamming effects and motion traits during the short interval when the slamming occurs.

MATHEMATICAL MODEL AND NUMERICAL PROCEDURE

PHYSICAL PARAMETERS AND CARTESIAN COORDINATE SYSTEM

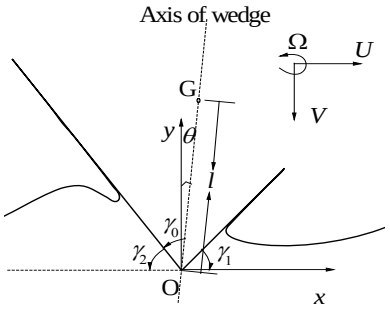

Fig. 1. Sketch of the problem

The 2-D problem considered here is illustrated in Fig. 1, which shows the wedge entering into the wave in three degrees of freedom. The Cartesian coordinate system $O-xy$ with the origin O fixed at the wedge tip is defined so that the x-axis points horizontally and the y-axis points upwards. The horizontal, vertical and rotational velocities about the gravity centre G are denoted as U, V and Ω, respectively. V is positive when pointing downwards, while Ω when anti-clockwise. θ is the heel angle measured from the wedge symmetry axis to the y axis. As the wedge rotates, θ varies with time. γ_0 is the angle between the symmetry axis and the surface of the wedge. The water density ρ, the initial vertical velocity V_0, and the distance l between the wedge's tip and centre of gravity are used for non-dimensionalization. In this case, the Froude number is defined as $F_r = V_0 / \sqrt{gl}$, in which g is the acceleration of gravity.

The deadrise angles γ_1 and γ_2 on the right and left hand sides, respectively, can be obtained from the following relationship

$$\gamma_1 = \frac{\pi}{2} + \theta - \gamma_0, \gamma_2 = \frac{\pi}{2} - \theta - \gamma_0 \tag{1}$$

During the water entry, the vertical distance s, the horizontal distance h, and the heel angle θ of the travelling wedge can be obtained through

$$s(t) = \int_0^t V(\tau)d\tau, \quad h(t) = \int_0^t U(\tau)d\tau \quad \theta(t) = \theta_0 + \int_0^t \Omega(\tau)d\tau \tag{2}$$

where is the initial heel angle at the moment of water entry. The displacement of wedge tip in the vertical direction can be written as

$$s_P = -s(t) + \cos\theta - \cos\theta_0 \tag{3}$$

and in the horizontal direction it becomes

$$h_P = h(t) + \sin\theta - \sin\theta_0 \tag{4}$$

GOVERNING EQUATION AND BOUNDARY CONDITIONS

When the fluid is assumed incompressible and inviscid and the flow is irrotational, the velocity potential ϕ can be introduced. This potential satisfies the Laplace equation in the fluid domain

$$\nabla^2\phi = 0 \tag{5}$$

and its gradient is equal to the fluid velocity. In the body-fixed system, the dynamic and kinematic boundary conditions on the instantaneous free surface S_F can be written in Lagrangian form as

$$\frac{D\phi}{Dt} = \frac{1}{2}\nabla\phi\cdot\nabla\phi - \frac{1}{F_r}(y - s + \cos\theta - \cos\theta_0 + A_0) \tag{6}$$

$$\frac{Dx}{Dt}=\frac{\partial\phi}{\partial x}-U-\Omega\cos\theta,\quad \frac{Dy}{Dt}=\frac{\partial\phi}{\partial y}+V+\Omega\sin\theta \tag{7}$$

where A_0 is the wave elevation at the moment of water entry. On the wetted surface S_0 of the body the impermeable boundary condition takes the form

$$\frac{\partial\phi}{\partial n}=(U-\Omega Y)n_x+(-V+\Omega X)n_y \tag{8}$$

where $\mathbf{n}=(n_x,n_y)$ is the normal vector to the body surface pointing out of the fluid domain, and $\mathbf{X}=(X,Y)$ is the position vector relative to the centre of gravity or the rotating centre G. The negative sign before V is due to the fact that V is positive when it is downwards. At a sufficiently large distance from the body, the disturbance is assumed to have diminished, and there is only the incident potential. The velocity of fluid tends to that due to the undisturbed potential ϕ_I, and the far field boundary condition can therefore be written as

$$\nabla\phi\to\nabla\phi_I \tag{9}$$

At $t=0$, the initial condition can be expressed as

$$y(x,t=0)=\eta_I(x,t=0),\quad \phi(x,\eta,t=0)=\phi_I(x,\eta_I,t=0) \tag{10}$$

At the initial stage of water entry, there is only a tiny part of the body immersed in the wave, and in order to maintain sufficient numerical accuracy, extremely small elements are needed. If a fixed fluid domain is used in the physical coordinate system O–xy, the choice of the truncated boundary should take into account the disturbed area at later stages. All this would lead to a large number of elements at the initial stage. To solve this problem, a stretched system $O-\alpha\beta$ proposed by Wu et al. [9] can be used here. The distance s travelled by the wedge in the vertical direction is set as the stretched ratio between the physical system and the stretched system. At the initial stage we can write

$$\phi(x,y,t)=s\varphi_D(\alpha,\beta,t)+\phi_I(x,y,t),\alpha=x/s,\beta=y/s \tag{11}$$

in which φ_D is the velocity potential due to the disturbance in the stretched system. The body surface boundary condition can then be written as

$$\frac{\partial\varphi_D}{\partial n}=(U-\Omega Y)n_\alpha+(-V+\Omega X)n_\beta-\frac{\partial\phi_I}{\partial n} \tag{12}$$

where $\nabla\varphi_D\to 0$ at a sufficiently large distance from the body. It should be pointed out that the normal derivatives of φ_D and ϕ_I in Eq. (12) are taken from the stretched and Cartesian coordinate systems respectively. At $t=0$, $\varphi_D=0$ on the free surface, or $\phi=\phi_I$. Substituting Eq. (11) into Eqs. (6) and (7), we have

$$\frac{D(s\varphi_D+\phi_I)}{Dt}=\frac{1}{2}[(\varphi_{D\alpha}+\phi_{Ix})^2+(\varphi_{D\beta}+\phi_{Iy})^2]-\frac{1}{F_r}(s\beta-s+\cos\theta-\cos\theta_0+A_0) \tag{13}$$

$$\frac{D(s\beta)}{Dt}=\phi_{D\beta}+\varphi_{Iy}+V+\Omega\sin\theta,\quad \frac{D(s\alpha)}{Dt}=\phi_{D\alpha}+\varphi_{Ix}-U-\Omega\cos\theta \tag{14}$$

The disturbance potential φ_D can be updated together with the free surface. In the subsequent time steps we can define $\phi(x,y,t)=s\varphi(\alpha,\beta,t)$. The body surface boundary condition for φ retains the same form as that in Eq. (8)

$$\frac{\partial\varphi}{\partial n}=(U-\omega Y)n_\alpha+(-V+\omega X)n_\beta \tag{15}$$

The free surface boundary conditions can be written as

$$\frac{D(s\varphi)}{Dt}=\frac{1}{2}(\varphi_\alpha^2+\varphi_\beta^2)-\frac{1}{F_r}(s\beta-s+\cos\theta-\cos\theta_0+A_0) \tag{16}$$

$$\frac{D(s\beta)}{Dt}=\varphi_\beta+V+\Omega\sin\theta,\quad \frac{D(s\alpha)}{Dt}=\varphi_\alpha-U-\Omega\cos\theta \tag{17}$$

It should be noted that the reason for using Eq. (11) at $t=0$ is to avoid φ which tends to infinity as $s\varphi$ equals the incident potential on the free surface and at a large distance from the body at $t=0$.

THE BOUNDARY ELEMENT METHOD

Through Green's identity, the Laplace equation in the fluid domain can be converted into the integral equation over the whole boundary

$$A(p)\phi(p)=\int(\ln r_{pq}\frac{\partial\phi(q)}{\partial n_q}-\phi(q)\frac{\partial\ln r_{pq}}{\partial n_q})dl_q \tag{18}$$

where $A(p)$ is the solid angle of boundaries at point p, and r_{pq} is the distance from the field point p to the source point q. Straight line elements with variables assumed to vary linearly within each element are distributed along the boundary. To perform the integration over each element in Eq. (18), we define

$$\mathbf{r}=\alpha\mathbf{i}+\beta\mathbf{j}=\sum_{i=1}^{2}h^i(u)\cdot\mathbf{r}^i,\quad \phi=\sum_{i=1}^{2}h^i(u)\cdot\phi^i \tag{19}$$

in which $\mathbf{r}$ is the position vector from the origin, with $\mathbf{i}$ and $\mathbf{j}$ being the unit vectors in the α and β directions, respectively. The shape functions are chosen as

$$h^1(u)=1-u,\quad h^2(u)=u \tag{20}$$

where $0\le u\le 1$. Substituting Eqs. (20) and (21) into (19), we have

$$A(p)\phi(p)=\sum_{j=1}^{N_e}\int_0^1 \ln r_{pq}\sum_{i=1}^{2}h^i(u)\frac{\partial\phi_j^i(q)}{\partial n}ldu-\sum_{j=1}^{N_e}\int_0^1\frac{\partial \ln r_{pq}}{\partial n}\sum_{i=1}^{2}h^i(u)\phi_j^i(q)ldu \tag{21}$$

where N_e is the total number of elements. The integrations within each element can be obtained through the analytical solution given by Lu, He & Wu [13].

THE PRESSURE

Based on the Bernoulli equation, the pressure can be written as

$$p=-\left[\phi_t+\frac{1}{2}\nabla\phi\cdot\nabla\phi+\frac{1}{F_r}(y-s+\cos\theta-\cos\theta_0+A_0)\right] \tag{22}$$

At each time step, the velocity potential ϕ can be solved through the numerical scheme given in the previous section, from which its gradient $\nabla\phi$ can be obtained. However, the temporal derivative of potential ϕ_t is still unknown explicitly. To deal with this problem, the auxiliary function method is adopted [14, 15]. Notice that the potential ϕ_t also satisfies the Laplace function in the fluid domain. The normal derivative of ϕ_t on the body surface can be written as [16]

$$\frac{\partial\phi_t}{\partial n}=\left(\dot{\mathbf{U}}+\dot{\mathbf{\Omega}}\times\mathbf{X}\right)\cdot\mathbf{n}-\mathbf{U}\cdot\frac{\partial\nabla\phi}{\partial n}+\mathbf{\Omega}\cdot\frac{\partial}{\partial n}\left[\boldsymbol{X}\times\left(\mathbf{U}-\nabla\phi\right)\right] \tag{23}$$

where $\mathbf{U}=U\mathbf{i}+V\mathbf{j}$, $\mathbf{\Omega}=\Omega\mathbf{k}$ with $\mathbf{k}=\mathbf{i}\times\mathbf{j}$, and the dot means the temporal derivative. Particular attention should be paid to accelerations in Eq. (22), which are unknown before the force is found. To decouple their nonlinear mutual dependence, we define

$$\phi_t=\chi_0+s\dot{U}\chi_1+s\dot{V}\chi_2+s\dot{\Omega}\chi_3-\mathbf{U}\cdot\nabla\phi+\mathbf{\Omega}\cdot\boldsymbol{X}\times\left(\mathbf{U}-\nabla\phi\right) \tag{24}$$

Here $\chi_i(i=0,\cdots 3)$ satisfy the Laplace equation. The body surface boundary conditions for the auxiliary functions can be written as

$$\frac{\partial\chi_0}{\partial n}=0 \tag{25}$$

$$\frac{\partial\chi_1}{\partial n}=n_\alpha \tag{26}$$

$$\frac{\partial\chi_2}{\partial n}=n_\beta \tag{27}$$

$$\frac{\partial\chi_3}{\partial n}=(Xn_\beta-Yn_\alpha) \tag{28}$$

Based on the Bernoulli equation, and considering zero pressure on the free surface, we have

$$\begin{aligned}\chi_0=&-\left[\frac{1}{2}\left|\nabla\varphi\right|^2+\frac{1}{Fr^2}(s\beta-s+\cos\theta-\cos\theta_0+A_0)\right]\\&+U\varphi_\alpha-V\varphi_\beta-\Omega\cdot\left[X\cdot(-V-\varphi_\beta)-Y\cdot(U-\varphi_\alpha)\right]\end{aligned} \tag{29}$$

$$\chi_i(i=1,2,3)=0 \tag{30}$$

In the far field, the disturbance potential is assumed to have sufficiently diminished, and there is only the incident potential. Consequently, the boundary conditions can be written as

$$\begin{aligned}\frac{\partial\chi_0}{\partial n}&=\frac{\partial\phi_{It}}{\partial \mathrm{n}}+U\frac{\partial\phi_{Ix}}{\partial n}-V\frac{\partial\phi_{Iy}}{\partial n}-\Omega\cdot\frac{\partial}{\partial n}\left[X\cdot(-V-\phi_y)-Y\cdot(U-\phi_x)\right]\\&=\frac{\partial\phi_{It}}{\partial \mathrm{n}}+(U-Y\Omega)\frac{\partial\phi_{Ix}}{\partial n}-(V-X\Omega)\frac{\partial\phi_{Iy}}{\partial n}-\Omega\cdot\left[n_x\cdot(-V-\phi_{Iy})-n_y\cdot(U-\phi_{Ix})\right]\end{aligned} \tag{31}$$

$$\frac{\partial\chi_i}{\partial n}(i=1,2,3)=0 \tag{32}$$

The above auxiliary functions can also be solved through the boundary element method discussed in Sec. 2.3. Once they are all found, ϕ_t can be obtained and used in Eq. (22) for pressure calculation.

COUPLED MOTION

The Newton's equation of motion for a body in waves can be written as

$$[\mathbf{M}][\mathbf{A}]=[\mathbf{F}]+[\mathbf{F}_e] \tag{33}$$

where

$$[\mathbf{M}]=\begin{bmatrix}m&0&0\\0&m&0\\0&0&I\end{bmatrix},[\mathbf{A}]=\begin{bmatrix}\dot{U}\\-\dot{V}\\\dot{\Omega}\end{bmatrix},[\mathbf{F}]=\begin{bmatrix}F_1\\F_2\\F_3\end{bmatrix},[\mathbf{F}_e]=\begin{bmatrix}0\\-mg\\0\end{bmatrix} \tag{34}$$

In Eq. (34), m is the mass of the two dimensional wedge of unit length, and I denotes the rotational inertia about the centre of gravity. The matrix $[\mathbf{F}]$ is the hydrodynamic force, which can be obtained through integrating the pressure from Eq. (22) along the wetted surface of the body. Thus we have

$$F_i=s\cdot\int_{S_0}pn_idS \tag{35}$$

where $(n_1, n_2, n_3) = (n_\alpha, n_\beta, Xn_\beta - Yn_\alpha)$ Based on the definition of the auxiliary functions in Eq. (24), the hydrodynamic force can be divided into two parts: one part containing the terms associated with unknown accelerations, and the other part containing the rest of the hydrodynamic force which has been solved through the numerical scheme given in the previous section. In this case, the unknown accelerations can be obtained through solving the uncoupled equation of motion with unknown terms moved to the left hand side of Eq. (33). Thus we have

$$[\mathbf{M}+\mathbf{C}][\mathbf{A}] = [\mathbf{Q}] + [\mathbf{F}_e] \tag{36}$$

where $[\mathbf{C}]$ is the matrix with the coefficients

$$C_{ij} = s^2 \cdot \int_{S_0} \chi_i n_j dS \tag{37}$$

and the coefficients of matrix $[\mathbf{Q}]$ can be obtained as

$$\begin{aligned} Q_i = -s \cdot \int_{S_0} \{ & \chi - (U\varphi_\alpha - V\varphi_\beta) + \Omega \cdot \left[X \cdot (-V - \varphi_\beta) - Y \cdot (U - \varphi_\alpha) \right] \\ & + \frac{1}{2} \nabla\varphi \cdot \nabla\varphi + \frac{1}{Fr^2}(s\beta - s + \cos\theta - \cos\theta_0 + A_0) \} \cdot n_i dS \end{aligned} \tag{38}$$

NUMERICAL RESULTS AND DISCUSSION

The wave environment in the above procedure can be changed according to the specific problem. In the reported case, the 5th order Stokes wave for deep water is adopted. Based on the manner described before for Eq. (1), the non-dimensional potential and wave elevation can be written as [17]

$$\begin{aligned} \phi_1 = \frac{1}{F_r}\sqrt{\frac{1}{k^3}} (& kAe^{ky_0}\sin\theta - \frac{1}{2}k^3A^3e^{ky_0}\sin\theta + \frac{1}{2}k^4A^4e^{2ky_0}\sin 2\theta \\ & - \frac{37}{24}k^5A^5e^{ky_0}\sin\theta + \frac{1}{12}k^5A^5e^{3ky_0}\sin 3\theta) \end{aligned} \tag{39}$$

$$\begin{aligned} \eta_1 = A[& (1 - \frac{3}{8}k^2A^2 - \frac{422}{384}k^4A^4)\cos\vartheta + (\frac{1}{2}kA + \frac{1}{3}k^3A^3)\cos 2\vartheta \\ & + (\frac{3}{8}k^2A^2 + \frac{297}{384}k^4A^4)\cos 3\vartheta + \frac{1}{3}k^3A^3\cos 4\vartheta + \frac{125}{384}k^4A^4\cos 5\vartheta] \end{aligned} \tag{40}$$

where

$$\vartheta = kx_0 - \omega t + \vartheta_0 \tag{41}$$

$$\omega = \frac{\sqrt{k}}{F_r}(1 + \frac{1}{2}k^2A^2 + \frac{1}{8}k^4A^4) \tag{42}$$

and ϑ_0, ω, and k are, respectively, the initial phase, wave circular frequency, and wave number. It should be noted that A is not the wave amplitude but $H/2$, in which H is the wave height.

COMPARISON

The case of a symmetric wedge entering into calm water vertically through free fall motion is used for comparison. Fig. 2 shows the time-histories of accelerations obtained numerically from the present procedure and by Wu (2004) and Xu et al. (2010), as well as the experimental results recorded by Wu (2004). The rotational inertia I is set equal to $45kgm^2$, the distance between the wedge tip and the centre of gravity is $l = 0.25$, and the included angle is $\gamma_0 = \pi/4$. The deadrise angles γ_1 and γ_2 of the symmetric wedge at $t = 0$ are both $\pi/4$, and the initial heel angle is $\theta_0 = 0$. This angle will not change for the case with free fall motion. The acceleration of gravity with frictional resistance deducted is denoted as g_e. It can be seen from Fig. 2 that the vertical accelerations obtained from the present procedure are very close to those obtained by Wu (2004) and Xu et al. (2010), and this implies that the present numerical methodology is accurate. In the next cases, unless specified otherwise, γ_0 and θ_0 are set equal to $\pi/4$ and 0, respectively.

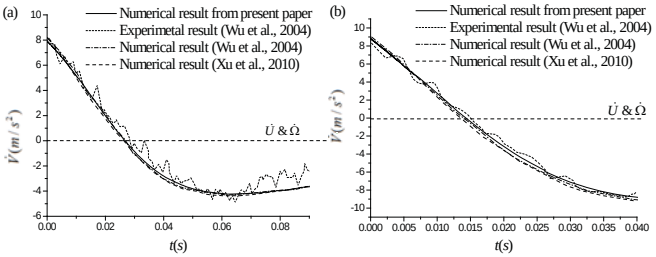

Fig. 2. Time-histories of acceleration for symmetric wedge entering water through free fall motion: (a) $ge = 8.0062ms^{-2}$, $M_b = 13.522kgm^{-1}$, $V_0 = 0.95623ms^{-1}$. (b) $ge = 8.9716ms^{-2}$, $M_b = 30.188kgm^{-1}$, $V_0 = 1.69673ms^{-1}$.

WATER ENTRY OF THE WEDGE INTO THE WAVE AT DIFFERENT FROUDE NUMBERS

Based on the dynamic boundary condition given by Eq. (6), it can be found that when the Froude number is larger, the gravity effect is less prominent. The same conclusion can also be made from the pressure equation (22). A limiting case is when the Froude number tends to infinity, and in this case the gravity effect is negligible. If the Froude number is larger, the disturbance potential is also larger, based on Eq. (11). It can also be found that the importance of the wave potential in the total potential becomes weaker, as proved by Eq. (39). To study the effect of the Froude number, the wedge with the mass $1kg/m$ and rotational inertia $45kgm^2$ is released to hit the wave crest freely at different initial velocities: 3m/s, 6m/s and 9m/s. The wave height and the wave length are respectively set equal to 0.8m and 6m. Based on the nondimensionalized procedure applied to Eq. (1), the corresponding Froude numbers are 1.92, 3.83, and 5.75. At $t = 0$, we have $\theta_0 = 0$ and $\gamma_0 = \pi/4$. Fig. 3 gives the free surface profiles and pressure distributions when the wedge has travelled the vertical distance $s = 0.4$. Based on the discussion by Sun et al. [12], when the water is not calm

and the wedge enters into the wave vertically, the results are not symmetric above the wedge axis due to the effect of the horizontal wave velocity component. However, based on the former discussion, it has been found that increasing the Froude number would make the wave effect weaker. Thus in Fig. 3, the free surface profiles and pressure distributions on the two hand sides of the wedge become more and more symmetric as the Froude number increases. A limiting case is when the Froude number tends to infinity. In this case the wave effect is negligible and the results on the two hand sides become completely symmetric.

Figs. 4-6 give the time-histories of acceleration, velocity and displacement for the wedge entering into the wave in three degrees of freedom with different Froude numbers. As shown in Fig. 4(a), when the Froude number is smaller, the absolute value of vertical deceleration $\dot{V}$ in non-dimensional sense is also smaller. This coincides with the results in Fig. 5(a), in which the absolute value of vertical velocity decreases more slowly with the decreasing Froude number. Thus in Fig. 6(a), the vertical distance travelled by the wedge with a smaller Froude number is larger due to smaller deceleration and larger velocity in vertical direction. This phenomenon seems to be in contradiction with the general idea that a body moves faster when the initial velocity or Froude number is larger. In fact, during the short interval of impact action, the body with a larger Froude number also suffers a larger impact pressure, which prevents the wedge from going down quickly. This can also be explained through the existence of a wave. The wedge with a smaller Froude number suffers a more unbalanced pressure distribution, see Fig. 3(b). Consequently, the hydrodynamic force in the vertical direction becomes smaller, and this directly leads to a smaller deceleration in vertical direction and larger accelerations in other directions. Thus, the accelerations in Fig. 4(b) and (c) with smaller Froude numbers are noticeably larger. Correspondingly, the velocities and displacements in Figs. 5 and 6 (b) and (c) increase as the Froude number decreases.

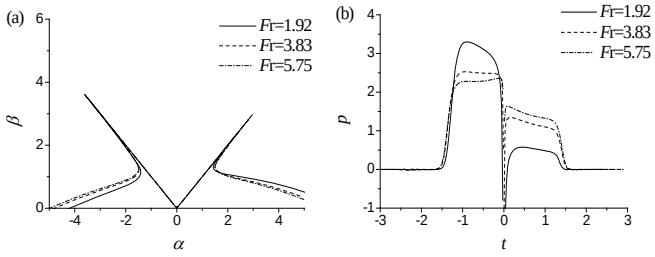

Fig. 3. Free surface profiles (a) and pressure distributions (b) for wedge entering into wave at different Froude numbers ($s = 0.4$).

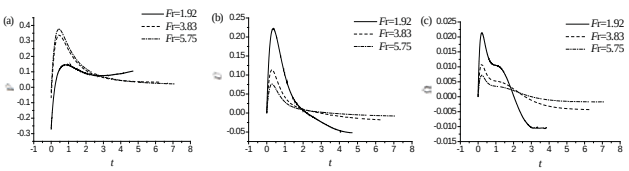

Fig. 4. Time-histories of (a) vertical, (b) horizontal, and (c) rotational acceleration for wedge entering into wave at different Froude numbers

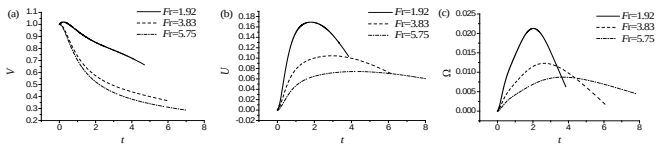

Fig. 5. Time-histories of (a) vertical, (b) horizontal, and (c) rotational velocity for wedge entering into wave at different Froude numbers

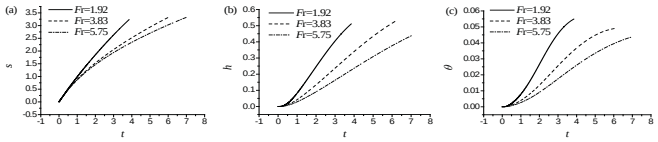

Fig. 6. Time-histories of (a) vertical, (b) horizontal, and (c) rotational displacement for wedge entering into wave at different Froude numbers

3.3. Water entry of the wedge into different waves

As can be seen from Eq. (39), the flow motion due to incident wave is proportional to $A\sqrt{k}/F_r$. It is evident that when $A\sqrt{k}/F_r << 1$, the wave effect can be neglected. If $A\sqrt{k}/F_r$ is not a small number and the Froude number F_r is fixed, the wave effect depends on the wave height $H = 2A$ and the wave number k. Two limiting cases are $H = 0$ and $k = 0$, both corresponding to calm water conditions.

Fig. 7 gives the free surface profiles and pressure distributions for the wedge hitting the wave crests with different heights, at a fixed vertical travelled distance $s = 0.4$. As H increases, the wave slope becomes increasingly steeper and the pressure distributions on the two hand sides become more and more unbalanced. The reason for this is that the horizonal velocity of the wave increases with H and the difference between the fluid velocity distributions on the two hand sides becomes more and more prominent. Fig. 8 gives the accelerations for the wedge hitting the wave crests with different heights. It is evident that as H increases, the absolute value of vertical acceleration decreases, while the horizontal and rotational accelerations increase noticeably. This can be explained through the pressure distribution in Fig. 7(b). The wave effect becomes increasingly prominent as H increases. As a result, the pressure on the seaward side becomes larger while that on the other side becomes smaller. This directly leads to the increase of the hydrodynamic force in the vertical direction and its decrease in other directions. As H decreases, the pressures on the two hand sides become gradually more symmetric, the hydrodynamic force in the vertical direction increases while decreasing in other directions. The limiting case is $H \to 0$, in which the wave effect is negligible and the hydrodynamic forces and accelerations in the horizontal and rotational directions also decrease to zero.

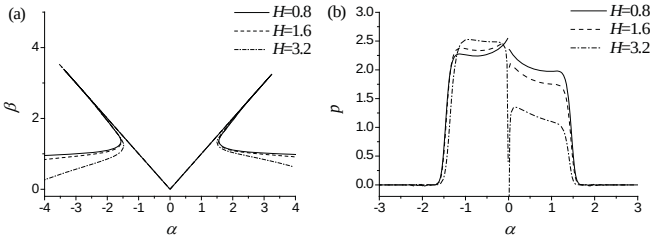

Fig. 7. Free surface profiles (a) and pressure distributions (b) for wedge entering into waves with different wave heights ($s = 0.4$)

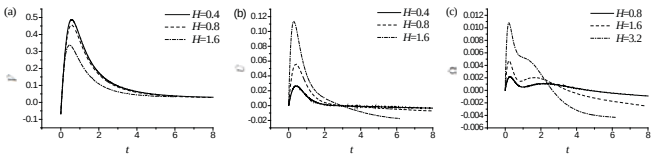

Fig. 8. Time-histories of (a) vertical, (b) horizontal, and (c) rotational acceleration for wedge entering into waves with different wave heights

Fig. 9 gives the free surface profiles and pressure distributions for the wedge hitting the wave crests with different wave numbers k , at the vertical distance travelled by the wedge $s = 0.4$. As k decreases, the wave effect becomes less prominent and therefore the pressure distributions on the two hand sides become more and more symmetric. In fact, estimating the wave effect only through k and h is not precise, as the effective deadrise angle between the wave and the wedge surface, as well as the wave velocity distributions in different phases are also very important for impact pressure [12]. In such a case, the pressure distribution in Fig. 9 shows some peculiar features, for example, the largest pressure is at $k = 0.17$, and this is because smaller k provides a smaller deadrise angle. Fig. 10 gives the accelerations for the wedge hitting the wave crests with different numbers k . It is evident that as k increases, the absolute value of vertical acceleration decreases. This is attributed to the smaller pressure in Fig. 9(b), and the deeper reason for this is that a larger k corresponds to larger deadrise angle on the two hand sides, see Fig. 9(a). As the wave number k increases, the horizontal acceleration in Fig. 10(b) decreases while the rotational acceleration in Fig. 10(c) increases. It should be noted that after a short time interval of slamming, the motion of the wedge is fully driven by the wave and its accelerations mainly depend on the velocity distribution and the slope of the wave in the wave field.

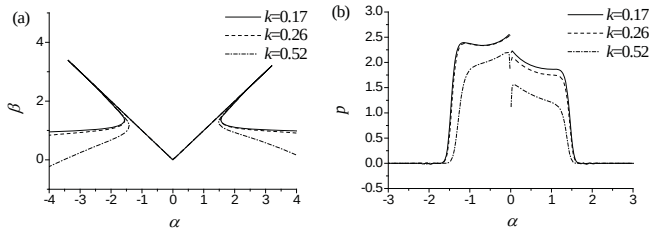

Fig. 9. Free surface profiles (a) and pressure distributions (b) for wedge entering into waves with different wave numbers ($s = 0.4$)

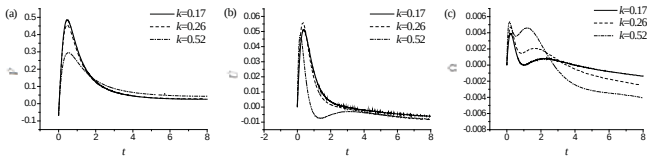

Fig. 10. Time-histories of (a) vertical, (b) horizontal, and (c) rotational acceleration for wedge entering into waves with different wave numbers

CONCLUSIONS

The problem of water entry of a wedge into waves in three degrees of freedom has been investigated using the fully nonlinear boundary element method based on the velocity potential theory. Extensive simulations have been undertaken for a wedge entering into the Stokes wave with a given initial vertical velocity, from which the following conclusions can be drawn:

(1) Except the calm water conditions, in all other cases the modes of wedge motion in the wave field vary greatly depending on the Froude number. As the Froude number increases, the absolute value of vertical acceleration increases, while the horizontal and rotational accelerations decrease. The reason for this is that the velocity distribution in the fluid field is noticeably changed by the wave. In this unsteady flow field, the Froude number is larger and the wave effect is less prominent. Thus we can conclude that it is not rational to neglect the wave effect absolutely in real ocean engineering problems, unless the Froude number is sufficiently large. In other words, calm water slamming is only a limiting case of the wave entry problem.

(2) When a wedge hits the peak of the Stokes wave with changing height at a given initial Froude number, a larger wave height will give a larger horizontal velocity in the fluid field, which will increase the pressure on the seaward side of the wedge and decrease on the back side. The wedge will surfer a more unbalanced pressure distribution, and this will lead to smaller acceleration in the vertical direction and larger in other directions.

(3) The effect of wave number is more complex. This is mainly due to the fact that the fluid field is affected by many other factors when the wave number k changes, for instance, the relative location and effective deadrise angle between the wedge and the wave.

(4) The present work analyses the impact between a wedge and water wave in a broad context, including the coupled effect. It has many practical implications, such as ship advancing in rough seas, wave interaction with coastal structures, and hostile wave hitting an offshore platform.

ACKNOWLEDGEMENTS

This work is supported by the National Natural Science Foundation of China (Grants No. 51579052, 51309125,

51579120) and the National Natural Science Foundation of Jiangsu (BK20151327).

REFERENCES

1. S.D. Howison, J.R. Ockendon, S.K, Wilson, Incompressible water-entry problems at small deadrise angles, J. Fluid Mech., 222, 215–230, 1991.

2. O.M. Faltinsen, Water entry of a wedge with Finite deadrise angle, J. Ship Res., 46(13), 39-51, 2002.

3. A. Korobkin, R. Guéret, Š. Malenica, Hydroelastic coupling of beam finite element model with Wagner theory of water impact, J. Fluids Struct., 22(4), 493-504, 2006.

4. Z.N. Dobrovolskaya, On some problems of similarity flow of fluid with a free surface, J. Fluid Mech., 36(4), 805–829, 1969.

5. R. Zhao, O. Faltinsen, Water entry of two-dimensional bodies, J. Fluid Mech., 246, 593–612, 1993.

6. Y.A. Semenov, A. Iafrati, On the nonlinear water entry problem of asymmetric wedges, J. Fluid Mech., 547, 231–256, 2006.

7. G.D. Xu, W.Y. Duan, G.X. Wu, Numerical simulation of oblique water entry of asymmetrical wedge, Ocean Eng., 35(16), 1597-1603, 2008.

8. G.X. Wu, Numerical simulation of water entry of twin wedges, J. Fluids Struct., 22, 99-108, 2006.

9. G.X. Wu, H. Sun, Y.S. He, Numerical simulation and experimental study of water entry of a wedge in free fall motion, J. Fluids Struct., 19(3), 277-289, 2004.

10. G.D. Xu, W.Y. Duan, G.X. Wu, Simulation of water entry of a wedge through free fall in three degrees of freedom, Math. Phys. & Eng. Science, 466, 2219-2239, 2010.

11. O.M. Faltinsen, Sea loads on ships and offshore structures, Cambridge University Press, 1990.

12. S.Y. Sun, S.L. Sun, G.X Wu, Oblique water entry of a wedge into waves with gravity effect, J. Fluids Struct., 52(1), 49-64, 2015.

13. C.H. Lu, Y.S. He, G.X. Wu, Coupled analysis of nonlinear interaction between fluid and structure during impact, J. Fluids Struct., 14(1), 127-146, 2000.

14. G.X. Wu, R. Eatock Taylor, Transient motion of a floating body in steep waves, 11th Workshop on Water Waves and Floating Bodies, Hamburg, Germany, 1996.

15. G.X. Wu, R. Eatock Taylor, The coupled finite element and boundary element analysis of nonlinear interactions between waves and bodies, Ocean Eng., 30(3), 387-400, 2003.

16. G.X. Wu, Hydrodynamic force on a rigid body during impact with liquid, J. Fluids Struct., 12(5), 549–559, 1998.

17. J.D. Fenton, A fifth-order Stokes theory for steady waves, J. Waterway Port Coastal and Ocean Eng., 111, 216-234, 1985.

CONTACT WITH THE AUTHORS

Shi Yan Sun
e-mail: shiyan_sun@126.com

Jiangsu University of Science and Technology
Mengxi Road, 212003 Zhenjiang
China

Hai Long Chen
e-mail: chenhailong@hrbeu.edu.cn

Harbin Engineering University
Nantong Street, 150001 Harbin
China

Gang Xu
e-mail: g.xu@just.edu.cn

Jiangsu University of Science and Technology
Mengxi Road, 212003 Zhenjiang
China

sciendo

POLISH MARITIME RESEARCH 1 (101) 2019 Vol. 26; pp. 125-133
10.2478/pomr-2019-0014

GENERATION AND PROPAGATION OF NONLINEAR WAVES IN A TOWING TANK

Marcin Drzewiecki[1,2]
Wojciech Sulisz[3]
[1] Gdańsk University of Technology, Poland
[2] Ship Deign and Research Centre CTO S.A., Gdańsk, Poland
[3] Institute of Hydroengineering of Polish Academy of Sciences IBW PAN, Gdańsk, Poland

ABSTRACT

The paper presents the results of the research focused on linear and nonlinear wave generation and propagation in a deepwater towing tank equipped with a single flap-type wavemaker of variable draft. The problem of wave generation and propagation has been theoretically formulated and solved by applying an analytical method; linear and nonlinear solutions were obtained. The linear solution has been verified experimentally. The laboratory experiments confirmed that a linear model can be applied to predict the generation and propagation of water waves of low steepness. However, according to the analysis, the discrepancies between wave profiles predicted by applying the linear and nonlinear models rapidly increases with increasing wave steepness. Additionally, the secondary phenomena which occur in the towing tank, including: disintegration of wave profile, wave reflections from the beach and wave damping, were analyzed. Knowledge on the nonlinear processes and phenomena is essential for modeling the environmental conditions during tests carried out to secure the safety of the naval and offshore constructions. The theoretical formulation was derived and the solution was obtained by the Institute of Hydroengineering of the Polish Academy of Sciences IBW PAN while the experimental research was carried out in Ship Hydromechanics Division of the Ship Design and Research Centre CTO S.A.

Keywords: wavemaker, towing tank, nonlinear waves, waves generation, waves propagation

INTRODUCTION

Physical modeling of the ocean hydrodynamics in towing tanks is vital for a sustainable development of naval architecture and offshore sectors. The understanding of the physics of the generation and propagation of nonlinear water waves in a towing tank is of fundamental importance for both scientists and engineers.

Numerous theoretical studies were conducted to describe the generation and propagation of waves in a hydrodynamic laboratory. Linear wavemaker theories were derived by Havelock [7] and Biesel and Suquet [1]. Laboratory experiments carried out in wave flumes confirmed suitability of the linear wave theory to mechanically generated waves of low steepness [19, 5, 9].

Research carried out in the Laboratório Nacional de Engenharia Civil in Lisbon, has shown that linear wavemaker theory is correct for regular waves investigated there [2]. However, for irregular waves, the measured transfer function was inconsistent with linear wavemaker theory. The authors indicate that it may arise from nonlinearities and energy losses.

The development of weakly-nonlinear wavemaker theories allowed for extending the range of applicability to steeper waves and gave insight into the physics of processes and side effects of the wave generation in a wave flume [12, 8, 16, 13, 15]. More complex numerical techniques were used to simulate nonlinear wave generation [14, 6, 10, 21, 22, 11]. The problem is that up to now, theoretical investigations have focused on the modelling of waves in typical wave flumes. Far less attention has been devoted to the problem of the generation and propagation of waves in towing tanks that in general are much longer and wider than flumes. The specific features of generation systems applied in towing tanks require special

attention and more advanced studies. The derived solutions have numerous limitations and drawbacks, and may not be applicable to explain many phenomena observed in towing tanks; this fact motivated the present study.

In this work, a theoretical approach is applied to predict the generation and propagation of nonlinear water waves in a towing tank. First, a boundary-value problem is formulated to describe the generation of nonlinear water waves in a towing tank and is solved by applying an analytical method. Then, the solution is applied to analyze the effect of wave frequencies and wave steepness on the generation and propagation of water waves in a long towing tank. Special attention is devoted to the magnitude of nonlinear wave components. Finally, theoretical results are compared with experimental data.

THEORETICAL FORMULATION

GOVERNING EQUATIONS

The problem of the generation and propagation of nonlinear water waves in a towing tank is considered. A right-hand Cartesian coordinate system is selected such that the *xy* plane is horizontal and coincides with the undisturbed free surface and *z* points vertically upwards, Fig. 1. It is assumed that the fluid is inviscid and incompressible, and that the fluid motion is irrotational. Moreover, it is assumed that the horizontal bottom and the vertical-side walls are impervious.

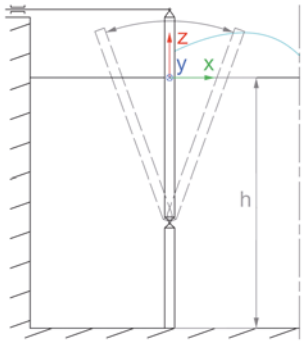

Fig. 1. Cartesian coordinate system in a towing tank for the considered problem

According to the assumptions, the velocity vector, $V(x, z, t)$, may be computed from a velocity potential $\Phi(x, z, t)$

$$V = \nabla\Phi\ (x, z, t) \tag{1}$$

where $\nabla(\cdot)$ is the two-dimensional vector differential operator. The fluid motion is governed by the continuity equation

$$\nabla^2\Phi = 0 \tag{2a}$$

and the Bernoulli equation

$$\Phi_t + \frac{1}{\rho}P + gz + \frac{1}{2}\left|\nabla\Phi\right|^2 = B\,, \tag{2b}$$

where ρ is the fluid mass density, P is the dynamic pressure, g is the acceleration due to gravity, and B is the Bernoulli constant.

The velocity potential, $V(x, z, t)$, satisfies the Laplace equation

$$\nabla^2\Phi = 0 \tag{3a}$$

At the free surface, the velocity potential, $V(x, z, t)$, has to satisfy the combined free-surface boundary condition

$$\begin{aligned}&\Phi_{tt} + g\Phi_z + (|\nabla\Phi|^2)_t \\ &+\frac{1}{2}\nabla\Phi\cdot\nabla|\nabla\Phi|^2 - B_t = 0, \\ &z = \eta(x,t)\end{aligned} \tag{3b}$$

and the dynamic boundary condition

$$\Phi_t + g\eta + \frac{1}{2}\left|\nabla\Phi\right|^2 - B = 0,\ z = \eta(x,t) \tag{3c}$$

At the wavemaker, the kinematic wavemaker boundary condition must be satisfied:

$$\chi_t + \Phi_z\chi_z - \Phi_x = 0, \quad x = \chi(z, t), \tag{3d}$$

At the sea bottom, the following boundary condition must be satisfied:

$$\Phi_z = 0, \quad z = -h \tag{3e}$$

Moreover, the velocity potential must satisfy boundary conditions at infinity and initial conditions [20]. The boundary conditions at infinity state that the first-order velocity potential at $x\to\pm\infty$ represents only outgoing waves.

PERTURBATION METHOD

The difficulties associated with an unknown location where the free-surface boundary conditions must be satisfied may be overcome by expanding the free-surface boundary conditions in a Taylor series about a known location that is assumed to be the undisturbed free surface $z = 0$. A similar procedure is applied to the kinematic wavemaker boundary condition. Accordingly, the combined free-surface boundary condition, Eq. (3b), the dynamic free-surface boundary condition, Eq. (3c), and the kinematic wavemaker boundary condition, Eq. (3d), may be written as follows

$$\begin{aligned}&\sum_{n=0}^{\infty}\frac{\eta^n}{n!}\frac{\partial^n}{\partial z^n} \\ &\cdot\left(\Phi_{tt} + g\Phi_z + (|\nabla\Phi|^2)_t + \frac{1}{2}\nabla\Phi\cdot\nabla|\nabla\Phi|^2 - B_t\right), \\ &= 0, \quad z = 0\end{aligned} \tag{4a}$$

$$\sum_{n=0}^{\infty}\frac{\eta^n}{n!}\frac{\partial^n}{\partial z^n}(\Phi_t + g\eta + \frac{1}{2}\left|\nabla\Phi\right|^2 - B) = 0, \tag{4b}$$
$$z = 0$$

$$\sum_{n=0}^{\infty} \frac{\chi^n}{n!} \frac{\partial^n}{\partial x^n} \left(\chi_t + \Phi_z \chi_z - \Phi_x \right) = 0, \quad x = 0 \tag{4c}$$

which usually helps to obtain a solution [8].

By applying Eq. (4), the boundary-value problem for the velocity potential, Eq. (3), may be written in the following form

$$\nabla^2 \Phi = 0 \tag{5a}$$

with boundary conditions

$$\begin{aligned} &\Phi_{tt} + g\Phi_z + \left(|\nabla\Phi|^2\right)_t + \\ &\frac{1}{2}\nabla\Phi \cdot \nabla|\nabla\Phi|^2 - B_t \\ &+\eta\left(\Phi_{tt} + g\Phi_z + \left(|\nabla\Phi|^2\right)_t + \frac{1}{2}\nabla\Phi \cdot \nabla|\nabla\Phi|^2 - B_t \right)_z \\ &+ \ldots = 0, \quad z = 0 \end{aligned} \tag{5b}$$

$$\begin{aligned} &\Phi_t + g\eta + \frac{1}{2}|\nabla\Phi|^2 - B \\ &+\eta\left(\Phi_t + g\eta + \frac{1}{2}|\nabla\Phi|^2 - B \right)_z \\ &+ \ldots = 0, \quad z = 0 \end{aligned} \tag{5c}$$

$$\chi_t + \Phi_z \chi_z - \Phi_x + \chi(\chi_t + \Phi_z \chi_z - \Phi_x)_x, + \ldots = 0, \quad x = 0 \tag{5d}$$

$$\Phi_z = 0, \quad z = -h \tag{5e}$$

Moreover, the velocity potential Φ, must satisfy boundary conditions at infinity.

An analytical solution to Eq. (5) may be found in the frame of weakly nonlinear wave theory. In order to obtain a solution, it is assumed that the quantities Φ, η, P, and B may be written in the form of the following series

$$\Phi(x, z, t) = {}_1\Phi + {}_2\Phi + \ldots, \tag{6a}$$

$$\eta(x, t) = {}_0\eta + {}_1\eta + {}_2\eta + \ldots, \tag{6b}$$

$$P(x, z, t) = {}_0P + {}_1P + {}_2P + \ldots, \tag{6c}$$

and

$$B(t) = {}_1B + {}_2B + \ldots, \tag{6d}$$

where a quantity with a left subscript n, n = 0,1,… is of the order of $(A_1k_1)^n$, $A_1k_1 \ll 1$, k_1 in which A_1 is the characteristic wave amplitude, k_1 is the characteristic wave number.

By substituting the formulas to the original boundary-value problem and collecting terms of the same order in wave steepness one obtains a set of the boundary-value problems with boundary conditions at z = 0 and x = 0.

$$\nabla^2 {}_1\Phi = 0, \quad -h \le z \le 0 \tag{7a}$$

$${}_1\Phi_{tt} + g\,{}_1\Phi_z - {}_1B_t = 0, \quad z = 0 \tag{7b}$$

$$\Phi_{tt} + g\,{}_1\Phi_z - {}_1B_t = 0, \quad z = 0 \tag{7c}$$

Moreover, the velocity potential must satisfy boundary conditions at infinity.

The boundary-value problem for the second-order velocity potential can be written in the following form

$$\nabla^2 {}_2\Phi = 0, \quad -h \le z \le 0 \tag{8a}$$

$${}_2\Phi_{tt} + g\,{}_2\Phi_z - {}_2B_t = -\left(|\nabla_1\Phi|^2\right)_t - {}_1\eta\left({}_1\Phi_{tt} + g\,{}_1\Phi_z\right)_z, \quad z = 0 \tag{8b}$$

$${}_2\Phi_x = {}_1\Phi_z\chi_z - \chi\,{}_1\Phi_{xx}, \quad x = 0 \tag{8c}$$

$${}_2\Phi_z = 0, \quad z = -h \tag{8d}$$

Moreover, the velocity potential must satisfy boundary conditions at infinity.

SOLUTION

LINEAR SOLUTION

The boundary-value problems, Eq. (7), for an excitation provided by simple-harmonic waves, may be solved in the present form. However, due to phase shift, it is more convenient to introduce spatial functions and separate a time-dependent factor. In order to conduct the separation, complex-valued spatial functions are introduced according to

$${}_1\Phi(x, z, t) = \mathrm{Re}\left[{}_1\phi(x, z)e^{-i\omega t}\right], \tag{9a}$$

$${}_1\eta(x, t) = \mathrm{Re}\left[{}_1\zeta(x)e^{-i\omega t}\right], \tag{9b}$$

$${}_1P(x, z, t) = \mathrm{Re}\left[{}_1p(x, z)e^{-i\omega t}\right], \tag{9c}$$

and

$${}_1B = \mathrm{Re}\left({}_1b\right), \tag{9d}$$

where Re denotes real part and $i = \sqrt{-1}$.

The spatial wave-field components may be written in the following form:

$${}_1\phi(x,z) = -\frac{ig}{\omega}\sum_{m=1} A_{1m}\frac{\cos\alpha_{1m}(z+h)}{\cos\alpha_{1m}h}e^{-\alpha_{1m}x}, \tag{10a}$$

$${}_1\zeta(x) = \sum_{m=1}^{\infty} A_{1m}e^{-\alpha_{1m}x}, \tag{10b}$$

where A_{11} is the amplitude of the progressive wave and A_{1m}, m = 2, 3, …, are the amplitudes of evanescent modes.

The eigenvalues must satisfy the following relations:

$$\frac{\omega^2}{g} = -\alpha_{1m}\tan\alpha_{1m}h, \quad m \ge 1, \tag{10c}$$

where the eigenvalues are $\alpha_{1m} = \{-ik_1, \alpha_{12}, \alpha_{13}, \ldots; k_1, \alpha_{12}, \ldots > 0\}$.

The coefficients of the eigenfunction expansions can be quantified from the kinematic wavemaker boundary condition

$$A_{1m} = \frac{4\,\alpha_{1m}\sin\alpha_{1m}h}{\alpha_{1m}h + \sin 2\,\alpha_{1m}h} \cdot \int_{-h}^{0} \hat{\chi}\cos\alpha_{1m}(z+h)dz \qquad \textbf{(10d)}$$

The linear transfer function, according to (10d), has been calculated for the considered wavemaker in the deepwater towing tank. It has been calculated for three possible water levels – 5.19 m, 5.69 m, 6.19 m – and shown in, respectively, Fig. 2, Fig. 3, Fig. 4.

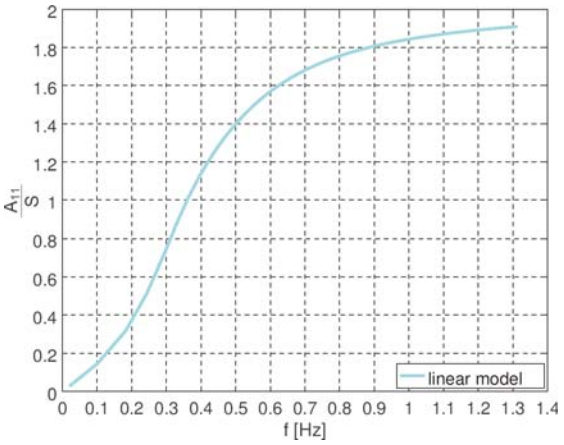

Fig. 2. Linear transfer function for a hinged wavemaker, h=5.19 m

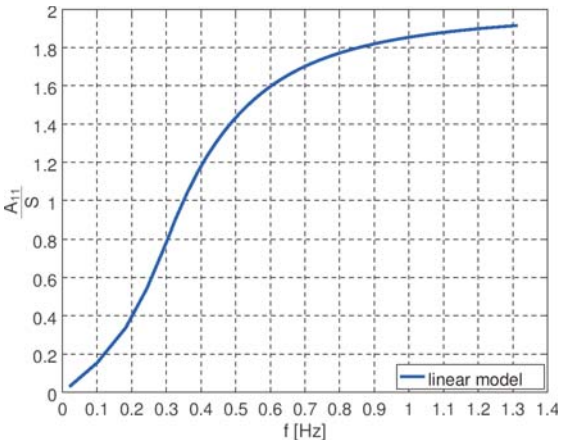

Fig. 3. Linear transfer function for a hinged wavemaker, h=5.69 m

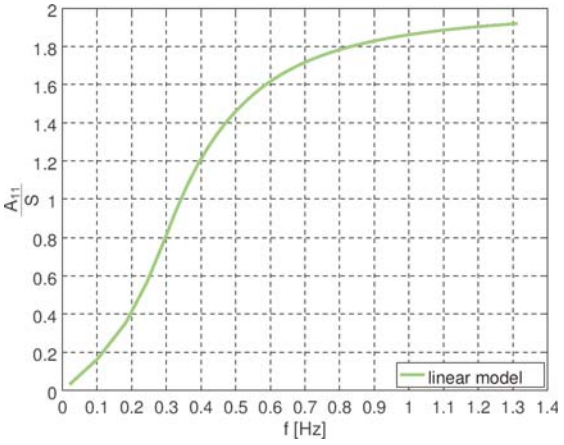

Fig. 4. Linear transfer function for a hinged wavemaker, h=6.19 m

NONLINEAR SOLUTION

It is convenient to solve the boundary-value problems, Eq. (8), by introducing spatial functions and separate a time-dependent factor [17]. In order to conduct the separation of time complex-valued spatial functions are introduced according to

$${}_2\Phi(x,z,t) = \mathrm{Re}\left[\,{}_2\phi(x,z)\,e^{-2i\omega t}\,\right] + {}^{0}_{2}\Phi(x,z)\,, \qquad \textbf{(11a)}$$

$${}_2\eta(x,t) = \mathrm{Re}\left[\,{}_2\varsigma(x)\,e^{-2i\omega t}\,\right] + {}^{0}_{2}\eta(x)\,, \qquad \textbf{(11b)}$$

$${}_2\eta(x,t) = \mathrm{Re}\left[\,{}_2\varsigma(x)\,e^{-2i\omega t}\,\right] + {}^{0}_{2}\eta(x)\,, \qquad \textbf{(11c)}$$

and

$${}_2B = \mathrm{Re}\,({}_2b). \qquad \textbf{(11d)}$$

The nonlinear components of the velocity potential and free-surface elevation may be expressed as follows

$$\begin{aligned} {}_2\phi = &-\frac{ig}{2\omega}\sum_{j=1}^{\infty} A_{2j}\frac{\cos\alpha_{2j}(z+h)}{\cos\alpha_{2j}h}e^{-\alpha_{2j}x} \\ &- i\omega\sum_{m=1}\sum_{s=1} A_{1m}A_{1s}\frac{\alpha_{1m}\alpha_{sm}}{4\omega^4/g^2} \\ &\cdot\frac{6\omega^4/g^2 + 4\alpha_{1m}\alpha_{1s} + \alpha_{1m}^2 + \alpha_{1s}^2}{4\omega^4/g^2 + (\alpha_{1m}-\alpha_{1s})^2} \\ &\cdot\frac{\cos(\alpha_{1m}+\alpha_{sm})(z+h)}{\cos\alpha_{1m}h\cos\alpha_{1s}h}e^{-(\alpha_{1m}+\alpha_{1s})x}\,, \end{aligned} \qquad \textbf{(12a)}$$

$$\begin{aligned} {}_2\zeta(x) = &\sum_{j=1}^{\infty} A_{2j}e^{-\alpha_{2j}x} + \frac{g}{4\omega^2}\sum_{m=1}^{\infty}\sum_{s=1}^{\infty} A_{1m}A_{1s} \\ &\cdot\frac{(\alpha_{1m}+\alpha_{1s})^2\left(\omega^4/g^2 + 3\alpha_{1m}\alpha_{1s}\right)}{4\omega^4/g^2 + (\alpha_{1m}-\alpha_{1s})^2}e^{-(\alpha_{1m}+\alpha_{1s})x}\,, \end{aligned} \qquad \textbf{(12b)}$$

where A_{21} is the amplitude of the free nonlinear wave, A_{2j}, $j = 2, 3, \ldots$, are the amplitudes of the nonlinear components of evanescent modes.

The eigenvalues must satisfy the following relations

$$\frac{4\omega^2}{g} = -\alpha_{2j}\tan\alpha_{2j}h,\ j \geq 1\,, \qquad \textbf{(12c)}$$

where $\alpha_{2j} = \{-ik_2, \alpha_{22}, \alpha_{23}, \ldots; k_2, \alpha_{22}, \ldots > 0\}$.

The nonlinear velocity potential consists of two main parts. The first part is associated with the summation over j and satisfies the homogeneous form of the combined free-surface boundary condition. The second part represents ${}_2\phi^F$ and satisfies the nonhomogeneous form of the combined free-surface boundary condition [17, 18].

The coefficients of the eigenfunction expansions can be quantified from the wavemaker kinematic boundary condition

$$A_{2j} = \frac{4\alpha_{2j}\sin\alpha_{2j}h}{\alpha_{2j}h + \sin 2\alpha_{2j}h}\int_{-h}^{0}\left[-{}_2\phi_z^F + ({}_1\phi_z\hat{\chi})_z\right]\cos\alpha_{2j}(z+h)dz,$$

$$x = 0 \qquad \textbf{(12d)}$$

In accordance with the linear and nonlinear solutions, simulations were carried out for the considered type of wavemaker.

The simulations included calculations of amplitudes: progressive wave A_{11}, undesirable free nonlinear wave A_{21}, resulting from using single flap-type wavemaker, and Stokes wave A_{2S} that accompanies the first harmonic. The calculations have been carried out for kh values from 0.1 to 1.8 with increments of 0.1 and for three possible water levels – 5.19 m, 5.69 m, 6.19 m. The kh is an multiplication of the wave number k and water level h. The comparison between the amplitudes of nonlinear waves: A_{21}, A_{2S} with amplitudes of linear waves A_{11} are presented in Tab. 1, Tab. 2, Tab. 3 and in Fig. 5, Fig. 6, Fig. 7, respectively.

Tab. 1. Linear and nonlinear wave components in the towing tank, h=5.19 m

kh	$\frac{\lvert A_{21}\rvert}{A_{11}}$	$\frac{\lvert A_{21}\rvert}{A_{2S}}$
0.1	0.71	0.96
0.2	0.31	0.83
0.3	0.16	0.61
0.4	0.06	0.30
0.5	0.05	0.28
0.6	0.13	0.83
0.7	0.23	1.49
0.8	0.32	2.17
0.9	0.41	2.75
1.0	0.48	3.17
1.1	0.54	3.41
1.2	0.58	3.50
1.3	0.60	3.47
1.4	0.62	3.36
1.5	0.63	3.19
1.6	0.64	2.99
1.7	0.64	2.78
1.8	0.63	2.56

Tab. 2. Linear and nonlinear wave components in the towing tank, h=5.69 m

kh	$\frac{\lvert A_{21}\rvert}{A_{11}}$	$\frac{\lvert A_{21}\rvert}{A_{2S}}$
0.1	0.76	0.96
0.2	0.34	0.84
0.3	0.18	0.63
0.4	0.08	0.35
0.5	0.04	0.21
0.6	0.12	0.68
0.7	0.21	1.28
0.8	0.30	1.89
0.9	0.38	2.42
1.0	0.45	2.79
1.1	0.50	3.00
1.2	0.54	3.08
1.3	0.56	3.04
1.4	0.58	2.94
1.5	0.58	2.79
1.6	0.58	2.61
1.7	0.58	2.41
1.8	0.58	2.22

Tab. 3. Linear and nonlinear wave components in the towing tank, h=6.19 m

kh	$\frac{\lvert A_{21}\rvert}{A_{11}}$	$\frac{\lvert A_{21}\rvert}{A_{2S}}$
0.1	0.80	0.96
0.2	0.36	0.85
0.3	0.19	0.66
0.4	0.09	0.38
0.5	0.04	0.18
0.6	0.10	0.57
0.7	0.19	1.13
0.8	0.28	1.69
0.9	0.36	2.17
1.0	0.42	2.51
1.1	0.47	2.70
1.2	0.50	2.77
1.3	0.53	2.74
1.4	0.54	2.64
1.5	0.54	2.49
1.6	0.54	2.33
1.7	0.54	2.16
1.8	0.53	1.98

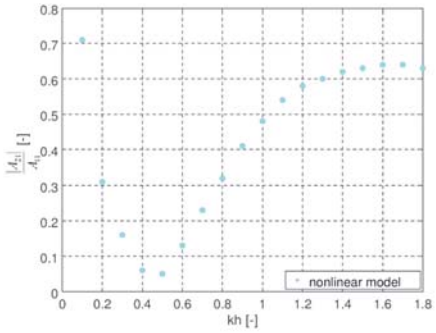

Fig. 5. Linear and nonlinear wave components in the towing tank, h=5.19 m

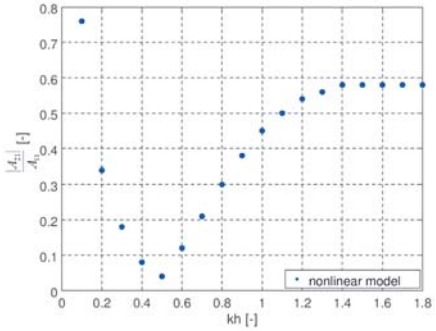

Fig. 6. Linear and nonlinear wave components in the towing tank, h=5.69 m

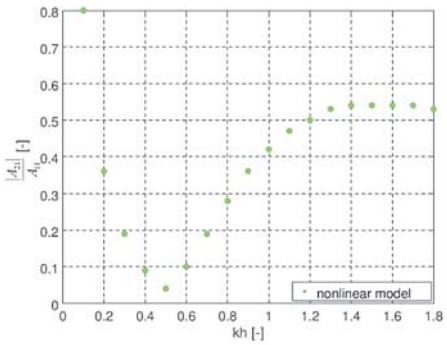

Fig. 7. Linear and nonlinear wave components in the towing tank, h=6.19 m

VALIDATION

LABORATORY FACILITIES

The proposed linear solution (10d) has been validated for deepwater towing tank of the following dimensions: length 270 m, width 12 m and depth 6 m, equipped with a single flap-type wavemaker, shown in Fig. 8.

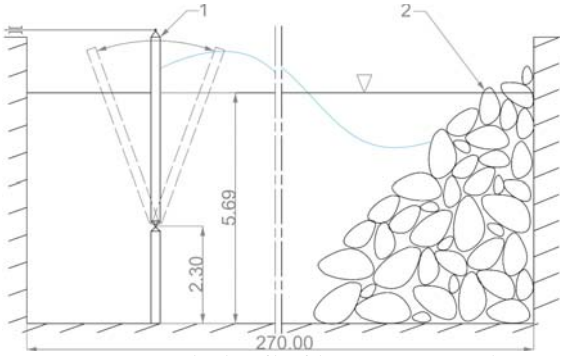

Fig. 8. Longitudinal profile of deepwater towing tank with the wavemaker (1) and sloped beach (2)

The wavemaker and deepwater towing tank of the Ship Design and Research Centre CTO S.A. are used for testing models of ships (Fig. 9) and anchored or bottom-fixed offshore structures e.g. oil rigs or wind turbines.

The model tests are carried out to predict the response of a structure to extreme sea state conditions.

The wavemaker is a position-controlled single flap-type device articulated above the channel bottom. It is equipped with hydraulically driven mechanism.

The wavemaker control system was modernized in 2015 – an analog control system was replaced by a new digital control system [3] further optimized in 2017 [4].

Fig. 9. The example seakeeping tests in CTO S.A.

THE EXPERIMENTS

The validation was based on the measurements of the flap displacements and wave profiles. The validation of the linear solution was carried out for regular waves of 5 cm height and frequencies from 0.3 Hz to 1.2 Hz with increments of 0.1 Hz. The water depth in the towing tank was equal to 5.69 m. The waves were measured using a wave gauge manufactured at CTO S.A. (Fig. 10). The wave gauge was mounted in the towing tank at the distance of 60 m from the flap. The displacements of the flap during wave generation were measured using linear displacement sensor WDS-1000-P60-SR-U manufactured by MicroEpsilon.

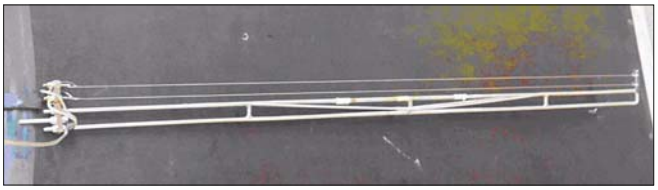

Fig. 10. Resistive wave gauge manufactured at CTO S.A.

Experimental results were compared with theoretical results. Due to idealization of the theoretical model, particular features of the actual towing tank are not taken into account in the presented formulation, e.g. flow damping between the wavemaker flap and towing tank walls as well as damping in waveguides area. This type of damping is out of scope of the present study. For that reason, a constant correction parameter *Cp* is introduced, evaluated so as to obtain the best match between the theoretical and experimental results. The resulting value is *Cp*=0.8.

The comparison between theoretical results and experimental data is presented in Fig. 11.

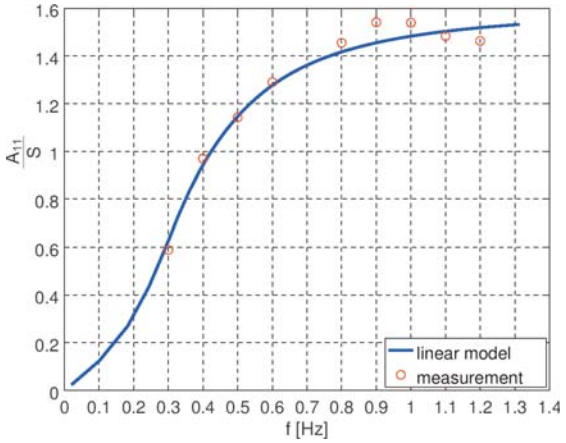

Fig. 11. The comparison between theoretical results and experimental data for water depth h=5.69 m

SECONDARY PHENOMENA

In addition to the main set of measurements conducted to verify the derived model, a series of additional measurements was conducted to provide insight into the physics of secondary phenomena observed during laboratory experiments conducted in the towing tank. The profiles of regular waves were measured

along the towing tank for the waves of the heights 2.5 cm, 5 cm, and 10 cm, and frequencies f from 0.3 Hz to 1.2 Hz with increment of 0.1 Hz. The secondary phenomena were investigated and analyzed using FFT.

DISINTEGRATION OF WAVE PROFILE

The measurements were conducted by a gauge mounted on the carriage moving towards the wavemaker and then backwards. The measurements allowed to calculate the spectrum spread factor s. This factor has been calculated by dividing the energy of the main wave by the energy of the entire wave spectrum. The value of s has been determined along the towing tank for three groups of wave frequencies f. The results averaged for five towing tank segments are presented in Fig. 12. It can be seen that for f smaller than 1.0 Hz, s is constant while it is dropping along the towing tank for f from 1.0 Hz. It arises from phenomenon of disintegration of wave profile and decay of main wave frequency into other frequency bands. This phenomenon increases strongly with an increase f from 1.0 Hz to 1.2 Hz.

WAVE REFLECTIONS FROM THE BEACH

During the measurements, the carriage was moving from the beach towards the wavemaker to capture the reflection from the rubble-mound beach. The reflected wave height and the incident wave height were extracted from the recorded signals in frequency domain by means of the Doppler shift for known velocity of the towing carriage. This allowed to identify beach reflection properties. The reflection coefficient R is the ratio of the height of the reflected wave divided by the height of the incident wave. The R was periodic along the test section and it was changing slightly. The value of R has been averaged along the towing tank test section for investigated incident wave frequencies. The results are shown in Fig. 13. It can be seen that for investigated rubble-mound beach, R is exponentially growing in the range from ca.10 % to ca. 30 % in function of f.

WAVE DAMPING

The measurements were carried out at both ends of the deepwater towing tank during generation of regular waves of 5 cm height and frequencies from 0.3 Hz to 1.2 Hz with increment of 0.1 Hz. The wave gauge was mounted on a towing carriage. The separate series of measurements were conducted on the up-wave and down-wave side of the towing tank. This technique allowed to determine wave damping along the towing tank. The relative difference between wave height on the up-wave and down-wave side of the towing tank with respect to the wave height on the up-wave side, D, is shown Fig. 14. It can be seen that damping of waves along the towing tank is exponentially growing with f from ca. 5 % damping for f = 0.4 Hz up to ca. 85 % damping for f = 1.0 Hz while the waves with f equal to 1.1 Hz and 1.2 Hz get almost completely damped.

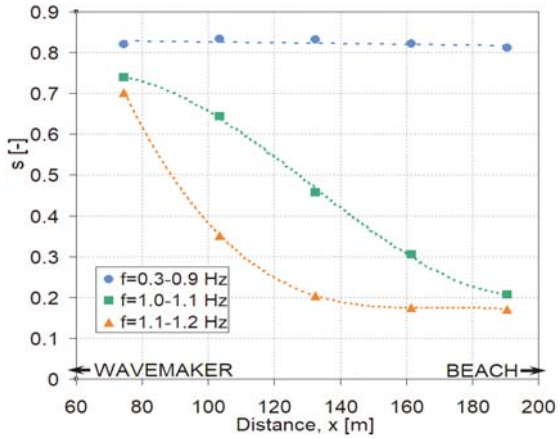

Fig. 12. The spectrum spread factor along the towing tank

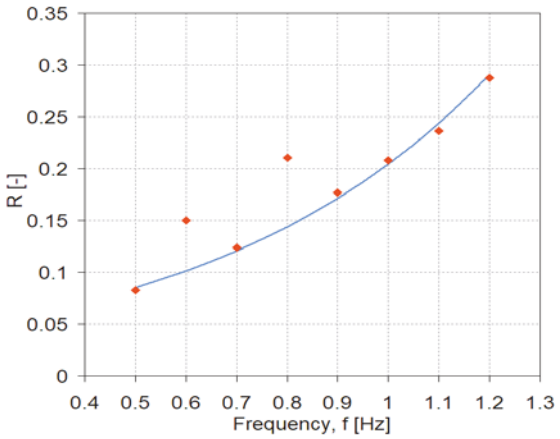

Fig. 13. Reflection coefficient versus wave frequencies for the rubble-mound beach

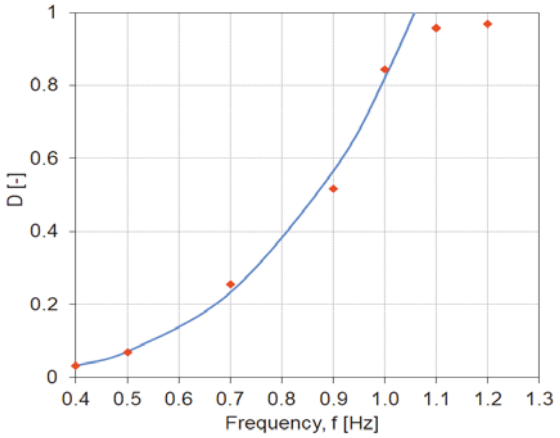

Fig. 14. Wave damping in the towing tank

CONCLUSIONS

A theoretical approach was applied to predict the generation and propagation of nonlinear water waves in a towing tank. The formulated boundary-value problem was solved by applying an analytical method. The derived model was applied to determine linear and nonlinear components of the free-surface oscillations along the towing tank.

The analysis of the results shows that for waves of very low steepness, the nonlinear wave effects and effects associated with the interaction of water waves in a generated wave train

are of secondary importance and a linear solution may be accepted to predict waves in a towing tank. However, the discrepancies between wave profiles predicted by applying the linear and nonlinear models rapidly increases with increasing wave steepness. The analysis shows that for waves of moderate steepness the nonlinear wave component may exceed many times its linear counterpart. The analysis indicates that this phenomenon is the result of a wave generation system that generates significant components of nonlinear free waves for a wide rage of wave frequencies.

Laboratory experiments were conducted in the towing tank to verify theoretical results. The free-surface elevation recorded by a wave gauge was compared with the results provided by the derived model. Fairly good agreement between theoretical results predicted by the linear model and experimental data is observed for a wide range of wave frequencies.

In addition to the main set of measurements conducted to verify the derived model, a series of additional measurements was conducted to provide insight into the physics of secondary phenomena observed during laboratory experiments conducted in the towing tank. The secondary phenomena affect the propagation and transformation of waves along the towing tank. Knowledge on the nonlinear processes and phenomena observed in the towing tank is essential for the modeling processes.

Future work should include verification of the nonlinear model, especially the presence of significant components of nonlinear free waves for the wave generation system in the deepwater towing tank.

ACKNOWLEDGEMENT

The research was financed by the Ministry of Science and Higher Education of the Republic of Poland and by Ship Design and Research Centre CTO S.A.

REFERENCES

1. Biesel F. and Suquet F.: *Laboratory wave generating apparatus*. Project Report No. 39, Minneapolis 1953.
2. Campos C., Silveira F. and Mendes M.: *Waves inducted by non-permanent paddle movements*. Coastal Engineering Proceedings, vol. 13, 1972 pp. 707–722.
3. Drzewiecki M.: *Digital Control System of the Wavemaker in the Towing Tank*. Automatyka, elektryka, zakłócenia, vol. 7, no. 4, 2016, pp. 138–146.
4. Drzewiecki M.: *Modelling, Simulation and Optimization of the Wavemaker in a Towing Tank. Trends in Advanced Intelligent Control, Optimization and Automation*. Springer International Publishing AG, 2017, pp. 570–579.
5. Galvin C. J.: *Wave-height prediction for wave generators in shallow water*. Technical Memorandum No. 4, U.S. Army Corps of Engineers, 1964, Washington, pp. 1–20.
6. Grilli S. and Horrillo J.: *Numerical Generation and Absorption of Fully Nonlinear Periodic Waves*. Journal of Engineering Mechanics, 123(10), 1997, pp. 1060–1069.
7. Havelock T. H.: *Forced surface-wave on water*. Philosophical Magazine, 7, 1929, pp. 569–576.
8. Hudspeth R. T. and Sulisz W.: *Stokes drift in 2-D wave flumes*. Journal of Fluid Mechanics, 230, 1991, pp. 209–229.
9. Keating T. and Webber N. B.: *The generation of periodic waves in a laboratory channel; a comparison between theory and experiment*. Proceedings of the Institution of Civil Engineers, 63, 1977, pp. 819–832.
10. Liu S-X., Teng B. and Yu Y-X.: *Wave generation in a computation domain*. Applied Mathematical Modelling, 29, 2005, pp. 1–17.
11. Liu X., Lin P. and Shao S.: *ISPH wave simulation by using an internal wave maker*. Coastal Engineering, 95, 2015, pp. 160–170.
12. Madsen O. S.: *On the generation of long waves*. Journal of Geophysical Research, 76, 1971, pp. 8672–8683.
13. Moubayed W. I. and Williams A. N.: *Second-order bichromatic waves produced by a generic planar wavemaker in a two-dimensional wave flume*. Journal of Fluids and Structures, 8, 1994, pp. 73–92.
14. Multer R H.: *Exact nonlinear model of wave generator*. Journal of Hydraulic Research, ASCE, 99, 1973, pp. 31–46.
15. Schaffer H. A.: *Second-order wavemaker theory for irregular waves*. Ocean Engineering, 23, 1996, pp. 47–88.
16. Sulisz W. and Hudspeth R. T.: *Complete second order solution for water waves generated in wave flumes*. Journal of Fluids and Structures, 7(3), 1993, pp. 253–268.
17. Sulisz, W.: *Diffraction of nonlinear waves by founded horizontal rectangular cylinder*. Journal of Waterway, Port, Coastal, and Ocean Engineering, ASCE, 124, 5, pp. 257–263.
18. Sulisz, W.: *Reflection and transmission of nonlinear water waves at a semi-submerged dock*. Archives of Mechanics, 65, 3, pp. 237–260.
19. Ursell F., Dean R. G. and Yu Y. S.: *Forced small amplitude waves: A comparison of theory and experiment*. Journal of Fluid Mechanics, 7, 1960, pp. 33–52.
20. Wehausen J.V. and Laitone,F.V.: *Surface Waves, Handbuch Der Physik*. Vol. 9, Springer-Verlag, Berlin 1960.

21. Zhang X. T., Khoo B. C. and Lou. J.: *Wave propagation in a fully nonlinear numerical wave tank: A desingularized method*. Ocean Engineering, 33, 2006, pp. 2310–2331

22. Zheng J., Soe M. M., Zhang C. and Hsu T-W.: *Numerical wave flume with improved smoothed particle hydrodynamics*. Journal of Hydrodynamics, 22(6) 2010, pp. 773–781

CONTACT WITH THE AUTHORS

Marcin Drzewiecki
e-mail: drzewiecki.marcin@op.pl

Gdańsk University of Technology
Narutowicza 11/12
80-233 Gdańsk

Ship Deign and Research Centre CTO S.A.
Szczecińska 65
80-392 Gdańsk
Poland

Wojciech Sulisz
e-mail: sulisz@ibwpan.gda.pl

Institute of Hydroengineering
of Polish Academy of Sciences IBW PAN
Kościerska 7
80-328 Gdansk
Poland

sciendo

POLISH MARITIME RESEARCH 1 (101) 2019 Vol. 26; pp. 134-144
10.2478/pomr-2019-0015

A MULTI-LAYERED POTENTIAL FIELD METHOD FOR WATER-JET PROPELLED UNMANNED SURFACE VEHICLE LOCAL PATH PLANNING WITH MINIMUM ENERGY CONSUMPTION

Shasha Wang
Mingyu Fu
Yuanhui Wang
Liangbo Zhao
College of Automation, Harbin Engineering University, China

ABSTRACT

Focusing on the influence of wind and surface currents on local path planning in the marine environment, a multi-layered potential field (MPF) method is proposed to minimize the energy consumption of a water-jet propelled unmanned surface vehicle (USV). A synthetic environment framework that can incorporate the information of the base potential field layer and the environment layer is constructed first. This framework provides a base for minimizing the energy consumption of the water-jet propelled USV through proper force weighting. For the purpose of USV path planning, the traditional potential field method is extended by including the velocity information of the USV and the approached obstacles to avoid collisions with dynamic obstacles. The proposed method integrates kinematic control to prevent considering the vehicle as a point mass or rigid body. Finally, simulation and comparison experiments are performed to demonstrate the energy-saving efficiency of the proposed local path planning approach for the water-jet propelled USV.

Keywords: water-jet propelled USV, local path planning, marine environment, minimum energy consumption, multi-layered potential field method

INTRODUCTION

The USVs have been widely used in various marine applications in the past decades, with military applications being dominant. When the USVs perform dangerous missions, such as sea patrol or coastal guarding in harsh environments, the risk to the personnel is obviously reduced due to the minimal involvement of human operators [1]. In addition, it should be noted that civilian applications, such as environmental monitoring [2] or search and rescue missions [3], are also important and promising for the USVs. In highly polluted lakes, USVs can be used to collect water samples without direct human participation [2]. Together with a micro aerial vehicle, the USV played an important role while surveying damages in parts of Marco Island after Hurricane Wilma in 2005 [3]. Therefore, USVs can be combined with other unmanned systems to perform various tasks without human intervention, and essentially exhibit highly nonlinear dynamics.

Path planning aims to guide the vehicle from its initial position to the destination while possessing accurate perception of the environment and effective collision avoidance capabilities [4]-[6]. The path planning process can generally have the form of three different approaches: global approach (path generated prior to launching the USV) [7], local approach (path generated while the vehicle is en-route) [8], and hybrid approach [9]. To obtain the path, different computational methods can be applied, such as optimization

methods based on evolutionary algorithms (EAs) and/or genetic algorithms (Gas) [10]), heuristic search algorithms (graph search techniques), and potential fields (artificial potential fields - APFs). However, GAs has the drawbacks of lacking convergence and expensive computational costs. Thus the generated path may lack consistency, which will limit its real-time implementation. Compared to optimization methods, the heuristic methods (graph search techniques) can quickly find an optimal path with the least number of nodes because they use the grid-based strategy [11][12]. However, a further path smoothing procedure is needed to deal with the non-holonomic constraints of the vehicle [11]. Moreover, they don't provide the global optimal path and are not suited to cases where the environment is highly dynamic and has strong effects on the robots.

In the potential field (PF) approach, the target points are assigned with attractive fields, while the obstacles are distributed with repulsive fields [13]. This approach is becoming more and more popular, due to its easy implementation and good collision avoidance capability. The input data to the potential field algorithm can be obtained directly from range sensors, without map calculations and estimations. Potential field algorithms are appropriate for underlying real-time control at the lack of global information, but the problem of local minima and target unreachability may appear. Therefore, this kind of problem needs to be handled by global algorithms at a higher layer [13]. Here, two major solutions have been worked out [14][15]. When facing moving obstacles and the time-varying environment, the APF can modify the path to avoid collisions. However, most potential field methods focus their attention on theoretical analyses and regard the vehicle as a mass point or rigid body without constraints. Moreover, the marine environment and the limited energy of the vehicle are not sufficiently taken into account or even ignored in path planning [16].

The influence of the marine environment cannot be ignored when developing the path planning algorithms for marine vehicles, especially for those with limited operating speed and relatively small dimensions and displacements. The environmental effects and energy consumption should be considered in the path planning in the ocean, which is different from the general path planning on land, to find the shortest path while avoiding the obstacles [17]. Although many researchers have proposed intelligent path planning algorithms to deal with the environmental influences of autonomous underwater vehicles (AUVs), very little work has been done for unmanned surface vehicles (USVs). Thus, if the generated path ignores the environmental effects, more fuel may be consumed, or the path may be too difficult to follow [18]. It is difficult to select the optimal path in terms of the expected energy consumption using only the kinematics-based or distance-based approach. In [19], Garau et al. presented the effect of current fields in the path planning problem using the A* search algorithm with time-optimal cost. They emphasized the importance of the marine environment in path planning. Considering the time-varying currents, an iterative non-linear optimization method was used in [20] to find the time-optimal path. The comparison has also been made with other selected path planning algorithms, such as RRT, Line-of-sight, A*, and Constant-Time Surfacing-A* [21]. In addition, numerous energy-efficient path planning approaches have been applied to improve the endurance of surface vehicles. However, non-holonomic constraints of vehicles were ignored in those approaches [22]-[24].

In view of the above issues, this work is devoted to developing a multi-layered potential field method for a water-jet propelled USV to minimize its energy consumption in the presence of marine environments, such as wind and surface currents. The diagram of the method is shown in Fig. 2. The performance of the proposed algorithm was verified through comparison of simulation results. The main contributions of the paper can be summarized as below:

1) Taking into account the influence of the wind and surface currents on the local path planning of a water-jet propelled USV, a multi-layered potential field method is proposed to minimize the energy consumption.
2) The paper constructs a synthetic environment framework, which incorporates the information of the base potential field layer and the environment layer.
3) The traditional potential field method is extended by including the velocity information of the USV and the obstacles to avoid collisions with dynamic obstacles.

PLANNING SPACE REPRESENTATION

PROBLEM STATEMENT

To achieve autonomous USV path planning in the maritime environment, two critical problems need to be addressed. The first problem is collision avoidance with dynamic obstacles composing kinematic constraints. The second problem is generation of the minimum energy consumption path under the influence of wind and surface currents. To address the aforementioned problems and challenges, a synthetic environment framework and multi-layered potential field method are developed in this paper.

Assumption 1: The position and velocity of both the USV and the target are well known.

Assumption 2: The positions and velocities of surface obstacles can be accurately measured online.

Assumption 3: Among the marine environmental effects, wind and surface currents are mainly considered in this paper.

Assumption 4: The obstacle velocity is equal to or less than the USV velocity, and its motion is linear and uniform.

KINEMATIC MODEL OF WATER-JET PROPELLED USV

The USV is equipped with water-jet propulsion, nozzle pump, rudder sensor, astern pump & sensor, compass, radar, GPS, anemoscope & dogvane, wireless system, etc. [25]. The equipment of the USV is shown in Fig. 1. To simplify the algorithm, the USV is assumed to be a three degree of

freedom (3-DOF) system, including surge, sway, and yaw [1]. Then, the kinematic model is formulated as:

$$\eta = J(\eta)\upsilon = \begin{cases} x = u\cos(\psi) - v\sin(\psi) \\ y = u\sin(\psi) + v\cos(\psi) \end{cases} \quad (1)$$

where $\eta = [x, y, \psi]^{\mathrm{T}}$ is the position and heading vector with coordinates in the earth-fixed reference frame ({E}-frame), and $\upsilon = [u, v, r]^{T}$ is the linear and angular velocity vector with coordinates in the body-fixed reference frame ({B}-frame).

$J(\eta) = \begin{bmatrix} \cos\psi & -\sin\psi & 0 \\ \sin\psi & \cos\psi & 0 \\ 0 & 0 & 1 \end{bmatrix}$ is the transformation matrix.

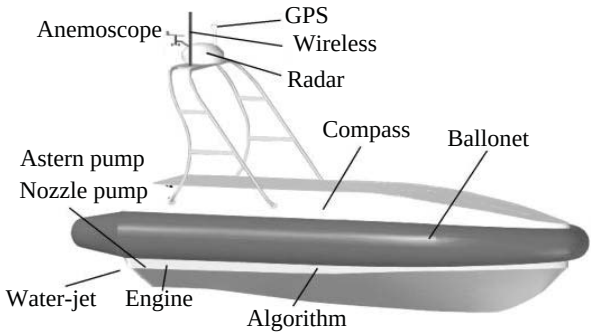

Fig.1. The equipment of water-jet propelled USV

The above condition can be equivalently formulated as

$$\begin{cases} \dot{x} = u_{total}\cos(\psi + \beta) \\ \dot{y} = u_{total}\sin(\psi + \beta) \\ \dot{\psi} = r \end{cases} \quad (2)$$

where, $u_{total} = u_{tol} = \sqrt{u^2 + v^2}$ is the resultant velocity for USV, and $\beta = \arctan(v/u)$ is the sideslip angle.

ENERGY CONSUMPTION MODEL OF WATER-JET PROPELLED USV

The propulsion adopts the water jet HJ292, made by Hamilton Company, the detailed parameters of which are listed in Appendix, Tab. 3. The output power P_e of the water-jet propeller is [26]:

$$P_e = \rho g A_j \upsilon_j [\frac{\upsilon_j^{\ 2}}{2g} + h_s + h_j - \zeta(\frac{\upsilon_s^2}{2g})] / \eta_s \eta_p \quad (3)$$

where g is the acceleration of gravity; ρ is the sea water density; A_j, A_{in}, A_w are the cross sectional areas of nozzle, water inlet, and bend, respectively; υ_j is the nozzle velocity; υ_s is the inlet velocity; h_s is the water-jet propeller loss; h_j is the vertical distance between inlet and water-jet center, and ζ is the kinetic energy utilization coefficient.

The nozzle velocity υ_j is:

$$\upsilon_j = -\left[\left[-\frac{q}{2} - ((\frac{q}{2})^2 + (\frac{p}{3})^3)^{\frac{1}{2}}\right]^{\frac{1}{3}} + \left[-\frac{q}{2} + ((\frac{q}{2})^2 + (\frac{p}{3})^3)^{\frac{1}{2}}\right]^{\frac{1}{3}}\right] \quad (4)$$

where $\upsilon_s = u_{total}$ and

$$\begin{cases} p = g\dfrac{h_j - \zeta\dfrac{\upsilon_s^2}{2g}}{\dfrac{1}{2} + \dfrac{e_{in}}{2}\left(\dfrac{A_j}{A_{in}}\right)^2 + \dfrac{e_w}{2}\left(\dfrac{A_j}{A_w}\right)^2 + \dfrac{e_j}{2}} \\ q = \dfrac{-C\left(\dfrac{n}{1000}\right)^3 \eta_p}{\rho A_j\left[\dfrac{1}{2} + \dfrac{e_{in}}{2}\left(\dfrac{A_j}{A_{in}}\right)^2 + \dfrac{e_w}{2}\left(\dfrac{A_j}{A_w}\right)^2 + \dfrac{e_j}{2}\right]} \end{cases} \quad (5)$$

The actual energy consumption W_t of the water-jet propelled USV is expressed as:

$$W_t = \sum_{i=1}^{N} d_i P_e / u_{tol} \quad (6)$$

where d_i is the length of i_{th} path segment during Δt, and N is the total number of path segments.

ENVIRONMENT FRAMEWORK

In the majority of previous works, the path planning algorithm has been primarily applied in the configuration space ($C-space$), which consists of the obstacle space (C_{obs}) and the collision-free space (C_{free}). Within the C - $space$, the movement of the USV can be represented as the configuration, i.e. the vector specifying all USV motion parameters, such as its position and orientation [26]. In general, the $C-space$ is the set of all possible configurations.

A new environment framework is constructed in the form of a synthetic field representing the influence of both the dynamic obstacles and the marine environment. This framework bears the name of the synthetic force function F_{syn} and includes two main layers (see Fig. 2):

1) The $C-space$ is the base potential field layer, denoted as U_{base}, which can be obtained from the data acquisition module of the USV navigation system [16]. Normally, the base potential field layer is represented as a binary grid map, where the obstacles and the collision-free space are distinguished in black and white. In each grid, the configuration has its coordinates relative to the $C-space$ frame coordinates, and the corresponding weights with values of 0 (C_{obs}) or 1 (C_{free}).

2) The marine environment influence factors are represented as the environment layer, denoted as the environment force function F_{env}. The ocean wave effect is not negligible in terms of force magnitude, but the frequency range does not affect vehicle maneuvering, and the marine waves mostly affect the floating body motions, which are more important for dynamic positioning than for path planning. According to Assumptions 2 and 3, this paper mainly considers the influence of wind and surface currents which are known in advance.

MULTI-LAYERED POTENTIAL FIELD METHOD

A multi-layered potential field method is proposed for planning the path of the water-jet propelled USV to minimize its energy consumption, considering the environmental impact of the wind and surface currents. Unlike conventional potential functions, the here proposed multi-layered potential field method constructs a synthetic environment framework which incorporates the information of the base potential field layer and the environment layer to generate the energy-saving efficiency path. In addition, the proposed method integrates kinematic control, and the attractive and repulsive functions are extended by including the velocity information of the USV and the obstacles to avoid collisions with dynamic obstacles.

ALGORITHM STRUCTURE

Fig. 2 outlines the schematic of the multi-layered potential field approach. The pre-processed synthetic field map is generated from the two-layered information. The first layer is called the base potential field layer and represents the general navigation information, which mainly reflects the influence of obstacles. The base potential field layer has two sub-layers: 1) the attraction potential field, on which the target point of the path is given as the specific mission requirement, and 2) the repulsion potential field, where the information of dynamic obstacles, for example moving vehicles, is calculated from the sensor data.

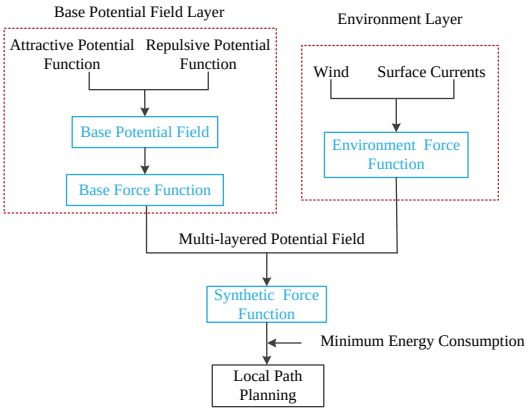

Fig.2. Schematic of the multi-layered potential field method

The second layer bears the name of the environment layer. It contains sub-layers with all the information of marine environmental factors, such as wind and surface currents, that can affect the USV voyage. All the information in the base potential field and the environment layers is used to search for a path. Details on how to obtain the synthetic field and the synthetic force function, as well as the minimum energy consumption strategies will be illustrated in the following sections.

BASE POTENTIAL FIELD LAYER

1) Attractive potential function

The conventional potential field method defines the attractive potential function as a function of the relative distance between the USV and the target, regardless of the USV velocity. Hence, the conventional method sometimes fails to provide a soft-landing solution, more precisely: the USV reaches the target with non-zero speed. To overcome this difficulty, the attractive potential function given by Eq. (7) is proposed [16]. This function contains the velocity information which provides soft landing. The idea of taking the velocity into account has been adapted in the following way:

$$U_{att}(d_{PG}, u_{tol}) = \lambda_1 d_{PG}(t)^m + \lambda_2 \left\| u_{tol}(t) \right\|^n \tag{7}$$

where $d_{PG}(t)$ is the Euclidean distance between the USV and the target, $u_{tol}(t)$ is the USV velocity at time t; λ_1, λ_2 are positive scalar parameters; and m, n are positive constants.

The main disadvantage of the above attractive potential function is that the attraction force significantly depends on the distance to the target. In order to solve this problem, the method makes use of some improvements. The benefit of the improved function is that the attractive potential field is almost constant, as a result of which the generated path is independent from the distance to the target when the USV is not close to it and the function can avoid the local minimum problem.

$$U_{att}(d_{PG}, u_{tol}) = F(P)\left(\frac{\alpha}{\beta^2} d_{PG} + \frac{\alpha}{\beta + d_{PG}} - \frac{\alpha}{\beta} + \lambda_2 \left\| u_{tol} \right\|^2\right) \tag{8}$$

where α, β are positive constants. The term $\lambda_2 \left\| u_{tol}(t) \right\|^2$ regarding the velocity is chosen to be quadratic. $F(P)$ is the rotation matrix defined as:

$$F(P) = \begin{bmatrix} \cos\theta & \sin\theta \\ -\sin\theta & \cos\theta \end{bmatrix} \begin{bmatrix} \cos(B(P)*\theta) & -\sin(B(P)*\theta) \\ \sin(B(P)*\theta) & \cos(B(P)*\theta) \end{bmatrix} \begin{bmatrix} \cos\theta & -\sin\theta \\ \sin\theta & \cos\theta \end{bmatrix} \tag{9}$$

The rotation matrix describes the nature of USV operations to be performed in order to avoid collisions and local minima efficiently.

In Eq. (9), $B(P)$ is $B(P) = e^{(-H(P)^q)}$; $H(P)$ is the resultant force; $B(P)$ is the decay function, and $q = 2$ is the decay

rate. When the magnitude of the resultant force approaches zero, the value of $B(P)$ is close to one. And as $H(P)$ grows, $B(P)$ decays rapidly to zero.

It can be seen that $\frac{\alpha}{\beta^2}d_{PG}+\frac{\alpha}{\beta+d_{PG}}-\frac{\alpha}{\beta}$ and $\lambda_2\|u_{tol}\|^2$ are both non-negative. This means that $U_{att}(d_{PG},u_{tol})$ approaches its minimum of zero if and only if both the USV velocity and the distance between the target and the USV approach zero.

The attractive force vector function pointing from the USV to the target can be calculated as the derivative of the above potential function:

$$\begin{aligned}\mathbf{F}_{att}(d_{PG},u_{tol}) &= -\nabla U_{att}(d_{PG},u_{tol})\\ &= F(P)\left(\frac{\partial U_{att}(d_{PG},u_{tol})}{\partial d_{PG}}\mathbf{n}_{PG}+\frac{\partial U_{att}(d_{PG},u_{tol})}{\partial u_{tol}}\mathbf{n}_{VPG}\right)\end{aligned} \tag{10}$$

where $\mathbf{n}_{PG}$ is the unit vector pointing from the USV to the target and $\mathbf{n}_{VPG}$ is the unit vector pointing in the USV velocity direction.

$$\frac{\partial U_{att}(d_{PG},u_{tol})}{\partial d_{PG}}=\frac{\alpha}{\beta^2}-\frac{\alpha}{(\beta+x)^2} \tag{11}$$

$$\frac{\partial U_{att}(d_{PG},u_{tol})}{\partial u_{tol}}=2\lambda_2\|u_{tol}\| \tag{12}$$

$$\begin{aligned}\mathbf{F}_{att}(d_{PG},u_{tol}) = \left(\left(\frac{\alpha}{\beta^2}-\frac{\alpha}{(\beta+d_{PG})^2}\right)\mathbf{n}_{PG}+\right.\\ \left.+2\lambda_2\|u_{tol}\|\mathbf{n}_{VPG}\right)F(P)\end{aligned} \tag{13}$$

The attractive force functions are shown in Fig. 3. When the velocity is constant, the force field proposed in this paper is almost constant when the USV is relatively far from the target. The force vector function in Fig. 3 is given by:

$$\mathbf{F}_{attMAX}(u_{tol})=F_{att}(d_{PG},u_{tol})|_{d_{PG}\to\infty}=\frac{\alpha}{\beta^2}\mathbf{n}_{PG}+2\lambda_2\|u_{tol}\|\mathbf{n}_{VPG} \tag{14}$$

$$\mathbf{F}_{attMIN}(u_{tol})=F_{att}(d_{PG},u_{tol})|_{d_{PG}\to 0}=2\lambda_2\|u_{tol}\|\mathbf{n}_{VPG} \tag{15}$$

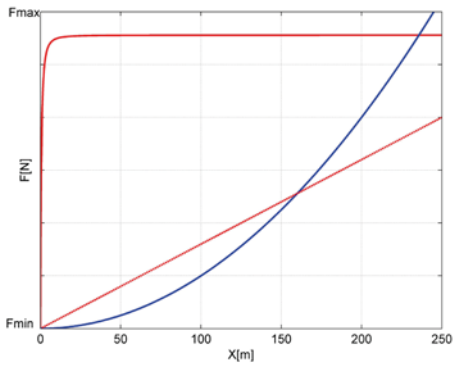

Fig.3. The improved attractive force function according to Eqs., (red solid line), and the linear and exponential characteristics of attractive force functions widely used in the literature, e.g. Eq. (7) (blue solid line and red dashed line, respectively).

2) Repulsive potential function

In order to avoid collisions with dynamic obstacles while taking the velocities of the USV and the obstacles into account, the repulsive potential function is proposed in the following form:

$$U_{rep}(d_{PO},u_{tol},u_{obs}) = \begin{cases}\frac{1}{2}\lambda_3\left(\frac{1}{d_{PO}}-\frac{1}{d_0}\right)^2 d_{PG}^2+\frac{1}{2}\lambda_4\|u_{tol}-u_{obs}\|^2, & d_{PO}<d_0\\ \frac{1}{2}\lambda_4\|u_{tol}-u_{obs}\|^2, & d_{PO}\geq d_0\end{cases} \tag{16}$$

where d_{PO} is the Euclidean distance between the USV and the obstacle, u_{obs} is the velocity of the dynamic obstacle; λ_3,λ_4 are scalar positive parameters; d_0 is the positive constant denoting the distance of influence of the obstacle.

The repulsive force vector function pointing from the USV to the obstacle can be calculated as the derivative of the potential function:

$$\begin{aligned}\mathbf{F}_{rep}(d_{PO},u_{tol},u_{obs}) &= -\nabla U_{rep}(d_{PO},u_{tol},u_{obs})\\ &= \frac{\partial U_{rep}(d_{PO},u_{tol},u_{obs})}{\partial d_{PO}}\mathbf{n}_{PO}+\frac{\partial U_{rep}(d_{PO},u_{tol},u_{obs})}{\partial(u_{tol}-u_{obs})}\mathbf{n}_{VPO}\end{aligned} \tag{17}$$

where $\mathbf{n}_{PO}$ is the unit vector pointing from the USV to the obstacle and $\mathbf{n}_{VPO}$ is the unit vector pointing in the direction of the relative USV velocity with respect to the dynamic obstacle.

$$\frac{\partial U_{rep}(d_{PO},u_{tol},u_{obs})}{\partial d_{PO}}=\lambda_3\left(\frac{1}{d_{PO}}-\frac{1}{d_0}\right)d_{PO}^{-2}d_{PG}^2 \tag{18}$$

$$\frac{\partial U_{rep}(d_{PO},u_{tol},u_{obs})}{\partial(u_{tol}-u_{obs})}=\lambda_4\|u_{tol}-u_{obs}\| \tag{19}$$

$$\mathbf{F}_{rep}(d_{PO},u_{tol},u_{obs}) = \begin{cases}\lambda_3\left(\frac{1}{d_{PO}}-\frac{1}{d_0}\right)d_{PO}^{-2}d_{PG}^2\mathbf{n}_{PO}+\lambda_4\|u_{tol}-u_{obs}\|\mathbf{n}_{VPO}, & d_{PO}<d_0\\ \lambda_4\|u_{tol}-u_{obs}\|\mathbf{n}_{VPO}, & d_{PO}\geq d_0\end{cases} \tag{20}$$

The base force function F_{base} is obtained by adding the attractive force function and the repulsive force functions given by Eqs. (12) and (19), respectively.

$$F_{base}=F_{att}(d_{PG},u_{tol})+\sum_{i=1}^{h}F_{rep}(d_{PO},u_{tol},u_{obs}) \tag{21}$$

where i is the number of obstacles and varies from 1 to h.

ENVIRONMENT LAYER AND SYNTHETIC FORCE FUNCTION

The websites of Korea Hydrographic and Oceanographic Administration (KHOA)[1] in Korea, National Oceanic and Atmospheric Administration (NOAA)[2] in the United States of America, and the National Centre for Atmospheric Research (NCAR), for instance, provide the marine environmental information. Moreover, data are available from a tidal atlas or admiralty charts for different time periods, based on which different astronomical influences can be predicted. Among them, the prediction of the wind is the most accurate and its actual effect is longer, while the data on surface currents contain uncertainties. Therefore, calculating the surface currents from the wind data is also of practical significance. The surface current velocity V_c can be calculated using the Ekman theory as:

$$V_c = \frac{0.0247 V_w}{\sqrt{\sin\phi}} \tag{22}$$

where V_w is the wind velocity and ϕ is the latitude.

The environment force function is:

$$F_{env} = \tau_{wind} + \tau_{current} \tag{23}$$

where $\tau_{wind}, \tau_{current}$ are the wind force and the surface currents force, respectively (for detailed calculations, see Appendix A).

Once the base force function and the environment force function are obtained, the synthetic force function (F_{syn}) is calculated as a function of F_{base} and F_{env} :

$$F_{syn} = \varepsilon_1 F_{env} + \varepsilon_2 F_{base} \tag{24}$$

where ε_1 and ε_2 are two force weights for F_{env} and F_{base}, respectively.

When the USV reaches the target gradually, the F_{base} decreases continuously and the proportion of the F_{env} is increasing, which leads to USV concussion at the target point. To address this problem, the F_{syn} is improved as follows:

$$F_{syn} = \varepsilon_1 F_{env} d_{PG} + \varepsilon_2 F_{base} \tag{25}$$

The energy consumption W_{syn}, which is the sum of the synthetic force functions F_{syn} at each position, can be expressed as:

$$W_{syn} = \sum_{i=1}^{N} d_i F_{syn(i)} = \eta W_t \tag{26}$$

where η is a positive constant, and $\eta \le 1$.

Assuming the maximum speed and the angular range of the operation, the linear and angular motion can be achieved independently. The linear and angular control laws are formulated as:

$$u_{tol} = \begin{cases} k_u F_{syn}, u_{tol} \le u_{\max} \\ u_{\max}, u_{tol} > u_{\max} \end{cases} \tag{27}$$

$$r = \begin{cases} k_r(\theta_{F_{syn}} - \psi), r \le r_{\max,} \\ r_{\max,}, r > r_{\max,} \end{cases} \tag{28}$$

where k_u, k_r are the gain coefficients, $u_{\max}, r_{\max}$ are the maximum values of the resultant velocity and angular velocity, and $\theta_{F_{syn}}$ is the angle between the direction of the synthetic force and the USV heading.

Fig. 4 depicts the synthetic force function (F_{syn}) with different force weights ε_1 and ε_2, which affects the USF path distance and energy consumption for local path planning. For convenience, we set up an obstacle-free simulation environment, where the color varying from blue to red represents different potential values from low to high as shown in the bar chart. For the simulation parameters, refer to Section 4.

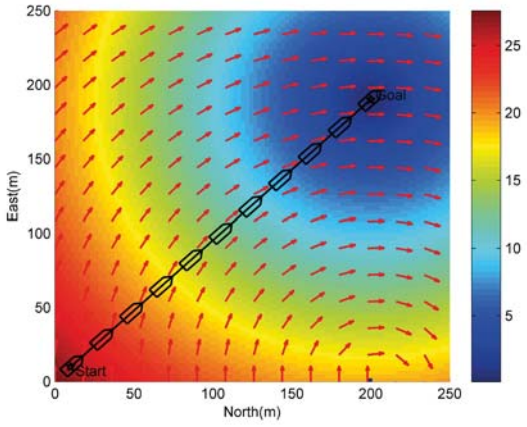

(a) ε_1=0, ε_2=1

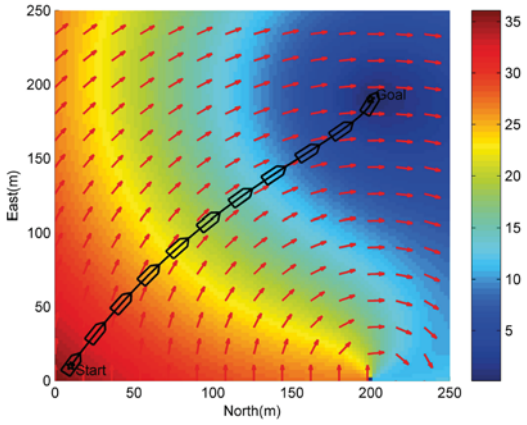

(b) ε_1=0.004, ε_2=1

[1] *KHOA website: http://www.khoa.go.kr*
[2] *NOAA website: http://tidesandcurrents.noaa.gov*

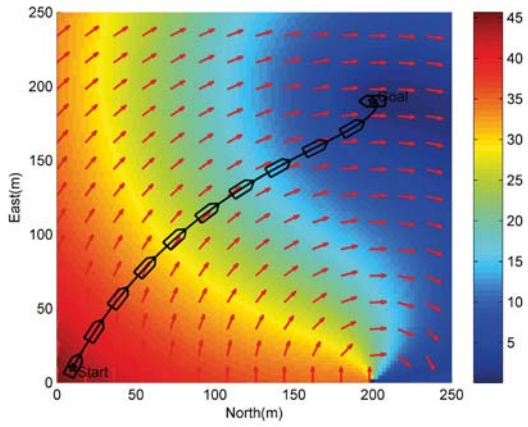

(c) ε_1=0.008, ε_2=1

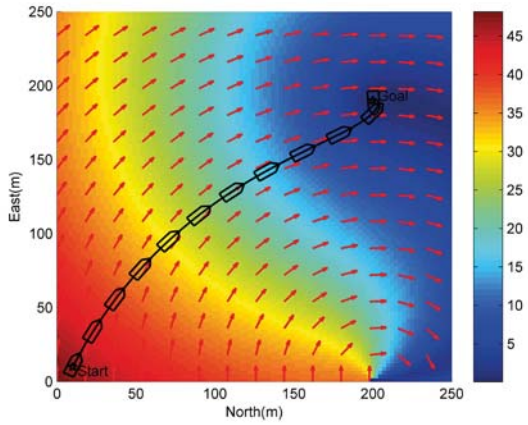

(d) ε_1=0.009, ε_2=1

Fig. 4. Simulations with different force weights

Tab.1. Energy consumption and travel distance for different force weights

$\varepsilon_1, \varepsilon_2$	Energy consumption W_{syn} (J)	Actual Energy consumption W_t (J)	Travel Distance (m)
$\varepsilon_1 = 0, \varepsilon_2 = 1$	4685469	5512316	262
$\varepsilon_1 = 0.004, \varepsilon_2 = 1$	4568981	5375272	265
$\varepsilon_1 = 0.008, \varepsilon_2 = 1$	4435467	5218196	272
$\varepsilon_1 = 0.009, \varepsilon_2 = 1$	4538579	5339504	274

When the marine environment is neglected, the shortest distance corresponds to the minimum energy consumption paths, otherwise the shortest distance and the minimum energy consumption paths can be different. From the simulation results shown in Fig. 4 and the data analysis of Tab.1, the influence of different force weighs on the travel distance and the energy consumption of the planned path can be obtained. When neglecting the wind and surface currents, i.e. $\varepsilon_1 = 0, \varepsilon_2 = 1$, the planned path is the shortest and the energy consumption reaches minimum. On the other hand, when considering the wind and the surface currents, the planned path has the minimum energy consumption for $\varepsilon_1 = 0.008, \varepsilon_2 = 1$, but the travel distance is not the shortest for these values. In order to achieve the minimum energy consumption, force weighting is used. The relationship between the actual energy consumption W_t and the energy consumption W_{syn} is $\eta = 0.85$.

SIMULATIONS

The proposed multi-layered potential field method for local path planning has been tested and verified in different marine environments subject to wind and surface currents. For clarity, the simulation results are compared with the situation which neglects the wind and currents. Performance evaluations of the proposed algorithm and the planned USV path are provided in Figs. 5-7 and Tab.2 In the simulation environment, the dimension of the simulation area is $250m \times 250m$, while the initial point and the target point of the USV voyage are $(10m, 10m), (200m, 190m)$, respectively. The concentric circle is a dynamic obstacle, and the outer circle is its influence range which is 3 times the length of the dynamic obstacle. Besides, the initial point and the target point of USV voyage are marked as black stars, while the instantaneous USV positions on the planned path are drawn as black solid line markers. The vector arrows represent the size and direction of the resultant forces of the wind and surface currents. The resultant direction of the wind and surface currents is gradually shifted eastward. The multi-layered potential field generated in the simulations is shown using the color which varies from blue to red to represent different potential values from low to high as shown in the bar chart. It can also be observed that the target point has the lowest potential field. Before starting the simulations, the following assumptions have been made:

1) The kinetic equation is not considered, and the USV only considers kinematic equations.
2) The water in the environment is assumed to have a constant density, ρ = const.
3) The wind and surface currents have the same direction, and the initial direction of the wind φ_{wo} is south.

The simulation parameters are defined as follows. $g = 9.8m/s$, $\theta = \pm 120^0$, $\rho = 1025kg/m^3$, $\rho_a = 1.29kg/m^3$, $V_w = 10m/s$, $\varphi_{w0} = 90^o$, $\alpha = 800$, $\beta = 9.6$, $\lambda_2 = 40$, $\lambda_3 = 35$, $\lambda_4 = 2$, $d_0 = 30m$, $u_{\max} = 10m/s$, $k_u = 0.0018$, $r_{\max} = 0.4rad/s$, $k_r = 0.0053$.

It should be noted that these parameters can be adapted to different environmental situations.

Remark 1: For interpretation of the references to colors in all figure legends, the reader is referred to the web version of this article.

Tab. 2. Energy consumption and distance in different dynamic environments

$\varepsilon_1 = 0.008, \varepsilon_2 = 1$	Energy consumption W_{syn} (J)	Travel Distance (m)
Fig. 5 (a)	4851863	275
Fig. 5 (b)	4698202	273
Fig. 5 (c)	4869640	275

$\varepsilon_1 = 0.008, \varepsilon_2 = 1$	Energy consumption W_{syn} (J)	Travel Distance (m)
Fig. 5 (d)	4774198	278
Fig. 6 (a)	4867783	275
Fig. 6 (b)	4716429	274
Fig. 6 (c)	4747234	272
Fig. 6 (d)	4591421	265
Fig. 7 (a)	4845201	274
Fig. 7 (b)	4751472	276
Fig. 7 (c)	5145850	271
Fig. 7 (d)	4727282	293

To validate the performance of the proposed algorithm, simulation studies were performed in different dynamic environments, including overtaking and crossing situations. The multi-layered potential field method was then run in the same dynamic obstacle environments using the same simulation parameters, and start and target points of the mission. The only difference in the comparison simulations was whether the simulation took into account, or neglected, the influence of wind and surface currents. The simulation results are shown in Figs. 5-7, which include a single dynamic obstacle and multiple dynamic obstacles in overtaking and crossing situations. The simulations of single dynamic obstacle overtaking and crossing situations are shown in Figs. 5-6, in which the effect of wind and surface currents is considered in Figs. (b) and (d), and neglected in Figs. (a) and (c)). Multiple dynamic obstacle simulation results are shown in Fig. 7, where the wind and surface currents are considered in (b) and (d). To further compare different simulation results, quantitative evaluations of the planned paths are given in Tab. 2. These data indicate that local path planning making use of the multi-layered potential field method can save on the energy cost while keeping the distance cost as low as possible. It can be seen that the energy consumption along the planned path under the environmental interference is relatively small, which proves the effectiveness of the proposed algorithm. Meanwhile, the above planned paths are able to successfully avoid dynamic obstacles.

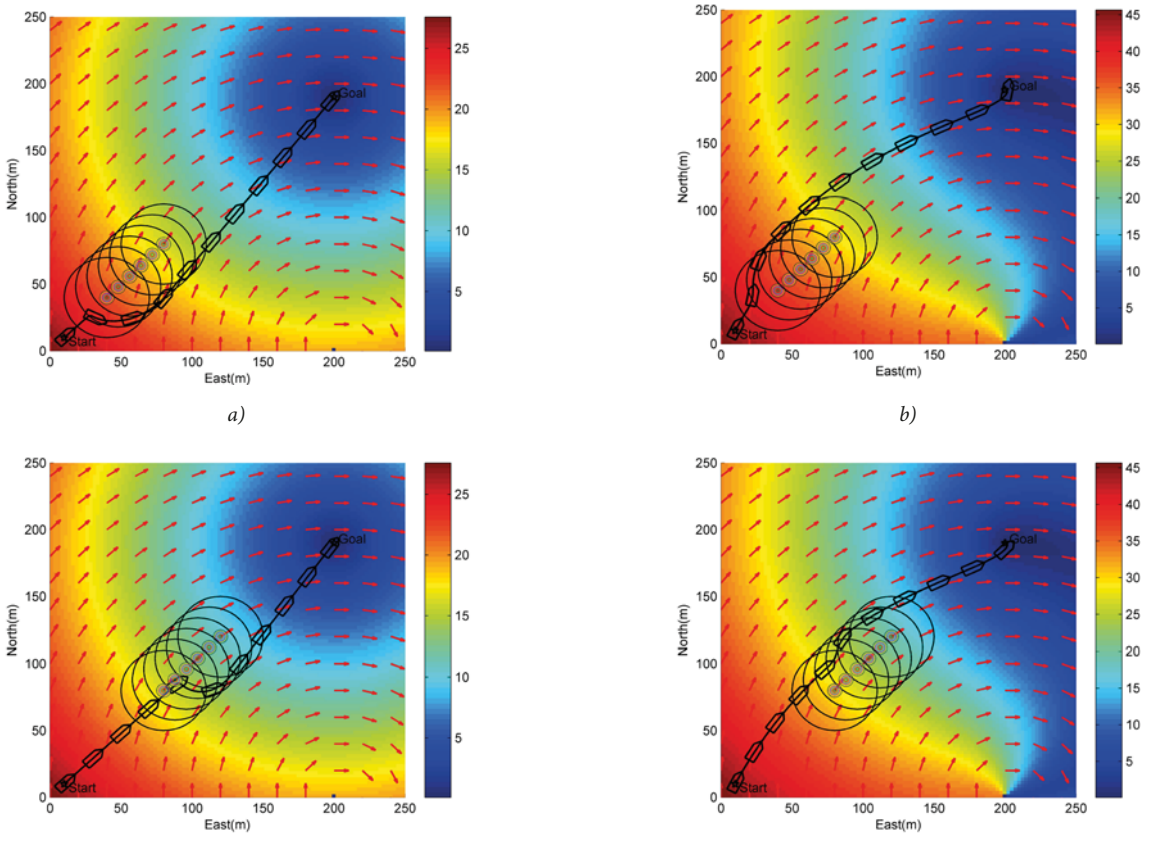

Fig. 5. Simulation results using multi-layered potential field method in a single dynamic obstacle-overtaking situation, while considering the effect of wind and surface currents – cases (b) and (d), and neglecting it – cases (a) and (c).

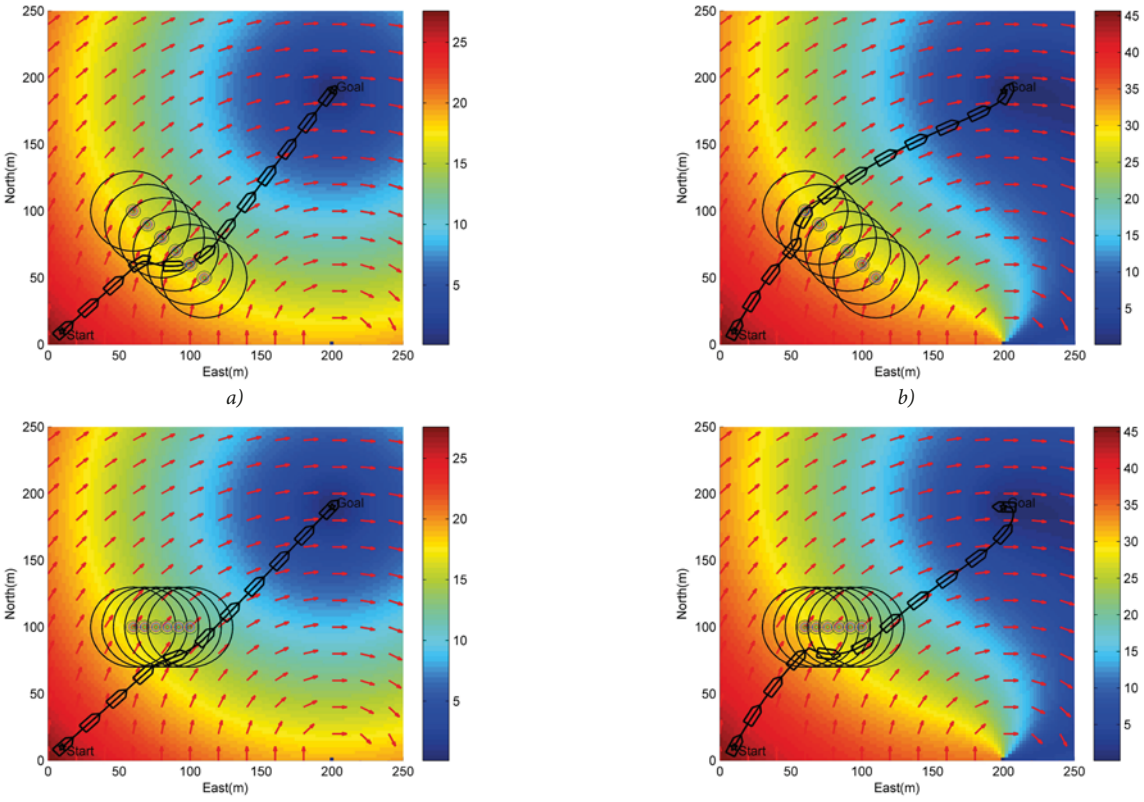

Fig. 6. Simulation results using multi-layered potential field method in a single dynamic obstacle-crossing situation, while considering the effect of wind and surface currents – cases (b) and (d), and neglecting it – cases (a) and (c).

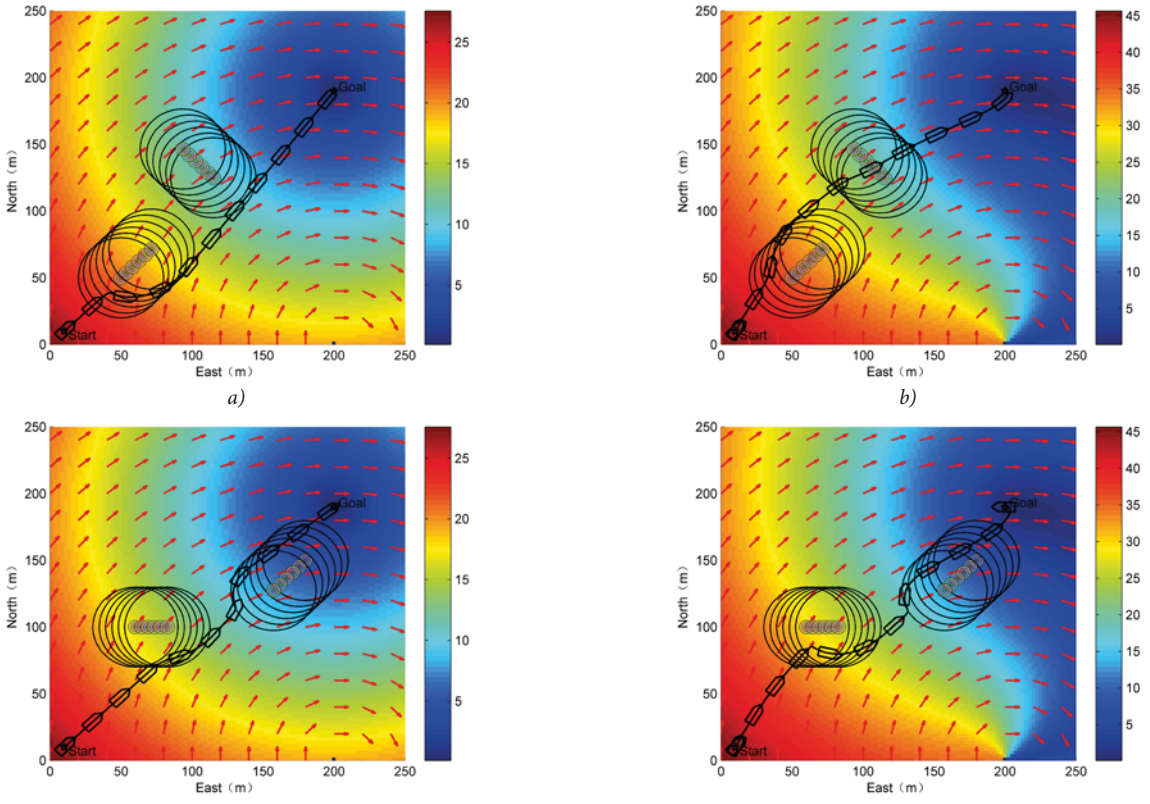

Fig. 7. Simulation results using multi-layered potential field method for multiple dynamic obstacles- overtaking and crossing situation, while considering the effect of wind and surface currents – cases (b) and (d), and neglecting it – cases (a) and (c).

CONCLUSIONS AND FUTURE PLANS

The multi-layered potential field method has been used for local path planning of a water-jet propelled USV in the presence of wind and surface currents, in order to achieve minimum energy consumption. Comparing to the previous researches, the proposed method constructs a synthetic environment framework, which incorporates the information of the base potential field layer and the environment layer. In addition, the traditional potential field method integrates kinematic control and is extended by including the velocity information of the USV and the obstacles to avoid the collision with dynamic obstacles. The performance of the proposed algorithm has been positively verified through comparison of simulation results, thus confirming the reliability and efficiency of the algorithm in avoiding dynamic obstacles and minimizing energy consumption.

For future work, the proposed algorithm will be improved in several ways to increase further the practicability of the planned paths. Firstly, it will undergo verifications in real-life experiments with physical USV models and, after that, in a real environment on board a USV to demonstrate its feasibility. Secondly, the hydrodynamic forces will be combined with the kinetic equation to consider their influence on USV performance. Thirdly, the developed method can be further extended to handle more complex cases, such as to track the moving target. From a general point of view, these future works will contribute to the development of autonomy of USV operation, which is also the ultimate goal of this research work.

APPENDIX A

Under three degrees of freedom, the force of wind and surface currents is represented by [26]:

$$\tau_{wind} = \left[X_{wind}, \quad Y_{wind}, \quad N_{wind}\right]^T \tag{29}$$

$$\tau_{current} = \left[X_{current}, \quad Y_{current}, \quad N_{current}\right]^T \tag{30}$$

and,

$$\begin{cases} X_{wind} = \dfrac{1}{2}\rho_a V_w^2 C_{Xw}(\gamma_w) A_f \\ Y_{wind} = \dfrac{1}{2}\rho_a V_w^2 C_{Yw}(\gamma_w) A_s \\ N_{wind} = \dfrac{1}{2}\rho_a V_w^2 C_{Nw}(\gamma_w) A_s L_{oa} \end{cases} \tag{31}$$

$$\begin{cases} X_{current} = \dfrac{1}{2}\rho V_c C_{Xc}(\mu_{cr}) A_{TC} \\ Y_{current} = \dfrac{1}{2}\rho V_c C_{Yc}(\mu_{cr}) A_{LS} \\ N_{current} = \dfrac{1}{2}\rho V_c C_{Nc}(\mu_{cr}) A_{LS} \cdot L_{oa} \end{cases} \tag{32}$$

where ρ_a is the air density; $C_{Xw}(\gamma_w), C_{Yw}(\gamma_w), C_{Nw}(\gamma_w)$ and $C_{Xc}(\mu_{cr}), C_{Yc}(\mu_{cr}), C_{Nc}(\mu_{cr})$ are the wind force coefficients and the surface current force coefficients, respectively.

Tab. 3. Parameters of water-jet propelled unmanned surface vehicle

Property (Unit)	Symbol	Value
Quality (Kg)	m	5540
Length (m)	L_{oa}	9.5
Width (m)	B	2.8
Depth (m)		1.43
Tilt angle (○)	β	25.6
Cross sectional diameter of inlet water (m)	D_{in}	0.223
Cross sectional diameter of nozzle (m)	D_j	0.182
Cross sectional diameter of bend (m)	D_w	0.23
Distance between center of gravity and stern (m)	X_{CG}	3.26
Forward projection area above waterline (m^2)	A_f	3.76
Lateral projection area above waterline (m^2)	A_s	13.41
Forward projection area below waterline (m^2)	A_{TC}	1.32
Lateral projection area below waterline (m^2)	A_{LS}	8.97
Energy loss coefficient of inlet (NA)	e_{in}	0.03
Energy loss coefficient of bend (NA)	e_w	0.06
Energy loss coefficient of nozzle (NA)	e_j	0.03
Transmission efficiency of drive shaft (NA)	η_s	0.95
The efficiency of the propeller (NA)	η_p	0.90
Propeller absorption Power (1000r/min) (NA)	C	27.13

REFERENCES

1. Liu Z, Zhang Y, Yu X, et al.: Unmanned surface vehicles: An overview of developments and challenges. Annual Reviews in Control, vol.41, pp:71-93, 2016.
2. Lazarowska, Agnieszka.: A new deterministic approach in a decision support system for ship's trajectory planning. Expert Systems With Applications, vol.71, pp:469-478, 2017.
3. Murphy R, Steimle E, Griffin C, et al. Cooperative use of unmanned sea surface and micro aerial vehicles at Hurricane Wilma. Journal of Field Robotics, 25(3):164–180, 2008.

4. Lazarowska A.: Swarm Intelligence Approach to Safe Ship Control. Polish Maritime Research, 22(4):34-40, 2015.

5. Li W, Ma W.: Simulation on Vessel Intelligent Collision Avoidance Based on Artificial Fish Swarm Algorithm. Polish Maritime Research, 23, 2016.

6. Shen Y, Zhao N, Xia M, et al.: A Deep Q-Learning Network for Ship Stowage Planning Problem. Polish Maritime Research, 24, 2017.

7. Chen D Z, Szczerba R J, Uhran J.: Planning conditional shortest paths through an unknown environment: a framed-quadtree approach. 1995.

8. Kamon I, Rivlin E.: Sensory based motion planning with global proofs. International Conference on Intelligent Robots and Systems. IEEE Computer Society, 1995.

9. Svec P, Gupta S K.: Automated synthesis of action selection policies for unmanned vehicles operating in adverse environments. Autonomous Robots 149-164, 2012.

10. Goldberg D E.: Genetic Algorithms in Search, Optimization and Machine Learning. xiii(7): 2104–2116,1989.

11. Petres C, Yan P, Patron P, et al.: Path Planning for Autonomous Underwater Vehicles. IEEE Transactions on Robotics, 23(2):331-341, 2007.

12. Lavalle S M.: Rapidly-Exploring Random Trees: A New Tool for Path Planning. Algorithmic & Computational Robotics New Directions, 293-308, 1998.

13. Ge S, Cui Y J.: Dynamic Motion Planning for Mobile Robots Using Potential Field Method. Autonomous Robots, 13(3):207-222, 2002.

14. Andrews J R, Hogan N.: Impedance Control as a Framework for Implementing Obstacle Avoidance in a Manipulator. Control of Manufacturing Processes and Robotic Systems. 243-251,1983.

15. Zhu Y, Zhang T, Song J.: Study on the Local Minima Problem of Path Planning Using Potential Field Method in Unknown Environments. Acta Automatica Sinica, vol.36(8), pp:1122-1130, 2010.

16. Liu Y, Song R, Bucknall R. A practical path planning and navigation algorithm for an unmanned surface vehicle using the fast marching algorithm. Oceans. IEEE, 2015.

17. Zhu Y, Zhang T, Song J.: Path planning for nonholonomic mobile robots using artificial potential field method. Control Theory & Applications, 27(2):152-158, 2010.

18. Kovács B, Szayer G, Tajti F, et al.: A novel potential field method for path planning of mobile robots by adapting animal motion attributes. Robotics & Autonomous Systems, 82(C):24-34, 2016.

19. Lee T H, Chung H, Myung H.: Multi-resolution path planning for marine surface vehicle considering environmental effects. Oceans. IEEE, 2011.

20. Garau B, Alvarez A, Oliver G.: Path Planning of Autonomous Underwater Vehicles in Current Fields with Complex Spatial Variability: an A* Approach, 2005.

21. Isern-González J, Hernández-Sosa D, Fernández-Perdomo E, et al.: Path planning for underwater gliders using iterative optimization. IEEE International Conference on Robotics and Automation, 1538-1543, 2011.

22. Soulignac M.: Feasible and Optimal Path Planning in Strong Current Fields. IEEE Transactions on Robotics, 27(1):89-98, 2011.

23. Lee T, Kim H, Chung H, et al.: Energy efficient path planning for a marine surface vehicle considering heading angle. Ocean Engineering, 107:118-131, 2015.

24. Song R, Liu Y, Bucknall R.: A multi-layered fast marching method for unmanned surface vehicle path planning in a time-variant maritime environment. Ocean Engineering, 129:301-317, 2017.

25. Gong-Xing W U, Jin Z, Lei W, et al.: Design of the basic motion control system for water-jet-propelled unmanned surface vehicle. Control Theory & Applications, 27, 2010.

26. Yue J.: Study on Modeling and Simulation of 6-DOF Motion of Water-jet Propelled Unmanned Surface Vehicle. Dalian Maritime University, 17-60, 2016.

CONTACT WITH THE AUTHORS

Shasha Wang
e-mail: wangshasha@hrbeu.edu.cn

Harbin Engineering University
No.145 Nantong Street, Nangang District
15001 Harbin
China

sciendo

POLISH MARITIME RESEARCH 1 (101) 2019 Vol. 26; pp. 145-152
10.2478/pomr-2019-0016

CONSENSUS FOR MULTIPLE UNMANNED SURFACE VEHICLE (MUSV) SYSTEMS WITH MARKOV SWITCHING TOPOLOGIES

Liyuan Wang[1, 2]
Wei Yue[3]
Rubo Zhang[1, 2]
[1] Key Laboratory of Intelligent Perception and Advanced Control State Ethnic Affairs Commission, Dalian, China
[2] College of Mechanical and Electronic Engineering, Dalian Minzu University, Dalian, China
[3] Marine Electrical Engineering College, Dalian Maritime University, Dalian, China

ABSTRACT

This paper is concerned with sampled-data leader following consensus of multiple unmanned surface vehicle (MUSV) systems with random switching network topologies and wave-induced disturbance. By modelling the switching of network topologies with the use of a Markov process and considering the effect of wave-induced disturbance, a new sampled-data consensus control protocol is proposed. By employing an appropriate Lyapunov-Krosovskii function method and the weak infinitesimal operation, a novel stability criterion is derived, which ensures that the MUSV system can reach robustly leader-following consensus with H_∞ performance satisfied. Based on this criterion, the Markov dependent switching consensus controller gains are obtained by solving a set of linear matrix inequalities. Finally, an illustrative example is given to verify the effectiveness of the proposed control scheme for MUSV systems.

Keywords: Consensus, unmanned surface vehicle (USV), Markov process, wave-induced disturbance

INTRODUCTION

During the past few years, formation control of multi-agent systems attracted great attention in system and control areas. This is partially due to the fact that there is an increasing need for utilizing multiple agents to perform difficult tasks, where it contributes to increasing efficiency, reducing system cost and providing redundancy against individual failure. To achieve the desired formation, several methods have been proposed but the leader-follower strategy seems to be much preferred in practice due to its simplicity and scalability [1].

As a special case of leader-following formation control, leader-following consensus control can enable vehicle's states or outputs to approach consistency. In the past few years, leader-following consensus control has attracted intensive attention for various forms of multi-agent systems [2–4]. However, the controlled plants are limited to general linear systems, unmanned aerial vehicles and robots. Few results are available in the literature discussing the consensus of MUSV systems. In particular, the vehicles in the marine environment are exposed to waved-induced disturbance, this way the problem becomes even more difficult. Hence, it is important to establish a dynamic USV model and the leader-following consensus control method for MUSV systems by taking the wave-induced disturbance into consideration. This gives rise to the first motivation of the current work.

With the rapid development of communication technologies, network-based multi-agent systems have been attractive, in which agents communicate with each other through a communication network [5]. However, due to the communication constraints, such as link failures, packet dropouts, external disturbances, channel fading, task execution alteration, etc, the connectivity of network topology might be randomly switching among multiple topologies in a deterministic manner. Thus, recent attention has been paid to consensus control of networked multi-agent systems in a stochastic framework, where the switching of the network topologies is described by a Bernoulli or Markov process. To mention a few, the consensus problem for a class of second-order multi-agent systems with Markovian characterizations is considered in [6], where the stochastic switching topology and the

random communication delay are dominated by two mutually independent Markov chains. A more general case with high-order nonlinear multi-agent systems is investigated in [7] and [8]. Different from [6–8], the consensus problem for heterogeneous linear time-invariant (LTI) networked multi-agent systems with switching topology and time-varying delays is discussed in [9], where a novel two-stage distributed consensus protocol is proposed. To reduce unnecessary communication, an event-triggered leader-following consensus problem for a multi-agent system with semi-Markov switching topologies is investigated in [10]. However, all the above consensus control methods do not conform to the actual engineering situation in the marine environment with randomly switching topologies and the robust consensus problem of MUSV systems has not been solved so far. This is the second motivation of the current work.

In light of the aforementioned statements, this paper aims to investigate sampled-data leader-following consensus of MUSV systems with randomly switching network topologies and wave-induced disturbance. Each USV is assumed to have access to its own states (including sway velocity, yaw velocity, heading angle, roll velocity and roll angle) and those of its neighbours at each sampling time. All sampled-data are transmitted through a communication network whose topology is steered by a Markov process. For such systems, we first present a sampled-data leader-following consensus protocol with "sampled" network topologies at each sampling time. Then, by using an appropriate Lyapunov-Krosovskii approach and the weak infinitesimal operation, sufficient condition is derived, which guarantees that the MUSV systems can reach robustly stochastic leader-following consensus with H_∞ performance satisfied. Moreover, the "topology-dependent" sampled-data consensus controller gains are obtained based on the condition. Finally, a numerical example is given to illustrate the effectiveness of the results derived in this paper.

Notation: The superscript T represents matrix transposition. $\mathbb{N}$ is the set of natural numbers. $\mathbb{R}^n$ denotes the n–dimensional Euclidean space. $I_n \in \mathbb{R}^n$ is an identity matrix. $diag\{a_i\}$ is a diagonal matrix with diagonal entries a_i. $P>0$ means that matrix P is symmetric positive definite. The symbol $*$ denotes the symmetric terms in a symmetric matrix.

PROBLEM FORMULATION

In this section, we first introduce some basic notions of graph theory. Then the dynamics of USV is presented. Finally, we state a leader-following consensus problem of MUSV systems with Markov switching topologies.

GRAPH THEORY

Let $G = \{\Delta, S, W\}$ denote a directed weighted graph of N – order, where $\Delta = \{v_1, v_2, \ldots, v_N\}$ and $S \subseteq \Delta \times \Delta$ are the set of nodes and edges, respectively, $W = [w_{ij}] \in \mathbb{R}^n$ represents the weighted adjacency matrix with $w_{ii} = 0$ for any i. An edge defined as $s_{ij}=(v_i, v_j)$ implies that node v_i can receive information from node v_j. Node v_j is considered as a neighbour of node v_i if $s_{ij} \in S$. The degree matrix of sub-graph G is denoted by $\overline{W} = diag\{w_1, w_2, \ldots, w_N\}$, where the diagonal element is represented as $w_i = \sum_{j=1}^{N} w_{ij}$ (which is also called the in-degree of node). Correspondingly, the Laplace matrix of the directed graph G is defined as $L = \overline{W} - W$. A path is a sequence of connected edges in a graph. If there exists a path between node v_i and node v_j, node v_i in the graph is said to be reachable from another node v_j. The union graph of a collection of directed graph $G_r (r=1, 2, \ldots, s)$, which is denoted by $\bigcup_{r=1}^{s} G_r$, is a directed graph with node set Δ and the edge set equal to the union of the edge sets of all of the graphs G_r in the collection.

USV DYNAMICS

The motion of a ship with six degrees of freedom includes sway, yaw, roll, surge, heave, and pitch [11, 12]. The main concern of this paper is the motion in sway, yaw, and roll. The influence of surge, heave, and pitch is treated as disturbance. Applying Newton's laws in a space-fixed coordinate system, one can have the equations for sway, yaw and roll as follows :

$$\begin{cases} m_{y_a} \dfrac{d^2 y_a}{dt^2} = F_{y_a}, \; sway \\ I_{zz_a} \dfrac{d^2 h_a}{dt^2} = N_a, \; yaw \\ I_{xx_a} \dfrac{d^2 f_a}{dt^2} = K_a, \; roll \end{cases}, \tag{1}$$

where x_a, y_a, and z_a denote the longitudinal xis, transverse axis, and normal axis, respectively; m_{y_a} and F_{y_a} denote the effective mass and the force of the ship in the y_a– direction, respectively; Izz_a and Ixx_a denote moments of inertia with respect to the z_a and x_a axes, respectively; h_a and f_a denote the heading angle and the roll angle, respectively; N_a and K_a denote moments with respect to the z_a and x_a axes, respectively.

By translating the equation system (1) to the motion coordinate system utilizing Taylor series expansions, Laplace transformation, and a model simplification, one can obtain the following state-space model [13]

$$\dot{x}(t) = Ax(t) + Bu(t) + Cw(t), \tag{2}$$

where $x(t)=[v(t) \;\; r(t) \;\; \psi(t) \;\; p(t) \;\; \phi(t)]^T \in \mathbb{R}^n$ with $v(t)$, $r(t)$, $\psi(t)$, $p(t)$ and $\phi(t)$ denoting the sway velocity caused by the rudder motion alone, yaw velocity, heading angle, roll velocity, and roll angle, respectively; $u(t)$ represents the rudder angle; $w(t) = [w_\psi(t) \;\; w_\phi(t)]^T$ denotes the wave-induced disturbance, and $w(t) \in L_2[t_0, \infty)$ with t_0 denoting the initial instant; $x_0 \in \mathbb{R}^n$ denotes the initial condition; A, B, and C are given by :

$$A = \begin{bmatrix} -1/T_v & 0 & 0 & 0 & 0 \\ K_{vr}/T_r & -1/T_r & 0 & 0 & 0 \\ 0 & 1 & 0 & 0 & 0 \\ w_n^2 K_{vp} & 0 & 0 & -2\varsigma w_n & -w_n^2 \\ 0 & 0 & 0 & 1 & 0 \end{bmatrix}, \; B = \begin{bmatrix} K_{dv}/T_v \\ K_{dr}/T_r \\ 0 \\ w_n^2 K_{dp} \\ 0 \end{bmatrix}, \; C = \begin{bmatrix} 0 & 0 \\ 1/T_r & 0 \\ 0 & 0 \\ 0 & w_n^2 \\ 0 & 0 \end{bmatrix},$$

where T_v and T_r denote time constants of transfer functions; ζ and w_n denote the damping ratio and the natural frequency under no damping, respectively; K_{vr}, K_{vp}, K_{dv}, K_{dr}, and K_{dp} denote given gains.

LEADER-FOLLOWING CONSENSUS PROTOCOL

Consider a collection of USVs consisting of N following USVs and one leader USV, where each USV is considered as a node in graph G. According to (2), the follower USV's dynamics is described by:

$$\dot{x}(t) = Ax_i(t) + Bu_i(t) + Cw(t), i = 1, 2, \ldots, N \quad (3)$$

Without loss of generality, the leading vehicle is labelled $i = 0$ and its dynamics is expressed by :

$$\dot{x}_0(t) = Ax_0(t) \quad (4)$$

It is assumed that the leader does not receive any information from the followers, i.e. it has no neighbours. A diagonal matrix $M = diag\{m_1, m_2, \ldots, m_N\} \in \mathbb{R}^{N\times N}$ is referred to be the leader adjacency matrix with $m_i \geq 0$ for any i. If the leader is a neighbour of node v_i, $m_i > 0$, otherwise, $m_i = 0$. In this paper, we assume that node 0 is globally reachable in the union graph $U^q_{r=1}G_r$. Then the Laplace matrix of the graph G can be represented as $H = L+M \in \mathbb{R}^{N\times N}$.

As mentioned above, the communication channel is subject to packet dropout, channel fading and external disturbances, which may yield intermittent failures in wireless communication between USVs. At a deeper level, this challenge translates into the change of network topology of MUSV systems. Due to the randomness of communication failure, it is assumed that the topology of MUSV systems is steered by a continuous-time Markov process, i.e., $G(\theta(t)) \in \{G_1, G_2 \ldots, G_q\}$ where $\theta(t)$ is a continuous-time Markov process with values in a finite set $\Theta = \{1, 2, \ldots, q\}$. The transition probabilities are defined as follows :

$$prob\{\theta(t+\Delta t) = s \mid \theta(t) = r\} = \begin{cases} \pi_{rs}\Delta t + o(\Delta t), & r \neq s \\ 1 + \pi_{rr}\Delta t + o(\Delta t), & r = s \end{cases}$$

where $\Delta t > 0$, $o(\Delta t) \to 0$ as $\Delta t \to 0$ and π_{rs} is the transition rate from mode r to mode s, which satisfies $\pi_{ss} = -\sum^q_{s=1,\, s\neq r} \pi_{rs}$ for $r \in \Theta$. Then it is easily known that $H(\theta(t)) \in \{H_1, H_2 \ldots, H_q\}$.

In this paper, we present the following sampled-data leader-following consensus controller for each USV system :

$$u_i(t) = K(\theta(kh)) \sum_{j=1, j\neq i}^{N} w_{ij}(\theta(kh))[x_i(kh) - x_j(kh)] + K(\theta(kh))m_i(\theta(kh))[x_i(kh) - x_0(kh)], \quad (5)$$

where: $K\theta(kh)$ is a consensus controller gain matrix to be designed later, $kh \leq t < (k+1)h$, $k \in \mathbb{N}$, h is the sampling period.

Defining the error variables $e_i(t) = x_i(t) - x_0(t)$ for $i = 1, 2, \ldots, N$ and substituting (5) into (3), one can obtain:

$$\dot{e}_i(t) = Ae_i(t) + BK(\theta(kh)) \sum_{j=1, j\neq i}^{N} w_{ij}(\theta(kh))[e_i(kh) - e_j(kh)] + BK(\theta(kh))m_i(\theta(kh))e_i(kh) + Cw(t) \quad (6)$$

Let's define an "artificial delay" as $d(t) = t-kh$, $t \in [kh, kh + h)$. Apparently, it is clear that $d(t)$ is piecewise-linear and $0 \leq d(t) < h$. Then, defining $e(t) = [e_1(t), e_2(t), \ldots, e_N(t)]^T$ and along with (6), the closed-loop error system can be written as follows:

$$\dot{e}(t) = (I_N \otimes A)e(t) + (H_r \otimes BK_r)e(t - d(t)) + (I_N \otimes C)w(t), \quad kh \leq t < (k+1)h, \quad k \in \mathbb{N} \quad (7)$$

where the matrix $H_r = H(\theta(kh))$ and $K_r = K(\theta(kh))$ for each fixed $\theta(kh) = r$.

Next, we introduce the following definition for the consensus problem investigated in this paper.

Definition 1: The closed-loop error system (7) with Markov protocol $\theta(t)$ is said to be robustly stochastic leader-following consensus if the closed-loop error system (7) with $w(k) = 0$ is robustly stochastically stable, i.e. for all finite initial condition $\phi(t_0)$and any given initial $\theta(t_0)$, there exists a finite number $\mu(t_0, \phi(t_0), \theta(t_0)) > 0$ such that:

$$\lim_{t\to\infty} E\{\int_0^t \| e(t) \|^2\} < \mu(t_0, \varphi(t_0), \theta(t_0)) \quad ,$$

holds, where E is the statistical expectation operator.

Our objective here is to design K_r such that the MUSV system can reach robustly stochastically leader-following consensus with the H_∞ performance constraint satisfied. In other words, we aim to design a controller such that the closed-loop error system (7) satisfies the following requirements:

Q1. The closed-loop error system (7) with $w(k) = 0$ is robustly stochastically stable.

Q2. The effect of $w(t)$ on $e(t)$ is attenuated at a desired level in the H_∞ sense. In particular, it is required that:

$$\|e(t)\|_2 < \gamma \|w(t)\|_2,$$

for all non-zero $w(t) \in L_2[t_0, \infty)$ at zero initial condition, where $\gamma > 0$.

CONSENSUS ANALYSIS AND CONTROLLER DESIGN

In this section, we will derive a sufficient condition on the stability of system (7). Then based on the stability criterion in Theorem 1, we are in position to give a sufficient condition on the existence of sampled-data consensus controller gains for MUSV systems.

Lemma 1 [14]. For any constant matrix $R > 0$, scalar $\tau > 0$ and vector function $\dot{e}$: $[-h, 0]$ such that the following integration is well defined, then:

$$-h\int_{-h}^{0}\dot{e}^T(t+\alpha)R\dot{e}(t+\alpha)d\alpha \le -[e(t)-e(t-h)]^T R[e(t)-e(t-h)]$$

Theorem 1. For given positive scalars h and γ, the closed-loop error system (7) is robustly stochastically stable with an H_∞ norm bound γ, if there exist symmetric positive definite matrices P_r, Q, R, W of appropriate dimensions, such that (8) holds for every feasible value $r \in \Theta$

$$\begin{bmatrix}\Pi_{11}^r & \Pi_{12}^r \\ * & \Pi_{22}\end{bmatrix} < 0, \tag{8}$$

where

$$\Pi_{22} = diag\{-R, -W\}, F_r = [I_N \otimes A \ -H_r \otimes (BK_r) \ \ 0 \ I_N \otimes C],$$

$$E_r = (I_N \otimes A)^T P_r + P_r(I_N \otimes A) + \sum_{s=1}^{q}\pi_{rs}P_s + Q - R - \frac{\pi^2}{4}W + \gamma^{-1}I,$$

$$\Pi_{11}^r = \begin{bmatrix} E_r & -P_r(H_r \otimes BK_r) + \frac{\pi^2}{4}W & R & P_r(I_N \otimes C) \\ * & -\frac{\pi^2}{4}W & 0 & 0 \\ * & * & -Q-R & 0 \\ * & * & * & -\gamma I \end{bmatrix}$$

Proof: Choose a Lyapunov-Krasovskii functional as:

$$V(t, e, \theta) = V_1(t, e, \theta) + V_2(t, e, \theta), \tag{9}$$

where:

$$V_1(t,e,\theta) = e^T(t)P_{\theta(t)}e(t) + \int_{t-h}^{t}e^T(s)Qe(s)ds + h\int_{-h}^{0}\int_{t+\alpha}^{t}\dot{e}^T(s)R\dot{e}(s)dsd\alpha,$$

$$V_2(t,e,\theta) = -\frac{\pi^2}{4}\int_{kh}^{t}[e(s)-e(kh)]^T W[e(s)-e(kh)]ds + h^2\int_{kh}^{t}\dot{e}^T(s)W\dot{e}(s)ds,$$

$P_{\theta(t)}, Q, R, W > 0$.

Then the weak infinitesimal operator of the stochastic process $\theta(t)$ acting on $V(t, e, \theta)$ at the point $\theta(t) = r$, is given by:

$$\begin{aligned}
&L[V(t,e,r)] \\
&= \dot{e}^T(t)P_re(t) + e^T(t)P_r\dot{e}(t) + \sum_{s=1}^{q}\pi_{rs}e^T(t)P_se(t) + e^T(t)Qe(t) \\
&- e^T(t-h)Qe(t-h) + h^2\dot{e}(t)R\dot{e}(t) - h\int_{-h}^{0}\dot{e}^T(t+\alpha)R\dot{e}(t+\alpha)d\alpha \\
&- \frac{\pi^2}{4}[e(t)-e(kh)]^T W[e(t)-e(kh)] + h^2\dot{e}^T(t)W\dot{e}(t) \\
&< \dot{e}^T(t)P_re(t) + e^T(t)P_r\dot{e}(t) + e^T(t)(\sum_{s=1}^{q}\pi_{rs}P_s + Q)e(t) \\
&- e^T(t-h)Qe(t-h) + h^2\dot{e}^T(t)(R+W)\dot{e}(t) \\
&- [e(t)-e(t-h)]^T R[e(t)-e(t-h)] \\
&- \frac{\pi^2}{4}[e(t)-e(t-d(t))]^T W[e(t)-e(t-d(t))].
\end{aligned} \tag{10}$$

Combining (10) and the system (7) together, one has :

$$L[V(t, e, \theta)] + \gamma^{-1}e^T(t)\,e(t) - \gamma w^T(t) < \xi^T(t)\,(\Pi^r_{11} - \Pi^r_{12}\Pi^{-1}_{22}\Pi^r_{12})\,\xi(t)$$

where:

$$\xi(t) = [e^T(t) \ \ e^T(t-d(t)) \ \ e^T(t-h) \ \ w^T(t)].$$

By using Schur's complement, one can see that if (8) is satisfied, $\Pi^r_{11} - \Pi^r_{12}\Pi^{-1}_{22}(\Pi^r_{12})^T < 0$ is also satisfied. Then for $t \in [kh, kh + h)$, if (8) is satisfied, one has:

$$L[V(t, e, \theta)] + \gamma^{-1}e^T(t)\,e(t) - \gamma w^T(t)w(t) < 0, \tag{11}$$

If $w(k) = 0$, then from (11), we can have that:

$$L[V(t, e, \theta)] < -\beta_1\|\xi(t)\|^2 < 0, \tag{12}$$

where $\beta_1 = \min(\lambda_{\min}(-\Pi^r_{11} + \Pi^r_{12}\Pi^{-1}_{22}(\Pi^r_{12})^T)) > 0$, $\lambda_{\min}(-\Pi^r_{11} + \Pi^r_{12}\Pi^{-1}_{22}(\Pi^r_{12})^T))$ is the minimum eigenvalue of $-\Pi^r_{11} + \Pi^r_{12}\Pi^{-1}_{22}(\Pi^r_{12})^T$. By Dynkin's formula, we have:

$$\begin{aligned}
&E\{V(t,e,\theta)\} - V(0,e(0),\theta(0)) \\
&= E\{\int_0^t L[V(s,e,\theta(s))]\}ds \\
&< -\beta_1\int_0^t E\{\|\xi(s)\|^2\}ds \\
&< -\beta_1\int_0^t E\{\|e(s)\|^2\}ds
\end{aligned}$$

On the other hand, we can show that:

$$E\{V(t, e, r)\} > \beta_2 E\{\|e(t)\|^2\},$$

where $\beta_2 = \min(\lambda_{\min}(P_r)) > 0$, $\lambda_{\min}(P_r))$ is the minimum eigenvalue of P_r. The above two inequalities imply that:

$$E\{\|e(t)\|^2\} < -\kappa_1\int_0^t E\{\|e(t)\|^2\}ds + \kappa_2 V(t_0, e(t_0), \theta(t_0))$$

where: $\kappa_1 = \beta_1\beta^{-1}{}_2 > 0$, $\kappa_1 = \beta^{-1}{}_2 > 0$.

Then, by Gronwall-Bellman lemma [15], we can obtain:

$$E\{\|e(t)\|^2\} < \kappa_2 e^{-\kappa_1 t}\, V(t_0, e(t_0), \theta(t_0)),$$

which after integration equals to:

$$E\{\int_0^t \|e(s)\|^2 ds\} < \kappa_1^{-1}\kappa_2(1 - e^{-\kappa_1 t})V(t_0, e(t_0), \theta(t_0)). \tag{13}$$

By taking limit of (13) as $t \to \infty$, the following is yielded:

$$\lim_{t\to\infty} E\{\int_0^t \|e(s)\|^2\, ds\} < \kappa_1^{-1}\kappa_2 V(t_0, e(t_0), \theta(t_0))$$

Note that $V(t_0, e(t_0), \theta(t_0)) > 0$, then by Definition 1, we know that system (7) is robustly stochastically stable.

If $w(k) \neq 0$, from (11) and (12), one has $\|e(t)\|_2 < \gamma\|w(t)\|_2$. Then, if (8) is satisfied, the system (7) is robustly stochastically stable with an H_∞ norm bound γ. This completes the proof.

Remark 1. Theorem 1 gives sufficient conditions on the stability of MUSV systems with Markov switching topologies and wave-induce disturbance. The condition of the criterion is formulated in the form of linear matrix inequalities (LMI). Due to the introduction of interior-point methods, the criterion in Theorem 1 can be solved numerically and efficiently. However, instead, if the condition of the criterion is formulated in the other form, such as an algebraic Riccati-type equation, it is very difficult to find solutions except for a few very special cases.

Remark 2: It is the first time when wave-induced disturbance and Markov switching topologies are considered and addressed in the same framework of MUSV systems. The problem investigated here is not only more challenging and complex but is also essentially different in the several aspects from existing ones such as [7].

1) *Different problems*: Reference [7] discussed consensus problem of a general nonlinear multi-agent systems with Markov switching topologies and communication delay. However, in this paper, we investigate the consensus problem in MUSV systems with Markov switching topologies and wave-induced disturbance.
2) *Different objects*: Reference [7] discussed the stability of multi-agent system solely, while in this paper, we aim to investigate the stability and robustness of MUSV systems together.
3) *Different mathematic techniques*: In the Lyapunov-Krasovskii functional candidate, reference [7] only considered the general item $V_1(t, e, \theta)$, while in this paper, the discontinuous Lyapunov-functional $V_2(t, e, \theta)$ is also considered, which may lead to a better result and lower computation complexity than the one using only the general item [16, 17].

Based on Theorem 1, we can now design the consensus controller (5). Pre and post-multiplying (8) with $diag\{P_r^{-1}, P_r^{-1}, I, R^{-1}, W^{-1}\}$ and its transposes, and define $P_r = I_N \otimes \Psi_r$, $X_r = \Psi_r^{-1}$, $P_r^{-1} Q P_r^{-1} = \tilde{Q}_r$, $P_r^{-1} R P_r^{-1} = R_r$, $P_r^{-1} W P_r^{-1} = \tilde{W}_r$ and $Y_r = K_r X_r$, we are now in position to present the following protocol design criterion.

Theorem 2. For given positive scalar γ, the leader-following consensus for MUSV systems (3) and (4) can be robustly stochastically achieved in H_∞ sense, if there exist real matrices, $\tilde{Q}_r > 0$, Y_r, $\tilde{R}_r > 0$ and $\tilde{W}_r > 0$ with appropriate dimensions such that :

$$\begin{bmatrix} \overline{\Pi}_{11}^r & \overline{\Pi}_{12}^r & \overline{\Pi}_{13}^r & \overline{\Pi}_{14}^r \\ * & \overline{\Pi}_{22}^r & 0 & 0 \\ * & * & \overline{\Pi}_{33}^r & 0 \\ * & * & * & -\gamma I \end{bmatrix} < 0 \quad , \tag{14}$$

where:

$$\overline{\Pi}_{12}^r = [h\overline{F}_r^T, h\overline{F}_r^T], \quad r = 1, 2, ..., q,$$

$$\overline{F}_r = [I_N \otimes (AX_r) - H_r \otimes (BY_r)\ 0\ I_N \otimes C], \ \overline{\Pi}_{14}^r = I_N \otimes X_r,$$

$$\overline{\Pi}_{22}^r = diag\{-P_r^{-1}\tilde{R}_r^{-1}P_r^{-1}, -P_r^{-1}\tilde{W}_r^{-1}P_r^{-1}\}$$

$$\overline{\Pi}_{13}^r = [\sqrt{\pi_{r1}}X_r \ ... \ \sqrt{\pi_{r,r-1}}X_r \ \sqrt{\pi_{r,r+1}}X_r \ ... \ \sqrt{\pi_{rq}}X_r],$$

$$\overline{\Pi}_{33}^r = diag\{-X_1, ..., -X_{r-1}, -X_{r+1}, ... -X_q\},$$

$$\overline{\mathrm{E}}_r = (I_N \otimes AX_r)^T + I_N \otimes AX_r + \pi_{rr}X_r + \tilde{Q}_r - \tilde{R}_r - \frac{\pi^2}{4}\tilde{W}_r$$

$$\overline{\Pi}_{11}^r = \begin{bmatrix} \overline{\mathrm{E}}_r & -H_r \otimes (BY_r) + \frac{\pi^2}{4}\tilde{W}_r & \tilde{R}_r & I_N \otimes C \\ * & -\frac{\pi^2}{4}\tilde{W}_r & 0 & 0 \\ * & * & -\tilde{Q}_r - \tilde{R}_r & 0 \\ * & * & * & -\gamma I \end{bmatrix}.$$

Moreover, the consensus controller gains are given by: $K_r = Y_r X_r^{-1}$.

Remark 3. The conditions in Theorem 2 include the parameters of network topology, the Markov transmission probabilities and the consensus controller gain. Thus, it is very convenient to employ Theorem 2 for the design of controller gain. Moreover, to handle the nonlinear terms $P_r^{-1}\tilde{R}_r^{-1}P_r^{-1}$, $P_r^{-1}\tilde{W}_r^{-1}P_r^{-1}$ in (14), one can use the inequalities $-P_r^{-1}\tilde{R}_r^{-1}P_r^{-1} \le -2(I_N \otimes X) + \tilde{R}$ and $-P_r^{-1}\tilde{W}_r^{-1}P_r^{-1} \le -2(I_N \otimes X) + \tilde{W}$. Then the nonlinear matrix inequalities can be transformed into strict LMIs. Therefore, for given network topology G_r and transition probabilities π_{rs}, one can obtain the consensus controller gain K_r based on the above formulated operation.

SIMULATION

For the system matrices A, B, and C in (2), choose the parameters as follows (see also [18]):

$$U = 7.8(m/s),\ T_v = 8/U,\ T_r = 8/U,$$

$$K_{dv} = 0.01U,\ K_{dr} = -0.6027U,\ K_{dp} = -0.0014U^2,$$

$$K_{vr} = -0.46(m/s),\ K_{vp} = -0.21U,\ w_n = 0.63(rad/s)$$

$$\xi = 0.86 + 0.0038U.$$

The external wave-induced disturbance is given by :

$$\begin{cases} w_\psi = 2\cos(2t) \\ w_\phi = -\cos(t) \end{cases}$$

All the possible information transmission relationships among USVs are given as a group of directed graphs which are shown in Fig. 1. Apparently, the following vehicles can achieve the information from the leading vehicle in Graph G_1 but lose connection with the leading vehicle in Graph G_2. Then we know that the leader node is globally reachable in the union graph of G_1 and G_2. The corresponding Laplace matrix can be written as:

$$H_1 = \begin{bmatrix} 2 & 0 & 0 & -1 \\ -1 & 2 & 0 & 0 \\ 0 & -1 & 1 & 0 \\ 0 & 0 & -1 & 1 \end{bmatrix}, \ H_2 = \begin{bmatrix} 1 & 0 & 0 & -1 \\ -1 & 1 & 0 & 0 \\ 0 & -1 & 1 & 0 \\ 0 & 0 & -1 & 1 \end{bmatrix}.$$

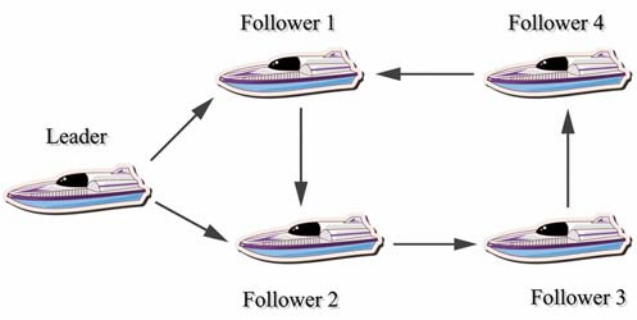

(1) Graph G_1

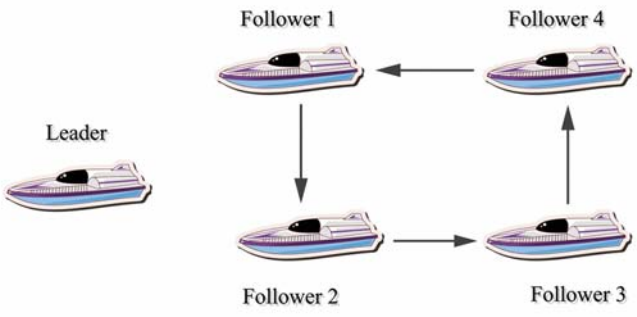

(2) Graph G_2

Fig. 1. All the possible directed graphs

Without loss of generality, it is assumed that all the weights are equal to 1. The network topologies of the MUSV systems are switched by a Markov chain with the transition matrix

$$[\pi_{sr}] = \begin{bmatrix} -0.5 & 0.5 \\ 1 & -1 \end{bmatrix}$$

By solving LMIs in Theorem 2 with $h = 0.3$ and $r = 2$, the controller gains are obtained as follows:

$$K_1 = [-0.0576 \;\; 0.1589 \;\; 0.1867 \;\; -0.0001 \;\; 0],$$

$$K_2 = [-0.0638 \;\; 0.1783 \;\; 0.2058 \;\; 0.0003 \;\; 0.0001].$$

By using Matlab software, the Markov states of the switching network topologies are obtained as shown in Fig. 2, where 0 and 1 in the y-axis denote the topology taking values in G_1 and G_2, respectively. The responses of MUSV error systems are depicted in Figs. 3, 4, 5, 6 and 7. Due to the derivative relations between the yaw velocity error $r_i(t)-r_0(t)$ and the heading angle error $\psi_i(t)-\psi_0(t)$, the changes of the two errors go in the opposite directions; so as the roll velocity error $p_i(t)-p_0(t)$ and the roll angle error $\phi_i(t)-\phi_0(t)$. From Figs. 3, 4, 5, 6 and 7, we can clearly see that all the above mentioned errors of MUSV asymptotically converges to zero within 6 seconds, though the followers often

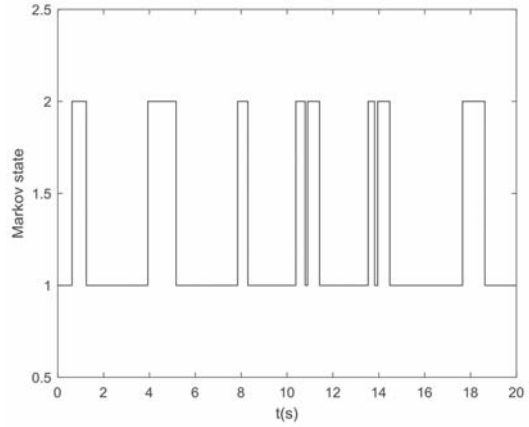

Fig. 2. Markov states of the switching network topologies

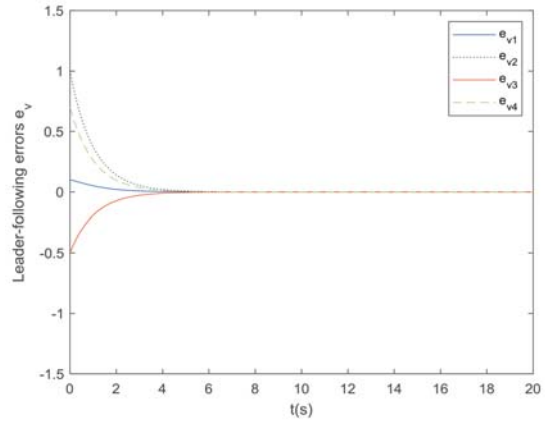

Fig. 3. The responses of the error $v_i(t) - v_0(t)$

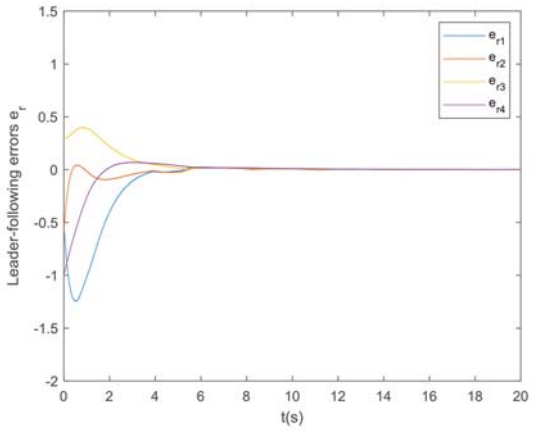

Fig. 4. The responses of the error $r_i(t) - r_0(t)$

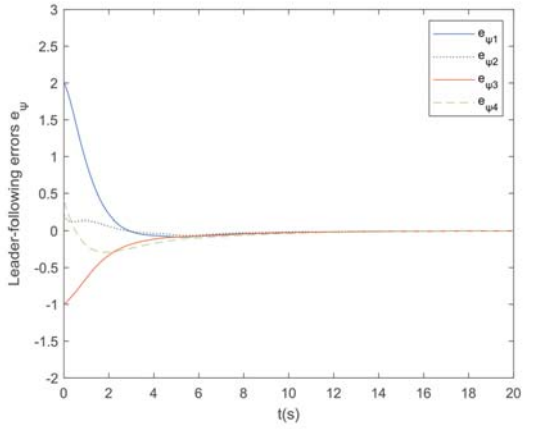

Fig. 5. The responses of the error $\psi_i(t) - \psi_0(t)$

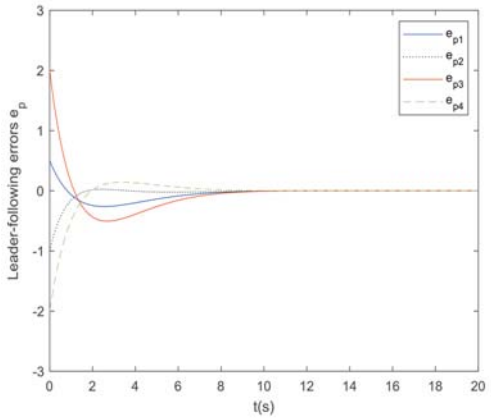

Fig. 6. The responses of the error $p_i(t) - p_0(t)$

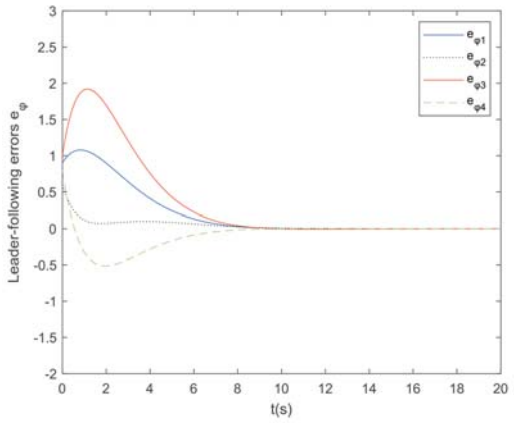

Fig. 7. The responses of the error $\phi_i(t) - \phi_0(t)$

lost connection with the leader vehicle and were affected by the wave-induce disturbance. Therefore we can conclude that the following USV's states indeed reach consensus with the leader USV's state, which illustrates the effectiveness of the proposed design method.

CONCLUSION AND FUTURE WORK

This paper studied sampled-data leader-following consensus of MUSV systems with Markov network switching topologies and wave-induced disturbance. A new sampled-data consensus protocol which can guarantee that the USV formation system achieve consensus robustly, has been proposed. It is The first time the leader-following consensus problem in MUSV systems has been discussed confirming the results of stability and robustness of multi-agent systems to the actual engineering situation in the marine environment with randomly switching topologies and wave-induced disturbance. A numerical example is given to verify the methods and the simulation results show that the control method can make the following vehicles keep consensus with their leading vehicle. Future research includes the modelling of MUSV system subject to wind-induced disturbance and the designing of consensus protocol constraint by the actuator saturation such as the maximum angle of steering gear.

ACKNOWLEDGEMENTS

This work is supported by the National Natural Science Foundation of China under Grant No. 61703072 and 61673084, and the Fundamental Research Fund for the Central Universities under Grant No. 3132017128.

REFERENCES

1. Luca C., Fabio M., Domenico P., and Mario T.: *Leader-follower formation control of nonholonomic mobile robots with input constraints.* Automatica, 2008, 44(5): pp. 1343–1349.
2. Xing L. T., Wen C. Y., Guo F. H., Liu Z. T., and Su H. Y.: *Event-based consensus for linear multi-agent systems without continuous communication*. IEEE Transactions on Cybernetics, 2017, 47(8): pp. 2132–2142.
3. Yu X, Liu L, Feng G. *Leader-following consensus of multiple unmanned aerial vehicles with input constraints and local coordinate frames.* 2016 IEEE International Conference on Advanced Intelligent Mechatronics, 2016, pp. 51061–1066.
4. Jia Y. N., Wang L.: *Leader-follower flocking of multiple robotic fish*. IEEE/ASME Transactions on Mechatronics, 2015, 20(3): pp. 1372–1383.
5. Liu Z. Q., Wang Y. L., Wang T. B.: *Incremental predictive control-based output consensus of networked unmanned surface vehicle formation systems*. Information Science, 2018, 457–458: pp. 166–181.
6. Yi J. W., Wang Y. W., Xiao J. W.: *Consensus in Markovian jump second-order multi-agent systems with random communication delay*. IET Control Theory and Application, 2014, 8(16): pp. 1666–1675.
7. Ding L., Guo G.: *Sampled-data leader-following consensus for nonlinear multi-agent systems with Markovian switching topologies and communication delay*. Journal of the Franklin Institute, 2015, 352: pp. 369–383.
8. Kaviarasan B., Sakthivel Chao Wang C., Alzahrani F.: *Resilient control design for consensus of nonlinear multi-agent systems with switching topology and randomly varying communication delays*. Neurocomputing, 2018, 311: pp. 155–163.
9. Li C. J., Liu G. P.: *Consensus for heterogeneous networked multi-agent systems with switching topology and time-varying delays*. Journal of the Franklin Institute, 2018, 355: pp.4198–4217.
10. Dai J. T., Guo G.: *Event-triggered leader-following consensus for multi-agent systems with semi-Markov switching topologies*. Information Sciences, 2018, 459: pp. 290–301.

11. Van der Klugt P. G. M.: *Rudder Roll Stabilization*. Ph. D. dissertation, Faculty Elect. Eng., Math. Comput. Sci., Delft Univ. Technol., Delft, The Netherlands, 1987.

12. Van Amerongen J., Van der Klugt P. G. M., and Van Nauta Lemke H. R.: *Rudder roll stabilization for ships*. Automatica, 1990, 26(4): pp. 679–690.

13. Wang Y. -L., Han Q. -L.: *Network-based heading control and rudder oscillation reduction for unmanned surface vehicles*. IEEE Transactions Control Systems Technology, 2017, 25(5): pp. 1609–1620.

14. Han Q.–L.: *Absolute stability of time-delay systems with sector-bounded nonlinearity*. Automatica, 2005, 41(12): pp. 2171–2176.

15. Bellman R., Stability theory of differential equations, McGraw-Hill, New York, 1953.

16. Peng C., Zhang J., Han Q. –L.: *Consensus of multi-agent systems with nonlinear dynamics using an integrated sampled-data-based event-triggered communication scheme*. IEEE Transactions on Systems, Man, And Cybernetics systems, 2018, (online).

17. Zhenman G., Yong H., Min, W.: *New constructing method of Lyapunov-Krasovskii functionals for stability of time-varying delay systems*. IECON 2017 – 43rd Annual Conference of the IEEE Industrial Electronics Society, 2017, pp. 5639–5643.

18. Fossen T. I.: *Guidance and Control of Ocean Vehicles*. Hoboken, NJ, USA: Wiley, 1994.

CONTACT WITH THE AUTHORS

Liyuan Wang
e-mail: wangliyuandmu@163.com

Dalian Minzu University
Liaohe West Road
Jinzhou New District, 116600 Dalian
China

Wei Yue
e-mail: yuewei811010@163.com

Dalian Maritime University
Ganjingzi Street, 116026 Dalian
China

Rubo Zhang
e-mail: zhangrubo@dlnu.edu.cn

Dalian Minzu University
Liaohe West Road
Jinzhou New District, 116600 Dalian
China

sciendo

POLISH MARITIME RESEARCH 1 (101) 2019 Vol. 26; pp. 153-161
10.2478/pomr-2019-0017

COMBUSTION AND EMISSIONS INVESTIGATION ON LOW-SPEED TWO-STROKE MARINE DIESEL ENGINE WITH LOW SULFUR DIESEL FUEL

Zhiyuan Yang
Qinming Tan
Peng Geng
Merchant Marine College, Shanghai Maritime University, China

ABSTRACT

With the implementation and expansion of international sulfur emission control areas, effectively promoted the marine low sulfur diesel fuel (MLSDF) used in marine diesel engines. In this study, a large low-speed, two-stroke, cross-head, common rail, electronic fuel injection marine diesel engine (B&W 6S35ME-B9) was used for the study. According to diesel engine's propulsion characteristics, experiments were launched respectively at 25%, 50%, 75%, 100% load working conditions with marine low sulfur diesel fuel to analyze the fuel consumption, combustion characteristics and emissions (NOx, CO_2, CO, HC) characteristics. The results showed that: Marine diesel engine usually took fuel injection after top dead center to ensure their safety control NOx emission. From 25% to 75% load working condition, engine's combustion timing gradually moved forward and the inflection points of pressure curve after top dead center also followed forward. While it is necessary to control pressure and reduce NOx emission by delaying fuel injection timing at 100% load. Engine's in-cylinder pressure, temperature, and cumulative heat release were increased with load increasing. Engine's CO_2 and HC emissions were significantly reduced from 25% to 75% load, while they were increased slightly at 100% load. Moreover, the fuel consumption rate had a similar variation and the lowest was only 178 g/kW·h at 75% load of the test engine with MLSDF. HC or CO emissions at four tests' working conditions were below 1.23 g/kW·h and the maximum difference was 0.2 or 0.4 g/kW·h respectively, which meant that combustion efficiency of the test engine with MLSDF is good. Although the proportion of NOx in exhaust gas increased with engine's load increasing, but NOx emissions were always between 12.5 and 13.0 g/kW·h, which was less than 14.4 g/kW·h. Thus, the test engine had good emissions performance with MLSDF, which could meet current emission requirements of the International Maritime Organization.

Keywords: NO_x emission; CO_2 emission; marine diesel engine; combustion; marine low sulfur diesel fuel

INTRODUCTION

Shipping costs are relatively cheap, and more than 80% of the amount trade transportation of global are achieved through maritime transport[1]. Diesel engine has widely used in ship for its high thermal efficiency and performance of safe and reliability. With the continuous development of the shipping industry, the amount of exhaust gas produced by the diesel engine is gradually increasing [2,3]. According to statistics, there were about 600 million tons sulfur oxides (SOx), 6.5 million tons of nitrogen oxides (NOx), 1.7 million tons particulate matters into the atmosphere from the ship emissions every year [4,5]. Moreover, more than 70 percent of global emissions from ships are within the range of 400 n mile from the coast, especially in high traffic ship sea ports, straits, etc., and even become the main source of emissions in the region. Exhaust emissions of marine diesel engine have seriously polluted the atmosphere and even affect human health [6,7]. All along, the diesel engine exhaust emissions influence the environment and human health of broad interest, and the study of energy saving and emission decreasing technology have aroused great attention [8].

As far as green house gas emissions are concerned, the combustion of diesel and gasoline fuels for transport purposes is the second largest source of CO_2 emissions worldwide [9].

After the pollution of carbon emissions has been proposed at 1997, CO_2 emission from ship has also been concerned. The Marine Environment Protection Committee (MEPC) of International Maritime Organization (IMO) has adopted the Energy Efficiency Design Index (EEDI) and Ship Energy Efficiency Management Plan (SEEMP) to reduce CO_2 emissions from ocean transportation. And these two ship energy efficiency indicators have been included in Annex VI of the MARPOL 1973/78 to implement forcibly [10,11]. In China, the fuel consumption were more than these in the United States and China had become responsible for the most CO_2 emissions of other countries. Chinese Ministry of Transport clearly stipulates: the CO_2 emissions of the existing ships would be decreased by 16% to 2020 [12,13].

There are also some other major harmful emissions from marine diesel engines including NOx and SOx. In order to reduce these emissions, International Maritime Organization (IMO) and some other related organizations (European Union) have made stringent restrictions for marine diesel engine emission. MARPOL 73/78 was adopted to prevent air pollution triggered by ships. Currently in Non Sulfur Emissions Control Area (Non-SECA) the sulfur content in diesel should be below 3.5% while below 1% in SECA, and even in some SECA it should be less than 0.5% or 0.1%, and NOx emissions should be less than 14.4 g/kW·h for the diesel engine whose speed is lower than 130 rpm. According to the statistics, under the existing emissions regulations, SOx and NOx emissions will increase by more than 40% to 2020 [14]. Therefore, the ship SOx and NOx emissions requirements of the next stage is further reduced There are three Emission Control Areas (ECAs) which have been planned in china, respectively for Yangtze River Delta, Pearl River Delta and Bohai Gulf.

All the previous studies for the emissions reported were on the slow-speed two strokes marine main diesel engines fueled with relatively high sulfur content of fuel. Some researchers also noticed that the CO\CO_2\HC\ NOx emission from those engines [15-18]. However, the marine diesel engine has been widely used Marine Low Sulfur Diesel Fuel (MLSDF) to reduce SOx emission. There is less research about the combustion and emissions characteristics of 2-stroke diesel engine with using MLSDF. So, through experiment on the MAN B&W 6S35ME 2-stroke diesel engine of Shanghai Maritime University Automatic Engine Room, and investigate the effects of the 2-stroke diesel engine using MLSDF on the combustion and emissions (NOx and CO_2). Mentioned effects may be useful to evaluate the emissions from the 2-stroke diesel engines exactly in the emission control area. This paper presents the results of laboratory tests on the effects of selected MLSDF on the level of emissions.

Tab.1 Main technical specifications of test engine

Model	MAN B&W 6S35ME-B
Type of the engine	6-cylinder, in-line, water-cooled, DI engine
Number of stroke	2
Compression ratio	21
Bore/stroke (mm)	350/1550
Fire order	1-5-3-4-2-6
Rated speed (rpm)	142
Rated power (kW)	3570
Scavenging port opening/ closing crank angle(deg)	142/218
Exhaust valve opening/ closing crank angle(deg)	115/278
Fuel injecting angle (deg)	2~5 after top dead center
Intake type	Exhaust turbine or auxiliary turbocharger

EXPERIMENTAL AND TEST METHOD

EXPERIMENTAL SETUP

The experimental setup is shown in Fig. 1. It used MAN B&W 6S35ME-B diesel engine, a large low-speed two-stroke, cross-head, common rail, electronic fuel injection diesel engine, and it is widely used in the marine as the ship's propulsion power plant in most areas of world. The main technical specifications of the test engine are shown in Table 1. The diesel engine was coupled with a QC-100 hydraulic dynamometer, and the torque and speed of the diesel engine were controlled by the engine test system. In this experiment, the engine's operating conditions were controlled and their related thermal parameters were monitored by No.7 computer in Fig. 1; cylinder pressure was collected and the crank angle signal was acquired by the pressure sensor of Kistler 6613CG1; the composition of exhaust gases was analyzed by flue gas analyzer of SEMTECH ECOSTAR; diesel fuel consumption was monitor by EPC-50B-type fuel gauge for diesel engine's different operating conditions.

The fuel used in the experiment includes light diesel fuel with less than 0.5% by the weight of sulfur, which is named marine low sulfur diesel fuel. The main properties of the test fuel are shown in Table 2. All of the parameters of the test fuel conform to international standard ISO 8217-2010.

Tab.2 Properties of the testing fuels

Parameter	Unit	Measured value	Parameter	Unit	Measured value
Cetane number		53	Carbon	m%	86.07
Low Heat Value	kJ/g	42.56	Hydrogen	m%	13.01
Viscosity 20°	mm^2/s	4.3	Nitrogen	m%	0.03
Density20°	kg/m^3	824.6	Oxygen	m%	0.60
Flash point	°C	82	Sulphur	m%	0.2
Acid value	mgKOH/g	0.41	Water	V%	<0.05

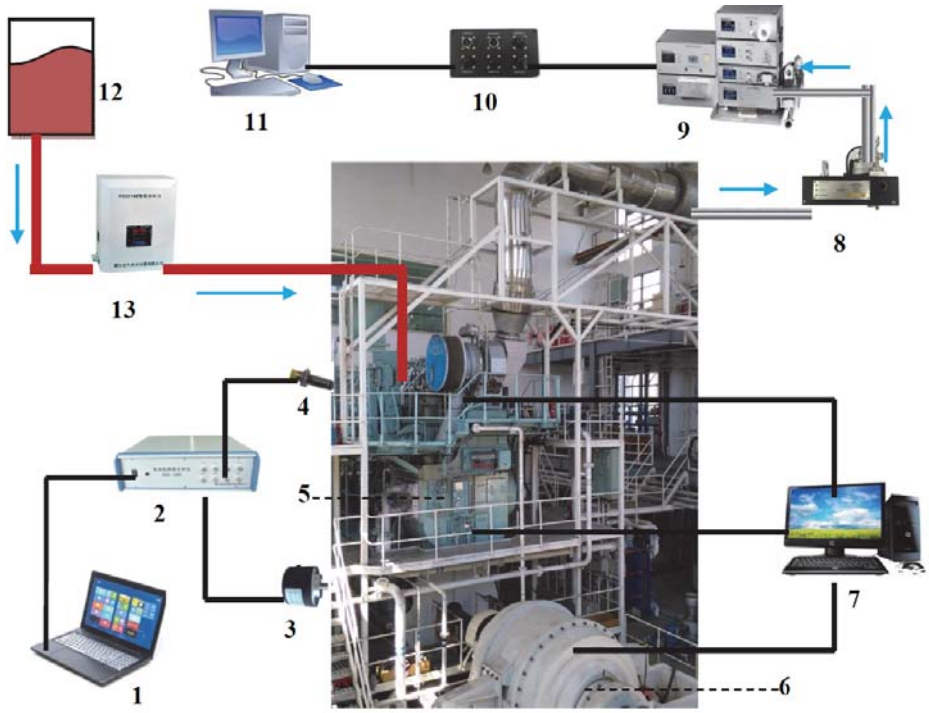

Fig. 1. Diagram of the experimental system 1.Computer for combustion analysis 2. Data acquisition 3. Crank angle sensor 4. Cylinder Pressure sensor 5. 2-stoke diesel engine 6. Hydraulic dynamometer 7. Computer for operate control and thermal parameter monitoring 8. Prefilter 9. SEMTECH ECOSTAR 10. Signal box 11. Computer for exhaust gas analysis 12. MLSDF Tank 13. Fuel consumption monitor

SAMPLING AND ANALYSIS

The pressure transducer Kistler 6613CG1, which were mounted on each cylinder head, measured the cylinder gas pressure of the engine. The pressure sensor was used with a charge amplifier and a shaft encoder to obtain the cylinder pressure data at 0.5 crank angle intervals. The pressure data were averaged 100 consecu-tive cycles for the experiment in all engine conditions. The averages of the pressure data were analyzed with a combustion analyzer to analysis the heat release rate, which was computed from the averaged cylinder pressure data using Equation (1) [18]:

$$\frac{dQ_g}{d\varphi} = \frac{dQ_n}{d\varphi} + \frac{dQ_w}{d\varphi} \quad (1)$$

Whereis the net heat release rate, and it was obtained by the traditional first law using Eq. (2) [19]:

$$\frac{dQ_n}{d\varphi} = \frac{\gamma}{\gamma-1} \cdot p \cdot \frac{dV}{d\varphi} + \frac{1}{\gamma-1} \cdot V \cdot \frac{dp}{d\varphi} \quad (2)$$

And is the heat loss rate, and it was determined from Equation (3) in which the hc was estimated by the Woschni model.

$$\frac{dQ_w}{d\varphi} = A_{ht} h_c (T - Tw)/6n \quad (3)$$

The gaseous emissions from the marine auxiliary diesel engine were measured with a mobile test system (SEMTECH-ECOSTAR, Sensor, Inc.) for NOx\$O_2$\HC\CO \$CO_2$ gas emissions. The principle of SEMTECH-ECOSTAR for NOx is based on Beer-Lambert law, including analyzing CO/CO_2 by Non-dispersive Infrared (NDIR) to, testing NOx by Non-dispersive Ultraviolet (NDUV), testing THC by Heated Flame Ionization Detector (HFID) and with paramagnetic oxygen test unit.

TEST METHOD

In this research, the tests were carried out at steady states to evaluate the effects of the MLSDF on the combustion, NOx, O_2, HC, CO and CO_2 gas emissions with different loads at the speed of 25%~100% rated speed for the propulsion characteristic test mode (Table 3). In all testing condition, the diesel engine was allowed to run for one hour after the cooling water temperature, exhaust gas temperature and lubricating oil temperature have reached steady-state values. The cooling water temperature was kept between 70°C and 80°C, and the piston cooling oil temperature was about 50°C, depending on the engine speeds and loads. Within 1 hour after each stable operation condition, every ten minutes to collect these data which including the cylinder pressure and composition of exhaust gas, automatic record the fuel consumption rate every 1 second duration. Each type parameter would be average to evaluate the diesel engine's combustion, emission, and economic performance.

Tab.3 Engine operating conditions

Load (%)	25	50	75	100
Power (kW)	892	1795	2677	3575
Speed (r/min)	89.5	112.8	129	142
Fuel consumption (kg/h)	197	342	478	644

RESULTS AND DISCUSSION

ECONOMIC PERFORMANCE

Compared with ordinary marine diesel fuel, the marine low sulfur diesel fuel has low flash point, low viscosity, low specific gravity, low lubricity, low calorific value and so on, which not only bring much difficulties for the ship fuel management, but also have an impact on diesel engines' combustion and emission performance. For example, low viscosity leads to the increase of fuel high pressure pump leakage and the decrease of fuel injection pressure, which may be lower than the valve opening pressure of the fuel and even stop the engine. The economic, combustion and emissions performances of MAN B&W 6S35ME-B9 with MLSDF will be analyzed below.

As can be seen from Table.3, according to the thrust characteristics, the fuel consumption per hour is gradually increased with the load increasing. However, the fuel consumption per unit of power per hour decreased after it first increased with the load increasing. The lowest fuel consumption rate is only 178 g/kW·h at 75% load. It is difficult for diesel engine to run at rated condition for the variability of load from the external environment of ship. Usually relatively low speed conditions are accepted to increase efficiency of ship propulsion. Therefore, the diesel engine fuel consumption rate is relatively low under about 75% load working conditions. Overall, during the high-load range of diesel engine, its cylinder temperature is high at injection timing and high pressure of fuel injection, which is more favorable for combustion. And if combustion efficiency is improved, its fuel consumption rate is lower than under low load conditions.

COMBUSTION CHARACTERISTICS

The in-cylinder pressure, heat release rate, cumulative heat release and temperature curves for different load are shown in Fig. 3 to Fig. 6. Pressure curve shown in Fig. 2 from the average of collected six pressure data of No.1 cylinder in one hour, and each pressure acquired was averaged over 1000 cycles to diminish the influence of cycle-by-cycle variation. The heat release rate, cumulative heat release and temperature were analyzed from the in-cylinder pressure data.

After the exhaust gas turbocharger boosting and the air cooler cooling, the fresh air is taken as the intake gas of two-stroke diesel engine. The in-cylinder temperature rests on temperature and pressure of intake gas, which would affect the process of fuel combustion. As shown in Fig. 3, despite the scavenge temperature changed little, when the load gradually increased from 25% to 100%, the scavenging pressure was significantly increased. So, the compression pressures and temperatures have increased, which is in favor of in-cylinder fuel combustion. We can see from Fig. 4 to Fig. 7 that the variation rules of cylinder thermal parameter curves are similar under the engine's different operator conditions. When engine's load was increased from 25% to 100%, the compress pressure at top dead center and the peak combustion pressure were obviously increased, and the whole pressure curve moved upward. Though the rule of heat release rate changed little, the cumulative heat release significantly increased and cylinder temperature curve moved upward. More importantly, the peak pressure and temperature are relatively high when the two-stroke marine diesel engines work at rated operating condition. Thereby, fuel injection after top dead center is accepted to reduce the peak cylinder pressure and maximum temperature, which can ensure their safety of cylinder and reduce the NOx formation.

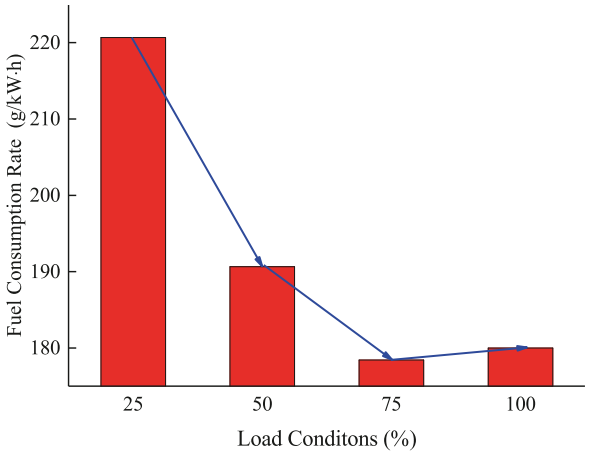

Fig. 2. Fuel consumption rate

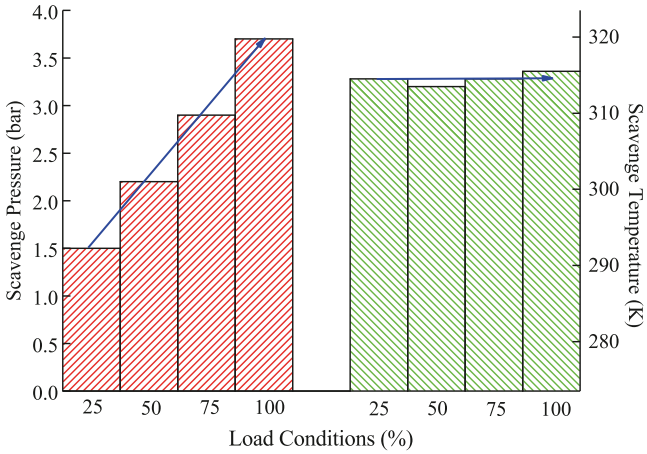

Fig. 3. Thermodynamic parameters of scavenge

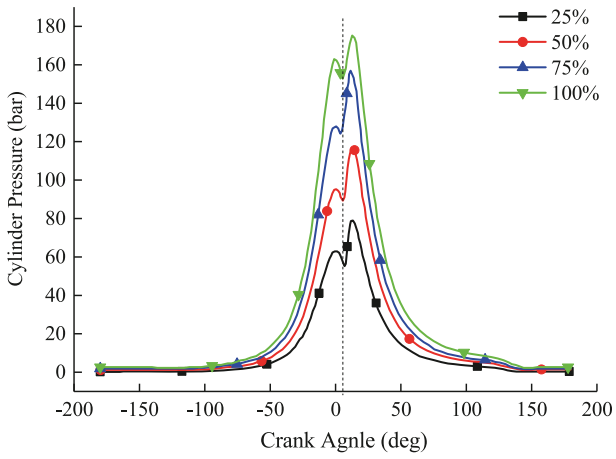

Fig. 4. In-cylinder pressure

In this experiment, the concentration and motion of the mixture in the cylinder remain about the same for the test fuels, and thus the combustion duration of the test fuels are influenced by the fuel injection timing, injection quantity and the temperature of the diffusive mixture. And the injection timing is same at the operating condition respectively with 25%, 50% or 75% load. As shown in Fig. 5 and Fig. 6, the combustion timing gradually moves forward with the load increasing, and this is because the injection pressure and temperature increase at the injection timing, which is effective to promote fuel evaporation and mixture of fuel and air, fuel injection quantity increases at high-load effectively, which improves fuel fog.

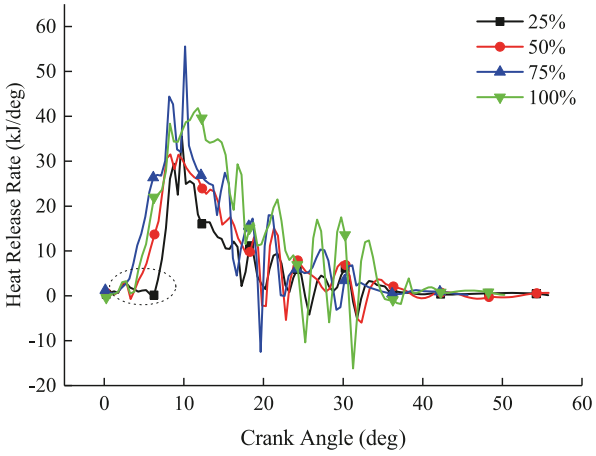

Fig. 5. In-cylinder heat release rate

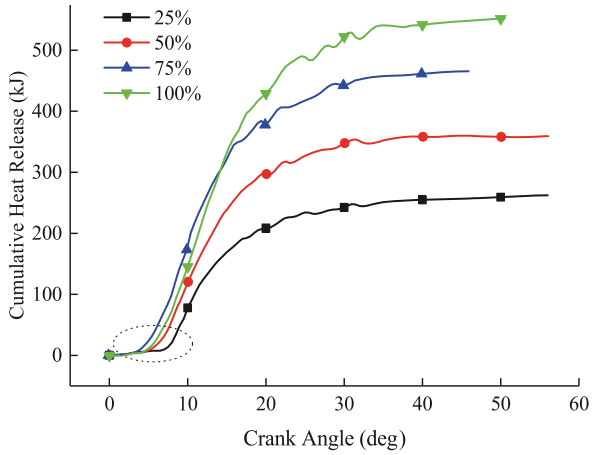

Fig. 6. In-cylinder cumulative heat release

That is why heat release rate and cumulative heat release increase by combustion improved at the same crank angle position. Thus, the inflection points of pressure curve after top dead center also follow forward (shown in dashed lines in Fig.4. However, the inflection point of the pressure and heat release rate at 100% load are later than at 75% load condition, which is caused by injection timing delayed. That because the cylinder pressure and temperature are really high at 100% load working condition. So, injection timing needs to be delayed to control their maximum combustion pressure and cylinder temperature. Curve shows that the heat release rate, cumulative heat release, temperature and pressure rises were relatively low at the pre-combustion of 100% load. However, all that in-cylinder thermal parameters at aft-combustion of 100% load were more than 75% load condition.

From what is mentioned above, we can keep the engines' NOx emissions not exceeded and advance the injection timing to improve combustion efficiency and reduce carbide emission at low-load condition. It is necessary to delay injection timing to control NOx emission at high load conditions. Thus we can adjust injection timing at different conditions according to the ship engines' emission required.

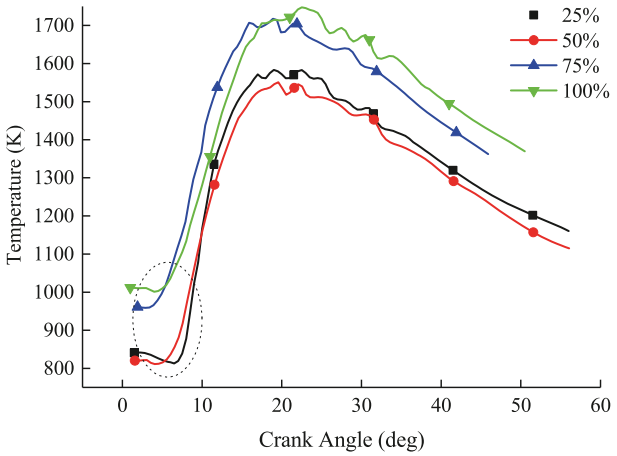

Fig. 7. In-cylinder temperature

THERMODYNAMIC PARAMETERS OF EXHAUST GAS

Thermodynamic parameters of exhaust gas at different engine speeds and engine loads for the diesel engine are discussed in this section Fig. 8 shows the pressure and temperature of exhaust manifold when the diesel engine operates on different speeds and loads. Exhaust pressure directly affects the performance of exhaust gas turbocharger and determines the pressure of the diesel engines' scavenge air, then affects the combustion and emissions performance of diesel engine. The exhaust gas pressure is relatively low at low load (the absolute pressure is only 1.4 bar at 25% load), which leads to poor effect of supercharge, low scavenging air pressure, bad ventilation effect and deterioration of combustion. So usually use an auxiliary blower to increase the scavenging pressure at low loads of marine diesel engines. As shown in Fig. 8, the temperature of exhaust manifold increases significantly with the increase of engine speeds and loads. When the diesel engine operates at the low engine speed and loads, the temperature of the exhaust manifold is less than 200°C, while the temperature can reach more than 370°C when the test engine operates at the high speed and load. The temperature of exhaust manifold has the significant influence on the emissions from the diesel engine, including NOx, CO and so on. Moreover, there are also some chemical reactions between NO and NO_2, due to the changes of the rate of conversion. The factors, which lead to the influence of the emissions, still need further research.

EMISSIONS

As shown in Fig. 9, the exhaust gas was consisted of about 80% N_2, 16%O_2, 4%CO_2 and minimal polluting gas. The polluting gas consists mainly of NOx, CO, CO_2 and HC, which accounted for only 0.1% of the total amount of exhaust gas. In the following, its various polluting gas emissions will be explored at different operating condition with the use of marine low sulfur diesel fuel.

1) NOx emission

The total NOx emissions from the engine exhaust at different engine speeds and loads are shown in Fig .9 and Fig. 10.

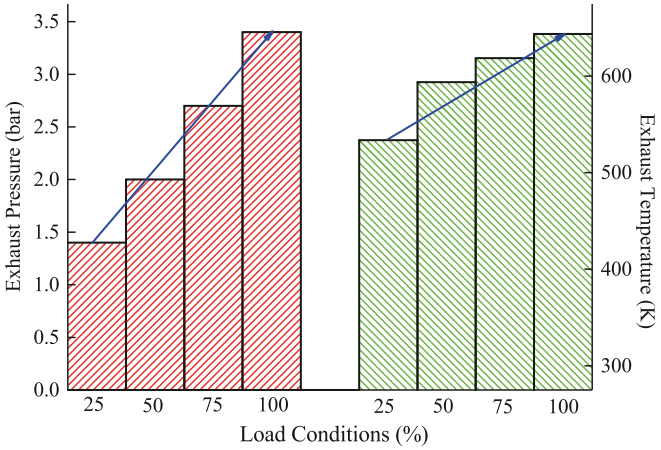

Fig. 8. Thermodynamic parameters of exhaust gas

When the diesel engine operates on the 25% load, the total NOx emissions is about 740 ppm, while increase significantly with the load increases from 50% to 100%. When the test engine operates on the high engine condition, the total NOx emissions can reach 880 ppm. The high temperature is the major factor leading to the increase of the total NOx emissions. The in-cylinder temperature increases significantly with the increase of the engine speeds and loads. However, the high temperature is not the only factors for NOx generation, but also with the oxygen concentration within environment and the time of during high temperature. Therefore, the NOx formation in-cylinder of diesel engine is a complex chemical reaction process [20,21]. As can be seen from Fig. 9, the NOx emissions at 25% load condition are more than 50% load condition. The main reason why the total amount of NOx increased is that the time of staying the high temperature zone is longer when the engine operates at 25% load with a relatively low speed. These are just the proportion of NOx in exhaust gas. However, the requirements of IMO for ship emissions are measured with the total emissions mass for each power out within one hour. As shown in Fig. 10, there is no rule to follow for NOx emissions with the load change. NOx emission is relatively low at 100% load condition for the test engine's four experimental conditions, and the NOx emission at 25% and 75% load were less than 50% working condition. NOx emissions were up to 12.96 g/kW·h at 75% load work condition. All mentioned above further indicates that the process of NOx formation is complex, which depends on the extent of the above three factors influence. Overall, the NOx emissions are always between 12.5 and 13.0 g/kW·h, which is less than 14.4 g/kW·h and meet the ships' emission requirements of IMO.

2) CO_2/CO/ HC emissions

It is well known that CO_2 emissions are the green house gas emissions, which will lead to the global warming. CO_2 is the primary green house gas and it is of high concern both for environmental reasons and fuel economy [22]. It is more important for the marine diesel engine because of its high fuel consumption and broad navigation area.

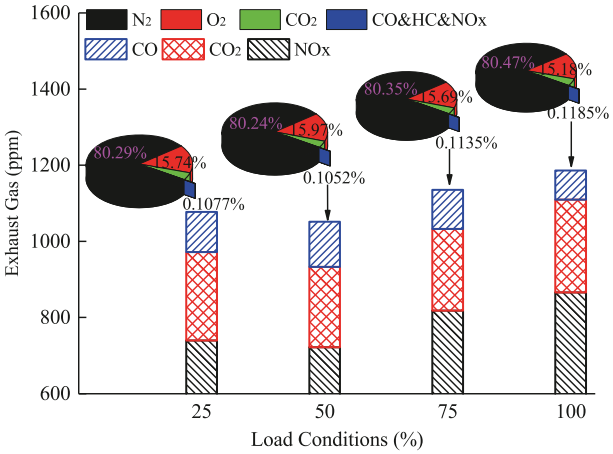

Fig. 9. Composition of exhaust gas

Thus, most of governments plan to decrease the CO_2/CO/ HC emissions in their reports on the work of the government. Fig. 10 shows the influence of the engine speed and load on the CO_2/CO/HC emissions. The variation rule of CO_2/HC emissions with the load changed is similar to parabola, while the rule of CO emissions is similar to inverse parabola.

CO_2 emissions of the 2-stroke diesel engine were close to 700 g/kW·h at the 25% load, while it is only 560 g/kW·h at high engine speed and load. CO_2 emissions are significantly reduced from 25% load to 75% load, but increased slightly at 100% load condition. The maximum difference of CO_2 emissions were 132 g/kW·h. As we all known, CO_2 is the production of C atoms' complete combustion from fuel and energy released is a certain for per unit of CO2 generated. The greater CO_2 emissions per unit power output means that energy consumption is greater per unit power output. It is suggested that the diesel engine has different thermal conversion efficiency for different operating conditions. Thermal conversion efficiency depends on the gas species and thermal parameters (temperature, pressure et.al) of combustion environment in-cylinder [23,24]. At low speed and low load work condition of diesel engine, heat transfer losses large for its low temperature of cylinder wall and piston, and its initial cylinder gas temperature and pressure are relatively low, moreover, its scavenge temperature and

pressure are relatively low. So, the thermal conversion efficiency is low and heat consumption per power output is bigger. However, CO_2 emissions per unit power output increase to some certain at 100% load working condition, which may be due to the proportion of CO_2 increased in exhaust gas cylinder. Just because three-atom gases CO_2 have a bigger specific heat capacity the performance of power output would be affected. The heat energy for power output is directly from the fuel combustion, and therefore directly determines the fuel consumption rate. Fig. 2 and Fig. 10 show that the low of fuel consumption rate variation is similar to its CO_2 emission.

In addition, fuel consumption rate is also closely associated with the combustion efficiency. The fuel would directly generate CO_2 and H2O after complete combustion, otherwise CO and HC will be generated.

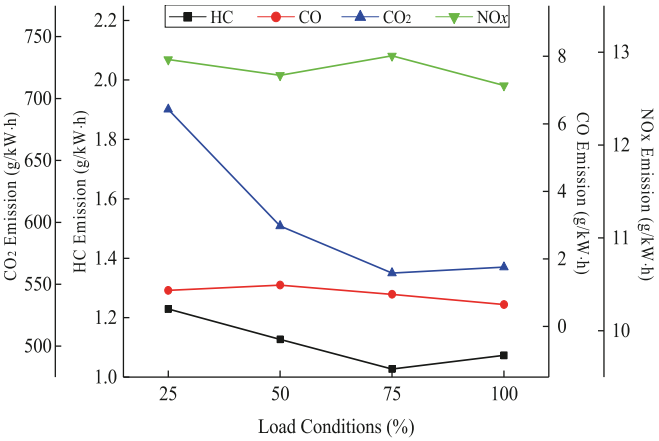

Fig. 10. Polluting gas in exhaust gas

As can be seen from Fig. 10, diesel engine's HC emission changing with conditions variation is similar with CO_2, while CO emission is first increased and then decreased. Diesel engine combustion process is very complex, and the main factors are the amount of air, thermal parameters of air, fuel injection pressure, fuel-air ratio, degree of evenly mixed oil mist and so on [25,26]. At low load operate conditions, the low pressure of fuel injection pressure is not conducive to fuel evaporation and mist air mixing, and its relatively low initial temperature is not conducive to flame spread, which affects the combustion efficiency to a certain extent, and HC and CO emissions increase. Based on the reverse principle, CO and HC emissions are relatively low at high load. Interestingly, HC emissions at 100% load condition are greater than 75% load conditions. Mainly because engine's speed is faster and combustion time is shorter, more HC is generated accompanied by the incomplete combustion. As can be also seen from Fig. 10, HC and CO emissions changed little at the four test operating conditions of diesel engine. The maximum difference is 0.2 or 0.4 g/kW·h respectively. Thereby indicating that the fuel burn fully through all over the load of the test 2-stroke marine diesel engine.

CONCLUSIONS

Experiments were conducted on an MAN B&W 6S35ME-B diesel engine, which is a large low-speed two-stroke, cross-head, common rail, electronic fuel injection diesel engine. Based on marine low sulfur diesel fuel, the influence were evaluated on the fuel consumption, combustion characteristic (in-cylinder pressure, temperature and heat release rate), and NOx/CO/HC/CO_2 emissions. The test diesel engine is widely used as the ship propulsion device in the marine. Based on the experimental data, the main conclusions are shown as follows:

1) The combustion starts after top dead center and ignition advances with the increase of engine loads from 25% to 75% load, more over the inflection points of pressure curve after top dead center also following forward. Engine's in-cylinder pressure, temperature, and cumulative heat release were increased as load increasing. While it is necessary to delay the injection timing at 100% load to control the maximum combustion pressure and NOx emissions.

2) With the use of MLSDF, fuel consumption rate of high load conditions is relatively lower than the low load. Fuel consumption rate of about 75% load conditions is relatively low. It is only 178 g/kW·h at 75% load of the test engine.

3) The NOx percentage of the exhaust gas increases with the engine load. There are more than three factors affecting NOx generation and its chemical reaction process is complex. The NOx emissions of the test engine with MLSDF are always between 12.5 and 13.0 g/kW·h, which is less than 14.4 g/kW·h and meets the ships' emission requirements of IMO.

4) CO_2 emissions are significantly reduced from 25% to 75% load, but increased slightly at 100% load condition. The maximum difference of CO_2 emissions were 132 g/kW·h. The greater CO_2 emissions per unit power output means that thermal conversion efficiency is lower and its fuel consumption rate would be greater.

5) The HC or CO emissions are low and its maximum difference is 0.2 or 0.4 g/kW·h respectively. It indicates that the fuel burn fully through all load of the test engine with MLSDF. HC or CO emissions decide combustion efficiency and affect fuel consumption rate.

ACKNOWLEDGEMENTS

The authors would like to acknowledge the financial supports to the research provided by the National Natural Science Foundation of China (51709163), Science and Technology Commission Shanghai Municipalit (18DZ1202902).

REFERENCES

1. Eyring V., Isaksen I.S.A., Berntsen T., Collins W.J., Corbett J.J., Endresen O., Grainger R.G., Moldanova J., Schlager H., Stevenson D.S.. Transport impacts on atmosphere and climate: shipping. Atmospheric Environment. 44(37), 4735-4771, 2010.

2. Jostein K. Sundet, Stig B. Dalsøren, Ivar S. A. Isaksen, Tore F. Berglen. Emission from international sea transportation and environmental impact. Journal of Geophysical Research Atmospheres. 108 (D17), 4560, 2003.

3. Eyring, V., Köhler, H.W., van Aardenne, J., Lauer, A.. Emissions from international shipping: 1. The last 50 years. Journal of Geophysical Research Atmospheres. 110 (D17), 1-12, 2005.

4. Bajic J., Simunovic, S., Steiner S.. Air Transport in the European System of CO_2 Emissions Trading. Hrvatsko Znanstveno Drustvo za Promet. 33(1-2), 123-129, 2013

5. Corbett, J.J., Fischbeck, P.S., Pandis, S.N.. Global nitrogen and sulfur inventories for oceangoing ships. Journal of Geophysical Research Atmospheres. 104(3), 3457-3470, 1999.

6. Koenig D. Global and regional approaches to ship air emissions regulation: the international maritime organization and the European Union. Advances in Space Research the Official Journal of committee on Space Research. 31(1), 25, 2013.

7. Eyring, V., Isaksen, I.S.A., Berntsen, T., Collins, W.J., Corbett, J.J., Endresen, O., Grainger, R.G., Moldanova, J., Schlager, H., Stevenson, D.S. Assessment of Transport impacts on climate and Ozone: shipping. Berichte Der Bunsengesellschaft Für Physikalische Chemie. 98 (9): 1109-1110, 2009.

8. Bond, T.C., Doherty, S.J., Fahey, D.W., Fprster P.M., Berntsen T., DeAngelo B.J., Flanner M.G., Ghan S., Karcher B., Koch D.. Bounding the role of black carbon in the climate system: a scientific assessment. Journal of Geophysical Research Atmospheres. 118(11), 5380-5552, 2013.

9. Andy H.F., Anthony J.M., Kirk R.S., Lan R., James W.M., Anil M., Ben G.A., Diarmid C.L., Alan D.D., Michael D., Nigel B., Cathryn T.S., Mark B., Paul W.. Public health benefits of strategies to reduce greenhouse-gas emission: overview and implications for policy makers. The Lancet. 374(9707), 2104-2114, 2010.

10. Psaraftis H.N.. Market-based measures for greenhouse gas emissions from ships: a review. Wmu Journal of Maritime Affairs. 11(2), 11:211-232, 2012.

11. Schinas O., Stefanakos C.N.. Selecting technologies towards compliance with MARPOL Annex VI: The perspective of operators. Transportation Research Part D-Transport and Environment. 28(28), 28-40, 2014.

12. Hongxia W., Hong F., Xueying Y., Ke W.. Development of natural gas vehicles in China: an assessment of enabling factors and barriers. Energy Policy. 85, 80-93, 2015.

13. Lamas M.I., Rodriguez C.G., Aas H.P.. Computational fluid dynamics analysis of NOx and other pollutants in the man B&W 7S50MC marine engine and effect of EGR and water addition. International Journal of Maritime Engineering. 155, 81-88, 2013.

14. Yang Z.L., Zhang D., Caglayan O., Jenkinson I.D., Bonsall S., Wang J., Huang M., Yan X.P.. Selection of techniques for reducing shipping NOx and SOx emissions. Transportation Research Part D-Transport and Environment. 17, 478-486, 2012.

15. Francersco D.N.., Claudia C.. Particulate matter in marine diesel engines exhausts: Emissions and control strategies. Transportation Research Part D-Transport and Environment. 40, 166-191, 2015.

16. Kowalski J. An experimental study of emission and combustion characteristics of marine diesel engine with fuel pump malfunctions. Applied Thermal Engineering. 65, 469- 476, 2014.

17. Gokalp B., Buyukkaya E., Soyhan H.S. Performance and emissions of a diesel tractor engine fueled with marine diesel and soybean methyl ester. Biomass and Bioenergy. 35, 3575-3583, 2011.

18. Rakopoulos D.C.. Heat release analysis of combustion in heavy-duty turbocharged diesel engine operating on blends of diesel fuel with cottonseed or sunflower oils and their bio-diesel. Fuel. 96(1), 524-534, 2012.

19. Khabbaz S.A., Mobasheri R.. Experimental investigation of the effects of Tri-aromatic utilization on combustion process, emission characteristics and engine performance of a DI diesel engine. Fuel. 123, 26-32, 2014.

20. Chaparala S.V., Raj A., Chung S.H.. Reaction mechanism for the formation of nitrogen oxides during coke oxidation in fluidized catalytic cracking units. Combustion Science and Technology. 187(11), 1683-1704, 2015.

21. Rangel L.P., Buchler P.M.. Study of nitrogen in the combustion of natural gas. Quimica Nova. 28(6), 957-963, 2005.

22. Sharpe B., Muncrief R.. Literature review: real-world fuel consumption of heavy-duty vehicles in the United States, China, and the European Union. Annales De Dermatologie Et De Vénéréologie. 140(12), S553, 2013.

23. Yoon S.J., Collins J., Thiruvengadam A., Gautam M., Herner J., Ayala A.. Criteria pollutant and greenhouse gas emissions from CNG transit buses equipped with three-way catalysts compared to lean-burn engines and oxidation catalyst technologies. Journal of Air and Waste Management Association. 63(8), 923-933, 2013.

24. Karavalakis G., Hajbabaei M., Durbin T.D., Johnson K.C., Zheng Z.Q., Miller W.J.. The effect of natural gas composition on the regulated emissions, gaseous toxic pollutants, and ultrafine particle number emissions from a refuse hauler vehicle. Energy. 50(1), 280-291, 2013.

25. Fontaras G., Martini G., Manfredi U., Marotta A., Krasenbrink A., Maffioletti F., Terenghi R., Colombo M.. Assessment of on-road emissions of four Euro V diesel and CNG waste collection 2 trucks for supporting air-quality improvement initiatives in the city of Milan. Science of the Total Environment. 426(5), 65-72, 2012.

26. Hajbabaei M., Karavalakis G., Johnson K.C., Lee L., Durbin T.D.. Impact of natural gas fuel composition on criteria, toxic, and particle emissions from transit buses equipped with lean burn and stoichiometric engines. Energy. 62(6), 425-434, 2013.

CONTACT WITH THE AUTHORS

Qinming Tan
e-mail: qmtan@shmtu.edu.cn

Merchant Marine College
Shanghai Maritime University
Shanghai 201306
CHINA

sciendo

POLISH MARITIME RESEARCH 1 (101) 2019 Vol. 26; pp. 162-173
10.2478/pomr-2019-0018

THE ANALYSIS OF OVERALL SHIP FUEL CONSUMPTION IN ACCELERATION MANOEUVRE USING HULL-PROPELLER-ENGINE INTERACTION PRINCIPLES AND GOVERNOR FEATURES

Hamid Zeraatgar
Amirkabir University of Technology, Department of Maritime Engineering, Tehran, Iran
M. Hossein Ghaemi
Gdańsk University of Technology, Faculty of Ocean Engineering and Ship Technology, Poland

ABSTRACT

The problem of reduction of greenhouse gas emissions in shipping is currently addressed by many research works and related industries. There are many existing and visionary technologies and ideas, which are conceptually defined or practically realised. This goal can be achieved in different ways, and reducing fuel consumption is one of the major methods. In these circumstances, the aim of this study is to analyse the possibility of fuel consumption reduction by using an alternative control strategy for low-speed marine diesel engines which would take into account the interactions between hull, propeller and main engine. For this purpose, a mathematical model including ship hull and propulsion system is developed. A case study is conducted for a ship for which the results of both the ship hull and screw propeller model tests are available. A low-speed two-stroke diesel engine is then selected for the considered ship. Two different governors are included in the model and their parameters are changed to investigate the dynamic behaviour of the system when simulating the forward acceleration mode in calm sea conditions. The research is mainly focused on variations of fuel consumption by the ship passing a certain distance to reach the nominal constant speed. It is concluded that, for a given travel distance, it is possible to save considerable amount of fuel at the expense of slight increase of journey time.

Keywords: Modelling and simulation; fuel consumption; hull-propeller-engine interactions; ship propulsion system; governor; control strategy

NOMENCLATURE

A_s	wetted surface (m^2)
C_{Ts}	total resistance coefficient
C_{F0s}	residual frictional resistance coefficient
C_{Rs}	residual resistance coefficient
C_{AA}	air resistance coefficient
δC_F	roughness coefficient
CF	total consumed fuel (kg)
D_p	propeller diameter (m)
E	error signal
h	fuel rack or fuel mass flow rate (kg/s)
H	geometrical pitch (m)
H_A	advance pitch (m)
H_S	pitch due to slip (m)
J_A	advance number
K_E	engine gain
K_R	controller gain
K_t	thrust coefficient
K_q	torque coefficient
L_{WLs}	water line length (m)
M	output of the governor
n_E	rate of revolution of engine shaft (rpm)
n_p	rate of revolution of propeller (rps)
$\dot{n}_P$	propeller angular acceleration (rad/s^2)
$\overline{n}$	commanded angular velocity of the shaft (rad/s)
n_{ss}	rotational speed of the shaft in steady-state conditions (rad/s)

Q_P propeller torque (kNm)
Rn_s Reynolds Number
R_t total resistance in calm water (kN)
R_{Ts} total resistance (kN)
S journey distance (Nm)
t time, thrust deduction factor
T thrust (kN)
T_E time constant of engine response (s)
t_f final journey time (duration of journay)
T_n net thrust (kN)
T_{Ri} time constant of governor
u surge velocity (m/s)
u_A advance speed (m/s)
$\dot{u}$ surge acceleration (m/s^2)
w wake fraction
$X_{\dot{u}}$ surge added mass (t)
Z_E number of engine cylinders
η_0 open water propeller efficiency
ω_E angular velocity of engine shaft (rad/s)
ρ water density (t/m^3)
τ engine response delay (s)

INTRODUCTION

In the ship design process, the ship resistance, as well as the propeller and engine performance are traditionally considered in calm water and steady-state conditions, individually. Then, at the end of design, the engine-propeller interaction in calm water conditions is considered for optimum design. However, not only the steady-state conditions, but also the dynamic hull-propeller-engine interactions taken into account in ship design are not real conditions. Several attempts have been made to include the dynamic interactions between the above three elements. This kind of study may lead to better understanding of real conditions of operation of such sub-elements as engine and propeller, which may have an impact on their design. It may also ensure better control of the engine, which may cut the fuel consumption, as well as improve the overall total ship performance and comfort of crew and passengers. The fuel consumption reduction means decreasing greenhouse gas emissions during ship operation. The purpose of this study is to analyse the possibility of fuel consumption reduction by using an alternative control strategy for low-speed marine diesel engines which would take into account the main interactions between hull, propeller, and main engine.

Schulten [7] considered the interactions between diesel engine, ship and propeller during manoeuvres in calm water. Bondarenko and Kashiwagi [1] studied the dynamic behaviour of a ship propulsion plant in actual seas. They concluded that a conventional governor cannot effectively control the ship propulsion plant in cases of large and abrupt propeller torque losses. This fact suggests the necessity of developing a new control algorithm which could effectively reject disturbances caused by propeller racing.

Theotokatos and Tzelepis [9] have studied the fuel consumption and gas emission generated by a ship engine using a simulation model of hull-propeller-engine interactions. They concluded that the combined engine-propeller-ship modelling can be used for mapping the engine and emission parameters to support the analysis of the propulsion system behaviour over the entire ship operating envelope. The usefulness of mapping of the propulsion system performance and emissions for minimizing the fuel consumption and gaseous emissions during ship operation was evidenced.

Taskar et al. [8] have used a model of engine coupled with a method to estimate wake in waves. They concluded that significant changes in propulsion performance have been observed in the presence of waves as compared to the steady state operation. It has been shown that the engine propeller response i.e. power fluctuations, propeller speed fluctuations, and torque fluctuations can be obtained through a coupled simulation making use of realistic engine and propeller models.

Mizythras et al. [5] have studied the performance of an engine and its elements during acceleration in rough seas using hull-propeller-engine interactions. Their analysis has revealed that the presence of the engine governor limiters and their application timing affect the overall ship's performance.

The hull-propeller-engine interaction simulation seems to be inevitably the future of ship dynamics simulations for assessing all aspects of performance of ship's sub-systems and the ship as a whole. However, there are numerous research issues which need to be addressed.

This paper deals with calculation of fuel consumption as an objective function taking into account the hull-propeller-engine interactions in calm water conditions when the ship accelerates from an arbitrary steady-state speed to the steady service speed. For this purpose, a mathematical model of ship hull and propulsion system is developed. A case study is conducted for a ship for which the results of both the ship hull and screw propeller model tests are available. A low-speed two-stroke diesel engine is then selected for the considered ship. Two different governors are included in the model and their parameters are changed to investigate the dynamic behaviour of the system when simulating the forward acceleration mode in calm sea conditions. The research is mainly focused on fuel consumption variation when the ship passes a certain distance to reach the nominal constant speed. It is concluded that, for a given travel distance, it is possible to save considerable amount of fuel at the expense of slight increase of journey time.

HULL-PROPELLER-ENGINE INTERACTIONS IN ACCELERATION MODE

The steady state for a ship is achieved when the hull, propeller, and engines operate in steady-state conditions. In this case, their variable parameters are well-matched and do not change in time. As soon as one of these three components operates in acceleration mode, the others are also forced

to work under changing conditions. The dynamics of each individual component affects other components. At the beginning of the acceleration mode, the ship is operated at low speed in steady-state conditions. The engine and the propeller also work steadily. Then, the full-ahead command is ordered and executed.

PRINCIPLES OF HULL DRAG FORCE MODELLING IN ACCELERATION MODE

Resistance at ship's steady speed

When designing a ship, the hull drag is typically considered for steady speed, straight path, and calm water conditions. However, several dynamic conditions may also be taken into account in simulations making use of a quasi-static model.

The hull resistance of the ship sailing along a straight path in calm water can be estimated using a regressive/empirical formula, a numerical method, and/or from model tests. The first two methods are usually employed in an early stage of ship design, while model testing is utilized at the final stage. The main equations are as follows:

$$R_{Ts} = \frac{1}{2}\rho_s C_{Ts} u^2 A_s \tag{1}$$

$$C_{Ts} = C_{Fos} + C_{Rs} + C_{AA} + \delta C_F \tag{2}$$

$$C_{Fos} = \frac{0.075}{\left(Log_{10}\mathrm{Rn}_s - 2\right)^2} \tag{3}$$

$$\mathrm{Rn}_s = \frac{u\, L_{WLs}}{\upsilon_s} \tag{4}$$

$$C_{Rs} = C_{Rm} \tag{5}$$

where u is the ship's surge velocity, and C_{Ts}, C_{F0s}, C_{Rs}, C_{AA} and δC_F are the ship's total, frictional, residual, air, and roughness resistance coefficients, respectively. R_{Ts} is the ship's total resistance, Rn_s is the Reynolds Number, L_{WLs} is the ship's length at the water line level, and A_s is the ship's wetted surface. The residual ship resistance coefficient is equal to the model coefficient obtained from model tests.

Resistance at acceleration

Having known the steady-state hull resistance, the total resistance is estimated by adding the surge added mass force term as follows:

$$R_t = R_{Ts}(u) + x_{\dot{u}}\dot{u} \tag{6}$$

where $R_{Ts}(u)$ stands for the steady-state hull resistance as function of its surge speed, u, and $x_{\dot{u}}\dot{u}$ is the surge added mass force, being the product of the surge added mass, $x_{\dot{u}}$, and surge acceleration, $\dot{u}$. R_t is the ship's total resistance in calm water. For a given ship, the surge added mass is a function of its breadth-to-length ratio and typically is assumed in the range of 5 to 10 percent of ship mass [4].

PROPELLER PERFORMANCE ALONG STRAIGHT PATH IN CALM WATER

Propeller performance is related to the thrust coefficient, K_t, torque coefficient, K_q, and propeller efficiency in open water conditions, η_0. It is presented as a function of advance number, J_A, wake fraction, w, thrust deduction factor, t, and cavitation. Normally, the propeller is designed at an early stage of design using the regression formula from a systematic series. It then has to be tested in: (1) open water conditions, (2) behind hull conditions, and (3) in the cavitation tunnel at the final stage of design. The propeller design condition is solely the calm water condition. Following the general formula for thrust generation by the propeller in open water and calm water conditions, the thrust delivered by the propeller and the required torque can be determined as:

$$T = K_t \cdot \rho \cdot {n_P}^2 \cdot {D_P}^4 \tag{6}$$

$$Q_P = K_q \cdot \rho \cdot {n_P}^2 \cdot {D_P}^5 \tag{7}$$

where:

$$K_T = f_1(J_A) = f_1(u_A, n_p) \tag{8}$$

$$K_Q = f_2(J_A) = f_2(u_A, n_p) \tag{9}$$

$$J_A = \frac{u_A}{n_p \cdot D_p} = \frac{n_p\left(H - H_S\right)}{n_p \cdot D_p} = \frac{H - H_S}{D_p} \tag{10}$$

$$H_A = H - H_S \tag{11}$$

$$u_A = u(1-w) \tag{12}$$

$$T_n = T(1-t) \tag{13}$$

$$R_t = T_n \tag{14}$$

In these formulas, T_n is the net thrust, T is the thrust, Q_p is the propeller torque, H is the geometrical pitch, H_s is the pitch due to slip, and H_A is the advance pitch. ρ is water density, n_p is the rate of revolution of the propeller shaft (in revolutions per second), and D_p is the propeller diameter.

Under the acceleration mode the surge speed, u, varies in time, as a result of which the advance speed, u_A, and the propeller speed also change. Thus, the advance ratio J_A changes nonlinearly. Additionally, the wake fraction and the thrust deduction coefficient also vary. Therefore:

$$J_A(t) = \frac{u_A(t)}{D_p \cdot n_p(t)} \tag{15}$$

$$T(t) = K_t\left(J_A(t)\right) \cdot \rho \cdot n_p(t)^2 \cdot D_p^4 \tag{16}$$

Here, the same propeller hydrodynamic coefficients from an open water propeller test are applied, even if the instantaneous kinematic variables are employed. In order to calculate the propeller thrust, the instantaneous value of $J_A(t)$ is to be calculated based on $n_p(t)$ and $u_A(t)$. The advance speed is related to the wake fraction which is calculated/measured in steady-state conditions at certain ship and propeller speeds.

$$u_A(t) = u(t)(1 - w(t)) \tag{17}$$

To the authors' best knowledge, there is no research addressing the wake fraction $w(t)$ in the acceleration mode. Therefore, its value is assumed equal to that of the ship service speed in steady-state conditions, which is either estimated by the regression formula or taken from the model test results for the ship under consideration. The following empirical formulae may be applied:

$$\begin{aligned} w &= -0.05 + 0.5 \cdot C_B \text{ (Taylor)} \\ w &= 0.7 \cdot C_P - 0.18 \text{ (Heckscher)} \\ w &= 0.45 \cdot C_P - 0.05 \text{ (Robertson)} \end{aligned} \tag{18}$$

The same conditions and assumptions are employed when estimating the thrust deduction factor from the regression formula:

$$t = 0.5 \cdot C_p - 0.12 \text{ (Hecker)} \tag{19}$$

As far as the propeller torque required in the acceleration mode is concerned, an additional torque due to added moment of inertia of propeller, J_{added}, must be counteracted by the engine torque:

$$K_q\left(J_A(t)\right) \cdot \rho \cdot n_p(t)^2 \cdot D_p^5 + J_{aaded} \cdot \dot{n}_p(t) \tag{20}$$

where $\dot{n}_p$ is the propeller rotational acceleration in rad/s^2.

The propeller surge added mass force, $m_{ap,}$ is approximated as:

$$m_{ap} = K_{ap} \cdot m_p \tag{21}$$

where K_{ap}=0.10 to 0.20 (Veritec, 1985) and m_p is the propeller mass.

The propeller moment of inertia is calculated as:

$$J_P = \frac{D_P^2}{K_p} \cdot m_P \tag{22}$$

where K_p takes values between 19 and 28, with 23 as the typically cited value.

The propeller added moment of inertia can be modelled using a simple method:

$$J_{added} = K_a \cdot J_P \tag{23}$$

where the suggested value of K_a is in the range from 0.25 to 0.30 (Saunders, [6]) or from 0.25 to 0.50 (Veritec, [10]).

An alternative method is the regression method by Macpherson et al. (2007):

$$\begin{cases} J_a = C_{IE} \cdot \rho \cdot D_P^5 \\ C_{IE} = C_1 \cdot EAR \cdot \dfrac{H}{D_P} - C_2 \end{cases} \tag{24}$$

where EAR is the expanded area ratio.

Tab. 1. Coefficients and (MacPherson et al. [4])

No. of blades (Z_p)	Z_p=3	Z_p=4	Z_p=5	Z_p=6
C_1	0.00477	0.00394	0.00359	0.00344
C_2	0.00093	0.0087	0.00080	0.00076

DIESEL ENGINE PERFORMANCE

The diesel engine is modelled using the most simplified mathematical model having the form of the first-order transfer function with delayed response [2]:

$$\frac{Q_E(s)}{h(s)} = e^{-\tau \cdot s} \cdot \frac{K_E}{1 + T_E \cdot s} \tag{25}$$

where h is the fuel rack or fuel mass flow rate [kg/s], τ is the response delay [s], K_E is the gain, and T_E is the time constant [s]. These quantities can be calculated as follows:

$$\tau = \frac{1}{2} \cdot \frac{2 \cdot \pi}{Z_E \cdot \omega_E} = \frac{\pi}{Z_E \cdot 2 \cdot \pi \cdot n_E} = \frac{1}{2 \cdot Z_E \cdot n_E} \tag{26}$$

$$T_E \approx 0{,}9 \cdot \frac{2 \cdot \pi}{\omega_E} \tag{27}$$

$$K_s = \frac{Q_E(n_{E0})}{h(n_{E0})} \tag{28}$$

where Z_E stands for the number of engine cylinders, and ω_E and n_E represent the angular velocity [rad/s] and the rate of engine shaft revolutions [rpm], respectively. Subscript '0' referrers to steady-state conditions at nominal point, e.g. Normal Continuous Rating (NCR). A detailed diesel engine model can be found in (Ghaemi [3]).

The engine is assumed to be equipped with a governor which keeps the shaft rotational speed at a constant level with respect to the operating point of the engine (see Fig. 1).

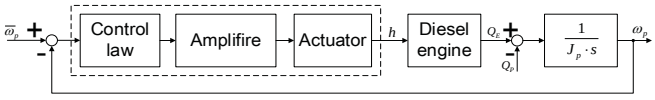

Fig. 1. Simplified engine-propeller block diagram.

If an electrical sensor of angular velocity is applied (for example a small generator), then the transfer function of this element may be represented by 1, due to a relatively small time constant in comparison with other elements.

A governor of PI-action is selected and defined as below:

$$G_R(s) = \frac{M(s)}{E(s)} = K_R\left(1 + \frac{1}{T_{Ri} \cdot s}\right) \tag{29}$$

where K_E and T_{Ri} are the gain constant and the time constant, respectively. $M(s)$ is the output of the governor and $E(s)$ is the error signal, defined as the difference between the commanded rotational speed and the actual one. In the time domain, the above relationship can be written as follows:

$$m(t) = K_p \cdot \left(\overline{n}(t) - n(t)\right) + K_i \cdot \int \left(\overline{n}(t) - n(t)\right) dt \tag{30}$$

where $\overline{n}(t)$ is the commanded rotational speed of the shaft.

The fuel index change, ΔX_f, can be calculated as follows:

$$\Delta X_f(t) = \frac{m(t)}{n_{ss}} \tag{31}$$

where n_{ss} stands for the rotational speed of the shaft in steady-state conditions with respect to the current operating point, OP:

$$OP = \frac{P_B}{P_{BNCR}} \tag{32}$$

The fuel index at the current operating point should be changed by the increment $\Delta X_f(t)$ of the steady-state index X_{fss}:

$$X_f(t) = X_{fss} + \Delta X_f(t) \tag{33}$$

Finally, the fuel rate (FR) is calculated as:

$$FR(t) = X_f(t) \cdot FR_{NCR} \tag{34}$$

HULL-PROPELLER-DIESEL ENGINE INTERACTIONS AT ACCELERATION MODE IN STRAIGHT PATH AND CALM WATER CONDITIONS

Interactions between hull, propeller and diesel engine occur during ship acceleration and stopping manoeuvres. The general relationship can be formulated as follows:

$$\begin{cases} -R_t(t) + T_n(t) = (\Delta + x_{\dot{u}})\dot{u}(t) \\ Q_E(t) - Q_P(t) = J_P \cdot \dot{\omega}_P(t) \\ T_E \dot{Q}_E(t-\tau) + Q_E(t-\tau) = X_f(t) \\ X_f(t) = X_{fss} + \dfrac{K_p \cdot \left(\overline{n}_E(t) - n_E(t)\right) + K_i \cdot \int \left(\overline{n}_E(t) - n_E(t)\right) dt}{n_{ss}} \end{cases} \tag{35}$$

where $n = n_E = n_p$.

For a given fuel injection scenario, the total amount of the consumed fuel, *CF*, and the journey distance, *S*, are as follows:

$$CF = \int_0^{t_f} FR(t)\, dt \tag{36}$$

$$S = \int_0^{t_f} u(t)\, dt \tag{37}$$

whwved numerically in the time domain.

CASE STUDY, SIMULATION AND RESULTS

For simulation purposes, a computer code is developed based on the delivered model using MATLAB-SIMULINK R2017a. The simulation model is applied to a ship whose hull model was tested for identifying the ship's resistance and whose propeller was tested in model scale. The ship is equipped with a two stroke low-speed diesel engine selected to match the required power, considering the open water and the relative rotative efficiency of the propeller, the hull and shaft efficiencies, and the mechanical efficiency, as well as the sea and engine margins.

SHIP AND ITS PROPULSION SYSTEM

To calculate the performance and perform simulations, a typical vessel, which is a Series 60 ship with block coefficient of 0.60, has been selected. The ship specification is given in Tab. 2. A model of this ship, of 4.58 meters in length, was fabricated, and standard resistance tests were conducted in NIMALA (National Iranian Marine Laboratory). The model test results extrapolated for the ship are given in Tab. 3.

A B-Wageningen type propeller was selected to propel the ship as specified in Tab. 4. It was tested in open water conditions using the model of 25 cm in diameter. The open water characteristics are shown in Fig. 2.

The prime mover is a MAN-B&W 8S65ME-C8.5 low-speed diesel engine. The Service Maximum Continuous Rating (SMCR) is set for 19433 kW at 92.8 RPM. The steady-state performance of the engine is given in Tab. 5 and illustrated in Fig. 3.

Tab. 2. Ship specifications

No.	Ship parameter	Symbol	Value
1	Displacement	Δ ∇	26980.220 [ton] 26245.350 [m^3]
2	Wetted length Length BP	L_{WL} L_{BP}	186.260 [m] 182.880 [m]
3	Beam	B	24.414 [m]
4	Draught	T	9.782 [m]
5	Ship speed	u	23.82 [Kn]
6	Block coefficient	C_B	0.600 [-]
7	Prismatic coefficient	C_P	0.615 [-]
8	Wetted surface	A	5762.200 [m^2]

Tab. 3. Ship resistance

No.	u [m/s]	Fn	Ct	Rt [kN]	Status
1	0.000	0.00	0.00000	0.000	A
2	1.000	0.023	0.0017700	5.260	A
3	2.000	0.047	0.0017700	21.040	A
4	3.000	0.070	0.0017700	47.340	A
5	4.00	0.094	0.0017760	84.170	A
6	5.13	0.120	0.0017760	138.430	M
7	5.984	0.140	0.0018060	191.526	M
8	6.839	0.160	0.0018070	250.361	M
9	7.694	0.180	0.0018060	316.960	M
10	8.549	0.200	0.0018297	396.061	M
11	9.404	0.220	0.0019500	510.911	M
12	10.259	0.240	0.0019619	611.559	M
13	10.686	0.250	0.0020545	694.845	M
14	11.114	0.260	0.0024144	883.286	M
15	11.969	0.280	0.0030059	1275.386	M
16	12.396	0.290	0.0033275	1514.372	M
17	12.824	0.300	0.0021962	1683.439	M
18	13.679	0.320	0.0035106	1945.546	M

A: Approximated
M: Model test

Tab. 4. Propeller specifications

Type	B-Wageningen Fixed pitch propeller
Diameter	7.590 [m]
Number of blades	5
Area ratio	0.5808
Pitch ratio	1.00 (at full pitch)

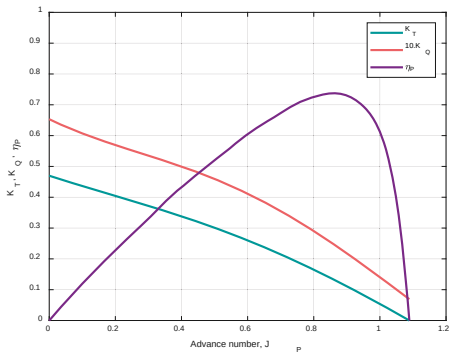

Fig. 2. Open water model test results for the propeller from Tab. 4 (NIMALA)

Tab. 5. Engine performance

Load	Power	Speed	SFOC	FR	Engine eff.
OP [%]	[kW]	[RPM]	[g/kWh]	[kg/s[	[-]
10	1943	43.1	188.0	0.101468	0.4485
15	2915	49.3	178.0	0.144131	0.4736
20	3887	54.3	174.0	0.187872	0.4845
25	4858	58.5	172.0	0.232104	0.4902
30	5830	62.1	170.0	0.275306	0.4959
35	6802	65.4	169.0	0.319316	0.4989
40	7773	68.4	167.5	0.36166	0.5033
45	8745	71.1	166.1	0.403485	0.5076
50	9717	73.7	164.9	0.445093	0.5113
55	10688	76.0	163.7	0.486007	0.5150
60	11660	78.3	162.6	0.526643	0.5185
65	12631	80.4	161.7	0.567342	0.5214
70	13603	82.4	161.1	0.608734	0.5233
75	14575	84.3	161.3	0.653041	0.5227
80	15546	86.1	161.7	0.698275	0.5214
85	16518	87.9	162.3	0.744687	0.5195
90	17490	89.6	163.1	0.792394	0.5169
95	18461	91.2	164.2	0.842027	0.5135
100	19433	92.8	165.5	0.893378	0.5094

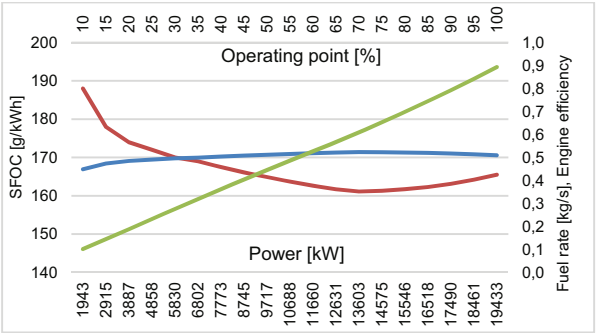

Fig. 3. Steady-state performance of MAN-B&W 8S65ME-C8.5

THE RESULTS

The simulations have been performed under the following assumptions:

1. The shaft, relative-rotative, and gearbox efficiencies are assumed constant and independent of operating conditions. Their exact values are equal to 0.98, 1.00 and 1.00, respectively.
2. The dynamic response of the engine to the torque variation due to fuel rate change is simplified and modelled by a first-order transfer function with time delay. Other engine characteristics involving thermal efficiency are taken from the steady-state engine performance, given in Fig. 3 (quasi-steady analysis).
3. The Normal Continuous Rating (NCR) is supposed to be the same as SMCR.
4. The fuel supply equipment (including fuel pump) is modelled based on the steady-state response. The dynamic behaviour of this equipment is not taken into account.
5. Generally, the governor is of PI-action type.
6. No limiter is applied in the governor, i.e. the governor output is not restricted by the permissible torque or scavenging pressure in the cylinders.
7. Based on the engine specifications provided by the engine manufacturer, the engine always operates above 70% of the NCR rotational speed.
8. The simulation time duration is fixed for a certain journey distance, the length of which is set equal to 15 km.

The overall schematic diagram of the simulation model is presented in Fig. 4.

The model was simulated first for NCR operation to check the steady-state values of selected variables. After approaching a proper set-up of the steady-state hull, propeller, and engine interactions, their results were regarded as initial values for the further unsteady-state analysis. Next, the model was tested for the "full ahead from zero – full stop – full ahead from zero" scenario to check its range of validity. The results of these tests provided positive verification of the model. After that, a simulation which reflects the real conditions at the acceleration from 70% to 100% of shaft rotational speed (at NCR) was conducted. This is equivalent to the engine power change from 29% to 100% of NCR. Basically, due to turbocharger inefficiency, when the operating point drops below 29% of NCR, the ship propelling becomes ineffective. Therefore, this simulation covered the full acceleration range of the propeller, which is also equivalent to full acceleration range of ship hull.

The simulations aimed at analysing the influence of the governor and its parameters on fuel consumption in the acceleration mode. For the first run, the governor parameters were adjusted using the Ziegler-Nichols method. Next, the simulations were repeated for two cases:

- **Case1:** The P-action governor gain varies from 1 to 27 (higher values make the control system unstable).
- **Case 2:** The proportional gain of the PI-action governor is adjusted and fixed for optimum, while the value of the integral gain varies from 1 to 23 (higher values cause control system instability). The optimum value of the proportional gain is determined equal to 12.15.

All of these simulations start from steady-state conditions at 70% of propeller rotational speed in relation to NCR. The system operation at this initial operating point is continued for 100 seconds to make sure that the variables have become steady. The simulations continue until the 15-km travel distance from the starting point is reached. The ship is sailing along a straight path in calm water conditions. Selected results of these simulations are shown in Figs. 5 to 13. They show the time-histories of engine, propeller, and hull dynamics at optimum governor gains, i.e. the proportional gain equal to 12.15 and the integral gain equal to 2.59 – according to the Ziegler-Nichols method. As shown in Fig. 5, when the fuel rack is changed, the rotational speeds of engine shaft and propeller start with very high acceleration. Their time-histories have one or two fluctuation peaks and in relatively very short time reach approximately the steady-state values. Fig. 6 shows the time-history of fuel consumption.

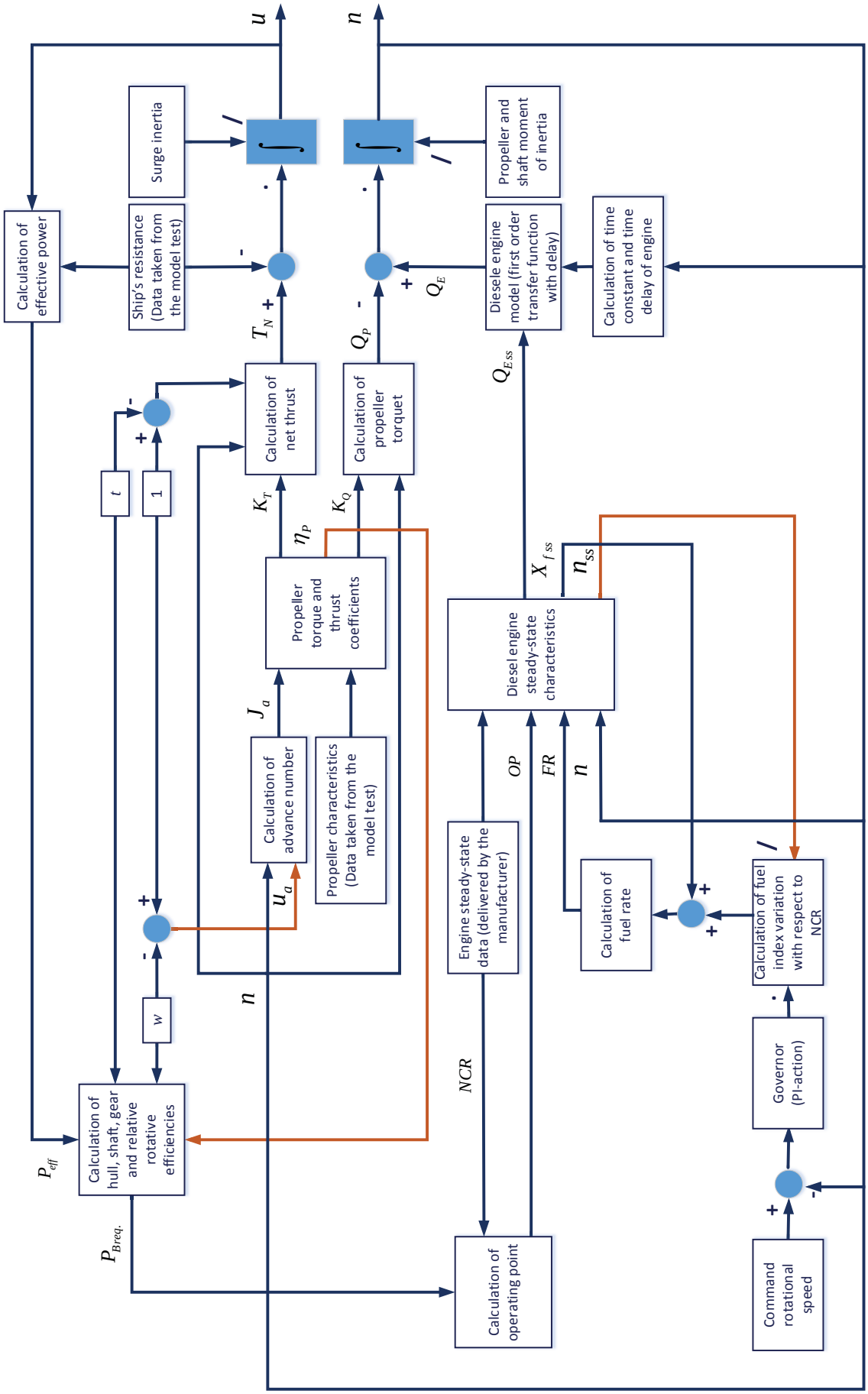

Fig. 4. Overall schematic diagram of the delivered mathematical model

The slope of the curve is reduced and fixed at a certain level after passing the transient state. This can be illustrated by fuel index or fuel rate variations, the latter shown in Fig. 7. During the first few seconds, the governor, which tries to maintain the rotational speed of the propeller at a constant desired level, changes the rate of the fuel delivered to the engine in a fluctuating manner. These early fluctuations are commanded by the integral part of the governor. The travelled distance and speed of the ship are depicted in Figs. 8 and 9, respectively. The time-history of the distance travelled by the ship has two different slopes. The first slope, which starts from zero and ends at second 100, represents the steady-state motion. The second slope starts from second 100, which is the beginning of the acceleration mode. Initially, the ship has the speed of 8.997 m/s, and then accelerates to reach the final steady-state speed of 11.743 m/s at second 510 (considering the maximum permissible fluctuations at the level of 1% as a criterion to determine the settling time).

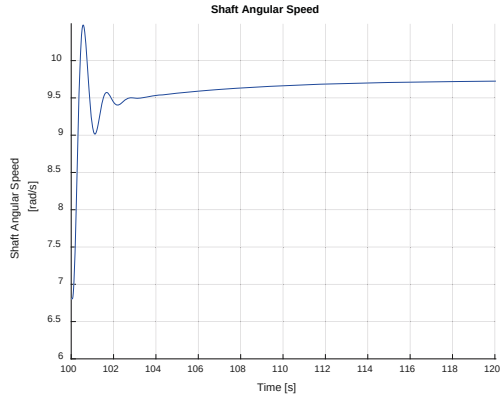

Fig. 5. Time-history of shaft angular speed

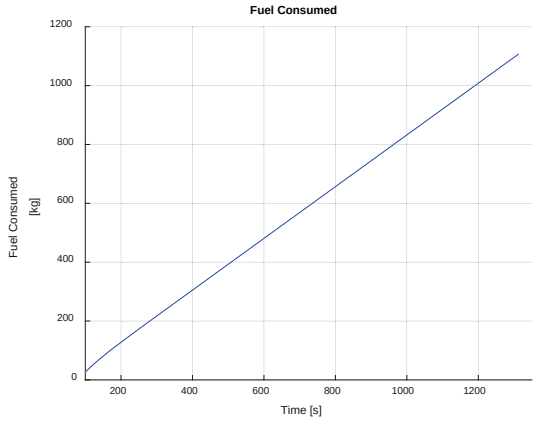

Fig. 6: Time-history of fuel consumption

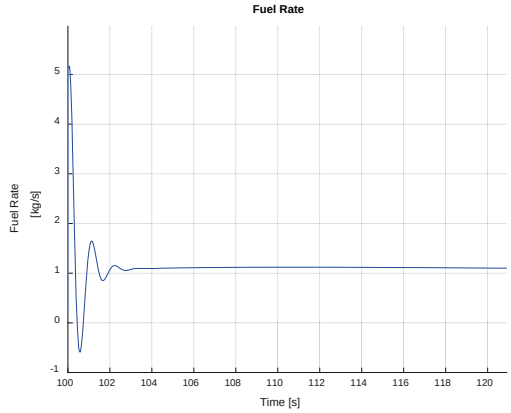

Fig. 7. Time-history of fuel rate

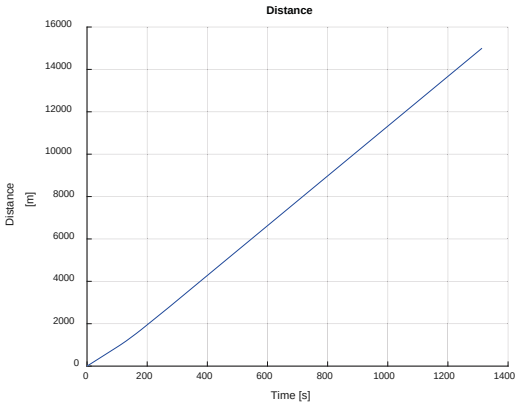

Fig. 8. Time-history of distance travelled by ship

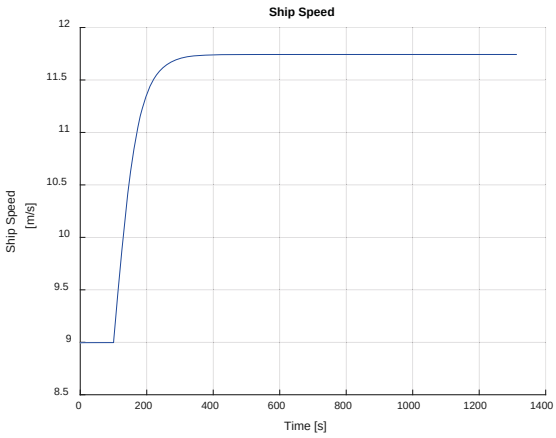

Fig. 9. Time-history of ship speed.

ANALYSIS

The above results show that the propeller and the engine need several tens of seconds to reach the steady-state mode, while the ship needs a several hundreds of seconds to come to the steady state. This is because of very high ship inertia,

compared to the engine shaft and the propeller. This issue becomes clearer when comparing the thrust generated by the propeller with ship's resistance and the torque required by the propeller with that generated by the diesel engine.

For this purpose, Fig. 10 and Fig. 11 compare the thrust-resistance time-histories and the engine torque-propeller torque time-histories, respectively. It can be clearly seen that large inertia of the ship makes that the difference between the current thrust generated by the propeller and the current ship's resistance is significant and a relatively a long time is required to reduce this difference. During this transient time, more thrust is generated than required. Similarly, the difference between the torque delivered by the engine and that required by the propeller is large. However, the time required for reducing this difference is shorter. If the power delivered by the engine (torque multiplied by the angular velocity) is compared with that required by the propeller (advance speed multiplied by the net thrust), it is visible that a relatively very long time is needed to reach the steady-state mode when these two variables are equal and matched. During this time, the supplied fuel could be decreased to adjust the "generated" power against the "required" power, see Fig.12.

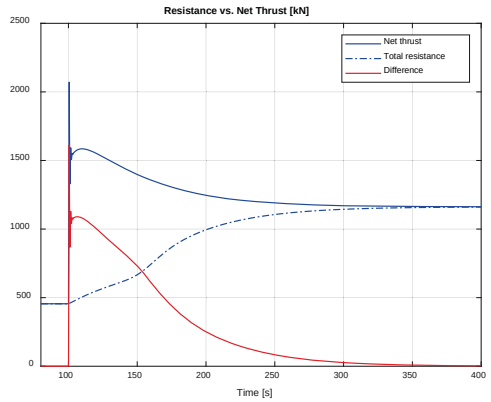

Fig. 10. Comparing time-histories of ship resistance and net thrust generated by propeller

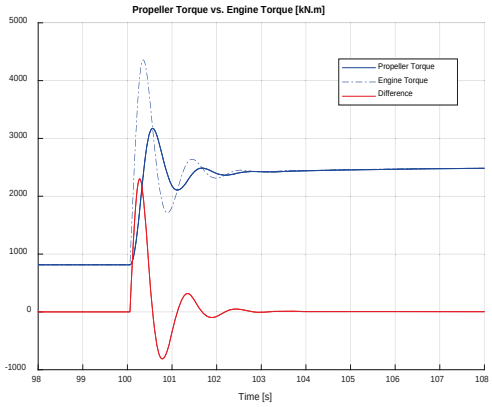

Fig. 11. Comparing time-histories of torque generated by engine and required by propeller

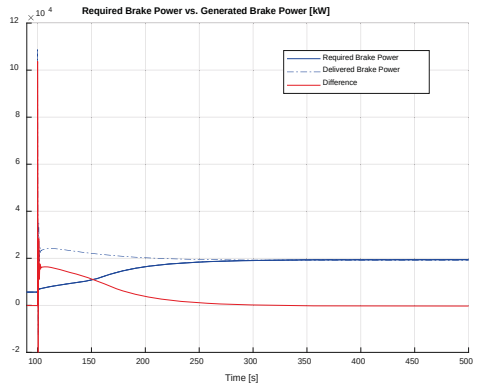

Fig. 12. Comparing time-histories of required and delivered power

Since the main goal of this study was investigating the role of the governor in fuel consumption at the acceleration mode, the governor parameters were assumed to vary from the minimum to the maximum permissible values, taking into account the stability of the control system. Therefore, combinations of "P" and "I" gains were assumed in the electronic governor, and the fuel consumption was analysed for these cases. In order to extract the effect of each of these two parameters, they were changed individually. It means that when the PI-action governor was applied, the proportional gain was kept constant and equal to the optimum value calculated based on the Ziegler-Nichols method. The governor gains, the time required by the ship to approach the 15-km distance, and the corresponding fuel consumption are given in Tab. 6.

As far as the proportional gain is concerned, Tab. 7 shows that a high gain value results in high fuel consumption, while a low gain yields low fuel consumption. Additionally, to achieve a relative 2.7% reduction of the travelling time, 11.5% more fuel is to be combusted. On the other hand, when the integral gain is changed, neither the travelling time nor the consumed fuel is visibly affected.

CONCLUSIONS

The study was focused on green shipping by fuel consumption reduction and included the interactions between hull, propeller and main engine.

Tab.6. Influence of governor integral gain on fuel consumption

Case II: PI-action governor (K_p=12.15)		
Governor integral gain K_i	Total time [s]	Total fuel consumption [kg]
1	1213.3	1081.419
2	1213.2	1081.221
3	1213.2	1081.153
4	1213.2	1081.119
5	1213.2	1081.099
6	1213.2	1081.087
7	1213.2	1081.078

Case II: PI-action governor (K_p=12.15)		
Governor integral gain K_i	Total time [s]	Total fuel consumption [kg]
8	1213.2	1081.072
9	1213.2	1081.068
10	1213.2	1081.065
11	1213.2	1081.063
12	1213.2	1081.062
13	1213.2	1081.061
14	1213.2	1081.060
15	1213.2	1081.060
16	1213.2	1081.060
17	1213.2	1081.061
18	1213.2	1081.061
19	1213.2	1081.062
20	1213.1	1081.061
21	1213.1	1081.060
22	1213.1	1081.056
23	1213.1	1081.042

Tab.7. Influence of governor proportional gain on fuel consumption

Case I: P-action governor		
Governor proportional gain K_p	Total time [s]	Total fuel consumption [kg]
1	1247.1	964.515
2	1230.8	1019.416
3	1225.2	1038.643
4	1222.3	1048.540
5	1220.6	1054.614
6	1219.4	1058.738
7	1218.5	1061.730
8	1217.9	1064.002
9	1217.4	1065.790
10	1217.0	1067.235
11	1216.6	1068.427
12	1216.4	1069.428
13	1216.1	1070.281
14	1215.9	1071.017
15	1215.7	1071.658
16	1215.6	1072.222
17	1215.4	1072.723
18	1215.3	1073.170
19	1215.2	1073.572
20	1215.1	1073.935
21	1215.0	1074.265
22	1214.9	1074.567
23	1214.9	1074.842
24	1214.8	1075.095
25	1214.7	1075.320
26	1214.2	1074.745
27	1214.2	1075.862

A mathematical model was developed, and the simulations were carried out for the selected case study. The objective of the simulations was investigating the amounts of fuel consumed by the ship in different scenarios to reach the nominal constant speed, when passing a certain distance.

The results have shown that the integral part of the governor has negligible influence on the amount of fuel consumed by the ship. On the other hand, the impact of the gain value of the proportional part on this variable is significant. The results also present the time needed for the ship to pass the distance of 15 km in the forward calm water acceleration mode after reaching the initial steady-state condition at second 100 (until this time the ship passes approximately 1 km). By changing the governor gain from 1 to 27 (the maximum value due to stability) the total time is changed from 1247 s to 1214 s., i.e. a small difference equal to 33 s is observed. However, the time needed for ship speed stabilisation varies from 582 to 1336 s., and this difference is relatively large (the same refers to the shaft rotational speed). The total fuel consumption varies from 964.515 kg (for K_p = 1) to 1075.862 kg (for K_p =27), which means the difference by 111.347 kg. Based on these outcomes, it can be concluded that to save 33 s of total time (which is 2.7% of the minimum calculated time for K_p = 27), the ship has to combust 111.347 kg more fuel (which is 11.5% more than the minimum calculated fuel consumption for K_p = 1.

That means that an attempt to keep the rotational speed as constant as possible by a conventional governor leads to a relatively significant increase of fuel consumption without any considerable influence on the travelling time. Therefore, one way to decrease the fuel consumption as a main criterion for green ship concept is to control ship acceleration. This study has demonstrated the effect of ship acceleration on fuel consumption. Indeed, situations in which the ship accelerates when sailing along a straight path are typical for ship departure, which is a very small part of ship voyage. However, there are other situations, such as navigation in waves for instance, during which the ship is constantly in acceleration conditions and the reduction of acceleration may considerably reduce the total fuel consumption. It should be added here that some optimisation criteria for a ship performing an acceleration manoeuvre can be found in [12].

REFERENCES

1. Bondarenko O., Kashiwagi M.: Dynamic behaviour of ship propulsion plant in actual seas, Journal of the JIME, Vol. 45, Special Issue, 2010.

2. Domachowski Z., Ghaemi M. H.: Marine control systems (in Polish, Okrętowe układy automatyki), Publication of Gdansk University of Technology, ISBN 9788373481770 837348177X, 2007.

3. Ghaemi M.: Changing the ship propulsion system performances induced by variation in reaction degree of turbocharger turbine, Journal of Polish CIMAC.-Vol. 6., No.1, 2011.

4. Lewandowski E.M., 2004, The Dynamics of marine craft, Manoeuvring and Seakeeping, World Scientific, Vol 22.

5. MacPherson D.M., Puleo V.R., Packard M.B.: Estimation of entrained water added mass properties for vibration analysis, SNAME New England Section, 2007.

6. Mizythras P., Boulougouris E., Theotokatos G.: Numerical study of propulsion system performance during ship acceleration, Ocean Engineering 149, 2018.

7. Saunders H.E.: Hydrodynamics in ship design, SNAME, 1957.

8. Schulten P.J.M.: The interaction between diesel engines, ship and propellers during manoeuvring, Ph.D. thesis, Delft, 2005.

9. Taskar B., Yum K.K., Steen S., Pedersen E.: The effect of waves on engine-propeller dynamics and propulsion performance of ships, Ocean Engineering. 122, 2016.

10. Theotokatos G., Tzelepis V.: A computational study on the performance and emissions parameters mapping of a ship propulsion system, Journal of Engineering for the Maritime Environment, 229 (1). pp. 58-76. ISSN 1475-0902, 2015.

11. Veritec: Vibration control in ships, ISBN 9788251500906,1985.

12. Wojnowski W., Marine Combustion Power Plants (Okrętowe Siłownie spalinowe, in Polish), Morski Instytut Rybacki, Gdańsk, 1991.

CONTACT WITH THE AUTHORS

Hamid Zeraatgar
e-mail: hamidz@aut.ac.ir

Amirkabir University of Technology
Department of Maritime Engineering
424 Hafez Ave
Tehran, Iran, 15875-4413
Iran

M. Hossein Ghaemi
e-mail: ghaemi@pg.edu.pl

Gdańsk University of Technology
Faculty of Ocean Engineering and Ship Technology
ul. G. Narutowicza 11/12
80-233 Gdansk
Poland

sciendo

POLISH MARITIME RESEARCH 1 (101) 2019 Vol. 26; pp. 174-182
10.2478/pomr-2019-0019

HYDRAULIC ANALYSIS OF CAUSES OF WASHOUT OF GDYNIA-ORŁOWO SEA-SHORE DURING THE FLOOD IN THE KACZA RIVER ESTUARY

Michał Szydłowski
Gdańsk University of Technology, Faculty of Civil and Environmental Engineering, Poland

ABSTRACT

In July 2016 in the Three-city agglomeration a rainfall episode of over a day duration and 150 mm summary rainfall height, occurred. This situation, extreme as for Polish conditions, caused significant freshets in rivers and streams running into Gdansk Bay, the Baltic Sea, and serving as collectors of rainfall waters for the sea-coast towns. In many areas of the Three-city flood phenomena and overflows took place. The flood also occurred in the catchment area of the Kacza river in Gdynia. The passing of flood water rise caused damage of many infrastructure objects located along the river valley. The estuary section of the river suffered most, especially sea-shore belt together with beach around the estuary which were significantly washed out. In this paper an approach was made to answer to the question on direct causes of the situation which occurred at the estuary of the Kacza river. To this end, there was worked out a hydrodynamic model of the considered section of the river, based on the solving of two-dimensional differential motion equations of free-surface liquid, and simulations of water flow propagation along the river's valley were performed for a few variants of hydraulic engineering infrastructure of river bed. Numerical hydraulic analysis made it possible to determine a role of the hydraulic engineering objects in forming the flood water rise as well as their impact on location and range of washout zones of sea-shore belt.

Keywords: hydrodynamics,flood,erosion of the coastal zone,Kacza river,Gdynia

INTRODUCTION

The Three-city agglomeration is located on the terrain adjacent to Gdansk Bay of the Baltic Sea, which is very differentiated as to its height over sea level. The terrain height changes from the Gdańskie Żuławy depression up to almost 200 m in the area of moraine hills a few kilometres distant from the Baltic Sea coastline. The so specifically shaped terrain of the Three-city affects spatial distribution and temporal run-off process of atmospheric precipitation, often causing the rise of local rainfall height due to an orographic mechanism [7, 8, 3]. Simultaneously, with the building development work carried out on the moraine hills, surface and bed rainfall run-off along the streams and rivers reaching Gdansk Bay has been increased . Beds of these watercourses serve to day as collectors in the rainfall catchment system. However their capacity is limited hence during violent rainfall run-off their overload resulting in flooding urban areas often occurs. In this century we have had to do with urban area flooding both in Gdańsk in 2001, 2010 and 2016 [2] as well as in Sopot and Gdynia in 2016 [9]. Additionally, a tendency to occurrence of heavy rainfalls of summary heights exceeding 100 mm [5] is a cause of elevated risk to urban area flooding in Three-city. This paper presents a hydraulic analysis of causes of a sea-shore washout at the Kacza river estuary in Gdynia-Orłowo during the flood of 2016. In July 2016 in the Three-city agglomeration a rainfall episode of over a day duration and 150 mm summary rainfall height occurred. It is impossible to determine precisely how the rainfall was distributed over

Fig. 1. The Kacza river estuary section with enumeration of flood- damaged places shown in Fig. 2. (image prepared by these authors on the basis of an ortophotomap from geodesic resources of Gdynia city, Gdynia Municipal Council licence No. PND.6642.1.1697.2018_2262_N, without scale)

Gdynia area and how big values of water flow rate in the river were as there is no control over the Kacza river catchment basin. However, it is probable that summary rainfall height could be similar to that measured in the same time at the station Gdańsk Oliwa (170,2 mm) and Gdańsk Osowa (161,9 mm) [5]. The so high daily rainfall amount was a direct cause that the Kacza river overflowed its banks in many sections of its full length. The freshet wave propagation resulted in the damaging of many infrastructure objects located along the river's valley. The estuary section of the river suffered most, especially the sea- shore belt together with the beach close to the Orłowo pedestrian pier at the river's estuary (Fig. 1), which appeared to be washed out along a significant length.

On the analyzed estuary section of the river (covering 800 m length from the Gdansk Bay coast) the greatest damages and losses were associated with heavy washout of banks and bed of the river and its valley beneath Szyprów street, water damming up and breaking the road embankment along Zapotoczna street, flooding the areas adjacent to the river –bed before the Orłowska street bridge as well as washout of the sea-shore belt together with the beach and touristic infrastructure below the bridge in Orłowska street. The photographs showing example damages resulting from the freshet run-off along the Kacza river estuary section are presented in Fig. 2.

Fig. 2. Damages in the Kacza river estuary area in Gdynia Orłowo as a result of the freshet in July 2016 (photos No. 1, 2, 3 – washout of sea-shore belt below Orłowska street bridge, photo No. 4 - breach in road embankment of Zapotoczna street. Location of subsequent shots – see Fig. 1. (acc. this author's archive)

In the context of the so vast damages of the river estuary and sea-shore belt an interesting question arouse as to a direct cause of the situation. Worth stressing that the flooding incidents do not depend only on freshet flow rate resulting from an increased run-off of rainfall water from the river catchment basin. On flooding danger also decide water states in particular flooded areas, and these depend not only on water flow rate but very much depend on current flow passage capacities of water-courses and their hydraulic engineering infrastructure such as bridges and culverts. The double culvert located in line of Zapotoczna street may serve as an example of such object in the Kacza river estuary section in Gdynia. During the flood of July 2016, as a result of blocking the culvert outlet by floating trees, branches and bed load, the river valley above the embankment of the Zapotoczna street filled in with water and after exceeding the top of the embankment (abt. 4 m above the river bed) suffered a washout resulting in an uncontrolled water run-off to the river bed. In this work an attempt was made to show which role for damage of the sea-shore belt and beach in Orłowo has been played by the increased (natural) rainfall run-off from the river catchment basin as well as by hydraulic engineering objects. To this end, it was necessary to work out a numerical model of the river and perform various simulations of freshet wave flow in the Kacza river bed along its estuary section. Simultaneously it should be stressed that in this work attention was paid only to potential causes of the sea-shore belt washout, but the washout phenomenon itself was not analyzed.

METHODS AND DATA

To correctly represent the complex structure of water flow over the flooded area it is necessary to carry out simulations by making use of a two-dimensional motion model of liquid. Moreover, while in the situation of stationary flow to use simplified models is sufficient, e. g. in the form of Helmholtz bi-harmonic equation [10], in the case of flood water flows varying with time the application of transient motion equations is necessary.

In the presented paper the simulations of water flow along the Kacza river bed were made with the use of a hydrodynamic model of two-dimensional flow of free-surface water. The model equations were solved by using the HEC-RAS calculation system [1], under transient flow conditions. The two-dimensional model of horizontal free-surface water flow applied in this system is a set of shallow -water flow equations [6]. The main assumption used for building the model is a slow variability of water motion . There is also assumed that vertical velocity component is negligible that results in a lack of vertical accelerations, pressure distribution is hydrostatic, and bed slope values are small. In the two-dimensional case, after neglecting momentum dissipation due to turbulence, as well as momentum dispersion resulting from velocity averaging, the form of the transient flow equations is as follows:

$$\frac{\partial h}{\partial t}+\frac{\partial(uh)}{\partial x}+\frac{\partial(vh)}{\partial y}=0 \quad (1)$$

$$\frac{\partial(uh)}{\partial t}+\frac{\partial(u^2h)}{\partial x}+gh\frac{\partial h}{\partial x}+\frac{\partial(uvh)}{\partial y}-gh(S_{ox}-S_{fx})=0 \quad (2)$$

$$\frac{\partial(vh)}{\partial t}+\frac{\partial(v\ h)}{\partial y}+gh\frac{\partial h}{\partial y}+\frac{\partial(uvh)}{\partial x}-gh(S_{oy}-S_{fy})=0 \quad (3)$$

The symbols x and y represent spatial variables, t - time, g - Earth gravity acceleration, h -water depth, u and v –flow velocity vector components averaged over the depth, S_o and S_f - terrain and energy linear slopes, respectively. The set of equations (1,2,3) is that of partial differential equations of hyperbolic type whose solution for an assumed initial-boundary conditions are the functions *u(x,y,t), v(x,y,t)* and *h(x,y,t)*. In certain cases where to neglect inertia force in the equations (2,3) is possible, the above mentioned model is simplified to the so called diffusion wave model. However, in the performed analysis such simplification was not implemented in view of a significant role of inertia forces in dynamics of freshet flow through the relatively narrow valley of the river in question and fast-varying motion conditions. In the calculation system HEC-RAS the flow equations (1,2,3) are solved by using the finite differences method [1]. Numerical solution of the equations requires to assume a space of solutions of the equations as well as boundary conditions. The solution space is composed by geometry of a surface over which water flow occurs and duration time of flow phenomenon. The geometry can be defined by assuming physical boundaries of flow, whereas the time is usually chosen on the basis of a necessary duration of simulation process. Moreover, to solve the flow equations it is necessary to define configuration of the terrain over which water flows as well as its coverage which affects hydraulic drag occurring during the motion.

The information about configuration of the terrain in the area of the Kacza river valley was taken from the numerical model prepared for the city of Gdynia (Gdynia Municipal Council licence No. PND.6642.1.1697.2018_2262_N). The model is characteristic of 5 m x 5 m horizontal mesh resolution and the average height error not greater than 0,8 m. Fig. 3 shows a visualization of the terrain of Kacza river valley elevation system in the analyzed section of its estuary. The terrain ordinates change upstream the river from 0 m on sea level at Gdansk Bay coast up to almost 16 m on the level of Szyprów street distant a little more than 800 m from the estuary. In this area the highest hills of the moraine range neighbouring the river reach 70 m above sea level. The boundary of the calculation area and its numerical mesh was so assumed as to obtain the possible highest values of water table ordinates but not exceeding river banks along the valley and to make the water flow possible only through the affluent cross-section (upper) at Szyprów street and confluent one (lower) located at Gdansk Bay coast. The numerical mesh was assumed of the density close to the terrain model resolution, by dividing the flow area into 5 m x 5 m squares.

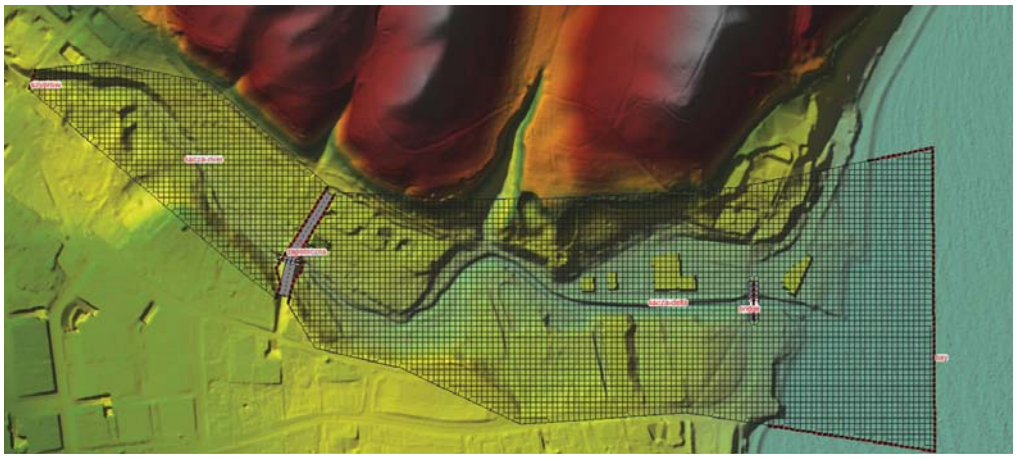

Fig. 3. The numerical model of the considered terrain around Kacza river (GMC licence No. PND.6642.1.1697.2018_2262_N) as well as the calculation area boundaries together with hydraulic engineering objects and sites where boundary conditions were set.

The limit conditions necessary to solve the hydrodynamic model equations are composed of initial conditions and boundary conditions. The first of them define values of searched functions (of filling and flow velocity) at the initial instant, i.e. before initiation of simulation of water flow phenomenon. In the carried out analyses there was assumed that the initial situation will correspond to usual (without freshet) flow conditions in Kacza river. The average multi-year flow rate in the river estuary is equal to about 0,3 m^3/s, that is two orders lower than flood flow rates which can reach even more than 20 m^3/s [9]. The so large discrepancy allows to neglect the initial (basic) flow rate in the river and to assume an initial condition in the form of a lack of water in the entire valley. The second of the limit conditions (boundary conditions) define all inflows and outflows through boundaries of the flow area. For the simulations two open sections of the river bank with set boundary conditions were selected. In the affluent cross-section (Szyprów street) there was assumed a water flow rate in the form of a hypothetical hydrograph of 20 m^3/s culmination corresponding to the flood situation in the estuary section of the river. For simulation of the flood the following temporal variability of flow rate was assumed : (T [h],Q [m^3/s]): (0,0), (3,5), (6,20), (9,20), (12,5). At the confluent cross-section(Gdansk Bay) free - water outflow into the sea was assumed. The remaining boundaries were assumed to form a close embankment simultaneously ensuring prevention against water coming to the considered areas.

In the numerical model of the river there was represented also the hydraulic engineering infrastructure located in the river bed, which determines freshet flow course through the considered river fragment. Beneath Szyprów street two important engineering objects are situated – the culvert in the road embankment of Zapotoczna street and the bridge in the line of Orłowska street. The culvert in question is fitted with two square channels of 1,5 m x 1,5 m each whose bottom from the outlet side is placed on the ordinate of 6,10 m above sea level. Simultaneously the road embankment crossing the entire river valley has the lowest ordinate of its crown located 10,0 m above sea level. Such situation results in that when the freshet wave exceeds the culvert channels passage capacity the water damming- up occurs in the valley upstream the embankment and the whole system works as a retention reservoir. However in view of that the road embankment was not designed and built as a water dam its structure and a lack of any emergency surface water draining system result in that, after filling up, water flow over the embankment top and washout of its body occur. Such situation happened during the flood of July 2016 after a partial blockage of the culvert inlet by floating wood material waste, which resulted in forming a breach in the embankment (Fig. 2, Photo 4) and in consequence leading to a collapse of the object. It resulted in an instantaneous significant rise of the flow rate in the valley below Zapotoczna street. In the numerical model of the engineering object it was made also possible to reconstruct the breach forming process.

Fig.. 4. The bridge over Kacza river in line of Orłowska street in Gdynia (a photo from this author's archive),

The second object (the bridge in line of Orłowska street) is built in the form of a reinforced concrete plate supported only on its heads (lack of abutments). Its breadth amounts to 11,0 m and the height to 1,5 m. The upper ordinate of the plate is close to that of the surrounding terrain. Below the bridge there are located pipelines which obstruct a significant part of the free cross-section area under the bridge from the side of inlet. (Fig. 4).

NUMERICAL SIMULATIONS AND DISCUSSION OF RESULTS

In the frame of the hydraulic analysis of transformation of freshet wave through Kacza river valley in its estuary section, the calculations of water flow conditions were carried out in three variants. In all three cases the same conditions of river inflow to the cross-section in the vicinity of Szyprów street, with 20 m^3/s culmination of freshet flow rate were assumed. The reconstructed phenomenon duration time was taken equal to 10 h for all the cases. In variant 1 the flow through full cross-section area of the culvert channels in the Zapotoczna street embankment as well as a lack of breach in the embankment, was assumed. Such situation results in that the maximum flow rate in the valley below this place does not exceed the river inflow culmination rate of 20 m^3/s. In variant 2 a scenario close to the episode of the flood in July 2016 was assumed ; it consisted in the decreasing of the flow passage capacity of the Zapotoczna street culvert's channels by blocking by 50% of their inlet cross-section area, that corresponds to the eye-witness accounts. There was also assumed that when water level exceeds the top of the embankment a washout of its body occurs and within an hour a breach of 15 m breadth in bottom and 8,0 m bottom ordinate over sea level is formed, that reproduces the historical event effects. To precisely reconstruct the accident was not possible due to a lack of measurements. A consequence of the so assumed scenario was the increasing of the maximum flow rate below the object over the value of the inflow culmination rate, resulting from a violent release of the water gathered (retained) in the valley (reservoir) above the road embankment. Variant 3 is identical to variant 2 as to the flow conditions through the culvert in the Zapotoczna street embankment, but the mode of hydraulic behaviour of the bridge in Orłowska street was modified. In the last variant the assumed cross-section height under the bridge was decreased by 30%, that was intended to reproduce the reduction of the cross-section directly under the bridge due to the presence of the already mentioned pipelines crossing the river valley as well as the stopping of floating wood waste and garbage in the reduced cross-section.

Fig. 5 presents example results of the transformation of freshet wave running through the estuary section of Kacza river valley (variant 2). As can be noticed, up to the instant of forming the breach in the embankment body of Zapotoczna street (at 7th hour of the simulation process) continuous filling in the valley above the embankment can be observed. After damaging the object a violent water outflow through the breach occurs, that results in gradual emptying the reservoir and in the same time instantaneous increasing the flow rate below the object as well as short- lasting spreading the range of flooding in this area.

During a flood, the valley above the embankment, the area situated directly below this object as well as flooding flats around the Kacza river estuary are usually flooded. Left-bank developed area of the Kacza river delta are also flooded, that was also observed during the historical event. However in the presented example simulation the terrain of the sea-shore belt and beach separated from the flooded area by Orłowska street did not suffer any flooding, which shows that the course of the investigated event was different from real one. This question is discussed in the further part of the paper. To find direct causes of damage of the sea shore and beach one should consider maximum parameters of a freshet wave appearing before the Orłowska street bridge which is placed directly above the river estuary and beach. The list of maximum values of water level ordinate and flow rate in three characteristic cross-sections of the valley, i.e. above and below the Zapotoczna street embankment as well as before the Orłowska street bridge, are presented in Tab. 1.

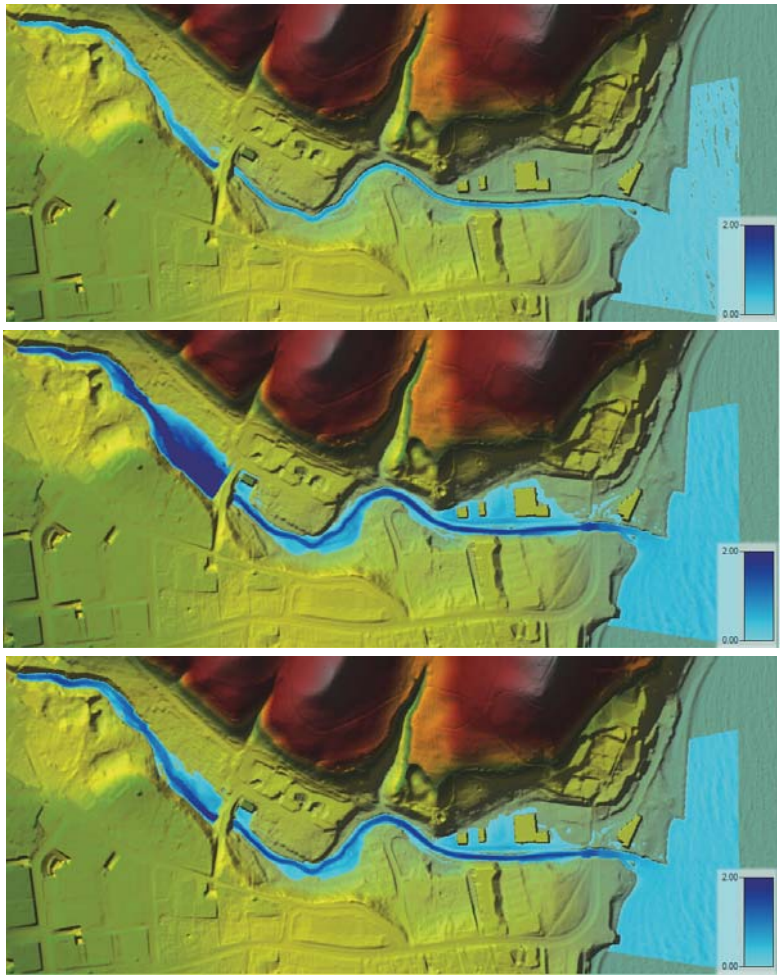

Fig. 5. Changes in the depth [m] and range of the flooded area, variant 2 ; after 2, 7 and 10 h runoff duration time in Kacza river, respectively

Tab. 1. Maximum parameters of freshet wave in Kacza river calculated in the selected cross-sections of the river valley

Variant	Above Zapotoczna street		Below Zapotoczna street		Above Orłowska street	
	Water level ordinate Hmax [m above sea level]	Flow rate Qmax [m³/s]	Water level ordinate Hmax [m above sea level]	Flow rate Qmax [m³/s]	Water level ordinate Hmax [m above sea level]	Flow rate Qmax [m³/s]
1	9.98	20.00	7.41	20.00	2.51	19.97
2	10.38	20.00	7.44	27.49	2.80	25.48
3	10.38	20.00	7.44	27.49	3.06	24.39

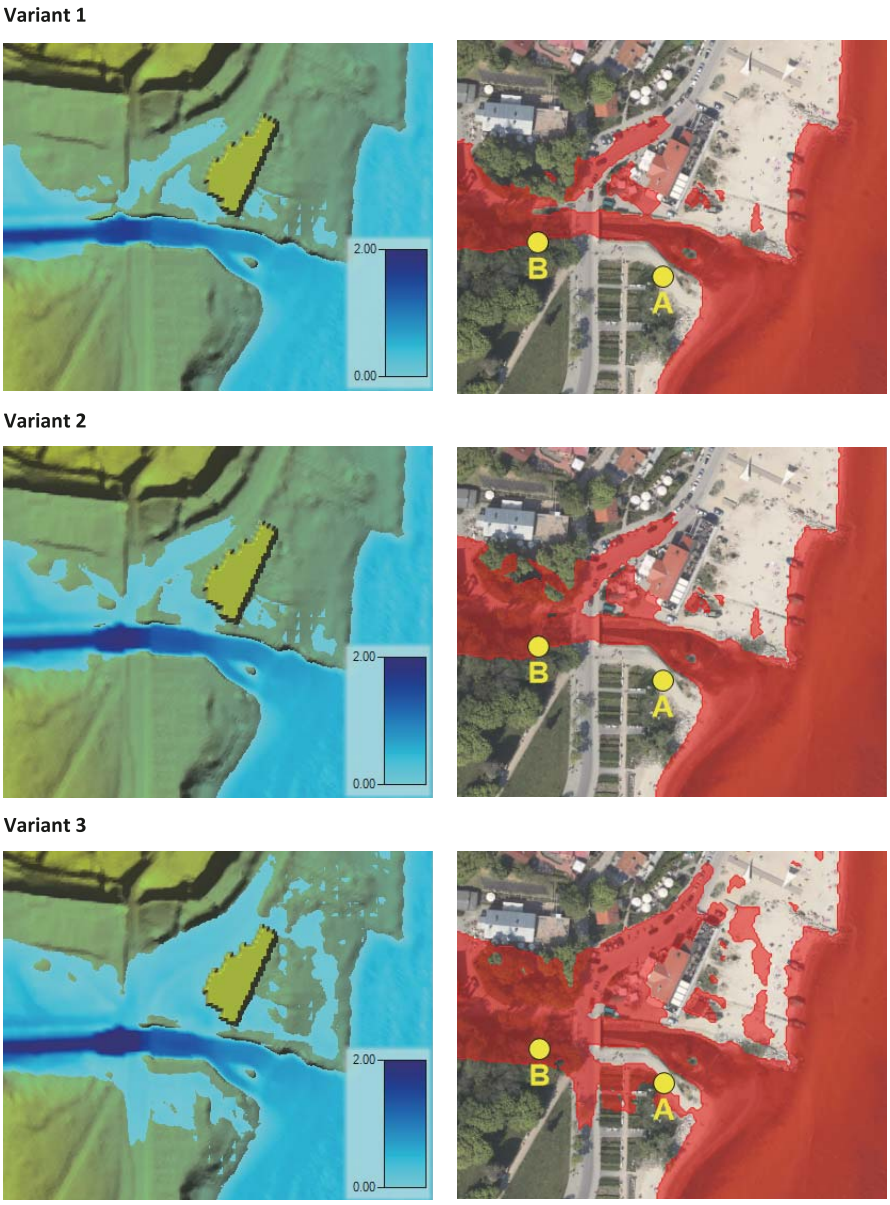

Fig. 6. Maximum depths [m] and range of flooded area in the region of Kacza river estuary and Gdynia- Orłowo beach together with depicted measurement points of maximum water level ordinates after the flood in July 2016 (A, B) (images prepared by this author on the basis of ortophotomap from municipal geodesic resources of Gdynia, Gdynia Municipal Council licence No. PND.6642.1.1697.2018_2262_N, without scale)

Comparing particular variants one can observed distinct differences in maximum values of the freshet wave hydraulic parameters. First of all values of the culmination flow resulting from the damage in the road embankment of Zapotoczna street (variant 2 and 3) are, below the damaged object, significantly greater (by almost 7.5 m³/s) than the crest of the wave running through the intact object (variant 1). The maximum flows increased as a result of the damage are also observed in the river estuary above Orłowska street. However in variant 3 where the limited flow passage capacity under the bridge is taken into account the reduction of freshet wave culmination is greater due to the greater water damming-up before the bridge and the greater water retention in the flooded areas in the river valley. In the valley cross-section before Orłowska street the damage of the road embankment results, in case of the full water flow cross-section under the bridge (variant 2), in the water damming up to the ordinate of 2.80 m above sea level, that is greater by almost 0.3 m than that resulting from the simulation without taking into account the object's damage (variant 1), but still not exceeding the bridge plate top ordinate of 2.95 m above sea level and that of the adjacent terrain. This results in a lack of water flow over the road toward the beach. It means that the freshet wave itself and the forming of the breach could not be the only cause of the observed washout in the river estuary area.

As results from the calculations, a factor of a decisive impact on the excessive damming-up of the water and its breaking through Orłowska street was the reduction in the free cross-section area under the bridge resulting from the installation of the pipelines across the river bed (Fig.4). The fact of taking into account the reduction of the free cross-section under the bridge during

Fig. 7. Maximum range of flooded area along the whole analyzed section of Kacza river in variant 3 together with depicted measurement points (A, B, C, D, E) of maximum water level ordinates after the flood in July 2016 (image prepared by this author on the basis of ortophotomap from municipal geodesic resources of Gdynia, Gdynia Municipal Council licence No. PND.6642.1.1697.2018_2262_N, without scale)

the numerical freshet run-off simulation (variant 3) results in a rise of water level ordinate up to 3.06 m above sea level and water run-off to the beach over the surface of the Orłowska street.

The differences in the calculated range of flooded area near the Orłowska street bridge and the beach are shown for particular simulation variants in Fig. 6. As can be seen, in successive variants the flooded area range increases and the zones of potential washing -out the sea shore belt and beach spread. Worth mentioning, that the flooded areas indicated in the last graph of Fig. 6 correspond to the location of the washout areas observed after the flood, shown in Fig. 1 (No. 1, 2 and 3). Simultaneously, neither in variant 1 nor 2 the flow streams north from the visible building and those on the southern side over the right bank of the river close to its estuary, were reproduced. This way the hypothesis has been proved on the decisive role of the reduced flow passage capacity of the cross-section under the Orłowska street bridge in forming the freshet run-off in the area of Kacza river estuary and its impact on the flood damages resulting in the washout of the sea-shore belt in Gdynia –Orłowo .

In order to quantitatively verify the numerical simulation results as well as simultaneously evaluate the model, a comparison was made between the calculated maximum water level ordinates and the geodesic-measured ordinates of maximum water level in the valley after the flood in July 2016. The measurements were conducted by a team of Gdansk University of Technology during its on-site visit [9]. The points where the measurements were taken are denoted by letters A through E in Fig. 6 and 7. Point A is placed beneath Orłowska street on the right side of the river away its main bed ; point B is placed above the Orłowska street bridge on the right flooding area of the river ; point C is situated on the left side of the river directly at its main bed; point D lays directly below the road embankment of Zapotoczna street; point E is placed above the road embankment. The common list of measurement and calculation results is given in Tab. 2.

Tab. 2. Geodesic measurements of maximum water level ordinates after the flood in July 2016, and results of respective simulation calculations

Measurement point	Water level ordinate [m] over sea level			
	measurement	simulation variant 1	simulation variant 2	simulation variant 3
A	1.75	brak	brak	1.72
B	3.18	2.93	3.04	3.17
C	3.74	3.62	3.77	3.77
D	7.45	7.15	7.41	7.41
E	10.34	9.98	10.38	10.38

Comparing the particular variants, one is able to find differences between the measured and calculated values as well as between the simulation results themselves. Starting the analysis from the upper run of the analyzed section of the river one can observe that in variant 1 where the simulation of blocking the culvert in the Zapotoczna street embankment (point E) is omitted, water run-off over the embankment top (10.0 m above sea level) does not occur and no washout of its body happens. Such situation was reproduced in variants 2 and 3 where the calculated maximum water level ordinate is close to that observed. The difference between variant 1 and variant 2 and 3 can be also seen directly below the embankment (point D). In this place where occurrence of the breach in the embankment is not reproduced in the calculations (variant 1) the calculated value of water level ordinate is underestimated by 0.3 m in comparison to that measured. After taking into account the damage (variant 2 and 3) the difference decreases to 0.04 m in both the cases, that reflects well on correctness of reproduction of real situation by these simulations. The situation in the middle part of the analyzed section (point C) turned out to be similar. Here the simulation result of maximum water level ordinate in variant 1 is also underestimated by 0.12 m against that measured, whereas the taking into account presence of the breach gives

the same results in variant 2 and 3, however greater than that measured by 0.03 m. While in the points E, D and C there were observed differences between the results from variant 1 (without the breach) and those from variants 2 and 3 (with the breach), in points B and A some difference additionally appears between the simulation results from variant 2 (with the breach in the Zapotoczna street embankment and the passable cross-section area under the Orłowska street bridge) and variant 3 (with the breach and the partly blocked cross-section passage area under the bridge). And, in point B it can be observed that, out of the three simulations, the result from variant 3 is closest to that measured, and in point A (placed directly near the beach, below the bridge) the flooding of this area was reproduced only in variant 3, whereas neither in variant 1 nor in variant 2 the flow over the bridge was properly reproduced. Generally, only the results achieved in the last calculation variant may be considered quantitatively close to the measurements, therefore credible, that has been the aim of validation of the model.

CONCLUSIONS

The presented analysis was aimed at investigation of a role of natural freshet wave resulting from extreme rainfall episode of July 2016 in Kacza river basin as well as hydraulic engineering infrastructure (culverts, bridge) located in the river valley estuary section in forming the washout of sea-shore zone and beach in Gdynia – Orłowo. To reach this aim it was necessary to prepare a numerical model of the river and conduct a few simulation variants of flood run-off. The performed and verified hydrodynamic calculations made it possible to offer the following conclusions summing up the investigations in question :

1. The application of the two-dimensional hydrodynamic model in the form of shallow water flow equations makes it possible to precisely reproduce course of transformation of freshet wave both in natural river beds and valleys and in confluents with engineering infrastructure.
2. The main cause of the flood in July 2016 over the Kacza river estuary section in Gdynia was an increased rainfall run-off from the river catchment basin. As the calculations (variant 1) proved, it could be the cause of flooding the areas above the embankment of Zapotoczna street and the valley (partially developed) above the bridge in line of Orłowska street. However it could not cause the water flowing over the top of Zapotoczna street embankment and forming the breach in it (that was really observed) and also the water flowing over the bridge in line of Orłowska street and the washout of sea-shore belt and beach because this infrastructure object (culvert) had a sufficient flow passage capacity.
3. The blockage of the culvert inlet by floating broken wood waste, as indicated by eye- witnesses of the damage, should be deemed the direct cause of forming the breach in the Zapotoczna street embankment, that was confirmed by the calculations in variant 2. Simultaneously, as the numerical simulations proved, the increased water run-off after breaking the Zapotoczna street embankment could not cause the water flowing over the Orłowska street bridge, and thus could not prevent to a large extent against occurrence of the washout of sea-shore belt and beach.
4. The reduction in the cross-section of flow passage area under the bridge due to the engineering infrastructure (pipelines) installed across the river valley above the bridge, proved by the calculations in variant 3, should be taken as the direct cause of the excessive water damming-up before the Orłowska street bridge and consequently the water overflowing above it towards the beach. Only the cumulated effect of the natural rainfall freshet, the breach in the Zapotoczna street embankment and the reduced cross-section of flow passage area under the bridge caused that the ordinate of Orłowska street was exceeded which in consequence triggered the water flowing down the reinforcements of sea shore and beach toward the sea, which resulted in their damage.
5. The performed simulation calculations in variant 3 were verified by comparing their results with geodesic measurements. The good conformity of calculation results of maximum water table ordinates with the observations proves that the carried out calculations and the way in which scenario of events was assumed, were correct. The achieved calculation results in the form of localization of flooded areas of sea-shore belt are in compliance with the places where damages on the beach and reinforcements were observed during on-spot inspections after the flood ; all that makes it possible to

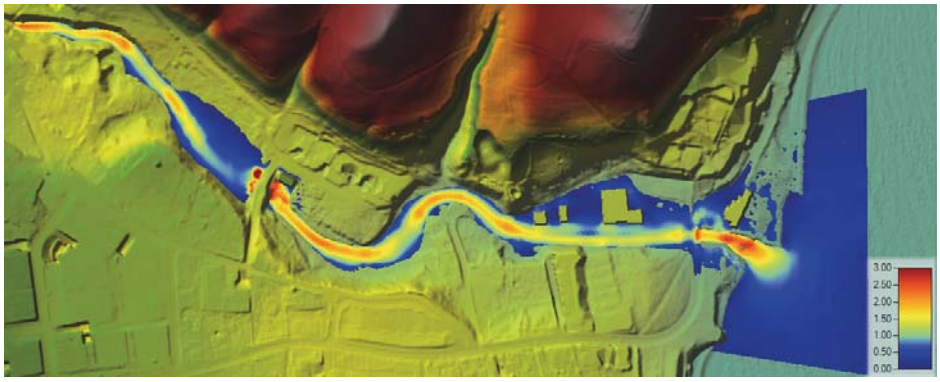

Fig. 8. Maximum calculated flow velocities [m/s] along the estuary section of Kacza river after the flood in July 2016, variant 3

consider the presented numerical analysis credible.

In conclusion it should be clearly stressed that the fact itself of occurrence of the flooding of the analyzed terrain does not allow to arbitrarily conclude that the washout did happen. The presented maps of flooded areas and/or water depth distributions may only indicate areas prone to washout with predominance of erosion. To confirm occurrence of a washout it is necessary to determine conditions for triggering off soil grains motion, e.g. a limit depth, limit velocity or limit shear stresses [4]. However this question has not been a subject of investigations in the presented work though the results of the worked out modelling could be used to this end by comparing the calculated velocity distributions (Fig. 8) with the above mentioned limit velocities, i. e. such whose exceeding commences motion of eroded material.

BIBLIOGRAPHY

1. Brunner, G.W.: *HEC-RAS, River Analysis System Hydraulic Reference Manual*. Computer Documentation Report, Report No. CPD-69, US Army Corps of Engineers, Hydrologic Engineering Center (HEC) 2010

2. Majewski W.: *Urban flash flood in Gdansk – 2001 Case study*. Meteorology Hydrology and Water Management Research and Operational Applications, 4(2), 2016, pp. 41-49.

3. Mikos-Studnicka P., Szydłowski M.: *The Influence of Hydrological Data Quality on Estimating The Runoff From City Catchment On The Example Of Strzyża Stream In Gdańsk*, Ecological Engineering, 44, 2015 , pp. 139-153.

4. Mrokowska M. M., Rowiński P. M., Książek L., Strużyński A., Wyrębek M., Radecki-Pawlik A.: *Laboratory studies on bedload transport under unsteady flow conditions*, Journal of Hydrology and Hydromechanics, 66(1), 2018, pp. 23-31. doi: https://doi.org/10.1515/johh-2017-0032

5. Szpakowski W., Szydłowski M. : *Probable Rainfall in Gdańsk in View of Climate Change*. Acta. Sci. Pol., Form. Cir., 17(3), 2018, pp. 175-183.

6. Szydłowski M., Szpakowski W., Zima P.: *Numerical simulation of catastrophic flood: the case study of hypothetical failure of the Bielkowo hydro-power plant reservoir*, Acta Geophysica, 61(5), 2013, pp. 1229

7. Weinerowska-Bords K., Szydłowski M, Bielecka K. : *Analysis of temporal and spatial variability of precipitation in the Strzyza catchment in Gdańsk*, Inżynieria Morska i Geotechnika, 6. , 2012

8. Weinerowska-Bords K. : *Development of Local IDF-formula Using Controlled Random Search Method for Global Optimization*. Acta Geophysica, 63(1), 2014, pp. 232-274.

9. Widerski T., Szydłowski M., Szpakowski W. : *Measurement and analysis of a flood wave propagation on the Kacza River in Gdynia in Northern Poland*. 17th International Multidisciplinary Scientific GeoConference SGEM2017, Water Resources. Forest, Marine and Ocean Ecosystems, 2017, pp. 453-460.

10. Zima P. : *Modeling of the Two-Dimensional Flow Caused by Sea Conditions and Wind Stresses on the Example of Dead Vistula*. Polish Maritime Research, Vol. 25, iss. s1(97), 2018, pp. 166-171.

CONTACT WITH THE AUTHOR

Michał Szydłowski
e-mail: mszyd@pg.edu.pl

Gdańsk University of Technology
Faculty of Civil and Environmental Engineering
11/12 Narutowicza St.
80 - 233 Gdańsk
Poland